Protein misfolding and demyelination as major contributing factors for the pathophysiology of genetic neurological pediatric disorder MPS IIIC

Mahsa Taherzadeh

Faculty of Medicine

Department of Anatomy and Cell Biology

McGill University, Montreal

Quebec, Canada

April 2023

A thesis submitted to McGill University in partial fulfillment of the requirements of the degree of Doctor of Philosophy

Dedication

To

My father, **Mehdi**

And in the memory of

Victims of Iranian revolution of **Woman, Life, Freedom.**

Contents

LIST OF FIGURES

LIST OF TABLES

LIST OF ABBREVIATIONS

AP: Adaptor proteins

APC (CC-1): Adenomatous polyposis coli (APC) clone CC1

ARSA: Arylsulfatase A

ARF: ADP-ribosylation factor

BDNF: Brain-derived neurotrophic factor

BSA: Bovine serum albumin

Cas9: CRISPR associated protein 9

CC: Corpus callosum

CCAC: Canadian Council on Animal Care

CMA: Chaperone-mediated autophagy

CMV: Cytomegalovirus

CNPase: 2′,3′-cyclic nucleotide 3′-phosphodiesterase

CNS: Central Nervous System

CRISPR: Clustered Regularly Interspaced Short Palindromic Repeats

CS: chondroitin sulfate

CTSA: Cathepsin A

CT-scan: Computed tomography-scan

CTSD: Cathepsin D

CTSH: Cathepsin H

DIV: Day in vitro

DNA: Deoxyribonucleic acid

DS: Dermatan sulfate

ECM: Extracellular matrix

EGFP: Enhanced green fluorescent protein

EM: Electron microscopy

ER: Endoplasmic reticulum

ERAD: Endoplasmic reticulum-associated degradation pathway

FGF: Fibroblast growth factor

GABA: Gamma aminobutyric acid

GAG: Glycosaminoglycan

GalC: Galactocerebroside

GGAs: Golgi-localizing, γ-adaptin ear domain homology

GlcA: Glucuronic acid

GlcAT: Glucuronyltransferase

GlcNAc: N-acetylglucosamine

GlcA: Glucuronic acid

HA: Hyaluronic acid

HGSNAT: Heparan sulphate acetyl-CoA: α-glucosaminide N-acetyltransferase

HS: Heparan sulphate

HSPG: Heparan sulfate proteoglycan

IFNγ: Interferon-γ

ICC: Immunocytochemistry

IdoA: L-iduronic acid

IGF-1: Insulin-like growth factor 1

IHC: ImmunohistochemistryLA

IS: Iduronate sulfate

KD: Krabbe disease

KI: Knock-in

KO: Knock-out

KS: Keratan sulfate

LAMP: Lysosomal associated membrane protein

LIMP-2: Lysosome integral membrane protein 2

LPS: Lipopolysaccharide

LSD: Lysosomal storage disorder

LV: Lentivirus

M6P: Mannose-6-phosphate

MAG: Myelin-associated glycoprotein

MBP: Myelin basic protein

MEF: Murine embryonic fibroblasts

MIP1-α: Macrophage inflammatory protein-1 alpha

MLD: Metachromatic leukodystrophy

MOG: Myelin oligodendrocyte glycoprotein

MPS: Mucopolysaccharidosis

MPS IIIC: Mucopolysaccharidosis type III C

Myt1: Myelin transcription factor 1

NF-M: Neurofilament medium chain

NG2: Nerve/glial antigen 2

NCL: Neuronal ceroid lipofuscinosis

NDST: N-deacetylase/N-sulfotransferase

NPC: Neural progenitor cells

NPC: Niemann–Pick type C

OL: Oligodendrocyte

Oligo2: Oligodendrocyte transcription factor2

PAPS: 3′-phosphoadenosine-5′-phosphosulfate

PC: Pharmacological chaperone

PDGF: Platelet-derived growth factor

PNS: Peripheral nervous system

PSD: Postsynaptic density

PSD-95: Postsynaptic density protein 95

RNA: Ribonucleic acid

SNAREs: Soluble N-ethylmaleimide-sensitive factor attachment protein receptor

Syn1: Synapsin 1

TEM: Transmission electron microscopy

TFEB: Transcription factor EB

TGN: Trans-Golgi network

TLR: Toll-like receptor

TNF-α: Tumor necrosis factor-alpha

UPR: Unfolded protein response

vGAT: Vesicular GABA transporter

vGLUT1: Vesicular glutamate transporter

WT: Wild type

ABSTRACT

Mucopolysaccharidosis type IIIC (MPS IIIC, Sanfilippo disease type C) is a rare neurodegenerative lysosomal storage disorder caused by mutations in heparan sulfate acetyl-CoA: α-glucosaminide N-acetyltransferase (HGSNAT) enzyme involved in degradation of heparan sulfate (HS). MPS IIIC starts with developmental delay, leading to childhood dementia and death before adulthood. No cure or effective treatment is currently available.

To understand pathophysiology of MPS IIIC and establish biomarkers of the disease, I studied a novel HGSNAT-deficient mouse strain (*Hgsnat*^{P304L}) expressing the enzyme with the analog of a human missense mutation (Pro304Leu). This mutation results in the enzyme misfolding.

In the first chapter of my thesis, I describe the analysis of pathophysiological changes in the Central Nervous System (CNS) in the *Hgsnat*^{P304L} model and compare them to those in a knock-out MPS IIIC (*Hgsnat-Geo*) mouse that has been previously developed and characterized in our laboratory (Martins *et al.* 2015). I used the Y-maze behavioral test to characterize memory deficits and transmission electron microscopy (TEM) and immunocytochemistry (ICC) to study synaptic pathology in CA1 pyramidal neurons and cultured hippocampal neurons. Alterations in gene expression levels in the hippocampi of *Hgsnat-Geo* and *Hgsnat*^{P304L} mice were analyzed by bulk mRNA sequencing. Our results demonstrated that *Hgsnat*^{P304L} mice had a more severe clinical phenotype compared to *Hgsnat-Geo.* My study also demonstrated that aggravation of the CNS pathology and clinical phenotype occurred because of the damaging effect of the misfolded HGSNAT mutant protein on neurons that caused impairment of the proteasomal system for degradation of misfolded proteins and lead to accelerated neuronal dysfunction and neurodegeneration.

In the second chapter of my thesis, I describe the discovery of myelination defects in the MPS IIIC. Since neuroinflammation is one of the hallmarks of MPS IIIC and activated microglia can potentially damage white matter tracts, I studied myelination and white matter integrity in the brains of *Hgsnat*^{P304L} mice and post-mortem brain samples of human MPS IIIC patients. I identified a drastic decrease in the levels of myelin-associated proteins, including Myelin-Associated Glycoprotein (MAG) and Myelin Basic Protein (MBP) in the brain tissues of MPS IIIC human patients and MPS IIIC mice. Using transmission electron microscopy (TEM), I demonstrated a reduced thickness of myelin layers in neuronal axons. I further showed that demyelination in MPS IIIC is associated with pathological changes in oligodendrocytes (OLs), which show a lysosomal storage phenotype and mitochondrial damage. My data, for the first time, reveals that demyelination occurs in an MPS III disorder and suggests that evaluation of white matter density can be used to test pathological changes in the brains of human patients.

Overall, the results of my research provide novel insights into mechanisms underlying MPS IIIC disease and can potentially help to establish novel therapies. Besides, defects in synaptic morphology, behavior, and myelination could become useful biomarkers to evaluate the efficacy of therapies or a clinical course of the disease.

RÉSUMÉ

La mucopolysaccharidose de type III C (MPS IIIC, maladie de Sanfilippo de type C) est une maladie de surcharge lysosomale rare et neurodégénérative causée par des mutations dans le gène codant pour l'enzyme acétylCoA: alpha-glucosaminide N-acétyltransférase (HGSNAT) impliquée dans la dégradation de l'héparane sulfate (HS). La présentation clinique de la MPS IIIC commence par un retard de développement, entraînant une démence infantile et la mort avant l'âge adulte. Aucun traitement curatif n'est actuellement disponible.

Pour comprendre la physiopathologie de la MPS IIIC et établir des biomarqueurs de la maladie, j'ai étudié une nouvelle souche de souris déficiente en HGSNAT (*Hgsnat*^{P304L}) exprimant l'enzyme avec l'analogue d'une mutation faux-sens humaine (Pro304Leu). Cette mutation entraîne un mauvais repliement de l'enzyme.

Dans le premier chapitre de ma thèse, j'ai fait une description physiopathologique du système nerveux central (SNC) du modèle murin HgsnatP304L que je compare avec le modèle murin knock-out MPS IIIC (*Hgsnat-Geo*) qui a été précédemment développé et caractérisé dans notre laboratoire. Pour cela, j'ai utilisé le test comportemental Y-maze pour caractériser les déficits de mémoire ainsi que la microscopie électronique à transmission (TEM) et l'immunocytochimie (ICC) pour étudier la pathologie synaptique dans les neurones pyramidaux CA1 et hippocampiques en culture. Les altérations des niveaux d'expression génique dans l'hippocampe des souris *Hgsnat-Geo* et *Hgsnat*^{P304L} ont été analysées par le séquençage de l'ARN. Nos résultats ont démontré que les souris *Hgsnat*^{P304L} avaient un phénotype plus sévère que *Hgsnat-Geo* et que cette aggravation de la pathologie serait secondaire au mauvais repliement de la protéine mutante HGSNAT sur les neurones causant ainsi l'altération du système protéasomal impliquée dans la dégradation des

protéines mal repliées et conduisant à un dysfonctionnement neuronal accéléré et à la neurodégénérescence.

Dans le deuxième chapitre de ma thèse, j'ai caractérisé les défauts de myélinisation observés dans la MPS IIIC. Étant donné que la neuroinflammation est l'une des caractéristiques de la MPS IIIC et que la microglie activée peut potentiellement endommager les voies de la substance blanche, nous avons étudié la myélinisation et l'intégrité de la substance blanche dans le cerveau de souris *Hgsnat*^{P304L} et des échantillons de cerveau post-mortem de patients humains atteints de MPS IIIC. J'ai identifié une diminution drastique des niveaux de protéines associées à la myéline, y compris la glycoprotéine associée à la myéline (MAG) et la protéine basique de la myéline (MBP) dans les tissus cérébraux des patients humains MPS IIIC et des souris MPS IIIC par immunohistochimie (IHC). En utilisant l'analyse TEM, j'ai confirmé l'épaisseur réduite des couches de myéline dans les axones neuronaux. J'ai aussi montré que la démyélinisation dans la MPS IIIC est associée à des modifications pathologiques des oligodendrocytes (OLs), qui présentent un phénotype de stockage lysosomal et des dommages mitochondriaux. Pour la première fois, nos données mettent en évidence la démyélinisation dans la MPS III, ce qui suggère que l'évaluation de la densité de matière blanche pourrait être utilisée pour évaluer les changements pathologiques dans le cerveau des patients humains.

En conclusion, mes résultats de recherche fournissent de nouvelles informations sur les mécanismes sous-jacents de la MPS IIIC qui pourraient potentiellement contribuer au développement de nouvelles thérapies. En outre, les défauts de morphologie synaptique, de comportement et de myélinisation pourraient devenir des biomarqueurs utiles pour évaluer l'efficacité des thérapies ou l'évolution clinique de la maladie.

ACKNOWLEDGEMENT

First and foremost, I would like to express my deepest gratitude to my supervisor, Prof. Alexey V. Pshezhetsky, for his continuous support and encouragement throughout my Ph.D. journey. Over the course of my Ph.D. studies, I have benefited greatly from his insights, technical knowledge, and expertise. His mentorship has improved the quality of my research and helped me develop critical skills that I will benefit in my future career. I will always remember and appreciate his contributions to my success.

I would like to extend my sincere gratitude to my co-supervisor, Prof. Carlos Morales, for his insightful comments, valuable suggestions, and constructive feedback. I would also like to thank my committee meeting members, Dr. Kennedy, Dr. Rosignel, and Dr. Bernard. Their insightful suggestions have helped me refine and improve my research quality.

I would like to express my heartfelt appreciation to my former and current lab members, Rachel Héon-Roberts, Annie LA Nguyen, Poulome Bose, Travis Moore, Afitz da Silva, Kalley Kho, Xuefang Pan, Patricia Dubot, Antoine Caillon, Gustavo Viana, and Suzanne Samarani. I am grateful for their support, encouragement, and collaboration, which have contributed significantly to my research and personal growth. I also extend my special thanks to Ekaterina Demina, who generously shared her expertise and taught me many lab techniques. Additionally, I would like to express my deep gratitude to Irene Londono. Her dedication and guidance provided me with essential support during my Ph.D. program. I feel truly fortunate to have had the opportunity to work alongside such a dedicated and knowledgeable individual, and I am profoundly appreciative of her invaluable contributions.

This work would not have been possible without our collaborators. Therefore, I would like to express my sincere thanks to Dr. Christian Beauséjour and Dr. Gaël Moquin-Beaudry for their valuable contribution in the production of LV-HGSNAT-GFP and LV-P311L-HGSNAT-GFP. I also extend my appreciation to Jeannie Mui for her assistance with TEM, Dr. Elke Küster-Schöck for her support with imaging microscopy, and Dr. Marisol Perez Marcogliese and Véronique, the personnel from the CHU Sainte-Justine animal facility, for their dedicated animal care during this thesis project.

I want to express my deepest appreciation to my family, including my mother Minou, my father Mehdi, my brother Meisam, and my sister Mina, for their unwavering love and support. Specifically, I want to thank my parents for their continuous encouragement, guidance, and backing throughout my entire life. They made countless sacrifices to ensure that I received the best education and could follow my aspirations.

Losing my father during my Ph.D. program was an incredibly difficult experience. His passing left a void in my life that I thought I could never fill. Continuing my Ph.D. program was a tremendous challenge, and there were times when I felt overwhelmed and unsure if I could carry on. However, with the help of my husband, Amin, who provided me with unwavering support and encouragement, I was able to find the strength to continue my Ph.D. program. His love, compassion, and understanding were a constant source of comfort, and his belief in me gave me the strength to carry on. I am deeply grateful to my husband for his unwavering support during this difficult time.

CONTRIBUTION TO ORIGINAL KNOWLEDGE

In order to study pathophysiology of MPS IIIC, establish biomarkers of the disease and develop therapies, two transgenic strains of mice deficient in HGSNAT, a knock-in mouse expressing the enzyme with human missense mutation P311L mutation that results in the enzyme misfolding (*Hgsnat*^{P304L}) and a knockout mouse (*Hgsnat-Geo*) (Martins *et al.* 2015) have been generated by our laboratory. In my doctoral research project, I performed a comparative analysis of pathological changes in the brains of *Hgsnat-Geo* and *Hgsnat*^{P304L} mouse models of MPSIIIC.

I used behavioral tests to characterize memory deficits in mice, and TEM and immunocyto/immunohistochemistry to study synaptic pathology in cultured hippocampal and CA1 pyramidal neurons. I demonstrated that synaptic defects are more pronounced in *Hgsnat*^{P304L} mice compared to *Hgsnat-Geo* and demonstrated that rapid progression of CNS pathology in the *Hgsnat*^{P304L} model is associated with increased ER stress in neurons triggered by the expression of misfolded HGSNAT. Using mRNA sequencing data and analyses of cultured neurons derived from *Hgsnat-Geo* mice overexpressing misfolded HGSNAT P304L mutant, I confirmed this hypothesis. Altogether, our results demonstrated, for the first time, the dominant-negative effects of the misfolded HGSNAT Pro304Leu protein variant and showed that defects in synaptic morphology, behavior, and indicators of the ER stress may become useful biomarkers to evaluate efficacy of therapies for MPS IIIC.

In this thesis, I also demonstrated that white matter injury and axonal demyelination play an important role in pathophysiology of MPS III. I analyzed axonal myelination and white matter density in the brains of *Hgsnat*^{P304L} mice and post-mortem brain samples of MPS IIIA, C and D patients by immunohistochemistry and found reduced levels of myelin-associated proteins. Results

of my experiments also revealed a reduction in thickness and structural defects in axonal myelin sheaths in the brains of *Hgsnat*^{P304L} mice, and two human patients compared to healthy controls.

Further, I characterized pathological changes in the oligodendrocytes in the corpus callosum of *Hgsnat*^{P304L} mice and found that these cells revealed numerous enlarged lysosomes containing either heparan sulfate or "zebra bodies" consistent with the accumulation of lipids and myelin fragments. Finally, I demonstrated that oligodendrocytes in the corpus callosum of *Hgsnat*^{P304L} mice were scarce and lacked maturation. Together, my experiments established that demyelination of axons is a novel important biomarker of disease progression in MPS III.

CONTRIBUTION OF AUTHORS

During the development of my doctoral project, I participated in the following publications:

1. Mahsa Taherzadeh, Erjun Zhang, Irene Londono, Sheng-Kwei Song, Timothy E. Kennedy, Carlos R. Morales, Zesheng Chen, Gregory A. Lodygensky and Alexey V. Pshezhetsky. Severe Neuronal Demyelination in Sanfilippo Disease. (In communication, bioRxiv: https://doi.org/10.1101/2023.04.12.536631)

Contribution of authors:

Mahsa Taherzadeh: Data curation, Formal analysis: performed statistical analyses and image processing, Methodology, Validation, Visualization, Investigation: curated and genotyped mice, collected and processed mouse tissues, performed analyses of samples by IHC, TEM, and immunoblots.

She conducted experiments and created visual representations in the form of Figure 1, Figure 3, Figure 4, Figure 5, Figure 8, Figure 9, and Figure 10. These figures illustrate my specific contributions to the project.

Erjun Zhang: Formal analysis, Investigation, Methodology

Irene Londono: Methodology

Sheng-Kwei Song: Methodology

Timothy E. Kennedy: Conceptualization, Writing - review & editing.

Carlos R. Morales: Conceptualization, Investigation, Methodology, Resources, Validation, Visualization, Writing - review & editing.

Zesheng Chen: Investigation, Methodology, Writing - review & editing.

Gregory A. Lodygensky: Conceptualization, Investigation, Methodology, Resources, Validation, Visualization, Writing - review & editing.

Alexey V. Pshezhetsky: Conceptualization, Formal analysis, Funding acquisition, Methodology, Project administration, Supervision, Visualization, Writing - original draft, Writing - review & editing corresponding author.

2. Xuefang Pan*, **Mahsa Taherzadeh***, Poulomee Bose, Rachel Heon-Roberts, Annie L.A. Nguyen, TianMeng Xu, Camila Para´, Yojiro Yamanaka, David A. Priestman, Frances M. Platt, Shaukat Khan, Nidhi Fnu, Shunji Tomatsu, Carlos R. Morales, and Alexey V. Pshezhetsky. Glucosamine amends CNS pathology in mucopolysaccharidosis IIIC mouse expressing misfolded HGSNAT. Journal of Experimental Medicine 2022 Vol. 219 Issue 8 Pages e20211860.
*X. Pan and M. Taherzadeh contributed equally to this paper.

Contribution of authors:

Mahsa Taherzadeh: Data curation, Formal analysis, Investigation, Methodology, Software, Validation, Visualization, Writing - original draft, Writing - review & editing (Prepared neuronal cell cultures, performed immunofluorescence analyses of samples with confocal, and electron microscopes, performed western blots, collected and processed mouse tissues, measured enzyme activity in cells and mouse tissues, sub-cloned mutant *Hgsnat* from pENTR1A plasmid into Plenti plasmid, produced virus and performed transduction experiments, processed samples for flow cytometry, performed the behavior tests (Y-maze), analyzed RNA sequence data, performed statistical analyses and microscope image processing).
She conducted experiments and created visual representations in the form of Figure 1 (A, B, and C), Figure 2 (F), Figure 3 (G and H), Figure 5 (A, B, C, and E), and Figure 6 (A, B, and C). These figures illustrate my specific contributions to this paper.

Xuefang Pan: Data curation, Formal analysis, Investigation, Methodology, Validation, Visualization, Writing - original draft, Writing - review & editing.
Poulomee Bose: Formal analysis, Investigation, Validation, Writing - original draft, Writing - review & editing.
Rachel Heon-Roberts: Formal analysis, Investigation, Resources, Writing - review & editing.
Annie L.A. Nguyen: Formal analysis, Investigation, Methodology, Writing - original draft, Writing - review & editing.
TianMeng Xu: Data curation, Formal analysis, Investigation, Methodology, Validation, Writing - review & editing.
Camila Pará: Investigation, Methodology, Writing - review & editing.
Yojiro Yamanaka: Methodology.

David A. Priestman: Formal analysis, Investigation, Writing - review & editing.
Frances M. Platt: Formal analysis, Investigation, Methodology, Writing - review & editing.
Shaukat Khan: Data curation, Formal analysis, Investigation, Validation.
Nidhi Fnu: Methodology, Validation.
Shunji Tomatsu: Data curation, Investigation, Methodology, Project administration, Resources, Supervision, Validation, Writing - review & editing.
Carlos R. Morales: Conceptualization, Investigation, Methodology, Resources, Validation, Visualization, Writing - review & editing.
Alexey V. Pshezhetsky: Conceptualization, Formal analysis, Funding acquisition, Methodology, Project administration, Supervision, Visualization, Writing - original draft, Writing - review & editing corresponding author.

3. Camila Pará, Poulomee Bose, Luigi Bruno, Erika Freemantle, **Mahsa Taherzadeh**, Xuefang Pan, Chanshuai Han, Peter S. McPherson, Jean-Claude Lacaille, Éric Bonneil, Pierre Thibault, Claire O'Leary, Brian Bigger, Carlos R. Morales, Graziella DiCristo, and Alexey V. Pshezhetsky. Early defects in mucopolysaccharidosis type IIIC disrupt excitatory synaptic transmission. JCI insight 2021 Vol. 6 Issue 15.

Contribution of authors:

Mahsa Taherzadeh: Methodology (Prepared neuronal cell cultures, produced virus and performed neuronal transduction)

Chapter 1

Introduction

CHAPTER 1: Introduction and literature review

1.1. Lysosomes

Lysosomes, which mean 'digestive body' in Greek are acidic membrane-bound intracellular organelles that were first discovered and named by Christian de Duve in 1955 [1], who later won a Nobel Prize for this discovery. Lysosomes contain more than 60 hydrolytic enzymes including proteases, nucleases, glycosidases, lipases, phospholipases, phosphatases, and sulfatases that function to degrade a wide variety of biological macromolecules including proteins, carbohydrates, lipids, RNA, DNA, and other substances. Most of the enzymes have an acidic pH optimum of 4.5-5 corresponding to that of the lysosomal lumen [2]. Following the breakdown of the material, the resulting amino acids, sugars, fatty acids, cholesterol, and nucleotides are transported through the lysosomal membrane with an assistance of specific transporter proteins for delivery to other cellular compartments for subsequent re-use in the biosynthetic process. Lysosomes are found in all eukaryotic cells and vary in their morphological features, size, and shape [3].

1.1.1. Biogenesis of lysosomal proteins and their function

The transcription start sites of genes encoding most of lysosomal proteins has a CLEAR motif (GTCACGTGAC) that binds to Transcription factor EB (TFEB), a member of the microphthalmia-associated transcription factor family, that triggers lysosomal gene expression [4]. The endoplasmic reticulum (ER) produces both soluble and membrane proteins that are necessary for lysosomal structure and function. These proteins are transported via vesicular transport to the Golgi complex and then to the trans-Golgi network (TGN), where they are undergoing a variety of post-translational modifications most important being glycosylation [5, 6].

Most soluble lysosomal proteins are transferred from TGN to the endosomal/lysosomal system via M6P receptor-mediated transport after modification of their N-linked oligosaccharide chains with the mannose-6-phosphate (M6P) markers [7]. In addition, alternative sorting receptors, such as lysosome integral membrane protein 2 (LIMP-2) and sortilin, deliver several soluble enzymes, including cathepsin D and H (CTSD and CTSH), ganglioside GM2 activator protein, and beta-glucocerebrosidase to lysosomes in an M6P-independent manner [5, 8-10].

The delivery of newly synthesized lysosomal membrane proteins from the TGN occurs in an M6P-independent manner, via clathrin-coated vehicles, either by an indirect route through the plasma membrane or by a direct intracellular pathway. Both pathways rely on specific amino acid sequence motifs. Consensus lysosomal targeting signals are tyrosine, (Fx)NPXY or (G)YXXφ, where φ is a bulky hydrophobic residue) or dileucine-containing ([D/E] XXXL[L/I] or DXXLL) sequences, usually located in the cytosolic N- or C-terminal domains of lysosomal proteins. These motifs are recognized by adaptor proteins (AP-1, -2, -3, and 4) and GGAs (Golgi-localizing, γ-adaptin ear domain homology, ADP-ribosylation factor (ARF)-binding proteins) [5, 11].

Soluble and integral membrane lysosomal proteins are two major classes of lysosomal proteins that play a variaty of different functions. Hydrolases, enzyme activators, and several transport proteins all belong to the class of soluble lysosomal proteins [12, 13].

Lysosomal membrane proteins include vacuolar ATPases, transporters, lysosome-associated membrane proteins (LAMPs), ion channels, soluble N-ethylmaleimide-sensitive factor attachment protein receptors (SNAREs), adaptor or scaffold complexes, tethering factors, and small GTPases. Lysosomal membrane proteins are involved in maintenance of lysosomal stability, biogenesis, position inside the cell, exocytosis, acidification, membrane repair, transport of

metabolites and ions across the membrane, phagocytosis, autophagy, cell death, and fusion with other cellular structures and vesicles [14] (Fig.1).

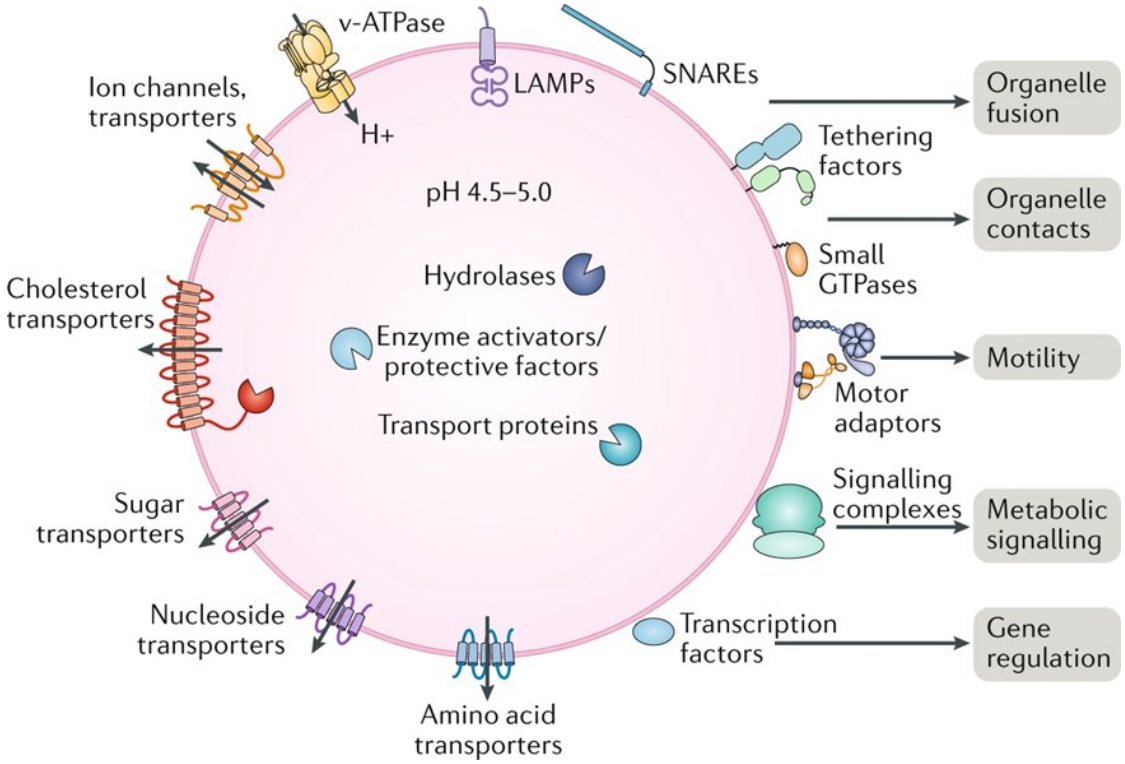

Figure 1. Major classes of lysosomal proteins and their function [14].

Lysosomes contain a specific set of soluble and integral membrane proteins. Soluble proteins, including acid hydrolases and enzyme activators, are present in the lysosomal lumen. Vacuolar ATPases, LAMPs, SNAREs, ion channels and transporters are proteins integrated into the lysosomal membrane. Reproduced with permission from Springer Nature (Ballabio & Bonifacino, 2020).

1.1.2. Major functions of the lysosome

Intra- and extracellular materials destined for degradation arrive to the lysosome from endocytosis, phagocytosis, macro-autophagy, micro-autophagy, and chaperone-mediated autophagy (CMA). Lysosomes play a critical role in the endolysosomal-autophagy network, which is crucial for maintaining cellular homeostasis through degradation of damaged organelles and recycling of their constituents [15]. Additionally, lysosomes play important roles in many other

cellular functions, including signal transduction, cholesterol homeostasis, carcinogenesis, immunological responses, and various physiological and pathological processes. They are also involved in the repair and secretion of plasma membranes (Fig. 2)[16, 17].

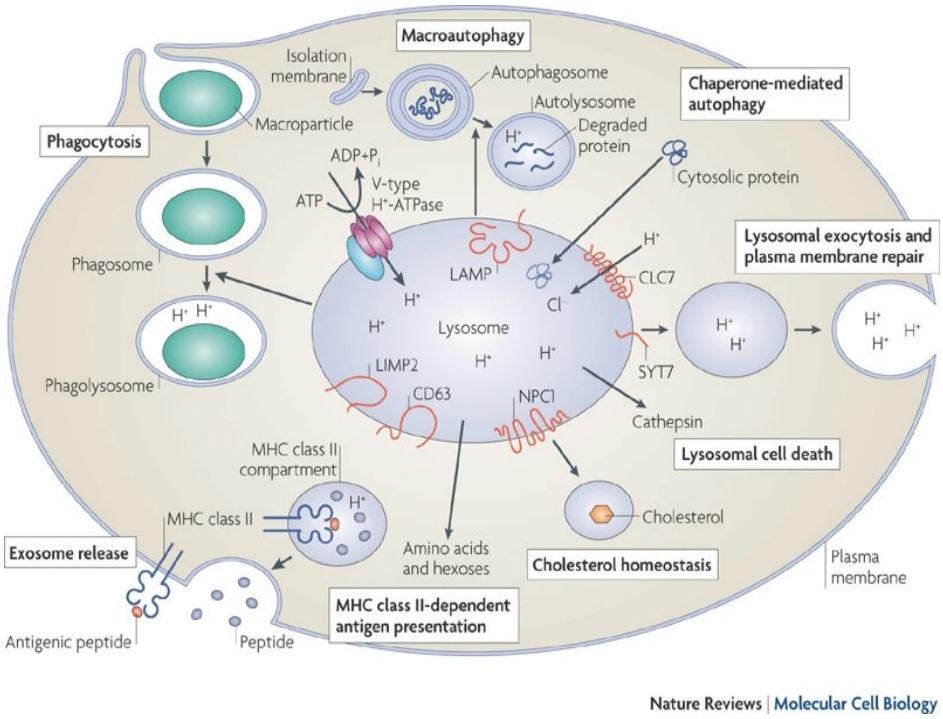

Figure 2. Main functions of the lysosome in cellular homeostasis [17].

In addition to the breakdown/digestion of macromolecules, lysosomes participate in various biological functions, including signaling, regulation of pH, cholesterol and calcium levels, repair of the plasma membrane, defense against pathogens, antigen presentation and cell death. Reproduced with permission from Springer Nature (Saftig & Klumperman, 2009).

1.2. Lysosomal storage diseases (LSDs)

Lysosomal storage diseases (LSDs) are progressive inherited metabolic diseases associated with the accumulation of undigested or incompletely digested macromolecules in lysosomes. LSDs affect all ages but most of them are prevalent in infancy and childhood. LSDs are mainly inherited as autosomal recessive traits, but some are X-linked, including MPS II, Fabry disease, and Danon disease. Over 70 monogenic diseases have been collectively described as LSDs in

humans, with a total incidence for all of them of 1 in 5000 live births [18-20]. Primary defects leading to LSDs occur in the genes encoding all classes of lysosomal proteins including hydrolases, transporters, activators, and membrane-associated proteins required for lysosome function or biogenesis. LSDs are often classified according to the biochemical type of accumulated material for mucopolysaccharidoses (MPS), sphingolipidoses, glycoproteinosis, glycogenosis, and disorders involving the production of lipofuscin, lipofuscinoses [19, 21] (Table 1).

The clinical phenotype and severity of LSDs exhibit considerable heterogeneity depending on the kind of accumulated substrates and the level of lysosomal protein deficiency, which ranges from a partial (<70%) to a complete loss of enzyme activity [15].

Approximately two-third of LSDs are pediatric neurological diseases [22] often manifesting with behavioral abnormalities, sleep disturbance, developmental delay, cognitive decline, intellectual regression, epilepsy, and childhood dementia [23, 24]. These symptoms may be confounded by signs of somatic pathologies, such as visceromegaly, skeletal dysmorphia, joint contractures, skin abnormalities, ataxia, muscle weakness, coarse facial features, short status, macrocephaly, hydrocephalus, gait disturbance, vision and hearing loss [25].

Table 1. LSDs classified according to accumulated materials [19, 21].

Disease (Alternative title)	Gene	Primary Storage	Enzyme deficiency	Neurological involvement
Mucopolysaccharidoses				
MPS I Hurler Syndrome	*IDUA*	Dermatan sulfate and heparan sulfate	α-Iduronidase	✓
MPS II Hunter Syndrome	*IDS*	Dermatan sulfate and heparan sulfate	Iduronate sulfatase	✓
MPS IIIA Sanfilippo Syndrome A	*SGSH*	Heparan sulfate	Heparan sulphamidase	✓
MPS IIIB Sanfilippo Syndrome B	*NAGLU*	Heparan sulfate	N-Acetyl-α-glucosaminidase	✓

MPS IIIC Sanfilippo Syndrome C	*HGSNAT*	Heparan sulfate	Acetyl-CoA: α-glucosaminide	✓
MPS IIID Sanfilippo Syndrome D	*GNS*	Heparan sulfate	N- acetylglucosamine-6- sulfatase	✓
MPS IVA Morquio Syndrome A	*GALNS*	Keratan sulfate and chondroitin 6 sulfate	N-acetylgalactosamine-6-sulfatase	✗
MPS IVB Morquio Syndrome B	*GLB1*	Keratan sulfate	β- Galactosidase	✗
MPS VI Maroteaux Lamy Syndrome	*ARSB*	Dermatan sulfate	Arylsulfatase B	✗
MPS VII Sly disease	*GUSB*	Dermatan sulfate, heparan sulfate and chondroitin-6-sulfate	β- Glucuronidase	✓
MPS IX	*HYAL1*	Hyaluronan	Hyaluronidase 1	✗
Sphingolipidoses				
Anderson-Fabry disease	*GLA*	Globotriaosyl-ceramide	α- Galactosidase A	✓
Farber lipogranulomatosis	*ASAH1*	Ceramide	Acid ceramidase	✓
Gaucher disease type I, II, III	*GBA*	Glucocerebroside, glucosylsphingosine	β Glucocerebrosidase (β- glucosidase)	✓ II & III
GM1 gangliosidosis: type I, II, III	*GLB1*	GM1 ganglioside, keratan sulfate and oligosaccharides	β- Galactosidase	✓
GM2 gangliosidosis Tay–Sachs disease	*HEXA*	GM2 ganglioside, glycosphingolipids and oligosaccharides	β- Hexosaminidase	✓
GM2 gangliosidosis, Sandhoff disease	*HEXB*	GM2 ganglioside, GA2 glycolipid and Oligosaccharides	β- Hexosaminidase	✓
GM2 gangliosidosis, GM2 activator deficiency	*GM2A*	GM2 ganglioside and Glycosphingolipids	GM2 ganglioside activator	✓
Krabbe Disease Globoid cell Leukodystrophy	*GALC*	Galactocerebroside and psychosine	Galactosylceramidase	✓
Metachromatic leukodystrophy	*ARSA* *PSAP*	Sulfatides	Arylsulfatase A and prosaposin	✓
Niemann–Pick disease types A, B	*SMPD1*	Sphingomyelin	Sphingomyelinase	✓
Niemann–Pick disease types C1 & 2	*NPC1* *NPC2*	Sphingomyelin	NPC1 and NPC2	✓
Oligosaccharidosis and Glycoproteinosis				
Aspartylglucosaminuria	*AGA*	Aspartylglucosamine	Aspartoglucosaminidase	✓

Schindler disease Kanzaki disease	*NAGA*	Sialylated or asialo glycopeptides and glycosphingolipids	α- N-Acetylgalactosaminidase	✓
Sialidosis	*NEU1*	Sialylated oligosaccharides and glycopeptides	Neuraminidase	✓
Galactosialidosis	*CTSA*	Sialyloligosaccharides	Protective protein cathepsin A (PPCA)	✓
Glycogenosis				
Glycogen storage disease II Pompe disease	*GAA*	Glycogen	Lysosomal α-glucosidase	✕
Danon disease	*LAMP2*	Cytoplasmic debris and glycogen	LAMP2	✕
Neuronal ceroid lipofuscinoses (NCL)				
NCL1 Haltia-Santavuori disease	*PPT1*	Lipidated thioesters, saposins A and D	Palmitoyl-protein thioesterase	✓
NCL2 Jansky-Bielschowsky disease	*TPP1*	Subunit c of mitochondrial ATP synthase	Tripeptidyl peptidase 1	✓
NCL3 Batten-Spielmeyer-Sjogren disease	*CLN3*	Subunit c of mitochondrial ATP synthase	Battenin	✓
NCL4 Parry disease and Kufs type A, B	*DNAJC5*	Subunit c of mitochondrial ATP synthase	DnaJ homolog subfamily C5	✓
NCL5	*CLN5*	Subunit c of mitochondrial ATP synthase	Ceroid- lipofuscinosis neuronal protein 5	✓
NCL 6	*CLN6*	Subunit c of mitochondrial ATP synthase	Ceroid- lipofuscinosis neuronal protein 6	✓
NCL 7	*MFSD8*	Subunit c of mitochondrial ATP synthase	MFS domain-cont. protein 8	✓
NCL 8	*CLN8*	Subunit c of mitochondrial ATP synthase	Ceroid- lipofuscinosis neuronal protein 8	✓
NCL10	*CTSD*	Saposins A and D	Cathepsin D	✓
Integral membrane protein disorders				
Cystinosis	*CTNS*	Cystine	Cystinosin	✓
Salla disease Sialic acid storage disease	*SLC17A5*	Sialic acids	Sialin	✓

1.3. Mucopolysaccharidoses (MPS)

MPS is a group of LSDs caused by deficiency of 11 lysosomal enzymes that break down long chains of sugar molecules called mucopolysaccharides or glycosaminoglycans (GAGs). The accumulation of the five main types of GAGs, including heparan sulfate (HS), dermatan sulfate (DS), chondroitin sulfate (CS), keratan sulfate (KS), and hyaluronic acid (HA), leads to damage and dysfunction in various tissues and organs (Table 1) [26, 27].

MPS symptoms may vary depending on the type of MPS and the severity of enzyme deficiency, but for majority of diseases they typically include physical symptoms (growth delay, abnormally short stature, joint stiffness and pain, hearing loss, and distinctive facial appearance), cognitive symptoms (intellectual regression and behavioral and developmental problems), respiratory symptoms (increased mucus secretion, frequent lung infections, and sleep apnea), and cardiovascular symptoms (heart valve disease, cardiac hypertrophy, and enlarged liver and spleen) [28, 29].

An elevated amount of GAGs, a partially degraded primary substrate in biological fluids, and reduced enzyme activity in patient cells are used to diagnose MPS. Patients with MPS I, II, III, and VII show neuropathic manifestations (Table 1) [26, 30]. The frequency of mucopolysaccharidoses differs among various disorders as well as between populations and geographic regions. In general, MPS III and I occur most frequently, whereas MPS VII and IX are considered to be the least common [30].

1.3.1. Mucopolysaccharidosis III (MPS III)

MPS III, also known as Sanfilippo syndrome, is caused by deficiency of one of the four enzymes required to break down HS. Four subtypes of MPS III (A, B, C, and D) are differentiated based on specific enzyme deficits (Table1 and fig. 3) [26, 31]. In all subtypes the primary enzyme deficiency leads to the accumulation of HS in cells, causing damage and dysfunction in various tissues and organs, with the main target being the brain [32].

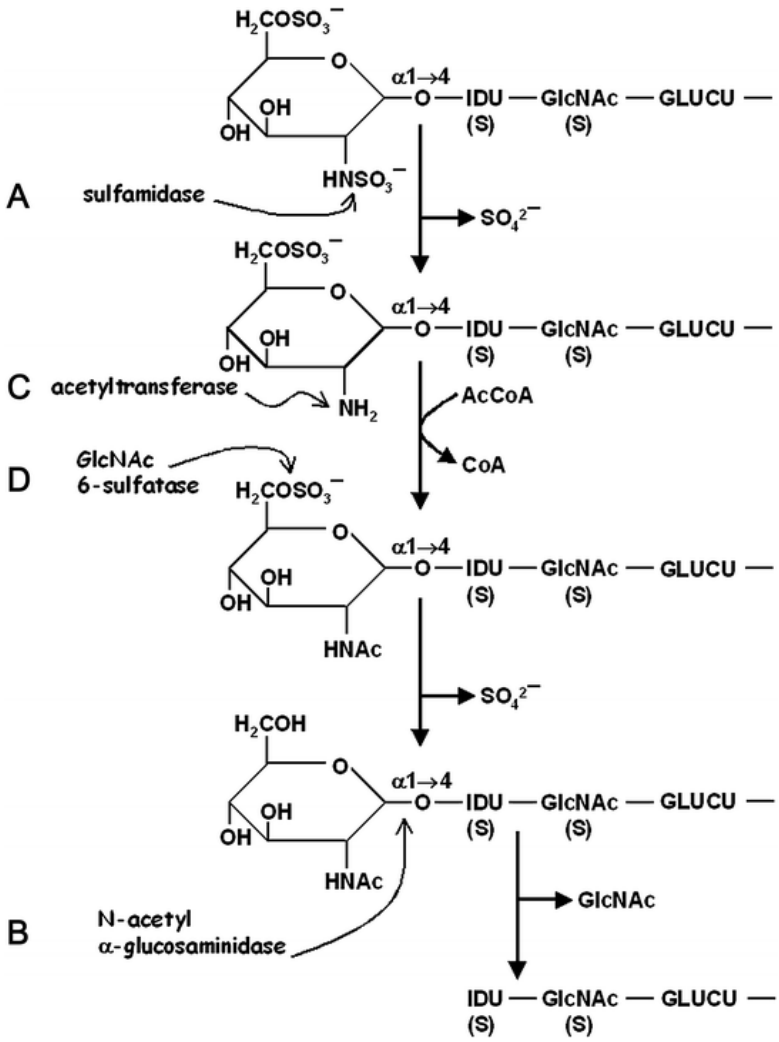

Figure 3. Enzymatic reactions involved in heparan sulfate breakdown, and their impairment in individuals with different subtypes of Sanfilippo syndrome [31].

GlcNAc = N-acetylglucosamine; IDU = L-iduronic acid; GLUCU = glucuronic acid. Reproduced with permission from John Wiley and Sons, journal of inherited metabolic disease, (Valstar et al., 2008).

The worldwide birth prevalence of MPS III ranges from 1:50 000–1:250 000. The most frequent types of MPS are IIIA and IIIB, while MPS IIIC is less common and MPS IIID is considered to be an ultrarare disease. MPS III is inherited in an autosomal recessive manner. Symptoms vary depending on the specific subtype and severity of enzyme deficiency but typically include mostly neurological symptoms such as developmental delay, speech delay, behavioral problems, hyperactivity, sleep disturbances, and progressive loss of cognitive function leading to dementia (Fig. 4) [33]. Joint stiffness, excessive mucus secretion, deafness and frequent pneumonia are the most common systemic problems.

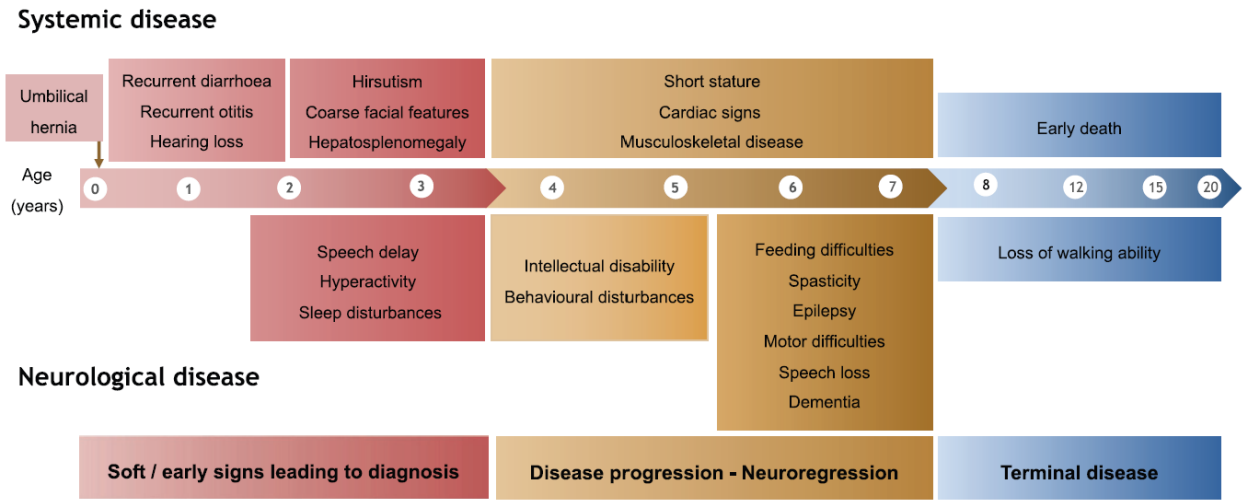

Figure 4. Typical clinical symptoms of MPS III patients and their age of onset [33].

1.3.2. Heparan sulfate (HS)

HS is the most common sulfated glycosaminoglycan present on the cell surface and in the extracellular matrix. It consist of repeating disaccharide units of glucuronic acid (GlcA) or L-iduronic acid (IdoA) and N-acetylglucosamine (GlcNAc) [26, 34].

1.3.2.1. Biosynthesis of heparan sulfate

Biosynthesis of HS glycans of proteoglycans occurs in the Golgi apparatus. The process starts from the attachment of GlcNAc residue to the non-reducing end of the acceptor linkage glucuronosyl-galactosyl-galactosyl-xylosyl (GlcAβ1,3Galβ1,3Galβ1,4Xyl) tetrasaccharide region, which is covalently bound to a core protein serine residue [35]. This attachment is performed by a member of the EXTL family of glycosyltransferases that use biosynthetic precursors 3′-phosphoadenosine-5′-phosphosulfate (PAPS) and UDP-sugars [36, 37]. The next step in the HS biosynthesis is the formation of the HS precursor by N-deacetylase/N-sulfotransferase (NDST) and glucuronyltransferase (GlcAT) enzymes. NDST catalyzes the transfer of a sulfate group from a sulfate donor molecule to the N-acetylglucosamine residue of the HS precursor, forming an N-sulfated disaccharide. GlcAT then catalyzes the addition of glucuronic acid residues to the growing HS chain [38]. The next step is the sulfation of the HS chain by sulfotransferases. These enzymes transfer sulfate groups to specific positions on the HS chain, leading to structural diversity. There are several different O-sulfotransferases, including 2-O-sulfotransferase, 6-O-sulfotransferase, and 3-O-sulfotransferase, each of which adds sulfate groups to specific positions on the HS chain (Fig. 5) [39, 40].

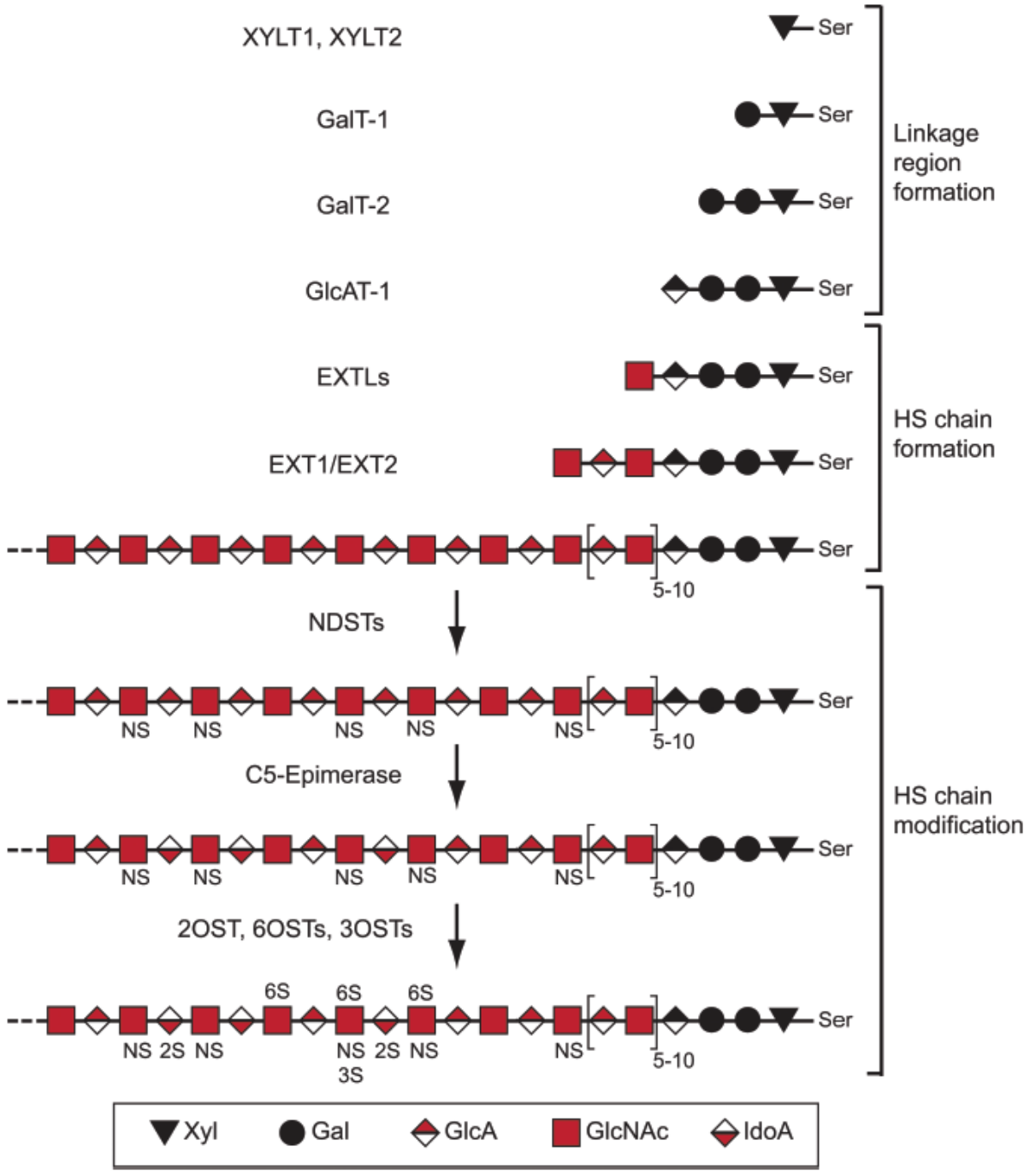

Figure 5. HS biosynthesis [36].

Various steps of HS biosynthesis involve specific groups of enzymes.

NS, N-sulfated GlcN; 6S, 6-O-sulfated GlcN; 2S, 2-O-sulfated IdoA; 3S, 3-O-sulfated GlcN; Ser, serine.

1.3.2.2. Physiological role of heparan sulfate

HS chains covalently attach to core proteins via a linker region to form heparan sulfate proteoglycans (HSPG). HSPGs are critical components of the extracellular matrix and play essential roles in various biological processes. HSPGs bind chemokines and cytokines to regulate inflammatory response [41]. They also act as co-receptors for several growth factors and morphogens involved in migration, invasion, differentiation, and tissue repair [42]. HSPGs also facilitate blood clotting, mediate endocytosis [43, 44], contribute to synapse formation and plasticity [45], and regulate cell behavior and tissue organization during embryonic development and organogenesis [46, 47]. Alterations in the structure and function of HS have been associated with several disorders, including cancer [48], inflammation [49], and neurological conditions [50].

1.3.2.3. Catabolism of heparan sulfate

Degradation of HS starts in the extracellular space, where two endosulfatases, SULF1 and SULF2, remove 6-O-sulfate groups from the HS chains [51]. Heparanase enzymes then cleave HS chains to produce HS fragments and release partially degraded HSPGs from the cell surface [52].

The final degradation of HS chains occurs in lysosomes through a series of steps catalyzed by different lysosomal enzymes, including exo-glycosidases (α-L-iduronidase (IDUA), β-D-glucuronidase (GUSB), and N-acetyl-α-D-glucosaminidase), sulfatases (iduronate-2-sulfatase (IDS), glucuronate-2-sulfatase (GDS), N-acetylglucosamine-6-sulfatase, N-sulphoglucosamine sulphohydrolase), and N-acetyltransferase (acetyl-CoA: α-glucosaminide N-acetyltransferase). These enzymes cleave the terminal groups located at the non-reducing end of the polymer.

Mutations in any of the enzymes involved in HS cleavage lead it's accumulation in lysosomes and cause one of the subtypes of MPS (fig. 6) [53, 54].

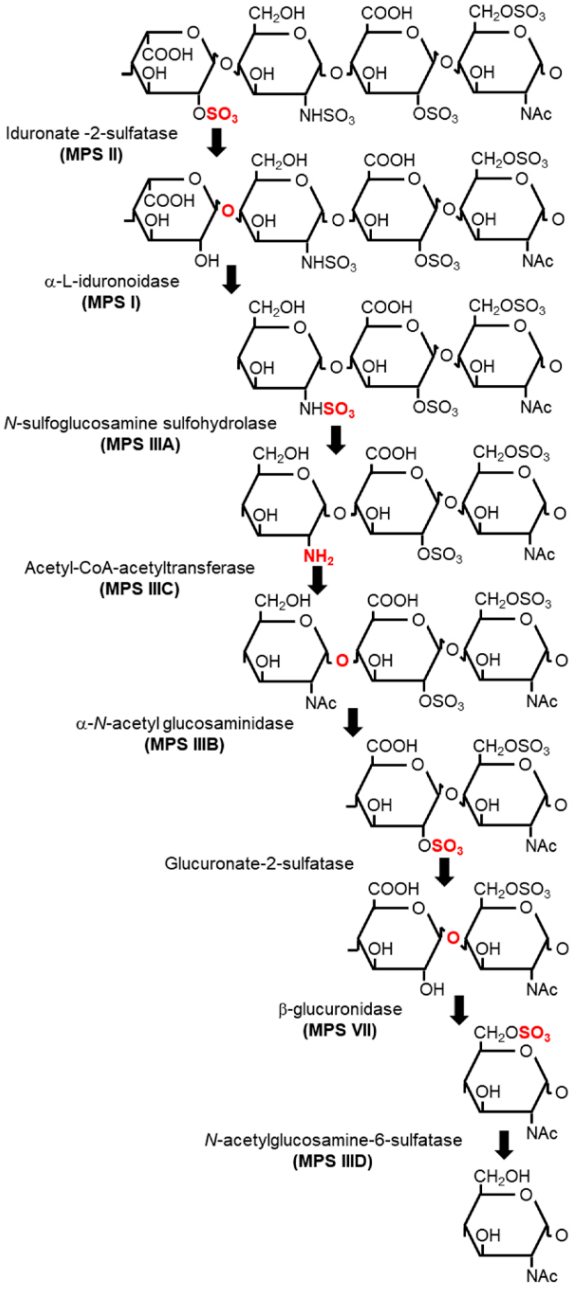

Figure 6. Heparan sulfate catabolic pathway [54].

Enzymes involved in the sequential degradation of heparan sulfate and mucopolysaccharidoses caused by their deficiencies are indicated [54].

1.3.3. Mucopolysaccharidosis type IIIC (MPS IIIC)

MPSIII C (MIM 252930), also known as Sanfilippo syndrome type C, is inherited in an autosomal recessive pattern and is estimated to affect one in every 1,500,000 live births worldwide [55]. The disease is caused by deficiency of the lysosomal transmembrane enzyme heparan sulfate acetyl-CoA: α-glucosaminide N-acetyltransferase (HGSNAT). The common symptoms of MPS IIIC are similar to those for other subtypes of Sanfilippo disease. They, typically, become apparent in early childhood and worsen over time [56].

1.3.3.1. HGSNAT

HGSNAT (EC 2.3.1.78) enzyme is encoded by the *HGSNAT* gene, which is located on chromosome 8p11.1, and consists of 18 exons [57, 58]. The protein is composed of 635 amino acids with 11 predicted transmembrane domains, an N-terminus located in the lysosomal lumen, a C-terminus in the cytosol, and five potential glycan chains linked to asparagine residues [58, 59].

HGSNAT is produced as a 77-kDa precursor protein in the endoplasmic reticulum (ER) and is transferred to the lysosome by an adaptor protein-mediated pathway. The precursor is then cleaved into two smaller chains, an α-chain (29-kDa) and a β-chain (48-kDa), which are kept together by disulfide bonds and assembled into oligomers [60]. HGSNAT binds its substrate, acetyl-CoA at the cytoplasmic side of the lysosomal membrane and becomes acetylated at the histidine residue (His^{269}) in the active site. This triggers a change in the enzyme conformation that facilitates the transport of the acetyl group to the lysosome. When HS interacts with the active site, terminal glucosamine is modified with the acetyl group to form N-acetylglucosaminide (fig. 7) [61-63].

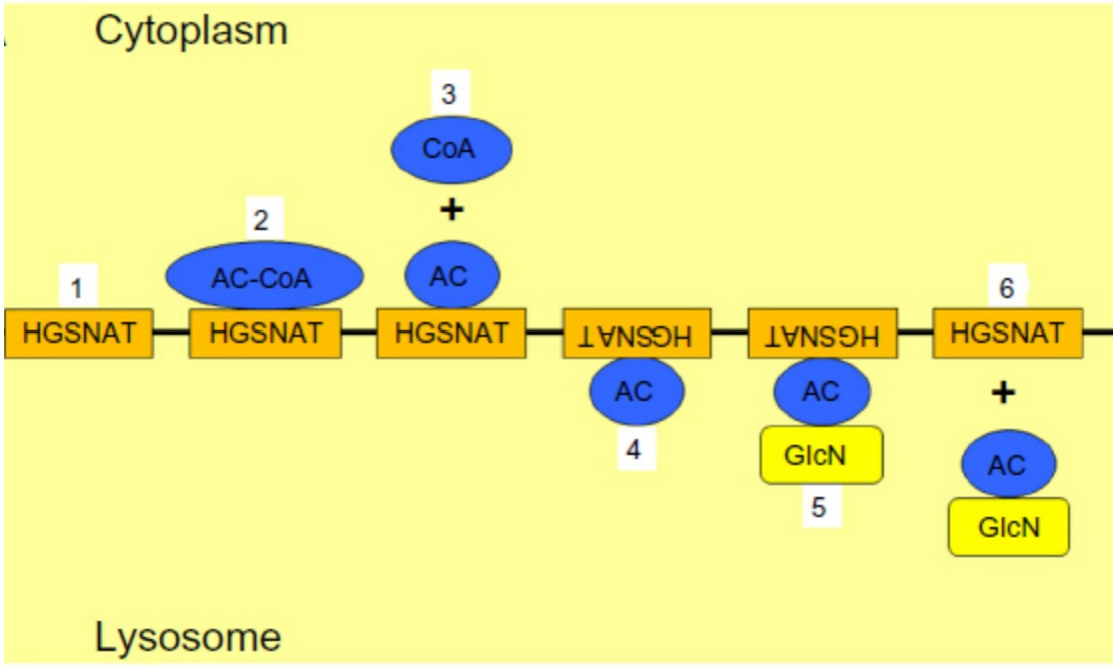

Figure 7. Proposed catalytic mechanism of HGSNAT [63].

HGSNAT (1) binds acetyl-CoA at the cytoplasmic side of the lysosomal membrane (2) and undergoes acetylation at histidine[269] residue in its active site (3). This triggers a conformational change that facilitates the transfer of the acetyl group to the lysosome (4). Upon interaction of heparan sulfate with the active site, the acetyl group binds the glucosamine residue of heparan sulfate (GlcN) (5) to form N-acetylglucosaminide (6). "The application of clinical genetics, 269-281" originally published by and used with permission from Dove Medical Press Ltd (Fedele, 2015).

More than 70 different mutations affecting all 18 exons and introns of *HGSNAT* have been identified. These mutations include missense, nonsense, splice-site, deletion, and insertion mutations, which reduce or eliminate HGSNAT activity, leading to the accumulation of HS in cells and tissues [25].

Approximately 55% of MPSIIIC patients are affected by missense HGSNAT mutations (Fig. 8 [59]), which prevent the correct folding of the enzyme and cause its retention in the ER and degradation in proteasomes. When expressed in cultured cells, these variants showed a negligible

enzymatic activity. Besides the mutant proteins were not glycosylated, and their proteolytic processing was lacking [25, 57, 59, 64-67].

1.4. Lysosomal storage disorders and endoplasmic reticulum stress

The ER is the primary organelle involved in folding proteins into tertiary and quaternary structures. It also plays important roles in signal transduction, and together with the lysosome, serves as the major intracellular reservoir of Ca^{2+}. High protein demand, inflammatory cytokines, and expression of mutant proteins can disturb ER hemostasis and activate the unfolded protein response (UPR). Activation of the UPR, leading to apoptosis, is a condition referred to as ER stress [68-71]. Previous studies showed alterations of Ca^{2+} homeostasis and UPR activation in a wide variety of LSDs, suggesting that ER stress contribute to the cellular pathology associated with these diseases [72].

Specifically, UPR activation was demonstrated in cultured fibroblasts from patients with both neurodegenerative (Neuronal ceroid lipofuscinoses, Tay-Sachs disease, Gaucher disease (GD) type II, Niemann–Pick C type 2) and non-neurodegenerative, (GDI nephropathic cystinosis) LSDs [73]. UPR activation was also revealed in the brain of GM1 gangliosidosis mice [74]. However, the involvement of the UPR in the pathophysiology of LSDs remains somewhat controversial. UPR activation varies depending on the source of tissue, the type of accumulated substance, and a type of mutation. Therefore, more systematic analyses using different animal and cellular models are required to determine the role of UPR activation in the pathology of a particular disease. For instance, in Gaucher disease, UPR activation has been reported in patients' fibroblasts, whereas there is no evidence of ER stress in bone marrow mesenchymal stromal cells or neurons [73, 75]. Moreover, analysis of the UPR in fibroblasts from patients with different types of mucopolysaccharidoses (MPS I, II, IIIA, IIIB, and IVA) and in the murine MPS IIIB model did

not reveal changes in the expression levels of several UPR-related genes [76]. In contrast, Kobolak et al. reported that ER stress is involved in the cytopathology of MPS II in neuronal precursor cells [77].

1.5. Main aspects of the CNS pathology in neurological LSDs

Although, lysosomes are present in all cells and tissue types, it is recognized that the CNS is highly susceptible to impaired lysosomal function since neurons are post-mitotic long-living cells that can progressively develop pathological phenotype [78]. Indeed, most of patients with LSDs (See Table 1 for specific examples) exhibit a neuronal dysfunction and neurodegeneration causing multiple with neurologic problems, such as developmental delay, myoclonic seizures, ataxia or stroke, motor weakness, and extrapyramidal signs [79, 80]. Many of these symptoms also present in other neurodegenerative disorders including Alzheimer's, Parkinson's, and Huntington's diseases [81].

Impairment of lysosomal function also affects the associated pathways, including autophagy, and axonal transport, that rely on proper lysosomal function [82]. In addition, lysosomal storage impairs endocytosis and exocytosis at synaptic terminals and, consequently, alters synaptic vesicle recycling and postsynaptic density. The described defects are the major neuronal challenges that eventually cause neuronal dysfunction and death in neuropathic LSDs (Fig. 8) [20, 83, 84].

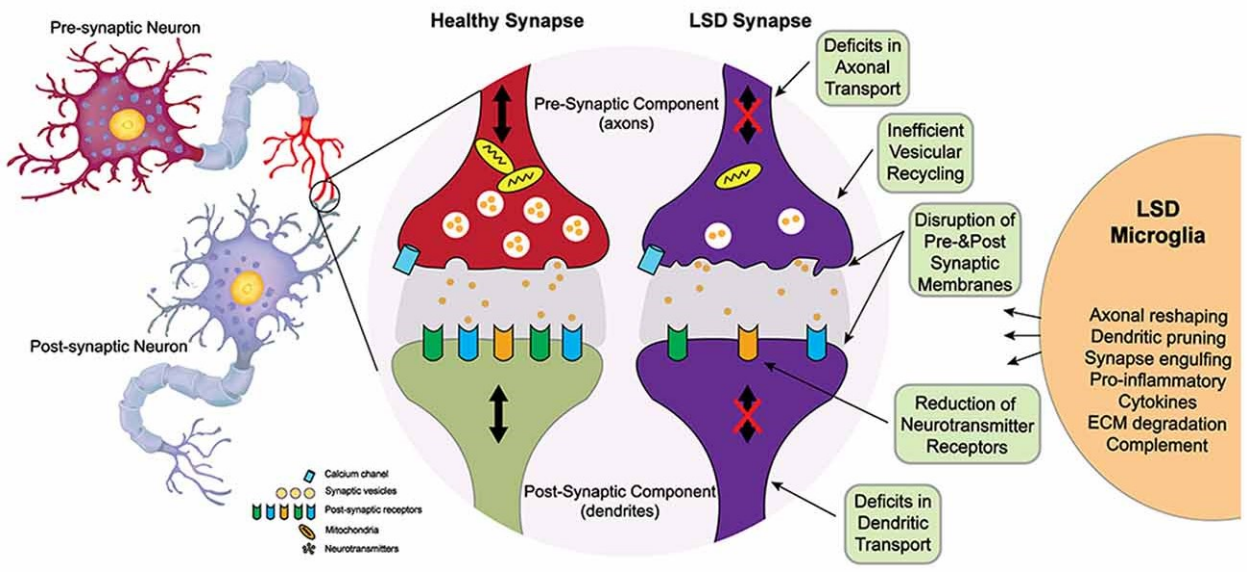

Figure 8. Pathological mechanisms affecting the CNS in neurological LSDs [84].
Potential mechanisms underlying neuronal dysfunction include impairment of synaptic vesicle trafficking, alterations in the availability of synaptic proteins, deficits in exocytosis and endocytosis of synaptic vesicles, and inflammation-mediated neurodegeneration.

1.5.1. Impairment of autophagy and axonal transport of lysosomes in LSDs

Due to unique morphology of neurons, involving long protrusions from the cell body, an efficient transport system, and constant turnover of cellular components through autophagy are essential for neuronal survival. Since lysosomes are the primary proteolytic compartments coupled to the main autophagic pathways, lysosomal dysfunction interrupts the autophagic-endocytic-lysosomal pathway, leading to neurodegeneration [81, 85]. In healthy neurons, early endosomes are enriched at the distal ends of the axons, whereas mature lysosomes are enriched in the cell body. It has been shown that the maturation of early endosomes involves their retrograde axonal transport [86]. Neuronal loss resulting from impaired autophagy and axonal trafficking of lysosomes has been shown in several neuropathic LSDs, including Niemann–Pick type C (NPC) disease [87, 88], Gaucher disease [89], Fabry disease [90], GM1 gangliosidosis [91], Batten

disease [92], Mucolipidosis type IV [93], Mucolipidosis type II [94], MPS II [95] , MPS IIIA [96] , MPS IIIB [97], and MPS IIIC [25].

1.5.2. Synaptic dysfunction in lysosomal storage disorders

Defects in synaptic transmission, documented in multiple LSDs and though to result from multiple defects in the neuronal hemostasis, including impairment of exocytosis and endocytosis of synaptic vesicles, disrupted microtubule networks leading to impaired vesicle trafficking, reduction of several pre- and post-synaptic proteins, and a deficiency of synaptic vesicles at the axonal terminals [20, 98-102].

1.5.2.1. Changes in synaptic vesicles formation, fusion, and recycling

Synaptic vesicles (SV) are small, electron-lucent vesicles in the terminals of neurons that store and release neurotransmitters. Several reports described that primary and secondary lysosomal storage changes the lipid composition of SV membrane, interferes with the function of SNARE proteins, and disrupts formation, fusion, and recycling of SVs [103-105]. In the similar fashion, disruption of the microtubule structure due to lysosomal storage in the axons impairs transport of synaptic vesicle precursors from the cell body, leading to a shortage of SVs in the axon terminals [20].

In MPS IIIA and NPC1 mice, a decrease in the rate of exocytosis and turnover of SVs has been observed [99, 101]. Neurons in the mouse model of Krabbe disease (KD) exhibit defects in axonal transport, resulting in decreased availability of SNARE proteins and recycling of SVs [98]. In both KD and metachromatic leukodystrophy (MLD) lysosomal dysfunction alters the recycling of lipid components during SV release and recycling, leading to deformation and impairment of synaptic function [84, 106]. Scarcity of synaptic vesicles has also been reported in cultured hippocampal neurons and the CA1 pyramidal neurons of MPS IIIC mouse model [21].

1.5.2.2. Alternation in pre- and postsynaptic proteins

Reduction of multiple pre- and postsynaptic proteins associated with lysosomal storage, potentially associated with impairment of synaptic function, has been documented in a number of neuropathic LSDs such as MPS I [107], MSP IIIA [100, 101], MPS IIIB [100, 108], MPS VII [109], KD [98], CLN3 [110], CLN5 [111], and CLN6 [112].

In particular, levels of synaptophysin, a presynaptic protein essential for synaptic vesicle endocytosis, were reduced in the MPS IIIB mice. Vitry *et al*. (2009) showed that HS storage in neurons activates synaptophysin degradation, resulting in its decrease [108]. A reduction in synaptophysin levels was also observed in human iPSC-derived neurons from patients with MPS VII [109], CLN6 sheep model [112], and CLN3 mouse model [110].

Studies from our laboratory (Pará *et al.,* 2020) demonstrated that PSD95 (post-synaptic protein 95), which plays an essential role in regulating glutamatergic synapse formation, was reduced in the brain and hippocampal cultured neurons of MPS IIIC mouse and in post-mortem cortices of human MPS I, II, IIIA, IIIC, and IIID patients. The authors further demonstrated that reduction in PSD95 levels in MPS IIIC neurons was caused by primary genetic deficiency of HGSNAT and HS storage. They rescued the levels of PSD95 in vivo and in vitro by correcting the primary genetic deficiency in neurons using viral vectors expressing the WT HGSNAT enzyme [113].

1.5.3. Neuroinflammation and neurodegeneration in LSDs

Besides intrinsic neuronal defects, neuronal survival is affected by neuroinflammation, the most common hallmark of brain pathology in neurological LSDs [20]. The key regulators of the inflammatory responses in the CNS are microglia and astrocytes. Microglia has several physiological functions within the healthy CNS. Specifically, they play a role in postnatal

development and adult neuronal plasticity by remodeling synaptic circuits. They also are involved in phagocytosis of apoptotic neuronal progenitor cells, and apoptotic neurons [114]. Astrocytes play important roles in the brain function, which includes regulation and recycling of ions and neurotransmitters, and maintenance of the blood–brain barrier [115]. In healthy brain, both types of glial cells support neuronal functions, whereas in pathological conditions, they lose some of their support functions or cause a damage [116]. Increased levels of activated microglia (microgliosis) and astrocytes (astrocytosis) affect CNS homeostasis and promote neurodegeneration by creating a neurotoxic environment that includes elevated levels of cytokines, chemokines, and pro-apoptotic molecules, ultimately leading to neuronal loss [117].

Catabolic defects in LSDs are known to induce an inflammatory response in the CNS. For example, in MPS, impaired degradation of HS triggers a neuroinflammatory response by interacting with toll-like receptors (TLR) in microglial cells. This activate a pro-inflammatory cascade in the microglia leading to a release of cytokines, such as tumor necrosis factor alpha (TNF-α) and macrophage inflammatory protein-1 alpha (MIP-1-alpha) [20, 113, 118]. In the case of the mouse model of MPS IIIC, astrocytosis and microgliosis are apparent in brain tissue as early as P25, even before the mice display any behavioral abnormalities (Taherzadeh *et al.* in prep).

In Twitcher mice (the naturally occurring KD model with a W332X mutation), as well as in recently generated twi-5J (E130K), and Twitrs (H168C) KD mouse models, death of oligodendrocytes and demyelination trigger neuroimmune responses [119-122]. In neuronopathic Gaucher disease, accumulation of the primary substrates, glucosylceramide and glucosylsphingosine, activates microglia cells [123]. In general, astrocytosis and microglial activation are observed in majority of neurologiocal LSDs, including glycosphingolipidoses, gangliosidoses, MPS I, II, III and VII, Sandhoff disease, and all types of NCLs [124, 125].

1.6. White matter

Historically, gray matter pathology has been considered the major factor contributing to cognition and learning defects in neurological disorders. However, brain imaging as well as cellular and molecular studies have revealed that pathological alterations in the white matter can also lead to significant cognitive impairment and increase the risk of long-term neurological problems.

White matter refers to the areas of the CNS that mainly consist of myelinated nerve fibers (axons), blood vessels and supporting cells such as oligodendrocytes, microglia, and astrocytes (Fig. 9) [126]. Because of the high lipid content of myelin, these areas appears whitish in contrast to gray matter, which is mainly composed of neuronal somas[127].

1.6.1. Axons

Axons or nerve fibers transmit electrical impulses and information away from the cell body. Axons contain both cytoskeletal elements and organelles, including mitochondria, transport vesicles, lysosomes, and axoplasmic reticulum. Actin filaments, microtubules, microtubule-associated proteins, and neurofilaments are the major constituents of the axonal cytoskeleton [128]. Actin filaments play a fundamental role in axon development and function by providing stability to microtubules and a scaffold for the axonal plasma membrane (axolemma) [129]. Microtubules and their motor proteins serve as tracks for transporting organelles along the axons [128]. Neurofilaments, on the other hand, maintain the structure of axons and determine axonal size (diameter), which affects the nerve conduction velocity [130, 131].

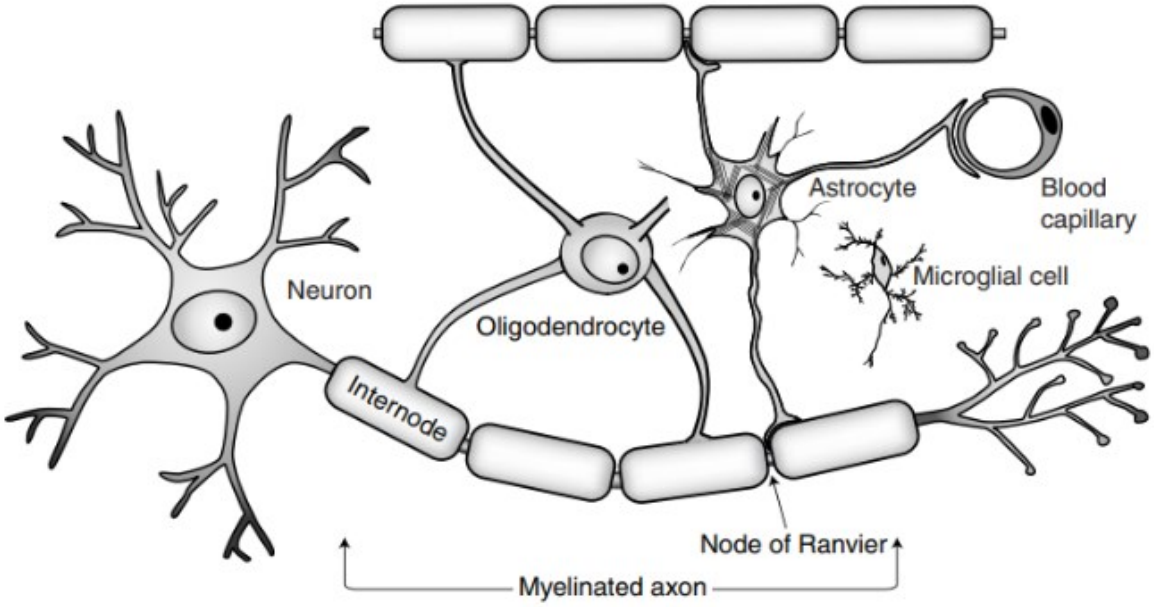

Figure 9. Major cellular elements of the white matter [127].

The white matter consists of axons covered by myelin and their glial cell partners, astrocytes, oligodendrocytes, and microglia [126, 127]. Reprinted from Elsevier Books, Julia M. Edgar,Ian R. Griffiths, Diffusion MRI, Copyright (2009), with permission from Elsevier.

1.6.2. Oligodendrocytes (OLs)

Oligodendrocytes are the myelinating cells of the CNS which were first observed and described by Ramon y Cajal and del Rio Hortega [132]. In the spinal cord, oligodendrocyte precursor cells/progenitors (OPCs) are derived from a specialized domain of the ventral ventricular zone. They further migrate throughout the spinal cord and differentiate into myelin-forming oligodendrocytes [133-135]. In the forebrain, OPCs originate from the medial ganglionic eminence, anterior entopeduncular area, lateral and/or caudal ganglionic eminences, as well as from the cortex [136].

During development, OPCs migrate long distances to their final destination. Their migration is guided by multiple signals, including growth factors, such as platelet-derived growth

factor (PDGF), fibroblast growth factor (FGF) [137, 138], hepatocyte growth factor [139], and chemotropic molecules, such as netrins and secreted semaphorins [140, 141]. OPCs then differentiate into mature oligodendrocytes, responsible for producing and maintaining the myelin sheath. The process of OPCs specification and differentiation is regulated by several transcription factors such as Oligodendrocyte transcription factor 1 (Olig1), Oligodendrocyte transcription factor 2 (Olig2), Mash, Myelin transcription factor 1 (Myt1), Nkx2.2, and Sox10 [142].

The oligodendroglial cell lineage and their developmental stage, from neural progenitor cells (NPCs) to mature OLs, can be determined using various markers. A2B5-positive progenitor cells can differentiate into both oligodendrocytes and astrocytes under specific environmental cues [143]. All cells of the oligodendroglial lineage express Olig1 and 2, as well as Sox10 and Nkx2.2, while PDGFR-α and Nerve/glial antigen 2 (NG2) are produced by OPCs and pre-oligodendrocytes (pre-OLs). During transition from OPCs to differentiated OLs, proteolipid protein (PLP), oligodendrocyte marker 4 (O4), oligodendrocyte marker 1 (O1) and 2′,3′-cyclic nucleotide 3′-phosphodiesterase (CNPase) are expressed. The differentiated oligodendrocytes are characterised by their ability to express myelin proteins including myelin basic protein (MBP), myelin-associated glycoprotein (MAG), myelin oligodendrocyte glycoprotein (MOG), and galactocerebroside (GalC) (Fig. 10) [144].

Mature OLs are primarily responsible for generation of the myelin sheath. One OL can produce myelin for multiple axons with diameters above 0.2 μm resulting in each axon being covered by a separate spiral of myelin [145]. In addition to myelination, OLs play several other important roles in the CNS, including maintaining axonal health by providing structural and metabolic support to axons and supplying them with nutrients [146], responding to axonal activity with depolarization induced by the activation of neurotransmitter receptors [147, 148], and

producing a number of neurotrophic factors such as nerve growth factor, brain-derived neurotrophic factor (BDNF), and neurotrophin 3 [149].

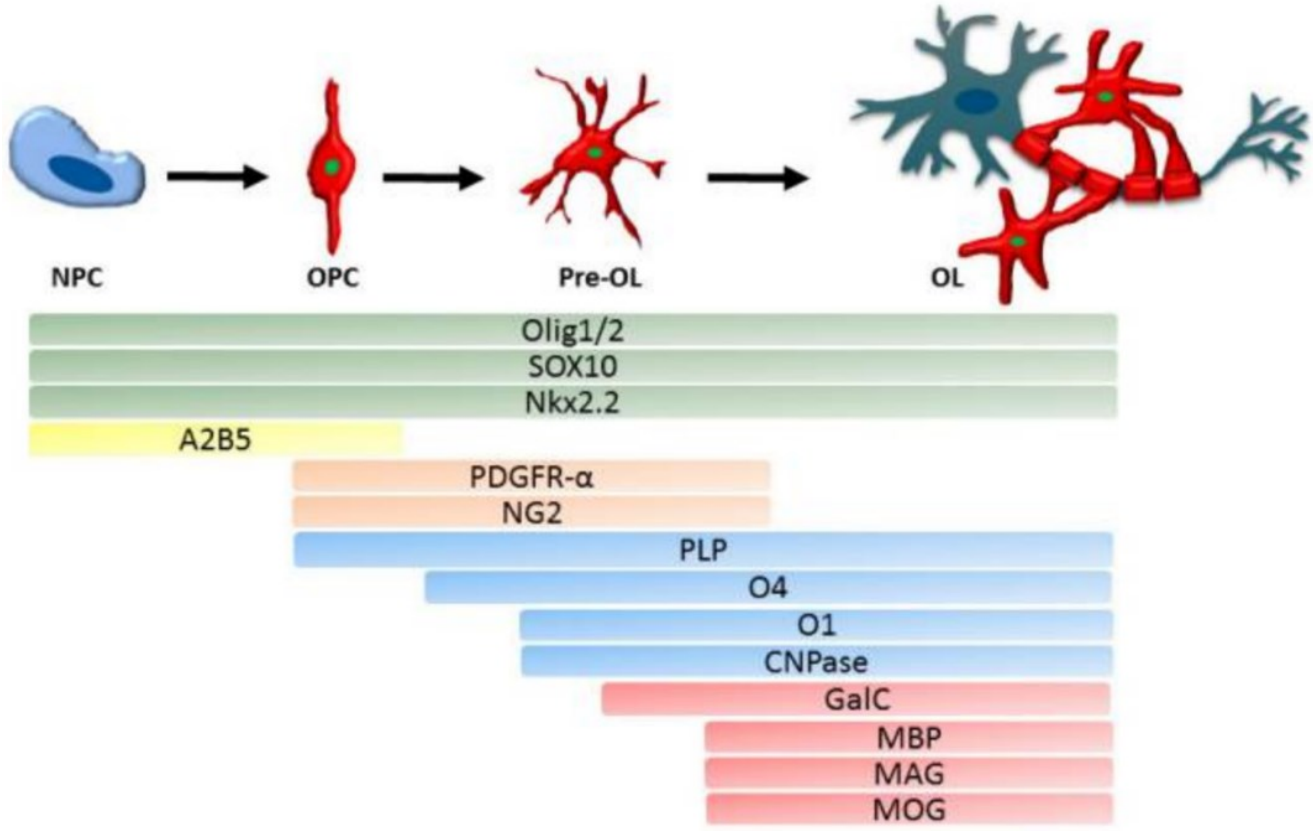

Figure 10. Protein markers expression during the differentiation of oligodendroglial lineages [144]. The diagram shows protein markers specific for each developmental stage of the oligodendrocyte lineages, starting from neuronal progenitor cells and ending with myelinating oligodendrocytes [144].

1.6.3. Myelin

1.6.3.1. Myelin structure and function

Myelin is a complex structure consistent of a multilayered protein-rich lipid membrane that is generated by OLs and insulates the axons of nerve cells in the central and peripheral nervous systems (PNS). By reducing the capacitance of the axon membrane, myelin increases the speed and efficiency of electric conduction along the axon [150, 151]. Besides, it provides support and nutrition to axons [150] and participates in synaptic formation and plasticity [152-154] . The

myelin sheath along the entire length of the axon contains gaps, so-called nodes of Ranvier. These nodes are rich in voltage-gated ion channels and allow for rapid saltatory conduction of nerve impulses along the axon [151, 155]. The myelinated segments between the two nodes of Ranvier are called internodes. The edge of the internode, called the paranode, is the main connection site between the axon and the OL [156]. Each myelin sheath is composed of two domains: compact and non-compact area. Compacted myelin, representing the bulk of the myelin sheath, is composed of a tightly packed membrane spiral with a thin cytoplasm between the layers. Non-compact myelin, found in the paranodal loops bordering the nodes of Ranvier, contains more cytoplasm [157].

1.6.3.2. Myelin composition

The lipid component of myelin (approximately 80% of its dry weight) is derived from the plasma membrane of OLs and is composed of cholesterol, phospholipids (e.g., sphingomyelin), and glycolipids (e.g., galactosylceramide) in a ratio of 40%:40%:20%, respectively [158, 159]. The lipids are important for the integrity of the myelin sheath and its stabilization [160], regulation of the membrane protein trafficking, signal transduction, and cellular adhesion [159].

The protein component of myelin (around 20% of its dry weight) is composed of several proteins, with MBP, PLP, MAG, and MOG being the most abundant (Fig. 11). MBP and PLP represent the majority of protein within the compacted myelin. They are responsible for generation of a compacted multilayered structure of the mature myelin. MAG is present in the non-compact myelin domain and plays an important role in myelin adhesion by regulating the interactions between myelin and axons. MOG is a transmembrane protein located at the surface layers of myelin sheaths and on the cell surface of oligodendrocyte and is involved in maintenance of myelin structure [157, 161-163].

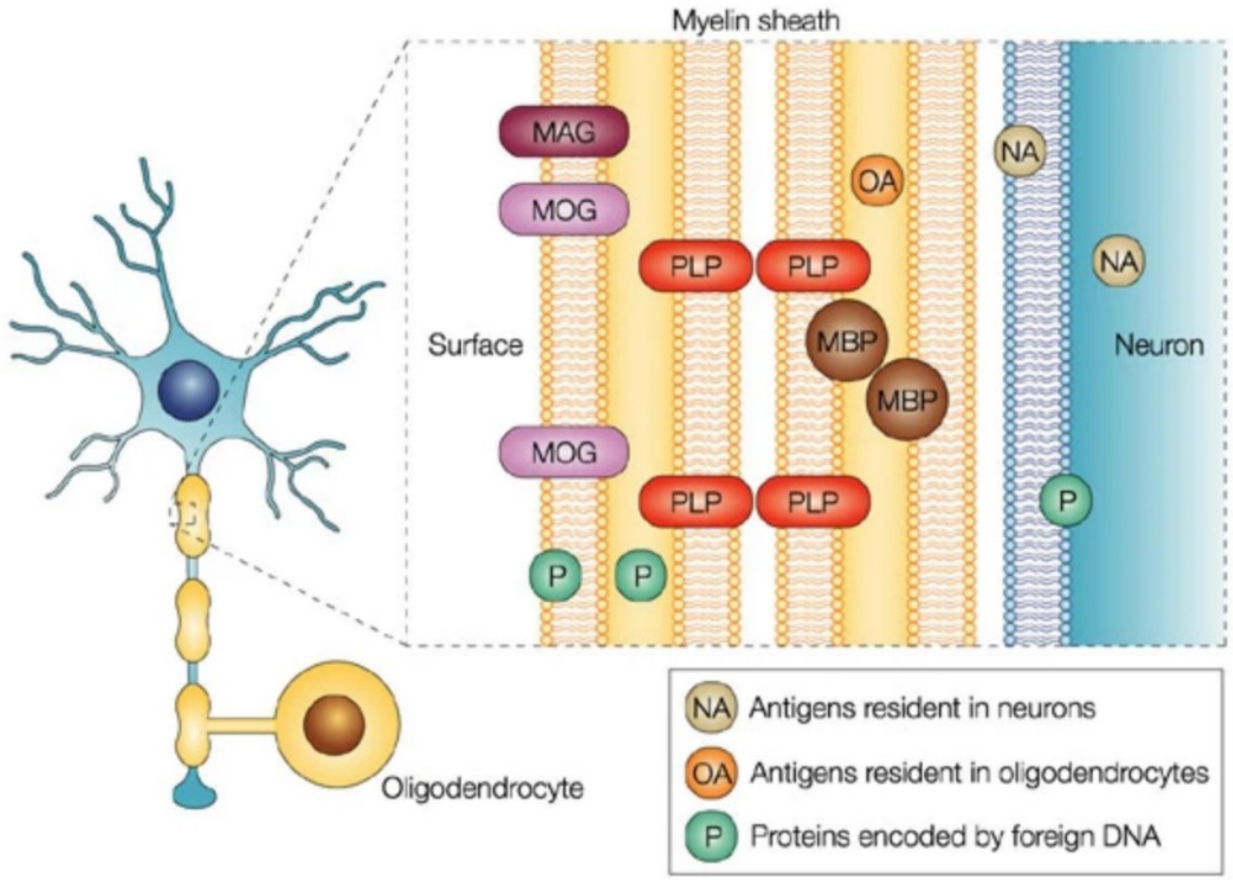

Figure 11. The architecture and molecular composition of myelin [161].

The myelin sheaths consist of lipids and several abundant proteins such as PLP, MBP, MAG and MOG. Reproduced with permission from Springer Nature (Hemmer et al., 2002).

1.7. White matter injury in LSDs

1.7.1. Demyelination

Multiple mechanisms contribute to primary demyelination in LSDs. Impairment of autophagy in LSDs leads to the accumulation of secondary storage materials in myelin-generating cells. Often these materials are toxic (such as sulfatide in MLD or psychosin in KD) and ultimately cause cell death. In addition, neuroinflammation and microgliosis in LSDs may lead to white

matter tract pathologies [164, 165]. Several neuronopathic LSDs are associated with certain level of the white matter disease (Table 2) [166-169].

Table 2. LSDs associated with white matter injury [169]

Disease	Primary storage	Neurologic symptomatology
Krabbe	Galactosylceramide, galactosylsphingosine (psychosine)	Spasticity, arrest of motor and mental development, mental regression which progresses to a severe decerebrate condition with no voluntary movements, and ultimately death.
Metachromatic leukodystrophy	Sulfatides	Motor weakness, ataxia, hypotonia, clumsiness, frequent falls, seizures, peripheral neuropathy and dementia.
Fabry disease	Globotriaosylceramide	Peripheral neuropathy, sensory abnormalities, dysesthesia, recurrent acute and chronic pain
Niemann-Pick type C disease	Unesterified cholesterol and several glycosphingolipids	Progressive impairment of psychomotor development, progressive ataxia, hypotonia, dystonia, loss of cognitive skills, and seizures
Gaucher disease	Glucosylceramide	Peripheral neuropathy, oculomotor apraxia, dysphagia, dystonia, seizures, ataxia
Gangliosidosis GM1	GM1 ganglioside, Keratan sulphate, oligos, glycolipids	Neurodegeneration extrapyramidal signs, gait disturbance
Gangliosidosis GM2	GM2 ganglioside, oligos, glycolipids	Progressive weakness, loss of motor skills, seizures, blindness, spasticity, and motor neuron disease.
MPSIII A & B	Heparan sulfate	Delayed speech and language development, intellectual disability, progressive neurologic deterioration, ataxia, gait disturbance

Krabbe and myeloid leukodystrophy (MLD) are the two LSDs that manifests with the most severe white matter pathology and progressive degeneration of the myelin sheaths. In Krabbe disease, deficiency of β-galactocerebrosidase (GALC) causes the accumulation of galactosylsphingosine, whereas in MLD, arylsulfatase A (ARSA) defects lead to the accumulation of sulfatide. Both galactosylsphingosine and sulfatide belong to sphingolipids which are essential components of myelin sheaths. However, the elevated levels and accumulation of these

compounds due to genetic deficiencies in GALC and ARSA are highly toxic to OLs, leading to apoptotic oligodendrocyte death and demyelination [169-171]. In both Krabbe disease and MLD, MRI brain imaging was especially instrumental for identification and characterization of white matter defects [172, 173].

Given the role of lysosomal hydrolases in the rapid turnover of glycosphingolipids for myelin maintenance, lysosomal dysfunction, that disrupts lipid metabolism, eventually leads to demyelination. For example, in patients affected with lysosomal glycosphingolipidoses, including Fabry disease, neurological forms of Gaucher disease [169] and infantile form of Niemann-Pick type C disease (NPC) [174] demyelination and white matter pathology have also been reported. In addition, in the case of NPC, the secondary storage of GM3 ganglioside in the lysosomes of OLs leads to their dysfunction and, ultimately, demyelination [175]. White matter abnormalities have also been reported in the patients diagnosed with other LSDs involving ganglioside accumulation, GM1 gangliosidosis [176], GM2 gangliosidosis/Tay-Sachs disease [177], multiple sulfatase deficiency [169], MPSIIIA [178], and MPSIIIB [179].

1.7.2. Axonopathy

Besides demyelination, axonopathy has been reported as a common trend among several neuropathic LSDs. Axonal dystrophy alternating with axonal swelling/spheroid formation is an indicator of impaired axonal transport. The areas of axonal swelling contain vesicles accumulating storage materials which emphasizes the significance of lysosomes in maintaining axonal homeostasis and axonal health [180, 181]. Axonal spheroids and dystrophies have been described in multiple LSDs, including KD, MLD, mannosidosis, GM1, and GM2 gangliosidosis, prosaposin deficiency, NPC1, MPS IIIC mouse model [20, 113] and cultured hippocampal neurons from MPS IIIA mice [20].

In 1991, Walkley et al. reported neuroaxonal dystrophy in GABAergic neurons in animal models of GM1 and GM2 gangliosidosis and demonstrated that it impairs neurotransmission in inhibitory circuits [182]. Neuroaxonal dystrophy of GABAergic glutamic acid decarboxylase (GAD)-positive and parvalbumin (PV)-positive neurons has also been reported in the cerebellar cortex and deep nuclei of the cerebellum in the NPC1 cat model [183]. Furthermore, a study by Pressey et al. (2012) showed that in the NPC1 mouse model, presynaptic vesicles cannot reach nerve terminals because they aggregate within axonal spheroids in white matter tracts [184]. Similar phenotype was observed for cultured MPS IIIC mouse neurons [113]. A study involving KD mouse model demonstrated that impaired axonal vesicular transport and accumulation of psychosine affected the structure of axons and caused axonal swelling [185]. Together, these studies suggest that axonopathy can lead to neuronal dysfunction in a broad range of LSDs.

1.8. Rational and objectives

To study the pathophysiology of MPS IIIC, a knockout MPS IIIC (*Hgsnat-Geo*) mouse was previously developed and characterized by Martins *et al.* (2015) and Para *et al.* (2021). Since more than 50% of MPS IIIC patients have at least one missense mutation, affecting HGSNAT folding and activity, we generated a novel HGSNAT-deficient mouse strain ($Hgsnat^{P304L}$), expressing the enzyme with the mouse analog of human missense mutation, Pro311Leu. This amino acid change results in the enzyme misfolding and mistargeting [59]. Performing a comparative analysis of disease progression and pathological changes in the brains of the *Hgsnat-Geo* and $Hgsnat^{P304L}$ mouse models of MPS IIIC is crucial for understanding the impact of misfolded HGSNAT mutant expression. Characterization of this model is also important to determine specific biomarkers of disease progression and support development of novel therapeutic strategies for the MPSIIIC patients.

Our preliminary data showed that progression of the disease in the *Hgsnat*^{P304L} mice is faster than in *Hgsnat-Geo* mice. Because in the tissues of both mouse strains HGSNAT activity is equally reduced to below detection levels, we hypothesize that the rapid progress of CNS pathology in the *Hgsnat*^{P304L} model is associated with increased level of the ER stress in the neurons triggered by expression of misfolded HGSNAT. To test our hypothesis, we proposed two specific aims. In the first aim, I have conducted biochemical, histological, and behavioral characterization of *Hgsnat*^{P304L} and *Hgsnat-Geo* mouse models. In the second aim, I transduced cells from the *Hgsnat-Geo* mice with the lentiviral vector expressing mutant HGSNAT-P311L-GFP protein to test if expression of misfolded HGSNAT-P311L protein in the cultured neuronal cells causes pathological changes (Chapter 2).

Previous studies involving MPS III patients and animal models have revealed that disrupted catabolism of HS in the brain causes neuroinflammation. As chronic neuroinflammation has been previously linked to white matter tract pathology, we hypothesized that evaluation of white matter integrity in MPS IIIC mice may provide novel insights into the pathophysiology of Sanfilippo disease and reveal specific parameters and regions of the brain for MRI analysis, a crucial non-invasive method for evaluation of pathological changes in the brain.

Our first objective was to determine whether white matter defects, in particular, axonal pathology and demyelination, occur in the brain tissues of *Hgsnat*^{P304L} mouse model, and available post-mortem brain samples MPS IIIA, C, and D patients. We used immunohistochemistry and transmission electron microscopy to confirm that demyelination occurs in the brain tissue of *Hgsnat*^{P304L} mice and all subtypes of human Sanfilippo disease. In the second objective, to better understand the mechanism underlying demyelination, we analyzed pathological changes in the oligodendrocytes in the brain of MPS IIIC mice.

Chapter 2

Glucosamine amends CNS pathology in mucopolysaccharidosis IIIC mouse expressing misfolded HGSNAT

CHAPTER 2: Glucosamine amends CNS pathology in mucopolysaccharidosis IIIC mouse expressing misfolded HGSNAT

Xuefang Pan[1]*, Mahsa Taherzadeh[1,2]*, Poulomee Bose[1], Rachel Heon-Roberts[1,2], Annie L.A. Nguyen[1], TianMeng Xu[1], Camila Par´a[1], Yamanaka[3], David A. Priestman[4], Frances M. Platt[4], Shaukat Khan[5], Nidhi Fnu[5], Shunji Tomatsu[5], Carlos R. Morales[2], and Alexey V. Pshezhetsky[1,2]

[1]Centre Hospitalier Universitaire Sainte-Justine Research Center, University of Montreal, Montreal, QC, Canada

[2]Department of Anatomy and Cell Biology, McGill University, Montreal, QC, Canada

[3]Goodman Cancer Research Centre, McGill University, Montreal, QC, Canada

[4]Department of Pharmacology, University of Oxford, Oxford, UK

[5]Nemours/Alfred I. duPont Hospital for Children, Wilmington, DE.

*X. Pan and M. Taherzadeh contributed equally to this paper.

Correspondence to Alexey V. Pshezhetsky

E-Mail : alexei.pchejetski@umontreal.ca.

CHU Sainte-Justine

3175 Côte Ste-Catherine, Montréal (QC) H3T 1C5 – Canada

Tel. (514) 345-4931/2736, Fax. (514) 345-4766

2.1. Abstract

The majority of mucopolysaccharidosis IIIC (MPS IIIC) patients have missense variants causing misfolding of heparan sulfate acetyl-CoA:α-glucosaminide N-acetyltransferase (HGSNAT), which are potentially treatable with pharmacological chaperones. To test this approach, we generated a novel *Hgsnat*^{P304L} mouse model expressing misfolded HGSNAT Pro304Leu variant. *Hgsnat*^{P304L} mice present deficits in short-term and working/spatial memory 2–4 month earlier than previously described constitutive knockout *Hgsnat-Geo* mice. *Hgsnat*^{P304L} mice also show augmented severity of neuroimmune response, synaptic deficits, and neuronal storage of misfolded proteins and gangliosides compared with *Hgsnat-Geo* mice. Expression of misfolded human Pro311Leu HGSNAT protein in cultured hippocampal *Hgsnat-Geo* neurons further reduced levels of synaptic proteins. Memory deficits and majority of brain pathology were rescued in mice receiving HGSNAT chaperone, glucosamine. Our data for the first time demonstrate dominant-negative effects of misfolded HGSNAT Pro304Leu variant and show that they are treatable by oral administration of glucosamine. This suggests that patients affected with mutations preventing normal folding of the enzyme can benefit from chaperone therapy.

2.2. Introduction

Mucopolysaccharidosis IIIC (MPS IIIC) or Sanfilippo syndrome type C is a rare genetic disease manifesting with neuropsychiatric problems, such as hyperactivity, aggressiveness, and autistic features, followed by developmental delay, hearing loss, and childhood dementia (Bartsocas et al., 1979). Most patients become paraplegic during adolescence and die before adulthood, but some survive until the fourth decade of life (Bartsocas et al.,1979) with progressive

dementia and retinitis pigmentosa (Berger-Plantinga et al., 2004; Ruijter et al., 2008; Scriver et al., 2001; Valstar et al., 2008).

The disease is caused by deleterious variants in the gene encoding the lysosomal membrane enzyme, heparan sulfate acetyl-CoA:α-glucosaminide N-acetyltransferase (HGSNAT), which catalyzes transmembrane acetylation of glucosamine residues of heparan sulfate (HS) before their hydrolysis by α-Nacetylglucosaminidase. Lysosomal storage of undegraded HS in the brain cells leads to neuroinflammation and neuronal dysfunction followed by neurodegeneration (reviewed in Heon- Roberts et al. [2020]). Of >70 disease-causing HGSNAT variants identified in MPS IIIC patients, 35 are missense (Martins et al., 2019). Expression studies showed that the resulting amino acid substitutions led to the synthesis of misfolded HGSNAT protein, unable to escape the ER and reach the lysosome (Fedele and Hopwood, 2010; Feldhammer et al., 2009b). These mutations are among the most frequent, with ∼55% of MPS IIIC patients affected with at least one of them. Previously, we could partially rescue 10 mutant misfolded HGSNAT variants by treating patient's cells with the inhibitor of HGSNAT, glucosamine (Feldhammer et al., 2009b), suggesting that these patients could potentially benefit from pharmacological chaperone (PC) therapy, applicable to disorders caused by missense pathogenic variants.

Lysosomal enzymes are secreted into the lumen of the ER in a largely unfolded state (Ellgaard et al., 1999). The WT enzyme folds into the appropriate (native) conformation with the assistance of various chaperones, such as immunoglobulin-binding protein (BiP), heat shock proteins, calnexin, and calreticulin (Ellgaard and Helenius, 2003). In contrast, mutant enzymes, although they might be catalytically active in the acidic milieu of the lysosome, are often not folded properly and cannot be transported to the lysosomes. These mutant proteins are retained in the ER and degraded by the proteasome-associated pathway (Helenius et al., 1992). However, molecules

that mimic substrate binding in the active site, such as competitive inhibitors, may work as PCs, stabilizing the proper position of active site residues and shifting the equilibrium toward the correctly folded state of the enzyme (Asano et al., 2000; Fan et al., 1999; Frustaci et al., 2001; Maegawa et al., 2007; Matsuda et al., 2003; Sawkar et al., 2002; Tropak et al., 2004). As a result, the correctly folded mutant enzyme passes the quality control system of the ER and undergoes further maturation and normal transport to the lysosome. Once a mutant enzyme chaperone complex reaches the lysosome, the chaperone is replaced by a highly concentrated (accumulated) substrate to allow the enzyme to function. Previous studies identified effective chaperones for several lysosomal enzymes, some showing therapeutic effect in mouse models of GM1 and GM2 gangliosidoses, Gaucher disease, and Fabry disease (reviewed in Desnick [2004] and Parenti [2009]). PC therapy is now being translated into clinical applications for cystic fibrosis (Arora and Naren, 2016) and for the lysosomal diseases Fabry, Gaucher, and Pompe (Boyd et al., 2013; Germain et al., 2016; Narita et al., 2016; Parenti et al., 2014). In particular, a PC drug for Fabry disease, Galafold (Germain et al., 2016), has received approval in the European Union and the U.S.

Because the constitutive knockout *Hgsnat-Geo* mice we generated previously (Martins et al., 2015) cannot be used to test chaperone therapy in vivo, in the current study, we produced a mouse expressing HGSNAT with the human misfolded variant Pro311Leu (Pro304Leu in the mouse protein). Mice homozygous for the $Hgsnat^{P304L}$ allele show a drastically bigger increase of neuroinflammation and synaptic defects compared with the knockout mice and have 2-mo-earlier onset of memory impairment, consistent with the dominant-negative effect of the misfolded HGSNAT mutant. Behavioral problems, synaptic defects, and majority of brain pathology were

rescued by treating mice daily with oral glucosamine, validating the use of chaperone therapy as a promising approach to treat MPS IIIC patients with missense variants.

2.3. Results

2.3.1. *Hgsnat*^{P304L} mice and *Hgsnat-Geo* knockout mice show complete deficiency of HGSNAT activity and similar storage of HS in tissues

The mouse *Hgsnat*^{P304L} strain with the Pro304Leu analog of human misfolded HGSNAT Pro311Leu variant (Feldhammer et al., 2009a) was produced essentially as described by Stephenson et al. (2010), following the scheme shown in Fig. S1. Genotyping the offspring from heterozygous breeding revealed an expected Mendelian frequency (25%) for mice homozygous for the *Hgsnat*^{P304L} allele. Similarly to knockout *Hgsnat-Geo* mice (Martins et al., 2015), homozygous *Hgsnat*^{P304L} mice of both sexes were viable and fertile, produced normal litter sizes, and showed normal body weight (BW) gain and general behavior similar to their WT or heterozygous siblings until the age of 7–8 mo, when they presented with BW loss, lethargy, and urinary retention.

HGSNAT protein could not be detected in neither WT nor *Hgsnat*^{P304L} mouse tissues by immunoblot with the commercially available antibodies because it is expressed at a very low level. Expression level of Hgsnat mRNA, measured by quantitative PCR (qPCR) in the brain, liver, and kidney (Fig. 1 A) or by total hippocampal RNA sequencing (data not shown) of the homozygous *Hgsnat*^{P304L} mice, was similar to that in the WT mice, and the message contained the expected c.911C>T change as demonstrated by Sanger sequencing of the RT-PCR products (Fig. 1 A). HGSNAT activity, measured with 4-muf-β-D-glucosaminide in the liver, kidney, and cultured embryonic skin fibroblasts (MEF cells) of homozygous *Hgsnat*^{P304L} mice, was reduced to 0.3–5.0% of that in WT mice, i.e., levels similar to those in the tissues of homozygous knockout

Hgsnat-Geo mice and below or close to the detection limit of the method (Fig. 1 B). In the brain tissues of both *Hgsnat*^{P304L} and *Hgsnat-Geo* homozygous mice, the residual *HGSNAT* activity against 4-muf-β-D-glucosaminide, was 12–15% of normal. However, the N-acetyltransferase *HGSNAT* activity in the brain homogenates, directly measured using 1[4,4-difluoro-5,7-dimethyl-4-bora-3a,4a-diaza-s-indacene-3-propionyl-glycylamino]-β-D-glucosamine (BODIPY-glucosamine; Choi et al., 2015), was reduced to below detection levels (Fig. 1 C). We, therefore, conclude that like human Pro311Leu HGSNAT (Feldhammer et al., 2009b), the mouse enzyme containing the Pro304Leu variant lacks catalytic activity. The residual activity against 4-muf-β-D-glucosaminide was detected only in the brains and not in other studied tissues of homozygous *Hgsnat*^{P304L} and *Hgsnat-Geo* mice or in the soluble mouse liver glycoprotein fraction, suggesting that our batch of 4-muf-β-D-glucosaminide substrate was free of contamination. We speculate, therefore, that the source of brain residual activity was an unknown hydrolase capable of cleaving nonacetylated β-D-glucosaminide.

Interestingly, levels of total β-hexosaminidase activity, measured at 4 mo in the brain, liver, kidney, and lungs of *Hgsnat*^{P304L} mice, showed elevation compared with those in both WT and *Hgsnat-Geo* mice, consistent with increased levels of lysosomal biogenesis and lysosomal storage (Fig. 1 D). This was also supported by higher levels of lysosome-associated membrane protein 2 (LAMP2)+ puncta in the somatosensory cortical (layers 4 and 5) pyramidal neurons in the brains of 4-mo-old *Hgsnat*^{P304L} compared with *Hgsnat-Geo* mice (Fig. 1 E). To determine whether knock-in mice also show increased levels of glycosaminoglycan (GAG) storage, we analyzed their brain tissues and urine by liquid chromatography tandem mass spectrometry (LC-MS/MS). This method measures the concentration of disaccharides produced by enzyme digestion of GAGs known to accumulate in MPS diseases: ΔDi-0S/4S (dermatan sulfate), ΔDiHS-NS and ΔDiHS-0S (HS), as

well as mono- (KS) and disulfated (DiS-KS) keratan sulfate. Disaccharides were quantified by negative ion mode of multiple reaction monitoring (Fig. 1, E and F). We observed drastically increased levels of HS-derived ΔDiHS-0S disaccharide in serum, urine, and brain and ΔDiHSNS disaccharide in the brains of homozygous *Hgsnat*^{P304L} and *Hgsnat-Geo* mice. The levels of HS disaccharides in *Hgsnat*^{P304L} mice showed a trend for an increase compared with *Hgsnat-Geo* mice, but no significant difference was found between the strains. The brain levels of mono- and disulfated KS- and DS derived ΔDi-0S/4S were similar for *Hgsnat*^{P304L} and *Hgsnat-Geo* mice and their WT counterparts at all ages (Fig. 1 G).

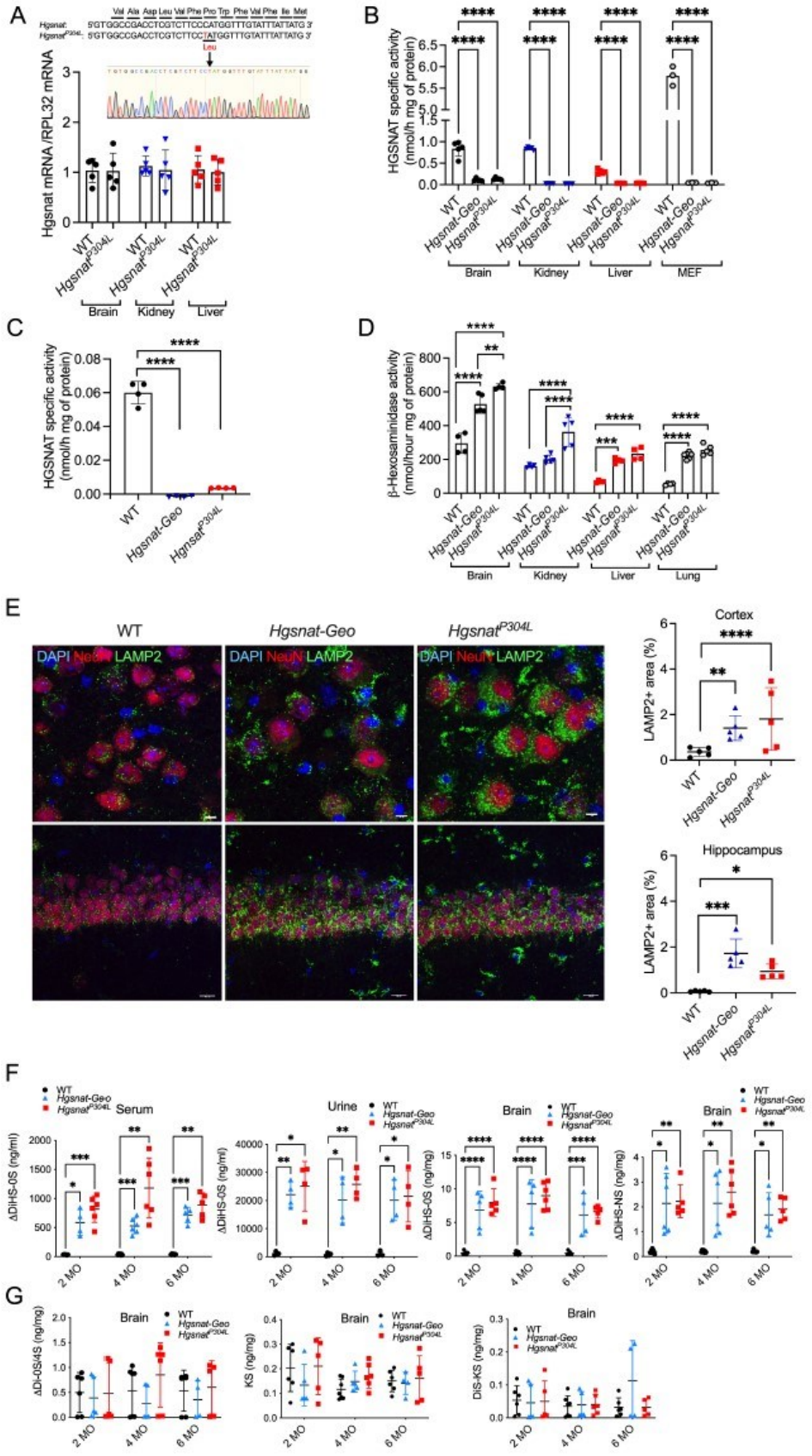
A
B
C
D
E
F
G
Hgsnat mRNA /RPL32 mRNA
HGSNAT specific activity (nmol/h mg of protein)
β-Hexosaminidase activity (nmol/hour mg of protein)
WT
Hgsnat-Geo
HgsnatP304L
Brain
Kidney
Liver
MEF
Lung
DAPI Neu1 LAMP2
Cortex
Hippocampus
LAMP2+ area (%)
Serum
Urine
ΔDIHS-0S (ng/ml)
ΔDIHS-0S (ng/mg)
ΔDIHS-NS (ng/mg)
ΔDi-0S4S (ng/mg)
KS (ng/mg)
DiS-KS (ng/mg)
2 MO
4 MO
6 MO

Figure 1. *Hgsnat*^{P304L} homozygous mice express mutant Hgsnat mRNA and show complete deficiency of HGSNAT activity and greater increase of lysosomal biogenesis, but similar GAG storage compared with *Hgsnat-Geo* mice. (A) Normal levels of Hgsnat mRNA containing c.911C>T mutation are expressed in the tissues of 4-mo-old *Hgsnat*^{P304L} mice. The values are normalized for the level of control RPL32 mRNA. Data, means, and SD of experiments performed with five mice (three male and two female) for each genotype are shown. All amplified PCR fragments were homozygous for c.911C>T mutation (inset). (B) HGSNAT activity toward 4-muf-β-D-glucosaminide in the tissues and in cultured MEF cells of 4-mo-old WT, homozygous *Hgsnat*^{P304L}, and *Hgsnat-Geo* mice is reduced to the background level in all studied tissues except for the brain. (C) HGSNAT activity measured using BODIPY-glucosamine is reduced to the background level in the brains of both *Hgsnat*^{P304L} and *Hgsnat-Geo* mice. (D) Activity of total lysosomal β-hexosaminidase shows a bigger increase in the tissues of *Hgsnat*^{P304L} compared with *Hgsnat-Geo* mice. (E) LAMP2 immunostaining is increased in cortical neurons of 4-mo-old *Hgsnat*^{P304L} mice compared with *Hgsnat-Geo* mice, suggesting higher levels of lysosomal storage. Panels show representative images of the somatosensory cortex (layers 4 and 5) and CA1 region of hippocampus of 4-mo-old *Hgsnat*^{P304L}, *Hgsnat-Geo*, and WT mice. Bars represent 15 μm. Graphs show quantification of LAMP2-stained area by ImageJ software. (F) Levels of disaccharides produced by enzymatic digestion of HS (ΔDiHS-0S and ΔDiHS-NS) were measured by MS/MS in blood serum, urine, and brain tissues of WT, *Hgsnat*^{P304L}, and *Hgsnat-Geo* mice at the age of 2, 4, and 6 mo (MO). (G) Levels of disaccharides produced by enzymatic digestion of DS (ΔDi-0S/4S), and KS and DiS-KS were measured in brain tissues of WT, *Hgsnat*^{P304L}, and *Hgsnat-Geo* mice at the age of 2, 4, and 6 mo. All graphs show individual data, means, and SD of experiments performed using tissues from four to seven mice per genotype per age. MEF cell data show results for three cultures, each obtained from pooled skin samples of three mice. P values were calculated by one-way ANOVA with Tukey post hoc test (A and C), nested one-way ANOVA test with Tukey post hoc test (E), or two-way ANOVA with Tukey post hoc test (B and D–F). *, $P < 0.05$; **, $P < 0.01$; ***, $P < 0.001$; ****, $P < 0.0001$.

2.3.2. *Hgsnat*^{P304L} mice show an earlier onset of behavioral changes, reduced longevity, and increased visceromegaly as compared with the *Hgsnat-Geo* strain

Previously, we have reported progressive behavioral changes in the homozygous *Hgsnat-Geo* mice, including hyperactivity and reduced anxiety at the age between 8 (6 in the female group) and 10 months, as well as deficits in spatial memory and learning at 10 months (Martins et al., 2015). To test whether increased lysosomal storage in *Hgsnat*^{P304L} mice coincided with earlier

onset of behavioral changes, mice were studied using Elevated Plus Maze (EPM, anxiety, and fear), OF (anxiety and hyperactivity), Novel Object Recognition (NOR, short-term memory) and Y-maze (YM, short-term and spatial memory) tests. The tests were performed every two months starting from the age of 2 months, each time with a naïve group of mice.

At the age of 4 months, both male and female *Hgsnat*^{P304L} mice showed abnormal behavior in all four tests, including increased hyperactivity (increased distance traveled in OF, Fig. 2A), reduced anxiety (increased distance traveled in the central part of the arena in OF, Fig. 2B), increased percentage of time spent in the open arms and increased number of open arm entries in EPM, Fig. 2C,D), and deficits in spatial as well as in short-term memory (reduced recognition index in NOR, Fig. 2E, reduced alteration rate in YM, Fig. 2F). In contrast, *Hgsnat-Geo* mice demonstrated normal behavior in YM at both 4 and 6 months, reduced alternation only at 8 months (Fig. 2F) and, as we reported previously, showed hyperactivity and reduced anxiety in OF test only between 8 (6 in the female group) and 10 months (Martins et al., 2015). Together, these data demonstrate that behavioral changes occur in *Hgsnat*^{P304L} mice at least 2-4 months earlier than in the *Hgsnat-Geo* mice.

Similar to *Hgsnat-Geo* mice and the mouse models of MPS IIIA and MPS IIIB (Bhaumik et al., 1999; Li et al., 1999), *Hgsnat*^{P304L} mice develop urinary retention resulting in abdominal distension and requiring humane euthanasia. However, their average life span is ~20 weeks less than the lifespan of *Hgsnat-Geo* mice (Fig. 2G). Like *Hgsnat-Geo* mice, *Hgsnat*^{P304L} animals do not develop skeletal abnormalities (Fig. S1). However, *Hgsnat*^{P304L} mice sacrificed around the age of 40 weeks show enlargement of liver, kidneys, and spleen, unlike *Hgsnat-Geo* mice which show only hepatomegaly (Fig. 2H).

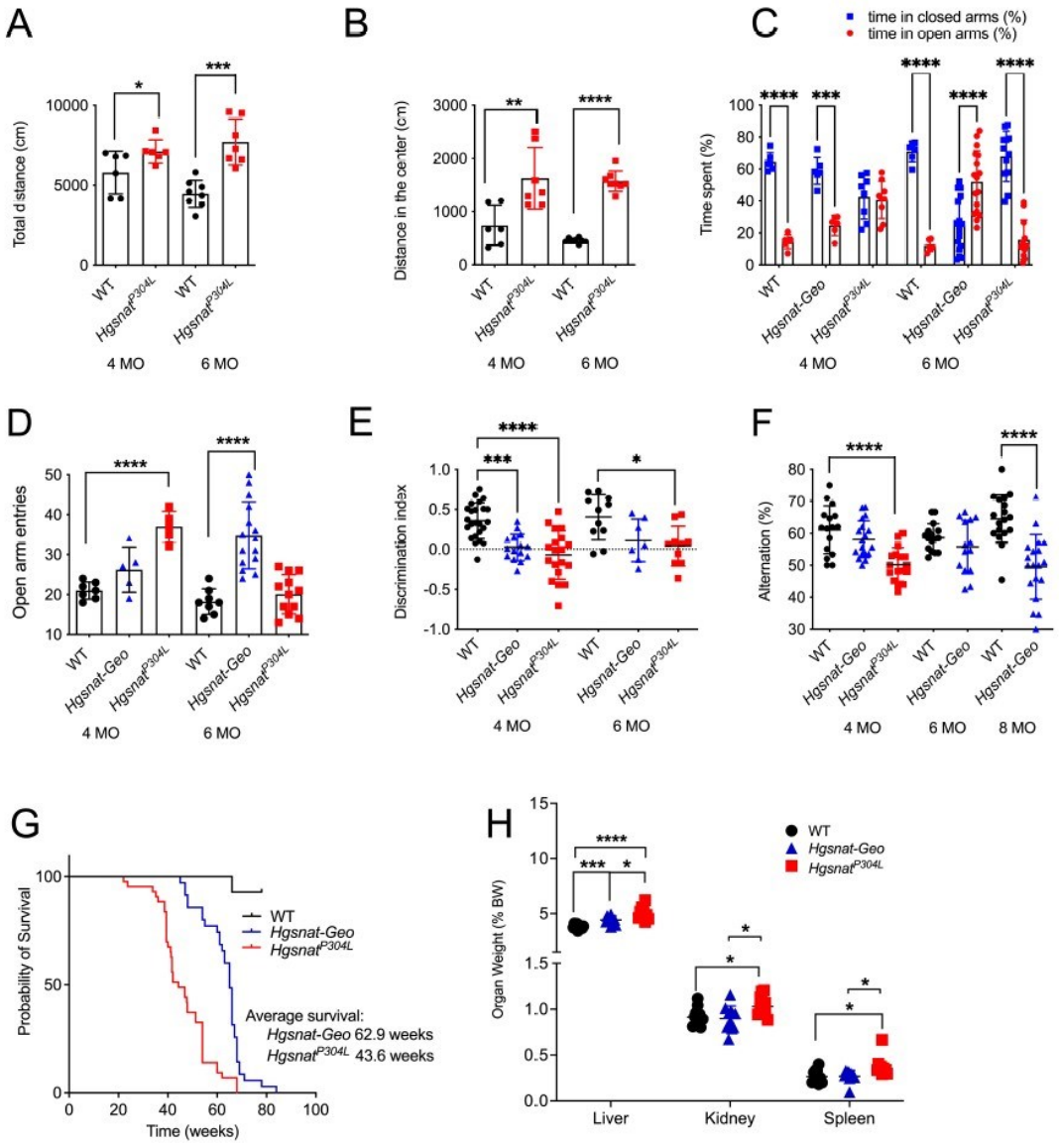

Figure 2. Pathological phenotypes of *Hgsnat-Geo* and *Hgsnat*^{P304L} mice. (A and B) Significant increase in total distance traveled in the OF (A) and the distance traveled in the central zone (B) by *Hgsnat*^{P304L} mice compared with age-matched WT controls. (C) Significant decrease and increase in the percentage of time spent in open arms and closed arms in the elevated plus maze, respectively, by *Hgsnat-Geo* and *Hgsnat*^{P304L} mice compared with age-matched WT controls. (D) Significant increase in the number of open arm entries in the elevated plus maze by *Hgsnat-Geo* and *Hgsnat*^{P304L} mice compared with age-matched WT controls. (E) Significant decrease in the discrimination index in *Hgsnat*^{P304L} mice at 4 and 6 mo (MO) in NOR test compared with age-matched WT controls. (F) *Hgsnat*^{P304L} and *Hgsnat-Geo* mice show onset of learning impairment in YM at 4 and 8 mo, respectively. All graphs show individual data, means, and SD of

experiments performed with 6–17 mice per genotype. P values were calculated by t test for experiments involving comparison of two groups (A and B), and ANOVA with Tukey post hoc test, when comparing three groups (C–F). (G) Kaplan–Meier plot showing survival of *Hgsnat*^{P304L} (n = 43) and *Hgsnat-Geo* male and female mice (n = 35) and their WT counterparts (n = 28). The significance of survival rate differences between strains was determined by the Mantel–Cox test ($P < 0.05$). By the age of 45 wk, most *Hgsnat*^{P304L} mice had to be euthanized on veterinarian request due to urinary retention, while *Hgsnat-Geo* mice survived to the average age of 63 wk. (H) Wet organ weight of 8-mo-old *Hgsnat*^{P304L}, *Hgsnat-Geo*, and WT mice is shown as a percentage of BW. Enlargement of visceral organs, compared with age-matched WT controls, is detected in *Hgsnat*^{P304L} but not in *Hgsnat-Geo* mice. All graphs show individual data, means, and SD of experiments performed with five or more mice per genotype. P values were calculated using two-way ANOVA with Tukey post hoc test. *, $P < 0.05$; **, $P < 0.01$; ***, $P < 0.001$; ****, $P < 0.0001$.

2.3.3. *Hgsnat*^{P304L} mice show more pronounced defects in synaptic neurotransmission compared with the *Hgsnat-Geo* strain

To characterize synaptic neurotransmission in MPS IIIC mice, we performed whole-cell patch-clamp recordings on acute slices from *Hgsnat*^{P304L} mice at P14-20 and P45-60. When the data were analysed together with our previous results for the age-matched groups of *Hgsnat-Geo* and WT mice (Para et al., 2021), we found that the amplitudes of miniature excitatory postsynaptic currents (mEPSC) were significantly reduced in both *Hgsnat-Geo* and *Hgsnat*^{P304L} mice as compared with WT mice. However, no significant difference was detected between *Hgsnat-Geo* and *Hgsnat*^{P304L} mice (Fig. 3A, B). Also, no differences in the mEPSCs kinetics between the two animal groups were observed (data not shown). Importantly, for both *Hgsnat-Geo* and *Hgsnat*^{P304L} mice, there was an age-dependent (P14-20 vs P45-60) significant decrease in mEPSC amplitudes (Fig. 3A) suggesting progressive synaptic deficits. The mEPSC frequency was significantly reduced in both *Hgsnat-Geo* and *Hgsnat*^{P304L} mice as compared with WT controls at both ages, however, at P45-60, *Hgsnat*^{P304L} mice displayed significantly reduced mEPSC frequencies as compared with *Hgsnat-Geo* mice (Fig. 3C). In contrast, aggravated defects in inhibitory neurotransmission were observed in *Hgsnat*^{P304L} mice as compared with the knockout model. At

both P14-20 and P45-60, *Hgsnat*^{P304L} mice showed significantly reduced frequencies of miniature inhibitory postsynaptic currents (mIPSC) as compared to WT or *Hgsnat-Geo* mice of the same age (Fig. 3D-F).

To test if changes in synaptic transmission were associated with those in the architecture of the synaptic compartment, we analyzed hippocampal tissues of *Hgsnat-Geo* and *Hgsnat*^{P304L} mice at the ages of 3 and 6 mo by transmission electron microscopy (TEM). As before (Par´a et al., 2021), we have measured the length and the area of postsynaptic densities (PSDs) and densities of synaptic vesicles in the terminals of asymmetric (excitatory) and symmetric (inhibitory) synapses of pyramidal CA1 neurons (Fig. 3, G and H).

At the age of 3 mo, the areas of excitatory PSDs of CA1 neurons in *Hgsnat-Geo* mice were similar to those in WT mice, while in the *Hgsnat*^{P304L} mice they were already significantly reduced. At the age of 6 mo, the areas of excitatory PSDs in hippocampal neurons of both MPS IIIC mouse models were reduced compared with WT mice, but the Hgsnat^{P304L} mice expressed a particularly drastic phenotype, with PSD areas ∼50% smaller than those in WT mice. A similar trend was observed for the excitatory PSD length: by 6 mo, PSD length in Hgsnat^{P304L} mice was significantly reduced compared with both WT and *Hgsnat-Geo* mice. The density of synaptic vesicles (total number of synaptic vesicles divided by the area of the terminal) also showed a more rapid decrease in *Hgsnat*^{P304L} mice, with a reduction by ∼43% at 3 mo and ∼60% at 6 mo compared with WT mice. In *Hgsnat-Geo* mice, they were reduced only by ∼30 and ∼40%, respectively (Fig. 3, G and H). Together, these data revealed that the *Hgsnat*^{P304L} strain shows more pronounced defects in neurotransmission and synaptic architecture compared with the *Hgsnat-Geo* strain.

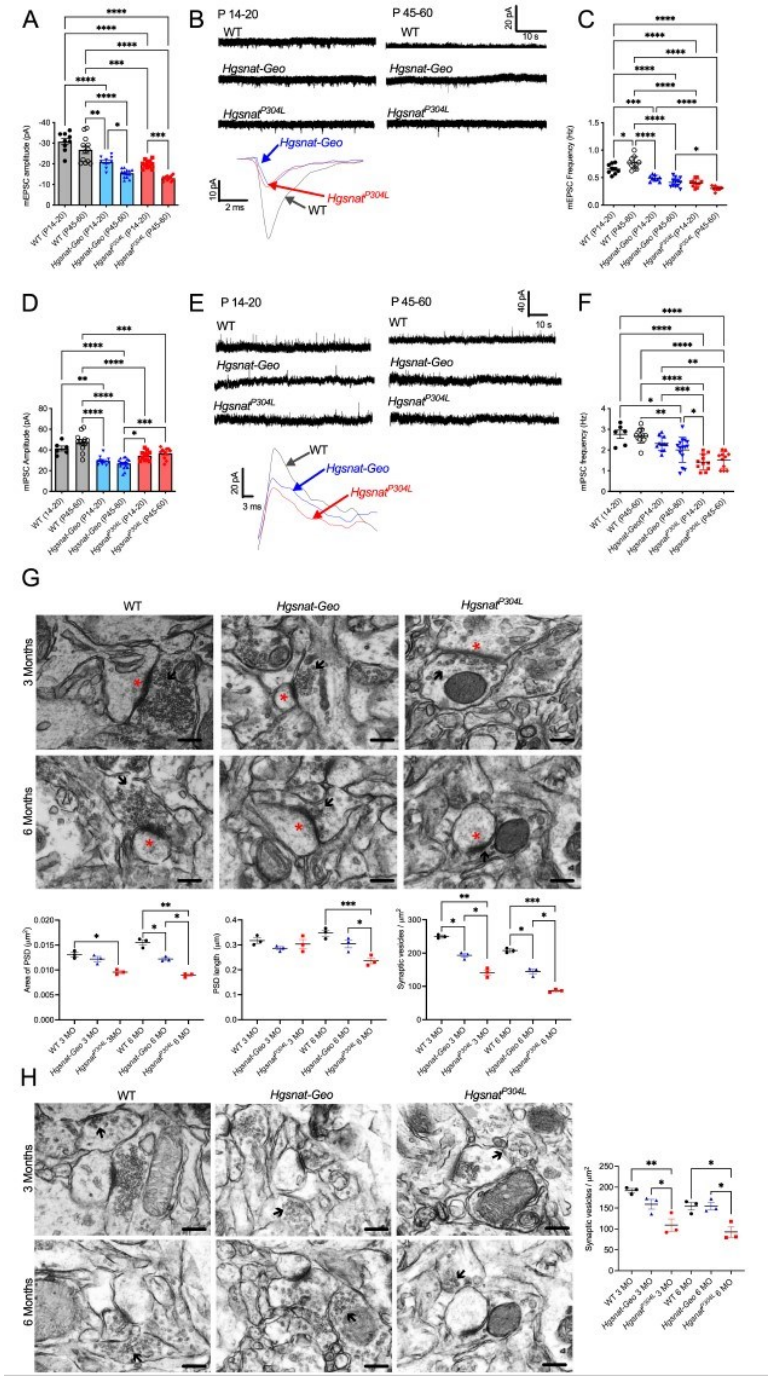

Figure 3. Synaptic defects in *Hgsnat-Geo* and *Hgsnat*^{P304L} mice. (A–F) Neurotransmission is impaired in *Hgsnat-Geo* and *Hgsnat*^{P304L} mice. Significant decrease in the amplitude (A) and frequency (C) of mEPSCs in *Hgsnat-Geo* and *Hgsnat*^{P304L} mice at the ages of P14–P20 and P45–P60 compared with age-matched WT controls. (B) Representative recordings of mEPSCs from WT, *Hgsnat-Geo,* and Hgsnat^{P304L} mice at P14–P20 and P45–P60, and overlay of representative individual mEPSC events from neurons of *Hgsnat-Geo*, Hgsnat^{P304L}, and WT mice. Significant decrease in the amplitude (D) and frequency (F) of

mIPSCs in *Hgsnat-Geo* and *Hgsnat*^{P304L} mice at the ages of P14–P20 and P45–P60 compared with age-matched WT controls. (E) Representative recording of mIPSCs from neurons of WT, *Hgsnat-Geo*, and *Hgsnat*^{P304L} mice at the ages of P14–P20 and P45–P60 and overlay of representative individual mIPSC events from neurons of *Hgsnat-Geo*, *Hgsnat*^{P304L}, and WT mice. All graphs show individual data, means, and SD of experiments performed with six or more mice per genotype. P values were calculated using one-way Kruskal–Wallis test with Dunn's multiple comparison post hoc test. (G and H) Reduction of synaptic vesicle densities, areas of PSDs, and length of PSDs in *Hgsnat-Geo* and *Hgsnat*^{P304L} CA1 pyramidal neurons. Density of synaptic vesicles, length (μm), and area (μm2) of PSDs were measured in asymmetrical (G) and symmetrical (H) pyramidal neurons from the CA1 region of the hippocampus. Synaptic terminals on the TEM images are marked with black arrowheads and PSDs with red asterisks. Data show values, means, and SD of the results obtained with three mice per genotype with 10–15 neurons quantified per animal. P values were calculated by nested one-way ANOVA test with Tukey post hoc test. Scale bars equal 200 nm in all panels. *, $P < 0.05$; **, $P < 0.01$; ***, $P < 0.001$; ****, $P < 0.0001$. MO, mo.

2.3.4. *Hgsnat*^{P304L} mice show accelerated progression in central nervous system (CNS) pathology

Comparative analysis of pathological changes in the brain of *Hgsnat-Geo* and *Hgsnat*^{P304L} mice demonstrated that they are aggravated in the knock-in mice. The levels of activated CD68+ microglia and GFAP+ astrocytes at 4 mo were significantly increased in the hippocampi and GFAP+ astrocytes in the hippocampi and somatosensory (layers 4–5) cortices of *Hgsnat*^{P304L} mice compared with both WT and *Hgsnat-Geo* strains (Fig. 4 A). This coincided with the significantly increased expression levels of inflammatory cytokines MIP1α and TNFα in the brains of *Hgsnat*^{P304L} compared with *Hgsnat-Geo* mice (Fig. 4 B).

The presence of LC3+ puncta was detected in cortical layer 4–5 pyramidal neurons of both *Hgsnat-Geo* and *Hgsnat*^{P304L} mice, but not of WT mice at 6 mo, suggesting an autophagy block (Fig. 4 C). Neurons of the same layers also contained increased levels of enlarged autofluorescent ceroid materials visible already at 4 mo (Fig. 4 D). Importantly, the number of cells containing autofluorescent material was significantly increased in *Hgsnat*^{P304L} compared with *Hgsnat-Geo*

mice, suggesting that the progression of this pathology is accelerated in the knock-in model. At 6 mo, neurons of the same layers were heavily stained with antibodies against the amyloid-β protein (AP; Fig. 4 E) or misfolded subunit C of mitochondrial ATP synthase (SCMAS; Fig. 4 F). Together, these data are suggestive of mitophagy block and a general impairment of proteolysis.

Levels of simple gangliosides GM2 and GM3 are drastically increased in the brains of MPS IIIA-D patients (Viana et al., 2020) and in the knockout MPS IIIC mouse model (Martins et al., 2015). To analyze if they are also induced in the brain of *Hgsnat*^{P304L} mice, glycosphingolipids were extracted from the pooled brain tissues of 2-, 4-, and 6-mo-old mice. Analysis of their fluorescently labeled glycan chains by normal-phase HPLC (Fig. 4 G) demonstrated that brain glycosphingolipid composition was significantly altered in both *Hgsnat*^{P304L} and *Hgsnat-Geo* mice, but, on average, changes in the *Hgsnat*^{P304L} mice were more pronounced. The most drastic changes were observed in the levels of GM3 (approximately sevenfold increase in *Hgsnat*^{P304L} and approximately sixfold increase in *Hgsnat-Geo* mice), followed by GM2 (five- and fourfold increases, respectively) and GA2 (three and two fold increases, respectively). Interestingly, *Hgsnat*^{P304L} mice showed a trend for a progressive increase in the levels of these gangliosides in contrast to *Hgsnat-Geo* mice, in which the levels remained similar at all studied ages. No changes were observed for complex gangliosides GM1a, GD1a, GD1b, and GT1b.

To confirm the HPLC results, we analyzed the presence and distribution of GM2 ganglioside in brain tissues by immunohistochemistry, using the human-mouse chimeric monoclonal antibody, KM966 (Nakamura et al., 1994). Numerous KM966+ neurons were present in the somatosensory cortex layers 4–5 and CA1 region of the hippocampus of both *Hgsnat*^{P304L} and *Hgsnat-Geo* mice. However, in both brain regions, the amounts of GM2+ cells were significantly increased in the knock-in compared with knockout mice (Fig. 4 H).

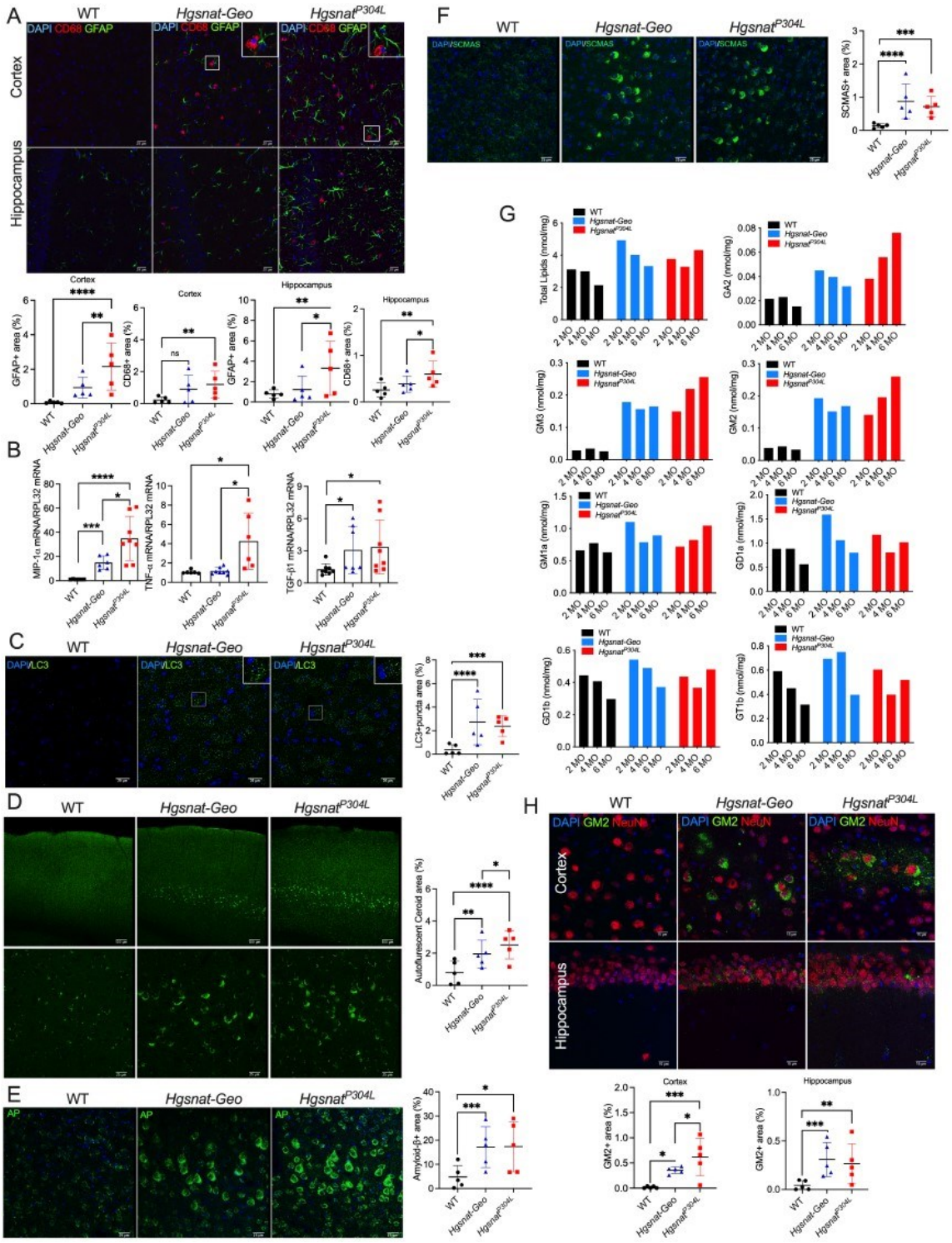

Figure 4. Aggravated pathological changes in the brains of *Hgsnat*^{P304L} mice. (A) Astromicrogliosis in brain hippocampal and cortex regions of MPS IIIC mice is indicative of neuroimmune response. Panels show representative confocal microscopy images of brain tissues of 4-mo-old *Hgsnat-Geo* and *Hgsnat*^{P304L}

mice and their age-matched WT controls stained with antibodies against CD68 (red) and GFAP (green) markers for activated microglia and astrocytes, respectively. DAPI (blue) was used as a nuclear counterstain. Graphs show quantification of fluorescence with ImageJ software. Individual data, means, and SD obtained for five mice per genotypes (three areas/mouse) are shown. P values were calculated using nested one-way ANOVA test with Tukey post hoc test. (B) Total brain tissues of *Hgsnat*^{P304L} mice show increased expression of inflammation markers, MIP1α, and TNFα compared with *Hgsnat-Geo* mice. The cytokine mRNA levels are normalized for the RLP32 mRNA content. Data show individual data, means, and SD. Five to eight mice were analyzed for each genotype. P values were calculated using one-way ANOVA with Tukey post hoc test. (C–F) Somatosensory cortices (layers 4–5) of *Hgsnat*^{P304L} mice show increased levels of markers of impaired autophagy and proteolysis compared with *Hgsnat-Geo* and/or age-matched WT mice: cytoplasmic LC3-positive puncta (C), granular autofluorescent ceroid materials (D), amyloid-β protein (AP; E), and misfolded SCMAS (F). Panels show representative confocal microscopy images of brain tissues of 4-mo-old (A, B, and D) or 6-mo-old (C, E, and F) *Hgsnat-Geo, Hgsnat*^{P304L}, and WT mice. Bars represent 20 μm in A and C, 100 and 25 μm in D, and 25 μm in E and F. Fluorescence was quantified with ImageJ software. Graphs show individual data, means, and SD obtained for five mice per genotype (three areas/mouse). P values were calculated using nested one-way ANOVA test with Tukey post hoc test. (G) Alteration of sphingolipid levels in the brains of *Hgsnat-Geo* and *Hgsnat*^{P304L} mice. Levels of glycans produced by enzymatic cleavage of total sphingolipid extracts of brain tissues from WT, *Hgsnat-Geo,* and *Hgsnat*^{P304L} 2-, 4-, and 6-mo-old mice were measured by normal HPLC. The values show percentage of the specific lipid. Pooled samples of three mice per age per genotype were analyzed. (H) Increased levels of GM2 ganglioside in the brains of *Hgsnat-Geo* and *Hgsnat*^{P304L} mice. Confocal microscopy images of brain cortex and hippocampus tissues of individual *Hgsnat-Geo, Hgsnat*^{P304L}, and WT 4-mo-old mice stained with antibodies against GM2 (green) and NeuN (red). DAPI (blue) was used as the nuclear counterstain. Scale bar equals 15 μm. Graphs show results of quantification performed using ImageJ software. Individual data, means, and SD obtained for five mice per genotypes (three areas/mouse) are shown. P values were calculated using nested one-way ANOVA test with Tukey post hoc test. *, $P < 0.05$; **, $P < 0.01$; ***, $P < 0.001$; ****, $P < 0.0001$. MO, mo.

2.3.5. Aggravated pathological alterations in gene expression and increased levels of protein markers of unfolded protein response (UPR) and ER stress in the brains of *Hgsnat*^{P304L} mice

To get insight into the molecular mechanisms underlying the severe phenotype of *Hgsnat*^{P304L} mice, we performed a bulk analysis of gene expression levels in the hippocampi of 4-mo-old mice by RNA sequencing. Three mice (one female and two male) were analyzed for each

genotype. The expression levels of each gene were compared between the *Hgsnat*^{P304L} and *Hgsnat-Geo* strains, as well as between each of the MPS IIIC strains and the corresponding WT controls.

A higher number of hippocampal genes with altered expression levels was found in *Hgsnat*^{P304L} (439 upregulated, 127 downregulated) compared with *Hgsnat-Geo* mice (221 upregulated, 124 downregulated; Fig. S2 A and Table S1). These genes were classified according to their biological function and linked to metabolic or signaling pathways using automated Gene Ontology (GO) terms annotation (Huang et al., 2009). The pathways involved in synaptic transmission (30–60% of all genes in the pathway) and neuronal growth/differentiation (10–30% of all genes) showed major downregulation in both strains (Fig. 5, A and B). Importantly, the expression levels of the genes involved in GABAergic neurotransmission were reduced only in the *Hgsnat*^{P304L} mice but not in *Hgsnat-Geo* mice, which was consistent with more pronounced defects in the inhibitory synapses detected in the knock-in mice by electrophysiology experiments (Fig. 5 A).

The most upregulated groups of genes were those encoding lysosomal and autophagosomal proteins, sphingolipid biosynthesis genes, and genes involved in inflammatory and innate immune response, consistent with induced lysosomal biogenesis, alterations of ganglioside levels, and inflammation observed in the mouse brains (Fig. 5, A and B). Specifically, several lysosomal (including Arsg, Ctsc, Ctsz, Ctsd, Npc2, and Slc12A4) and inflammatory genes showed a significant increase only in *Hgsnat*^{P304L} but not in *Hgsnat-Geo* mice, mirroring higher levels of lysosomal storage and neuroimmune response in the 4-mo old knock-in animals (Fig. 5 A).

A direct comparison of *Hgsnat*^{P304L} and *Hgsnat-Geo* expression profiles did not reveal significant changes in the expression of a gene or genes that could be directly responsible for the enhanced pathology in the knock-in mice. However, the pathways related to inflammation,

cytokine production, apoptosis, and lipid biosynthesis were upregulated, while those involved in synaptic function, neurogenesis, and mitochondrial biogenesis and function, downregulated in *Hgsnat*^{P304L} compared with *Hgsnat-Geo* mice. Besides, compared with WT mice, the levels of genes related to lysosomal/ endosomal biogenesis (such as Kcne2, Tfeb, Cst3, Gata2, Rilp, Pld1, Tlr7, and Tmem59) and inflammatory response (Tlr7, Il-2, Il-25/Il-17, Ifngr1, Csf2rb2, Il15ra, and Il17rc) showed a trend for a bigger increase in *Hgsnat*^{P304L} than in *Hgsnat-Geo* mice (Fig. S2, B and C). In similar fashion, genes involved in inhibitory synapse showed a trend for bigger reduction (Fig. S2 D).

Interestingly, a similar trend was observed for Xbp1, Atf4, Ern1, Atf6, Atf3, and Hspa5 genes, which induction has been previously associated with the ER stress and UPR (Fig. S2 E). This suggested a higher degree of the ER stress and UPR in the brain cells expressing the misfolded HGSNAT enzyme. To test this further, we have analyzed brain tissues by immunohistochemistry using antibodies against O-linked GlcNAc glycan and found increased levels of O-GlcNAc–modified proteins, an indication of the ER stress often associated with impaired cellular proteolysis (Chatham and Marchase, 2010), in the CA1 and cortical neurons of *Hgsnat*^{P304L} compared with *Hgsnat-Geo* mice (Fig. 5 D). We have also found increased levels of polyubiquitinated protein aggregates in the homogenates of dissected cortices of *Hgsnat*^{P304L} compared with *Hgsnat-Geo* mice (Fig. 5 E). This was consistent with the increased number of pyramidal neurons containing ubiquitin positive materials in somatosensory cortex layers 4 and 5 of *Hgsnat*^{P304L} compared with *Hgsnat-Geo* mice (Fig. 5 F). These results, together, confirmed higher levels of ER stress and UPR in the neurons of the knock-in MPS IIIC mice. Other markers of ER stress, C/EBP homologous protein (CHOP) and BiP, did not show an increase in the brains of *Hgsnat*^{P304L} compared with *Hgsnat-Geo* mice at either 6 or 8 mo (Fig. S2, F and G).

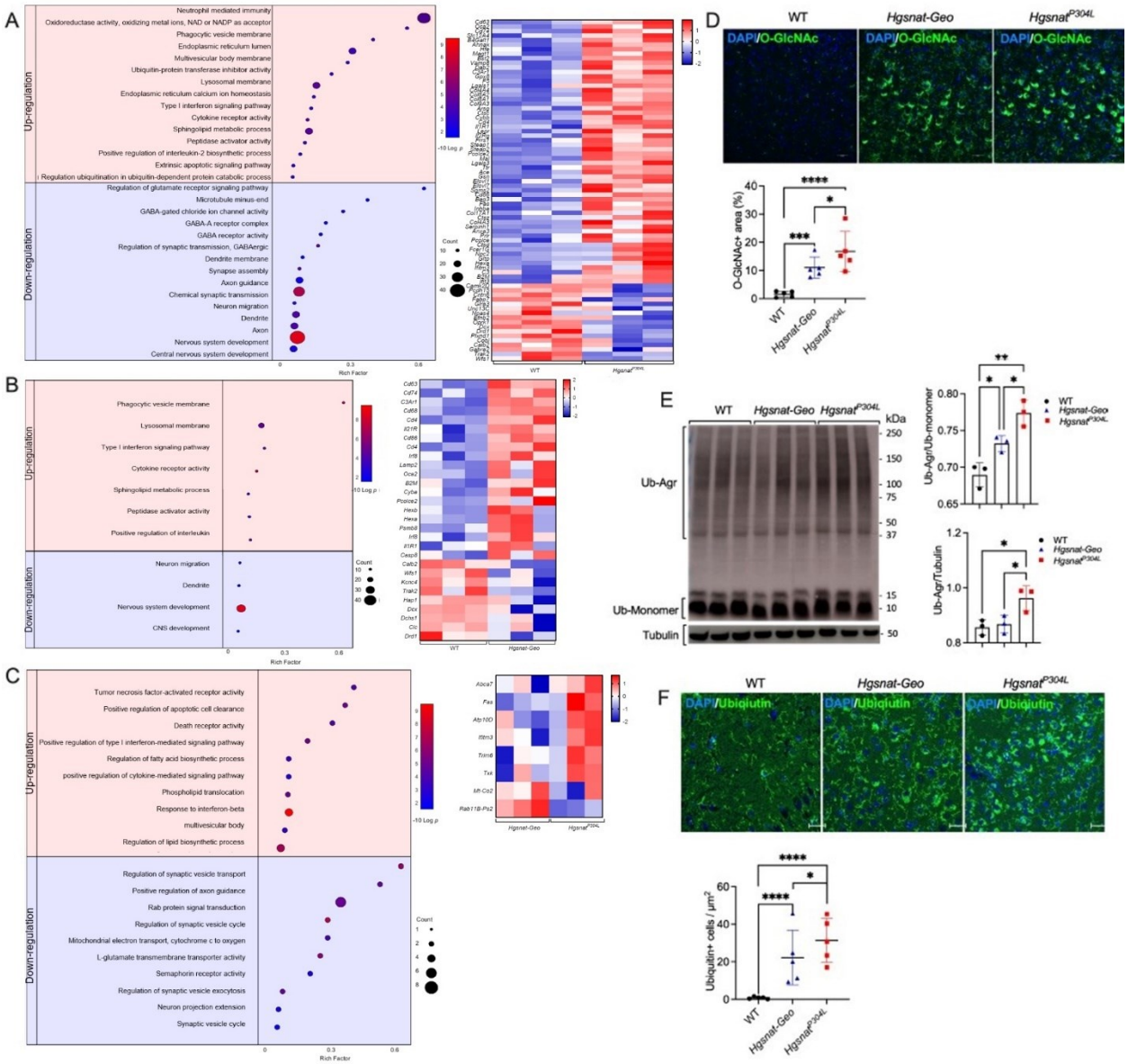

Figure 5. Aggravated pathological alterations in the gene expression and increased levels of protein markers of UPR and the ER stress in the brains of *Hgsnat*^{P304L} mice. (A–C) Hippocampal mRNA profiling in 4-mo-old MPS IIIC mice reveals increased expression of genes involved in lysosomal, lipid synthesis, and proinflammatory processes and reduced expression of genes involved in synaptic transmission, vesicular transport, and neurogenesis. Dot plots (left) show significantly enriched GO terms (biological processes, molecular functions, and cellular components) and heatmaps (right) of the genes significantly upregulated and downregulated in the hippocampi of *Hgsnat*^{P304L} mice compared with WT mice (A), *Hgsnat-Geo* mice compared with WT mice (B), and *Hgsnat*^{P304L} mice compared with *Hgsnat-Geo* mice (C). GO terms are plotted in the order of gene ratios, and each pathway is shown as a circle with

the color representing the P values (−log10) and the size representing the number of differentially expressed genes. The heatmap colors and their intensity show changes in gene expression levels. Data were obtained by sequencing mRNA samples extracted from three mice per genotype. (D) Brain cortex of *Hgsnat*^{P304L} 6-mo-old mice shows increased levels of O-GlcNAc–modified proteins compared with *Hgsnat-Geo* and WT mice. Panels show representative images of brain cortex (layers 4–5) immunostained for O-GlcNAc (green). DAPI (blue) was used as a nuclear counterstain. Scale bar equals 25 μm. Graphs show results of quantification performed using ImageJ software. Individual data, means, and SD obtained for five mice per genotype (three areas/mouse) are shown. P values were calculated using nested one-way ANOVA test with Tukey post hoc test. (E) Increased levels of ubiquitinated protein aggregates are detected in the brain homogenates of *Hgsnat*^{P304L} mice by immunoblotting. Graphs show combined intensities (individual values, means, and SD) of protein ubiquitin+ bands, quantified with ImageJ software and normalized by either intensity of tubulin bands or bands of ubiquitin monomers. Three mice per genotype were analyzed. P values were calculated using ANOVA with Tukey post hoc test. (F) Somatosensory cortex (layers 4–5) of *Hgsnat*^{P304L} mice shows increased levels of pyramidal neurons containing cytoplasmic ubiquitin+ materials. Panels show representative confocal microscopy images of brain tissues, stained for ubiquitin, of 6-mo-old *Hgsnat-Geo, Hgsnat*^{P304L}, and WT mice. Scale bar equals 25 μm. Graph shows results of quantification performed using ImageJ software. Individual data, means, and SD obtained for five mice per genotypes (three areas/mouse) are shown. P values were calculated using nested one-way ANOVA test with Tukey post hoc test. *, $P < 0.05$; **, $P < 0.01$; ***, $P < 0.001$; ****, $P < 0.0001$. Source data are available for this figure: Source Data F5.

2.3.6. Expression of the P304L HGSNAT variant in hippocampal cultured neurons of *Hgsnat-Geo* mice causes ER stress and aggravates deficits in the expression of synaptic proteins and synaptic architecture

To test directly whether the expression of the mutant Pro311Leu human HGSNAT variant aggravates neuronal dysfunction, we expressed it in the primary cultured hippocampal neurons of *Hgsnat-Geo* mice. To confirm that the Pro311Leu variant caused misfolding of the HGSNAT protein and its retention in the ER, we transduced HEK293 cells and human cultured skin fibroblasts with the lentiviral vectors (LVs) that encode the WT HGSNAT-GFP fusion protein and its Pro311Leu variant. Cells expressing GFP marker were isolated by cell sorting and propagated. As expected, we detected highly increased HGSNAT activity in the cells overexpressing human

WT HGSNAT, while the activity in the cells overexpressing the mutant variant was similar to that of non transduced cells (Fig. S3 A). The WT protein was correctly processed as detected by the appearance of a 29-kD band on the Western blot (Fig. S3 B). It was also showing a "halo-like" pattern around the LysoTracker Red–stained lysosomes on the images obtained by a high-resolution confocal fluorescent microscopy suggesting that it was correctly targeted to the lysosomal membrane (Fig. S3 C). In contrast, the mutant HGSNAT-GFP fusion protein was detected only in the form of a 75-kD precursor (Fig. S3 B) and did not show any colocalization with LysoTracker Red or P115-stained Golgi apparatus (Fig. S3, C and D). Instead, it was retained in the ER as demonstrated by its colocalization with the ER marker, Calreticulin (Fig. S3 F). In both fibroblasts (Fig. S3, C and D) and HEK293 cells (data not shown), Pro311Leu HGSNAT-GFP protein also formed cytoplasmic aggregates.

We further transduced primary hippocampal neurons of *Hgsnat-Geo* mice with either LV-HGSNAT-GFP or LV-P311LHGSNAT-GFP to detect whether mutant protein expression aggravated synaptic defects. The cells were studied by immunocytochemistry to detect markers of synaptic vesicles (Syn1), GABAergic (VGAT/Gephyrin), and glutamatergic (VGLUT1/PSD-95) synapses. Non transduced neurons of WT, $Hgsnat^{P304L}$, and *Hgsnat-Geo* mice were studied for comparison.

Analysis of non transduced cells confirmed that neurons from both $Hgsnat^{P304L}$ and *Hgsnat-Geo* mice showed a similar reduction in density of Syn1+ puncta along the MAP2-stained dendrites as well as of PSD95+ in juxtaposition with VGLUT1+ puncta (Fig. 6, A–C) compared with WT neurons. This was consistent with our electrophysiology results, demonstrating that glutamatergic synapse is similarly affected in both strains. In contrast, the number of Gephyrin+/VGAT+ puncta in juxtaposition was reduced in neurons from $Hgsnat^{P304L}$ but not in

those from *Hgsnat-Geo* mice, confirming that the GABAergic synapse is affected only in the knock-in mice (Fig. 6 C).

Transduction of neurons from *Hgsnat-Geo* mice with LV HGSNAT-GFP rescued levels of synaptic protein markers (dendrite-associated Syn1 puncta, VGLUT1+ puncta in juxtaposition with PSD-95+ puncta; Fig. 6, A–C). In contrast, the *Hgsnat-Geo* neurons expressing mutant Pro311Leu HGSNAT-GFP protein showed levels of inhibitory VGAT+/Gephyrin+ synaptic puncta in juxtaposition significantly lower than those in the non transduced cells (Fig. 6 D). The levels of excitatory VGLUT+/PSD-95+ puncta in juxtaposition in *Hgsnat-Geo* neurons expressing Pro311Leu HGSNAT-GFP showed a nonsignificant trend for reduction. Together, these results confirm that expression of Pro311Leu HGSNAT aggravates synaptic deficits caused by deficiency of HGSNAT activity and HS storage. Moreover, it expands the locus of the deficit toward the inhibitory GABAergic synapse.

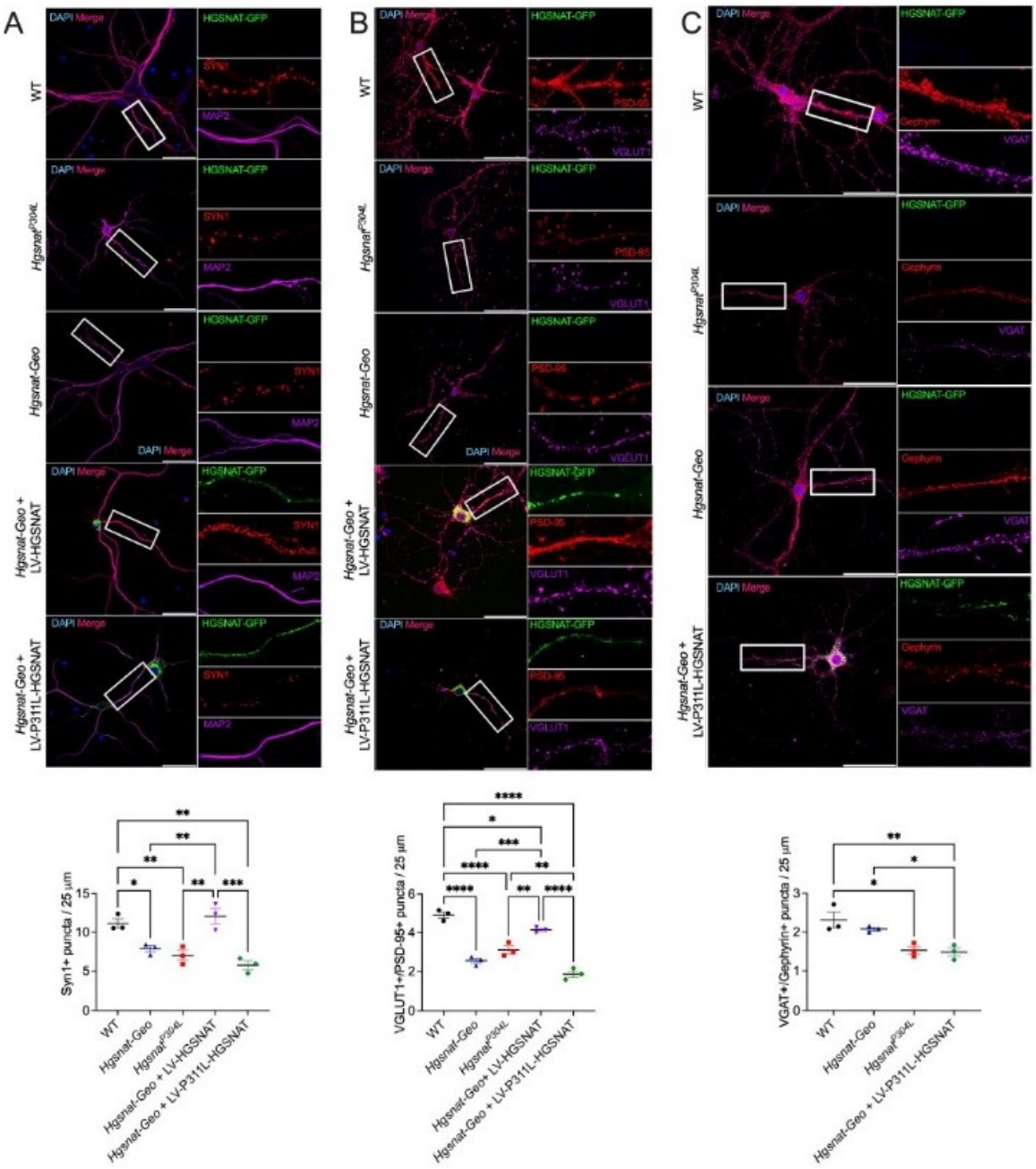

Figure 6. Expression of *Hgsnat*^{P304L} and human P311L mutant HGSNAT variants aggravates GABAergic synaptic defects in cultured primary hippocampal mouse neurons. (A) Hippocampal neurons from *Hgsnat*^{P304L} and *Hgsnat-Geo* mice show reduction in density of Syn1+ puncta in proximity to MAP2+ dendrites compared with WT cells. The levels of Syn1+ puncta are rescued by expression of WT active human HGSNAT but not of the P311L variant. (B) Hippocampal neurons from *Hgsnat*^{P304L} and *Hgsnat-Geo* mice show an equal reduction in density of PSD-95+/VGLUT1+ puncta in juxtaposition. The levels of PSD-95+/VGLUT1+ puncta in juxtaposition are rescued by expression of WT active human

HGSNAT but not of the P311L variant. (C) Densities of Gephyrin+/VGAT+ puncta in juxtaposition are reduced in neurons from *Hgsnat*^{P304L} mice but not from *Hgsnat-Geo* mice compared with WT cells. Primary hippocampal neurons of *Hgsnat-Geo* mice transduced with LV-P311L-HGSNAT show reduction of Gephyrin+/VGAT+ puncta in juxtaposition compared with WT and non transduced *Hgsnat-Geo* cells. The panels show representative confocal images of neurons and enlargements of selected axonal and dendritic fragments. Scale bars equal 40 μm. Graphs show results of puncta quantification with ImageJ software. Puncta were quantified in 20-μm-long segments of dendrite or axon, 30 μm away from the neuronal soma. Individual data, means, and SD from three independent cultures, each involving pooled embryos from at least three mice per genotype, are shown. For each culture, 5–10 neurons were analyzed. P values were calculated using nested one-way ANOVA test with Tukey post hoc test. *, $P < 0.05$; **, $P < 0.01$; ***, $P < 0.001$; ****, $P < 0.0001$.

2.3.7. Treatment of *Hgsnat*^{P304L} mice with a PC, glucosamine, partially restores the activity of the mutant enzyme and ameliorates clinical phenotype

A competitive inhibitor of HGSNAT, glucosamine, rescues folding and activity of the missense HGSNAT variants in cultured skin fibroblasts from MPS IIIC patients (Feldhammer et al., 2009b). Thus, we tested whether, by reducing the load of the misfolded Pro304Leu protein, this drug ameliorates the clinical phenotype in *Hgsnat*^{P304L} mice. Importantly, mice tolerate well chronic oral daily doses of glucosamine ≤2.0 g/kg, and it can penetrate the brain parenchyma (Popov, 1985).

First, we tested if glucosamine increases deficient HGSNAT activity in cultured MEF cells of *Hgsnat*^{P304L} mice. The compound was added daily in a range of concentrations (inhibitory constant [Ki] 3–10) to the cell culture medium, for a total of 5 d. Then, the cells were cultured overnight in the medium without glucosamine, harvested, and lysed to measure HGSNAT activity. Glucosamine in the concentration of 7 mM (Ki 10) had the maximal effect, increasing the residual activity ∼1.5-fold (Fig. 7A). We further tested the drug in a group of 12 male and 12 female homozygous *Hgsnat*^{P304L} mice and 12 male and 12 female WT mice. Starting from the age of 3 wk (after weaning), mice were administered water supplemented with 10 mg/ml glucosamine.

Similar-size control groups of WT and homozygous *Hgsnat*^{P304L} mice received normal drinking water. After 7 d, three mice from each group were sacrificed, and HGSNAT activity was measured in the homogenates of their brain tissues. The remaining animals continued to be treated until the age of 16 wk, when they were studied by the YM and NOR behavior tests and sacrificed at the age of 18 wk to measure HGSNAT activity, HS levels, and pathological changes in the CNS tissues. To test if chronic consumption of glucosamine results in major metabolic changes, mouse BW was measured monthly, and blood glucose levels were analyzed as described previously (Fougerat et al., 2018). No difference between treated and untreated *Hgsnat*^{P304L} mice was detected for both parameters (Fig. S4, A–C), although, for an unknown reason, the blood glucose level in treated *Hgsnat*^{P304L} mice was slightly lower than in untreated WT mice.

Brain residual levels of HGSNAT activity were significantly increased, although by a small margin, already after 7 d of treatment with glucosamine (Fig. 7 B). A similar increase was also observed in the brains of 5-mo-old mice, after 13 wk of treatment (Fig. 7 C). The level of HGSNAT activity measured in the liver of treated *Hgsnat*^{P304L} mice was also increased compared with that of untreated mice (Fig. 7 D). However, no difference in total β-hexosaminidase activity was observed between treated and untreated mice (Fig. 7, E and F).

When mouse memory and learning were tested using YM, we observed a significant increase in the percentage of alternations between the maze arms in treated mice, suggesting a rescue of the memory deficit (Fig. 7 G). In the NOR test, WT mice spent more time exploring a novel than a familiar object, showing a positive discrimination index, whereas untreated *Hgsnat*^{P304L} mice spent equal time exploring both objects or spent more time with a familiar object (negative discrimination index), showing signs of repetitive behavior (Fig. 7 H). For treated mice, we observed a significant increase in the discrimination index and the percentage of time spent

with a novel object (Fig. 7, H and I). Together, these data suggest that deficits in short-term memory in *Hgsnat*^{P304L} mice were delayed by glucosamine treatment. Consistent with memory improvements, we also observed a partial rescue of the deficient protein marker of the excitatory synapse, VGLUT1, and a synaptic protein Syn1 in the hippocampal CA1 neurons of treated *Hgsnat*^{P304L} mice (Fig. 7, J and K). At the same time, the deficient levels of PSD-95 in *Hgsnat*^{P304L} mice were not increased by the treatment (Fig. 7 J).

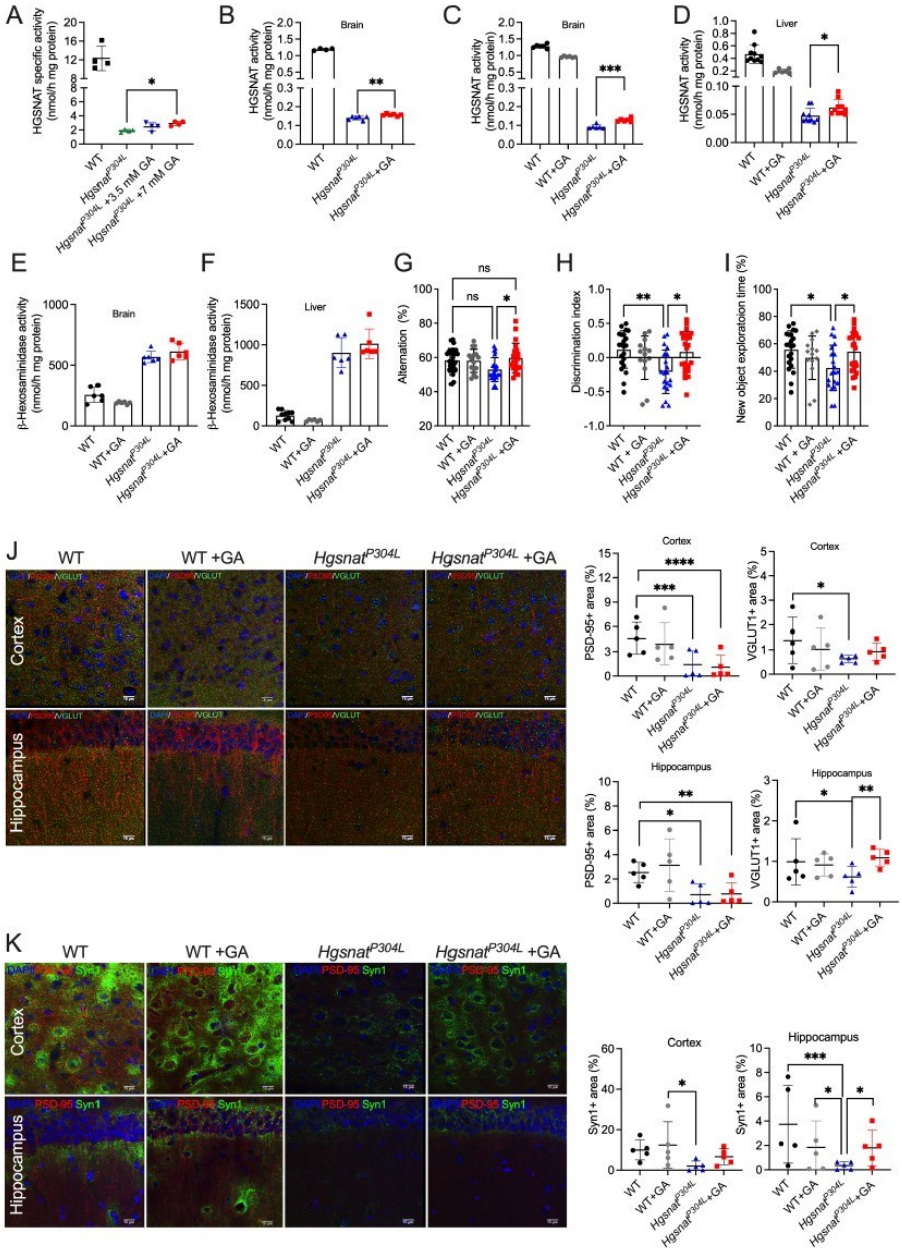

Figure 7. *Hgsnat*^{P304L} mice treated with glucosamine show significant increase of HGSNAT activity in brain and liver tissues, reveal delay in development of deficits in memory and learning, and partial rescue of synaptic protein markers in the CA1 area of the hippocampus. (A) HGSNAT activity, measured using the fluorogenic substrate, muf-β-D-glucosaminide, was increased in cultured MEF cells of homozygous *Hgsnat*^{P304L} mice with glucosamine (+GA) for 5 d compared with untreated cells. Graph shows individual results, means, and SD of experiments conducted with four to six different cell cultures, each established from pooled tissues of three mice. (B–D) HGSNAT activity is also increased in the brain (B and C) and liver (D) tissue homogenates of 4-mo-old *Hgsnat*^{P304L} mice treated with glucosamine (+GA) for 1 wk (B) or 13 wk (C and D) compared with untreated *Hgsnat*^{P304L} mice of the same age. (E and F) No decrease in total β-hexosaminidase activity in both organs was detected for *Hgsnat*^{P304L} mice treated with glucosamine for 13 wk. Individual results, means and SD from experiments performed with 6–10 mice per genotype, per treatment are shown. P values were calculated using an unpaired t test. (G–I) *Hgsnat*^{P304L} mice, treated with glucosamine, show rescue or a trend for improvement of deficits in spatial/short-term memory in the YM test (G) and short-term memory in the NOR test at the age of 4 mo (H and I) compared with untreated *Hgsnat*^{P304L} mice. Individual results, means and SD from experiments performed with 24 mice per genotype, per treatment are shown. P values were calculated using one-way ANOVA with Tukey post hoc test. (J) Deficient levels of protein markers of glutamatergic synaptic neurotransmission, VGUT1 and PSD-95, are rescued in the CA1 hippocampal area of *Hgsnat*^{P304L} mice, treated with glucosamine at the age of 4 mo. Panels show representative images of brain cortex (layers 4–5) and CA1 area of the hippocampus, stained for PSD-95 (red) and VGLUT1 (green), of 4-mo-old WT and *Hgsnat*^{P304L} mice treated or not with glucosamine. Scale bar equals 15 μm. The graph shows quantification of fluorescence with ImageJ software. Individual results, means, and SD from experiments performed with five mice per genotype (three areas/mouse), per treatment are shown. P values were calculated using nested one-way ANOVA test with Tukey post hoc test. (K) Deficient level of synaptic vesicular protein Syn-1 is rescued in the somatosensory cortex area of *Hgsnat*^{P304L} mice, treated with glucosamine at the age of 4 mo. Panels show representative images of brain cortex (layers 4–5) and CA1 area of the hippocampus, stained for PSD-95 (red) and Syn1 (green), of 4-mo-oldWT, and *Hgsnat*^{P304L} mice treated or not with glucosamine. Scale bar equals 15 μm. The graph shows quantification of fluorescence with ImageJ software. Individual results, means, and SD from experiments performed with five mice per genotype (three areas/mouse), per treatment are shown. P values were calculated using nested one-way ANOVA test with Tukey post hoc test. *, $P < 0.05$; **, $P < 0.01$; ***, $P < 0.001$; ****, $P < 0.0001$.

To test if delayed memory impairment in treated *Hgsnat*^{P304L} mice coincided with a reduction in the development of brain pathology, we analyzed fixed brain slices of treated and

untreated *Hgsnat*^{P304L} mice, as well as their WT counterparts, for markers of primary and secondary storage (HS/LAMP2 and GM2 ganglioside, respectively), micro- and astrogliosis (CD68 and GFAP, respectively), and misfolded protein accumulation (SCMAS, autofluorescent ceroid materials, and O-GlcNAc–modified proteins). These biomarkers were prioritized because, as described above, they were a key for discriminating between the aggravated phenotype of *Hgsnat*^{P304L} and a milder phenotype of *Hgsnat-Geo* mice. In addition, we studied GAG levels and the levels of ubiquitinated protein aggregates.

The pathological features showing the best response to glucosamine treatment were an accumulation of autofluorescent ceroid materials (Fig. 8 A) and misfolded SCMAS (Fig. 8 B) in the deep cortical pyramidal neurons, as well as accumulation of GM2 ganglioside in pyramidal neurons of somatosensory cortex and CA1 area of the hippocampus (Fig. 8 C). All three biomarkers were reduced in treated mice almost to the levels observed in the WT mice of similar age. The level of total brain HS measured by LC-MS/MS analysis showed modest but significant reduction in mouse brain homogenates; however, it still remained at a significantly higher level than in WT mice (Fig. 8 D). The LC-MS/ MS data were supported by the results of immunohistochemistry that has revealed a significant reduction of HS+ areas in the pyramidal neurons of both cortex and hippocampus (Fig. 8 E). The size and abundance of lysosomes (LAMP2+ area) showed significant reduction only in the cortex and just a trend for reduction in the hippocampus (Fig. 8 E). At the same time, glucosamine treatment did not change the severity of astromicrogliosis, one of the hallmarks of CNS pathology in MPS IIIC and other neurological MPS diseases. The levels of CD68+ cells were similar for untreated and treated mice in the cortex and hippocampus, whereas GFAP+ cells were unchanged in the cortex, but, for an unknown reason, increased in the hippocampus of treated mice (Fig. S4 D). The levels of ubiquitinated

protein aggregates and O-GlcNAc–modified proteins were still undetectable at 4 mo of age in the brains of both treated and untreated *Hgsnat*^{P304L} mice as well as WT mice (data not shown).

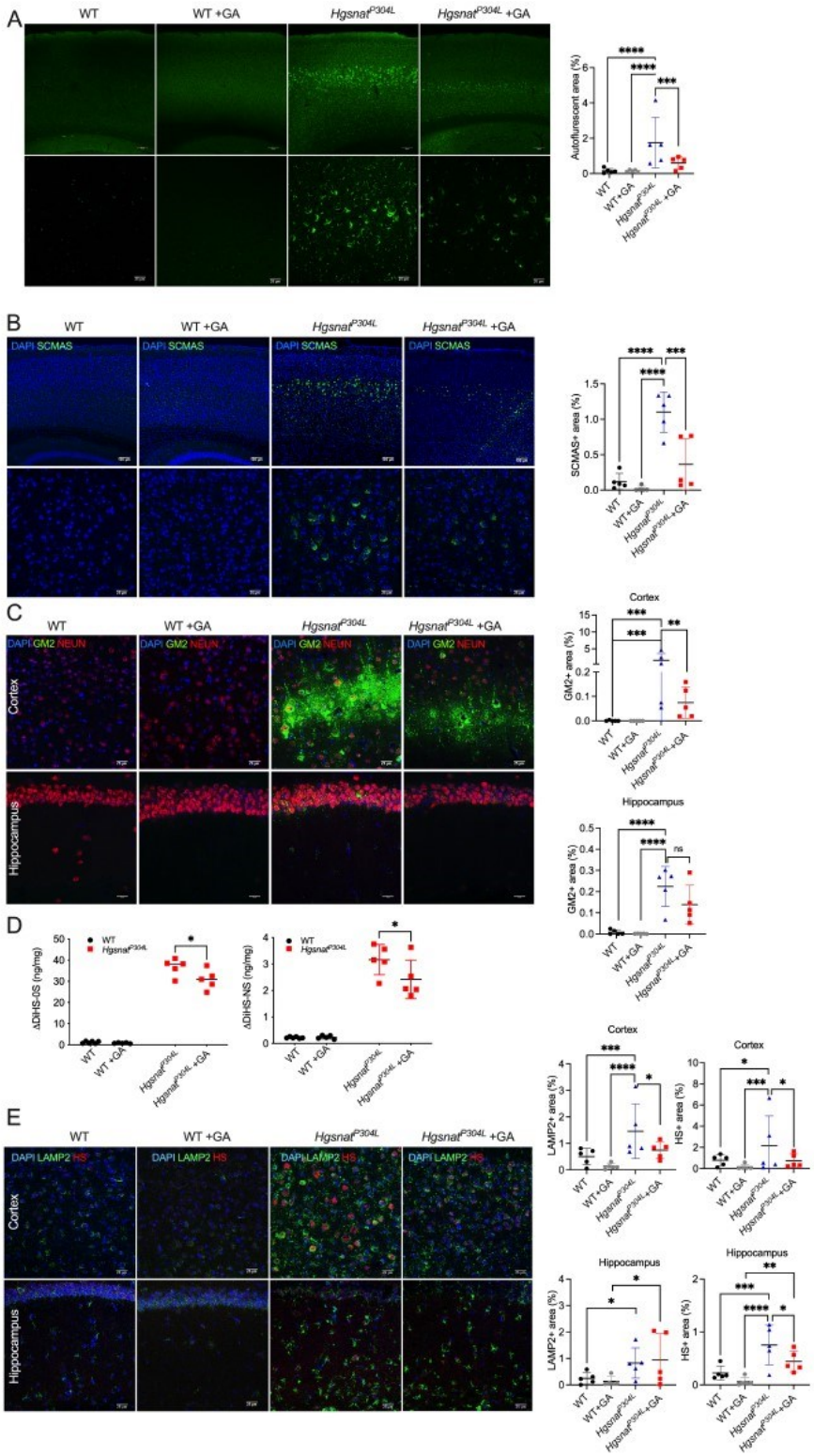

Figure 8. The levels of biomarkers of CNS pathology in the somatosensory cortex are normalized and brain storage of HS is reduced in *Hgsnat*^{P304L} mice treated with glucosamine. (A) Reduction of granular autofluorescent ceroid material in cortical neurons. Panels show representative images of brain cortex (layers 4–5) of 4-mo-old WT and *Hgsnat*^{P304L} mice treated or not with glucosamine (GA) showing autofluorescent ceroid inclusions in the neurons (green). Scale bar equals 100 μm (upper panels) and 25 μm (lower panel). The graph shows quantification of autofluorescence with ImageJ software. (B) Reduction of GM2 ganglioside in cortical neurons. Panels show representative images of somatosensory cortex (layers 4–5) of 4-mo-old WT, and *Hgsnat*^{P304L} mice treated or not with glucosamine showing immunostaining for GM2 ganglioside and NeuN. DAPI was used as a nuclear counterstain. Scale bar equals 100 μm (upper panels) and 25 μm (lower panel). The bar graph shows quantification of GM2 staining with ImageJ software. (C) Reduction of misfolded SCMAS aggregates in cortical neurons. Panels show representative images of somatosensory cortex (layers 4–5), stained for SCMAS, of 4-mo-old WT and *Hgsnat*^{P304L} mice treated or not with glucosamine. DAPI (blue) was used as a nuclear counterstain. Scale bar equals 100 μm (upper panels) and 25 μm (lower panel). The bar graph shows quantification of SCMAS staining with ImageJ software. All graphs show individual data, means, and SD obtained for five mice per genotype per treatment (three areas/mouse). P values were calculated using nested one-way ANOVA test with Tukey post hoc test. (D) Levels of disaccharides produced by enzymatic digestion of HS (ΔDiHS-0S and ΔDiHS-NS), measured by MS/MS, are reduced in brain tissues of 4-mo-old *Hgsnat*^{P304L} mice treated with glucosamine. All graphs show individual data, means, and SD obtained for five to six mice per genotype per treatment. P values were calculated using two-way ANOVA test with Tukey post hoc test. (E) Reduction of HS+ and LAMP2+ puncta in cortical neurons. Panels show representative images of brain cortex (layers 4–5) and CA1 region of hippocampus, stained for LAMP2 (green) and HS (red), of 4-mo-oldWT and *Hgsnat*^{P304L} mice, treated or not with glucosamine. Scale bar equals 25 μm. Graphs show quantification of HS and LAMP2 staining with ImageJ software. All graphs show individual results, means, and SD from experiments conducted with five mice (three panels per mouse) per genotype per treatment. P values were calculated using nested one-way ANOVA test with Tukey post hoc test. *, $P < 0.05$; **, $P < 0.01$; ***, $P < 0.001$; ****, $P < 0.0001$.

2.4. Discussion

Correction of a primary genetic defect by either enzyme replacement or gene therapy/hematopoietic stem cell gene therapy remains the major approach for developing novel treatments for neurological MPS, including Sanfilippo disease. However, outcomes of all recent

clinical trials involving MPS III patients are either still unknown or failed to produce desired effects, prompting researchers to explore novel alternative treatments. In particular, approaches based on the use of small molecule drugs to reduce neuroinflammation (Parker et al., 2020; NCT04018755 clinical trial), activate autophagy (Lotfi et al., 2018; Monaco et al., 2020), reduce or block stored HS (De Pasquale et al., 2021), rescue activity/expression of the mutant enzymes (Feldhammer et al., 2009b; Matos et al., 2014), and stimulate translational readthrough of premature termination codons (Gomez-Grau et al., 2015) have been described.

Development of a chaperone therapy for MPS IIIC requires a generation of a novel murine model expressing misfolded HGSNAT protein. For this purpose, we selected a Pro304Leu mutation, an analog of a pathological human variant Pro311Leu, which we previously identified in severely affected MPS IIIC patients (Feldhammer et al., 2009a; Feldhammer et al., 2009b; Martins et al., 2019). Now, we show that the knock-in *Hgsnat*^{P304L} mouse has a drastically aggravated clinical phenotype compared with our previously developed gene-targeted *Hgsnat-Geo* mouse model, with a constitutive disruption of gene expression (Martins et al., 2015). In particular, the onset of behavioral abnormalities for the knock-in *Hgsnat*^{P304L} mouse was observed at 4 mo, at least 2–3 mo before that in the *Hgsnat-Geo* mouse. In addition, the lifespan was reduced by ∼20 wk compared with the *Hgsnat-Geo* mouse, and, at sacrifice, *Hgsnat*^{P304L} mice showed a pronounced enlargement of kidney, liver, and spleen, unlike *Hgsnat-Geo* mice, which had only mild hepatomegaly. Most of the CNS disease progression biomarkers, including neuroimmune response, astromicrogliosis, and accumulation of primary and secondary storage materials, were aggravated in *Hgsnat*^{P304L} mice compared with *Hgsnat-Geo* mice of the same age. Moreover, the severity of synaptic deficits in CA1 and cultured *Hgsnat*^{P304L} hippocampal neurons was increased and expanded to the GABAergic synapse. Because the residual brain level of HGSNAT

acetyltransferase activity, measured with the specific BODIPY-glucosamine substrate, was reduced to below detection levels in both strains, we speculate that the difference in the clinical severity is most likely related to a toxicity of the mutant misfolded HGSNAT P304L variant expressed in the cells of the *Hgsnat*^{P304L} mouse.

RNA sequencing analysis of mouse hippocampi demonstrated that the same types of pathways were altered in both knockout and knock-in compared with WT mice. In particular, lysosomal biogenesis was increased, as well as the pathways related to inflammatory and immune response. On the other hand, the expression of genes involved in neurogenesis and synaptic transmission was decreased. However, the number of significantly changed pathways (especially of those related to GABAergic synapse) and the degree of gene alterations were higher in the *Hgsnat*^{P304L} mouse, reflecting an increased severity of CNS pathology. Several pathways induced in the *Hgsnat*^{P304L} mouse were related to ER stress/UPR. This, together with the increased levels of ER stress biomarkers (O-GlcNAc–modified proteins, ubiquitinated protein aggregates) detected in the hippocampal and cortical pyramidal neurons in the knock-in mouse, prompted us to hypothesize that expression of the HGSNAT mutant misfolded variant puts an additional constraint on the ER in these cells. This can further impair proteasomal protein degradation (Bifsha et al., 2007) and, together with autophagy block, can result in aggravated neuronal dysfunction, accumulation of toxic misfolded protein aggregates, neuroimmune response, and eventually neurodegeneration. In accordance with this hypothesis, we observed a similar level of a primary substrate, HS, in the brains, plasma, and urine of *Hgsnat-Geo* and *Hgsnat*^{P304L} mice. However, the levels of LAMP2+ neuronal puncta and β-hexosaminidase activity in the brains of *Hgsnat*^{P304L} mice were significantly higher. Because both markers reflect increased lysosomal biogenesis, we speculate that misfolded protein response poses an additional stress on the lysosomal system and

causes increased storage of the secondary metabolites: gangliosides, ceroid materials, and misfolded proteins. Because the presence of storage bodies in axonal spheroids disrupts axonal transport and causes deficiency of synaptic vesicles (Par´a et al., 2021), this could also translate to further aggravation of synaptic phenotypes.

To test this hypothesis, we transduced cultured hippocampal neurons established from embryos of *Hgsnat-Geo* mice with LVs expressing either human WT HGSNAT or the P311L HGSNAT variant. In preliminary experiments, we demonstrated that the mutant HGSNAT protein was misfolded, did not have any enzymatic activity, was not proteolytically processed, did not undergo targeting to Golgi or lysosomes, and was retained in the ER. Moreover, when overexpressed, it formed cytoplasmic inclusions. When levels of synaptic proteins in cultured hippocampal *Hgsnat-Geo* neurons overexpressing WT human HGSNAT enzyme were compared to those in non transduced cells from WT, *Hgsnat-Geo*, and $Hgsnat^{P304L}$ mice, we observed a complete rescue of the markers of inhibitory and excitatory synapses. In contrast, neurons overexpressing the mutant P311L enzyme showed a reduction in the density of inhibitory synapses and further reduction in the density of excitatory synapses to the levels detected in the $Hgsnat^{P304L}$ neurons. These results directly confirm that the mutant P311L HGSNAT protein is responsible for the aggravation of synaptic deficits, especially those affecting the GABAergic synapse that are known to lead to seizures and autistic behavioral features (Chao et al., 2010). Further natural history study is required to establish whether human MPS IIIC patients with missense mutations resulting in protein misfolding also present an aggravated phenotype; however, our recent analysis of a large group of novel Brazilian patients suggests that they are at least as severely affected as those having nonsense mutations or indels (Martins et al., 2019).

We attempted to reduce the burden caused by the misfolded mutant enzyme in the *Hgsnat*^{P304L} mice by treating them with glucosamine, a known HGSNAT chaperone. This compound increases the levels of residual HGSNAT activity in cultured fibroblasts of human MPS IIIC patients with several missense mutations, including P311L (Feldhammer et al., 2009b). A similar effect was observed in the current study in MEF cells of *Hgsnat*^{P304L} mice, confirming that the drug also has a beneficial effect on the mouse P304L HGSNAT mutant. Thus, glucosamine was provided to the mutant mice in drinking water and was well tolerated. The treatment was started in asymptomatic mice at weaning and conducted for 13 wk until the mice were 4 mo old. At this time point, behavioral testing revealed a rescue or partial rescue of defects in short-term, working, and spatial memory. Analysis of CNS pathology showed significantly reduced defects in cortical pyramidal and hippocampal CA1 neurons associated with the disease phenotype, including accumulation of autofluorescent ceroid material, primary (HS) and secondary (GM2 ganglioside, unfolded SCMAS) storage materials, and induced lysosomal biogenesis. However, the treatment failed to reduce the number of astrocytes and microglia, which stayed drastically elevated in both cortex and hippocampus. As we reported previously (Martins et al., 2015), activation of microglial cells is caused by secreted oligomers of HS that act directly on TLR-4 receptors (Ausseil et al., 2008). A similar mechanism could also underlie activation of astrocytes, although we could not detect lysosomal storage in this type of cells (Martins et al., 2015). Because the HS storage is reduced only partially, neuroinflammation remains unaffected in treated mice. It is tempting to speculate that these biomarkers, although important for assessment of overall CNS pathology progression, do not directly correlate with behavioral deficits. In contrast, the reduced levels of synaptic proteins VGLUT1 and Syn1 in the hippocampus were rescued by glucosamine therapy, once again reinforcing our previous conclusion that synaptic defects underlie the behavioral

changes in MPS IIIC mice (Par´a et al., 2021). Future studies, however, are required to confirm whether glucosamine also improves electrophysiological phenotypes in treated mice or increases their longevity.

The residual HGSNAT activity in the brain and liver of treated mice showed a moderate (∼1.5-fold) but statistically significant increase, suggesting a partial rescue of the mutant enzyme. Nevertheless, we cannot exclude the possibility that glucosamine induced the expression of an unknown acetyltransferase or hydrolase active against unacetylated muf- β-glucosaminide substrate. Although we have observed promising behavioral improvement, it remains to be determined whether such a small increase in the residual HGSNAT activity and HS catabolism is sufficient to produce a long-term correction of the clinical phenotype in *Hgsnat*^{P304L} mice. It also remains to be determined whether glucosamine treatment would lead to any improvements in the knockout *Hgsnat-Geo* mice. Alternatively, glucosamine can reduce the pool of the misfolded HGSNAT variant accumulating in the ER, thus decreasing the load on ubiquitin-mediated protein degradation pathway and ER stress. Paradoxically, glucosamine, which is known to induce the ER stress and UPR in multiple types of cells (reviewed in Beriault and Werstuck [2012]), did not induce ER stress markers in the brain of treated mice, including accumulation of ubiquitinated aggregates, or levels of O-GlcNAc–modified proteins, which at 4 mo remained at the normal level in both treated and untreated groups.

Administration of glucosamine in concentrations of 1–2 g/kg/d, similar to those we used in this study, is safe in mice, but in humans it is hardly achievable (Miller and Clegg, 2011). Thus, identifying HGSNAT chaperones with higher potency and bioavailability either by library screening or by a rational design is required before such an approach can be tested in human patients. Besides, since glucosamine does not increase residual activity of the deficient N-

sulfoglucosamine sulfohydrolase enzyme in the cultured fibroblasts of MPS IIIA patients affected with missense mutations (unpublished data), specific chaperones must be identified for other subtypes of MPS III. Importantly, our current study establishes that, while secondary accumulation of misfolded proteins and gangliosides shows a drastic response to chaperone treatment, neuroimmune response is not reduced. This suggests that the efficacy of chaperone therapy can be further improved when combined with drugs that primarily address neuroimmune response, such as recently described blockers of the IL-1β pathways (Parker et al., 2020).

In conclusion, the results of this study validate the novel *Hgsnat*^{P304L} mouse strain as a model closely mimicking the phenotype of the early-onset, fast-progressing MPS IIIC patients, useful for testing prognostic biomarkers of the disease and novel therapies. It also suggests that introducing mutations with CRISPR/Cas9 may be a better approach for generation of animal models of lysosomal storage disorders than producing constitutive knockouts. Importantly, our work establishes that misfolded mutant HGSNAT protein expression is a key contributing factor for the pathophysiology of MPS IIIC and suggests that treatment with chaperones capable of rescuing the folding process of such mutants should be considered as a possible therapy for this disease.

2.5. Materials and methods

2.5.1. Murine models

Approval for animal experimentation was granted by the Animal Care and Use Committee of the Sainte-Justine Hospital Research Center. Mice were housed in an enriched environment with continuous access to food and water, under constant temperature and humidity, on a 12-h light/dark cycle. Mice were kept on a normal chow diet (5% fat, 57% carbohydrate). *Hgsnat-Geo* mice have been previously described (Martins et al., 2015). *Hgsnat*^{P304L} knock-in C57Bl/6J mouse strain was

generated at McGill Integrated Core for Animal Modeling using CRISPR/Cas9 technology, targeting exon 9 of the Mus musculus gene Hgsnat. To generate knock-in founders, a single guide nucleotide RNA (sgRNA) was designed using the CRISPR online tool (http://crispr.mit.edu) to target a genomic site on the murine Hgsnat locus with minimal potential off-target effects. sgRNA and Cas9 mRNA were microinjected into zygotes with single-stranded oligodeoxynucleotide, barring a c.911C>T mutation encoding for the P304L change (Fig. S1 A; 100 ng/µl single-stranded oligodeoxynucleotide, 20 ng/µl sgRNA, and 20 ng/µl Cas9).

The zygotes were further cultured overnight in EmbryoMax KSOM drops (Millipore) covered with mineral oil (Irvine Scientific) in a 35-mm dish at 37°C in a 5% CO2 incubator. The embryos, which developed up to the 2-cell stage, were transferred to oviducts of pseudo-pregnant females to generate chimeric mouse litters. Pups were delivered at full term and, at weaning, were genotyped by Sanger sequencing of single allele fragments, obtained by PCR amplification of genomic DNA from tail clips. The adult founder mice containing the allele with the desired mutation were mated with C57Bl/6N mice (Envigo). Genotypes of the offspring were determined by amplifying a 988-bp product from purified mouse tail DNA (forward primer: 59-ATGGAGTGCCTGATGGGAGG-39; reverse primer: 59-GATCTA GAAACGGCCCGAAGA-39). Because the c.911C >T mutation eliminated the NcoI restriction site, to distinguish between mutant and WT amplicons, the PCR products were further digested with NcoI (Cat# R3193S; New England Biolabs) at 37°C for 1 h and then run on a 2% agarose gel. Fragments of 688 and 300 bp were detected for the WT allele and an undigested 988-bp fragment for the targeted *Hgsnat*^{P304L} allele (Fig. S1, B and C). To test for the presence of potential off-target effects, the sgRNA sequence (59-TGAACGTCGCCAGGTCGCGG-39) was blasted against the Mus musculus genome. Fragments of 763 bp of the Spg7 gene exon 7, presenting the highest identity score, were

amplified by PCR from genomic DNA of F1 and WT mice (forward primer: 59-CTTTTGGAGCTGTGGCCCTA-39; reverse primer: 59-AGTGGAAGATTTTGCCAGGC-39) and analyzed by Sanger sequencing for the presence of deleterious variants. This analysis did not reveal mutations in the Spg7 gene in the F1 generation (Fig. S1, D and E). The F1 mice were bred to C57Bl/6J mice to generate heterozygous mice that were further backcrossed to C57Bl/6J for four generations to eliminate mutations resulting from potential off-target effects, not predicted by BLAST (Basic Local Alignment Search Tool) analysis. Finally, the heterozygous pairs were bred to generate WT, heterozygote, and homozygous mutants. In all experiments WT littermates were used as a control.

2.5.2. Sex consideration

Equal cohorts of male and female mice were studied separately for each experiment, and statistical methods were used to test whether the progression of the disease, levels of biomarkers, or response to therapy were different between male and female animals. Because differences between sexes were not detected, the data for male and female mice and cells were pooled together.

2.5.3. Enzyme activity assays

The specific enzymatic activities of HGSNAT, β-hexosaminidase, and β-galactosidase were assayed essentially as previously described (Martins et al., 2015). Tissues extracted from mice or pellets of cultured cells were snap-frozen in liquid nitrogen before storage at −80°C. 50-mg samples were homogenized in 250 µl of H2O using a sonic homogenizer (Artek Systems Corp.). Cultured MEF cells were harvested by scraping and lysed in H2O by 10-s sonication on ice (60 W). For HGSNAT assays, 5-µl aliquots of the homogenates were combined with 5 µl of McIlvain buffer (pH 5.5), 5 µl of 3 mM 4-methylumbelliferyl-β-D-glucosaminide (Moscerdam), 5 µl of 5 mM acetyl-coenzyme A, and 5 µl H2O. The reaction was incubated for 3 h at 37°C and

stopped with 975 µl of 0.4 M glycine buffer (pH 10.4), and fluorescence was measured using a ClarioStar plate reader (BMG Labtech). Blank samples were incubated without the homogenates, which were added after the glycine buffer.

The activity of β-hexosaminidase was measured by combining 2.5 µl of 10× diluted homogenate (~2.5 ng of protein) with 15 µl of 0.1Msodiumacetate buffer (pH 4.2), and 12.5 µl of 3Mm 4-methylumbelliferyl N-acetyl-β-D-glucosaminide (Sigma-Aldrich) followed by incubation for 30 min at 37°C. The reaction was stopped with 0.4 M glycine buffer (pH 10.4), and fluorescence was measured as above.

The activity of acidic β-galactosidase was measured by adding 12.5 µl of 0.4 M sodium acetate, 0.2 M NaCl (pH 4.2), and 12.5 µl of 1.5 mM 4-methylumbelliferyl β-D-galactoside (Sigma-Aldrich) to 10 µl of 10× diluted homogenate (~1 ng protein). After 15-min incubation at 37°C, the reaction was stopped with 0.4 M glycine buffer (pH 10.4), and fluorescence was measured as above.

HGSNAT N-acetyltransferase activity assay with BODIPY glucosamine substrate in brain homogenates was performed by combining 6 µl of homogenate (~6 µg protein), 6 µl McIlvain's phosphate/citrate buffer (pH 6.5), 4 µl of 10 mM acetyl CoA in H2O, and 4 µl of 40mMBODIPY-glucosamine (Choi et al., 2015). After incubation for 3 h at 37°C in a 96-well PCR plate (BioScience), the reaction was terminated by the addition of 180 µl of 100 mM HCl. 20-µl aliquots of the final reaction mixture were transferred to a 96-well filter plate (Millipore; 40-mm nylon mesh) pre-embedded with 100 µl Toyopearl cation exchange media SP 650M (Tosoh) for each well. Before the assay, the resin was washed twice with 250 µl H2O per well, and the plates were centrifuged at 50 g for 30 s to remove any excess water. The fluorescent neutral reaction product was eluted with four 90-µl aliquots of 1 M HCl by centrifugation of the plates at 50 g for 30 s.

Combined eluent (360 µl) was transferred to 96-well Reader Black polystyrene plates (Life Science), and the amount of fluorescent product was measured.

2.5.4. Behavioral analysis

The spontaneous alternation behavior, spatial working memory, and exploratory activity of mice were evaluated using a white YM as previously described (Pan et al., 2017). The maze consisted of three identical white Plexiglas arms (40 × 10 × 20 cm, 120° apart) under dim lighting conditions. Each mouse was placed at the end of one arm, facing the center, and allowed to explore the maze for 8 min. All experiments were performed at the same time of day and by the same investigator to avoid circadian and handling bias. Sessions were video-recorded, and arm entries were scored by a trained observer unaware of the mouse genotype or treatment. Successful alternation was defined as consecutive entries into a new arm before returning to the two previously visited arms. Alternation was calculated as (number of alternations/total number of arm entries − 2) × 100.

NOR test was used for assessing short-term recognition memory (Akkerman et al., 2012; Antunes and Biala, 2012). Mice were placed individually in a 44 × 33 × 20-cm (length × width × height) testing chamber with white Plexiglas walls for a 10-min habituation period and returned to their home cage. The next day, mice were placed in the testing chamber for 10 min with two identical objects (red plastic towers, 3 × 1.5 × 4.5 cm) and returned to the home cages, and 1 h later, were placed back into the testing chamber in the presence of one of the original objects and one novel object (a blue plastic base, 4.5 × 4.5 × 2 cm) for 10 min. After each mouse, the test arena as well as the plastic objects were cleaned with 70% ethanol to avoid olfactory cue bias. The discrimination index (DI) was calculated as the difference in the exploration time between the novel and old object divided by total exploration time. A preference for the novel object was

defined as DI significantly >0 (Ennaceur and Delacour, 1988). Mice who showed a side preference, noted as DI ± 0.20 during the familiarization period, and those who had a total exploration time <3 s were excluded from analysis.

The OF test was performed as previously described (Amegandjin et al., 2021). Briefly, mice were habituated in the experimental room for 45 min before commencement of the test. Each mouse was then gently placed in the center of the OF arena and allowed to explore for 20 min. The mouse was removed and transferred to its home cage after the test, and the arena was cleaned with 70% ethanol before commencement of the next test. Analysis of behavioral activity was done using Smart video tracking software (v3.0; Panlab Harvard Apparatus); the total distance traveled and percentage of time spent in the center zone were measured for hyperactivity and anxiety assessment, respectively.

The elevated plus maze test was performed as described by Amegandjin et al. (2021). Eachmouse was placed in the center of the elevated plus maze and allowed to freely explore undisturbed for 10 min. After each testing, the mouse was returned to the home cage and the arena was cleaned with 70% ethanol before commencement of the next test. Analysis of behavioral activity (percentage of time spent in the center zone, closed arms, and open arms and the number of open arm entries) was done in Smart v3.0 software.

2.5.5. TEM

At 3 and 6 mo, three mice from each group were anesthetized with sodium pentobarbital (50 mg/kg) and perfused with PBS, followed by 2.5% glutaraldehyde in 0.2 M phosphate buffer (pH 7.2). The brains were extracted and postfixed in the same fixative for 24 h at 4°C. The hippocampi were dissected, mounted on glass slides, stained with toluidine blue, and examined on a Leica DMS light microscope to select the CA1 region of the hippocampus for EM. The blocks

were further embedded in Epon, and 100-nm ultrathin sections were cut with an Ultracut E ultramicrotome, mounted on 200-mesh copper grids, stained with uranyl acetate (Electron Microscopy Sciences) and lead citrate, and examined on a FEI Tecnai 12 TEM. For quantification, the micrographs were taken with 13,000 and 30,000× magnification.

2.5.6. Neuronal cultures

Primary hippocampal neurons were cultured from the brains of embryos at gestational day 16 (E16). The hippocampi were isolated and treated with 2.5% trypsin solution (T4674; Sigma - Aldrich) for 15 min at 37°C. The cells were washed three times with HBSS (14025-092; Gibco) and mechanically dissociated by pipetting, using glass Pasteur pipettes with three different opening sizes (3, 2, and 1 mm). The cells were counted with the viability dye trypan blue (15250061; Thermo Fisher Scientific) using a hemocytometer and resuspended in Neurobasal media (21103-049; Gibco) containing L-glutamine, B27, N2, penicillin, and streptomycin. The cells were plated at a density of 60,000 cells per well, respectively, in a 12-well plate on coverslips previously coated with poly-L-lysine (P9155; Sigma-Aldrich). Cells were cultured for 21 d, and 50% of medium was changed every 3 d.

2.5.7. Whole-cell recordings in acute hippocampal slices

Acute hippocampal slices were prepared as described (Croce et al., 2010). Briefly, animals were anaesthetized deeply with isoflurane and decapitated. The brain was dissected carefully and transferred rapidly into an ice-cold (0–4°C) solution containing 250 mM sucrose, 2 mM KCl, 1.25 mM NaH2PO4, 26 mM NaHCO3, 7 mM MgSO4, 0.5 mM CaCl2, and 10 mM glucose (pH 7.4). The solution was oxygenated continuously with 95% O2 and 5% CO2, 330–340 mOsm/liter. Transverse hippocampal slices (thickness, 300 μm) were cut using a vibratome (VT1000S; Leica Microsystems), transferred to a bath at room temperature (23°C) with standard artificial cerebral

spinal fluid (ACSF) at pH 7.4 containing 126 mM NaCl, 3 mM KCl, 1 mM NaH2PO4, 25 mM NaHCO3, 2 mM MgSO4, 2 mM CaCl2, and 10 mM glucose, continuously saturated with 95% O2 and 5% CO2, and allowed to recover for 1 h. During the experiments, slices were transferred to the recording chamber at physiological temperature (30–33 °C) continuously perfused with standard ACSF, as described above, at 2 ml/min. Pyramidal CA1 neurons from the hippocampus were identified visually using a 40× water immersion objective. Whole-cell patch-clamp recordings were obtained from single cells in voltage- or current-clamp mode, and only one cell per slice was recorded to enable post hoc identification and immunohistochemical processing. Recording pipettes (4–6 MΩ) were filled with a K-gluconate–based solution for voltage-clamp recordings (130mMK-gluconate, 10mM KCl, 5 mMdiNa-phosphocreatine, 10 mMHepes, pH 7.4, 2.5mM MgCl2, 0.5mMCaCl2, 1mMEGTA, 3mMATP-Tris, 0.4mMGTPLi, and 0.3% biocytin, 280–290 mOsm/liter).

After obtaining whole-cell configuration, passive membrane properties were monitored for 5 min, and current clamp recordings were done to measure action potential characteristics. Slices were then perfused with 0.5 μM tetrodotoxin (TTX; to isolate miniature events) for 3 min before commencing voltage clamp recordings. Cells were voltage clamped at −70 mV for mEPSCs recording and then held at 0 mV (calculated from the reversal potential of Cl) for mIPSCs recording. Data acquisition (filtered at 2–3 kHz and digitized at 15 kHz; Digidata 1440A; Molecular Devices) was performed using the Axopatch 200B amplifier and the Clampex 10.6 software (Molecular Devices). Both mEPSCs and mIPSCs were recorded for 7 min and a running template on a stable baseline (minimum of 30 events) was used for the analysis of miniature events on MiniAnalysis. Clampfit 10.2 software was used for analysis of action potential characteristics and other passive membrane properties.

For some experiments, to verify that all mEPSCs are blocked,slices were perfused with 5 μM6,7--2,3-dione and 50 μM AP5 in addition to the TTX while recording mEPSCs at −70 mV after addition of α-amino-3-hydroxy-5-methyl-4- isoxazolepropionic acid and N-methyl-D-aspartate receptor blockers. Similarly, for some experiments, slices were perfused with 100 μMbicuculline methiodide and 50 μMAP5 in addition to the TTX in the ACSF to verify that all mIPSCs were blocked at 0 mV.

2.5.8. Real-time qPCR

RNA was isolated from snap-frozen brain, kidney, and liver tissues using TRIzol reagent (Invitrogen) and reverse transcribed using iScript Reverse Transcription Supermix (#1708840; Bio-Rad) according to the manufacturer's protocol. qPCR was performed using a LightCycler 96 Instrument (Roche) and SsoFast EvaGreen Supermix with Low ROX (#1725211; Bio-Rad) according to the manufacturer's protocol. RLP32mRNAwas used as a reference control. The primers used are listed in Table 1.

Table 1. **Primers**

Gene	Sequence
Hgsnat forward	5′-TAGGGGGTTAGCTCTCGTCC-3′
Hgsnat reverse	5′-CCTCGTTGCAGGATAGAAGTCA-3′
MIPα forward	5′-GCCCTTGCTGTTCTTCTCTG-3′
MIPα reverse	5′-CAGATCTGCCGGTTTCTCTT-3′
TNFα forward	5′-TCTTCTCATTCCTGCTTGTGG-3′
TNFα reverse	5′-CACTTGGTGGTTTGCTACGA-3′
TGF1β forward	5′-GTCAGACATTCGGGAAGCAG-3′
TGF1β reverse	5′-CTGCCGTACAACTCCAGTGA-3′
RPL32 forward	5′-TTCTTCCTCGGCGCTGCCTACGA-3′
RPL32 reverse	5′-AACCTTCTCCGCACCCTGTTGTCA-3′

2.5.9. RNA extraction and transcriptome sequencing

Total RNA was extracted from ~30 mg of hippocampal tissue using the RNeasy Mini Kit (Qiagen), according to the manufacturer's instructions. RNA was quantified using the NanoDrop 8000. Samples with a 28S/18S ratio >1.8, an OD 260/280 ratio >1.9 and an RNA integrity number >9 (Agilent Bioanalyzer 2100) were chosen for cDNA library construction. Library preparation and sequencing were performed at the Genomics Platform of the Institute for Research in Immunology and Cancer, Montreal. All cDNA libraries were sequenced using single-end strategy (40 M reads per sample) on an Illumina NextSeq500 platform with a read length of 75 bp (single-end mode). Raw data were converted to FASTQ files using bcl2fastq (v2.20) and allowed 0 mismatches in the multiplexing barcode. Data were analyzed by BioJupies using default parameters. Gene expression–level differences were accepted as statistically significant if they had a P value <0.05, and the result was visualized by an in-house Matlab code. The data are available at Sequence Read Archive website, accession number PRJNA832487 (https://www.ncbi.nlm.nih.gov/sra/PRJNA832487).

2.5.10. Normal-phase HPLC (NP-HPLC) for glycosphingolipids (GSLs) in mouse brain extracts

GSLs were analyzed essentially as described previously (Neville et al., 2004). Lipids from aqueous mouse brain homogenates (~2.5 mg wet weight in 0.5 ml) were extracted with chloroform and methanol overnight at 4°C. The GSLs were then further purified using solid-phase C18 columns (Telos; Kinesis). After elution, the GSL fractions were dried down under a stream of nitrogen at 42°C and digested with recombinant endoglycoceramidase (rEGCase I, prepared by Genscript) to release the oligosaccharide headgroups. The liberated free glycans were then fluorescently labeled with anthranilic acid (2AA). To remove excess 2AA label, labeled glycans were purified using DPA-6S SPE columns (Supelco). Purified 2AA-labeled oligosaccharides were

separated and quantified by NP-HPLC as previously described (Neville et al., 2004). The NP-HPLC system consisted of a Waters Alliance 2695 separations module and an in-line Waters 2475 multi λ-fluorescence detector set at excitation λ 360 nm and emission λ 425 nm. As a solid phase, a 4.6 × 250-mm TSK gel-Amide 80 column (Tosoh Bioscience) was used. A 2AAlabeled glucose homopolymer ladder (Ludger) was included to determine the glucose unit (GU) values for the HPLC peaks. Individual GSL species were identified by their GU values and quantified by comparison of integrated peak areas with a known amount of 2AA-labeled BioQuant chitotriose standard (Ludger). Protein concentration in homogenates was determined using the BCA assay (Sigma-Aldrich).

2.5.11. Immunohistochemistry

Mouse brains were collected from animals, perfused with 4% PFA in PBS, and postfixed in 4% PFA in PBS overnight. Brains were cryopreserved in 30% sucrose for 2 d at 4°C, embedded in Tissue-Tek OCT Compound, cut in 40-µm-thick sections, and stored in cryopreservation buffer (0.05 M sodium phosphate buffer, pH 7.4, 15% sucrose, and 40% ethylene glycol) at −20°C pending immunohistochemistry. Mouse brain sections were washed three times with PBS and permeabilized/blocked by incubating in 5% BSA and 0.3% Triton X-100 in PBS for 1 h at room temperature. Incubation with primary antibodies, diluted in 1% BSA and 0.3% Triton X-100 in PBS, was performed overnight at 4°C. The antibodies and working concentrations used are listed in Table 2.

Table 2. **Antigens and dilutions**

Antigen	Host/Target species	Dilution	Manufacturer
Synapsin-1	Rabbit anti-mouse	1:200	Abcam (ab64581)
GFAP	Rabbit anti-mouse	1:300	DSHB (8-1E7-s)
LAMP2	Rat anti-mouse	1:200	DSHB (ABL-93-s)
HS (10E4 epitope)	Mouse anti-mouse	1:200	AMSBIO (F58-10E4)
NeuN	Rabbit anti-mouse	1:250	Millipore Sigma (MABN140)
CD68	Rabbit polyclonal to CD68	1:200	Abcam (ab125212)
G_{M2}	Mouse humanized	1:400	KM966
LC3B	Rabbit anti-mouse	1:200	GeneTex (GTX82986)
VGLUT1	Rabbit anti-mouse	1:1,000 (cells) and 1:200 (tissues)	Abcam (ab104898)
PSD-95	Mouse anti-mouse	1:1,000 (cells) and 1:200 (tissues)	Abcam (ab99009)
Ubiquitin	Mouse	1:200	Abcam (ab7254)
β-Amyloid (D54D2)	Rabbit anti-mouse	1:200	Cell Signaling (8243S)
SCMAS	Rabbit anti-mouse	1:200	Abcam (ab181243)
Anti-*O*-GlcNAc	Mouse anti-mouse	1:400	Kerafast (EJH004)
MAP2	Chicken anti-mouse	1:2,000	Abcam (ab5392)
Vesicular γ aminobutyric acid (GABA) transporter vGAT	Rabbit anti-mouse	1:1,000	Synaptic Systems (131003)
Gephyrin	Mouse anti-mouse	1:1,000	Synaptic Systems (147021)
Calreticulin	Rabbit anti-human	1:200	Sigma-Aldrich (208910)
IgG	Goat anti-rabbit, anti-mouse, anti-rat, or anti-chicken Alexa Fluor 488–, Alexa Fluor 555–, or Alexa Fluor 633–conjugated	1:400	Thermo Fisher Scientific

The mouse brain sections were washed three times with PBS and counterstained with Alexa Fluor–labeled secondary antibodies (dilution 1:400) for 2 h at room temperature. After washing three times with PBS, the mouse brain sections were treated with True-Black Lipofuscin Autofluorescence Quencher (23007, dilution 1:10; Biotium) for 1 min, and then again washed three times with PBS. The slides were mounted with Prolong Gold Antifade mounting reagent with DAPI (P36935; Invitrogen) and analyzed using a Leica DM 5500 Q upright confocal microscope (10×, 40×, and 63× oil objective, NA 1.4). Images were processed and quantified using ImageJ 1.50i software (National Institutes of Health) in a blinded fashion. Panels were assembled with Adobe Photoshop.

2.5.12. Immunocytochemistry

Cultured neurons on day in vitro 21 were fixed in 4% paraformaldehyde and 4% sucrose solution in PBS (pH 7.4). The cells were permeabilized with 0.1% Triton X-100 in PBS for 5 min, and nonspecific binding sites were blocked with 5% BSA in PBS for 1 h and incubated overnight at 4°C with primary antibodies in 1% BSA in PBS (see Table 2 for the source of antibodies and their dilutions). The next day, neurons were washed three times with PBS and labeled with Alexa Fluor 488– or Alexa Fluor 555–conjugated goat anti-rabbit or Alexa Fluor 633–anti-mouse IgG (1:1,000, all from Thermo Fisher Scientific) for 1 h at room temperature. Coverslips were washed three times again in PBS, mounted on slides using ProLong Gold mounting medium, containing DAPI (P36935; Invitrogen), and analyzed by LSM510 Meta Laser or Leica TCS SPE confocal microscopes (63× glycerol-immersion objectives, NA 1.4). Images were processed with Leica Application Suite X software and Photoshop 2021 (Adobe) and quantified using ImageJ 1.50i. Quantification was blinded and performed in at least three different experiments.

2.5.13. Western blot

Cerebral cortical tissues were homogenized in five volumes of radioimmunoprecipitation assay lysis buffer (50 mM Tris-HCl, pH 7.4, 150 mM NaCl, 1% NP-40, 0.25% sodium deoxycholate, 0.1% SDS, 2 mM EDTA, and 1 mM PMSF), containing protease and phosphate inhibitor cocktails (4693132001 and 4906837001; Sigma-Aldrich), using a Dounce homogenizer. The homogenates were kept on ice for 30 min and centrifuged at 13,000 g at 4°C for 25 min. The supernatant was centrifuged again at 13,000 g for 15 min, the protein concentration in resulting lysates was measured, and 20 μg of protein from each sample was separated by SDS-PAGE on 4–20% precast polyacrylamide gel (4561096; Bio-Rad). Western blot analyses were performed according to standard protocols using the following antibodies: anti-Grp78 (BiP; rabbit polyclonal, 1:2,000; Stressgen), CHOP (1:50, mouse; Developmental Studies Hybridoma Bank [DSHB]), anti-

ubiquitin, (1:1,000, rabbit; Sigma-Aldrich), and α-tubulin (1: 2,000, mouse; DSHB). Equal protein loading was confirmed by Ponceau S staining and normalized for tubulin immunoreactive band. Detected bands were quantified using ImageJ 1.50i software (National Institutes of Health).

2.5.14. Production of the LV for expression of WT and mutant human HGSNAT

The plasmid expressing missense HGSNAT mutant P304L was obtained by site-directed mutagenesis of previously described pENTR1A-HGSNAT-GFP plasmid, containing the codon optimized cDNA of WT human HGSNAT fused at the C-terminus with GFP (Par´a et al., 2021). HGSNAT-P311L-GFP cDNA was further subcloned to LV plasmid (pLenti CMV/TO Puro DEST [775-1], Plasmid #17432; Addgene; Campeau et al., 2009), using Gateway technology according to the manufacturer's instructions (Gateway LR Clonase II Enzyme mix, #11791020; Invitrogen). To produce an LV expressing HGSNATP311L-GFP protein under the control of the CMV promotor, the HEK293T cells were co-transfected with pLenti-HGSNAT-P311L-GFP plasmid, the packaging plasmids REV (Plasmid #12253; Addgene) and pMDL (gag-pol; Plasmid #12251; Addgene), and the envelope plasmid VSVG (Plasmid#12259; Addgene) in the presence of Lipofectamine 2000 Transfection Reagent (11668019; Invitrogen). After 30 h, the cell medium containing lentivirus was collected and used to transfect primary mouse neurons or human skin fibroblasts.

2.5.15. Analysis of GAGs by LC-MS/MS

Analysis of brain glycans was conducted as previously described by Viana et al. (2020). Briefly, 30–50 mg of mouse brain tissues were homogenized in ice-cold acetone and centrifuged at 12,000 g for 30 min at 4°C. The pellets were dried, resuspended in 0.5 N NaOH, and incubated for 2 h at 50°C. Then, the pH of the samples was neutralized with 1 N HCl, and NaCl was added to the reaction mix in a final concentration of 3 M. After centrifugation at 10,000 g for 5 min at

room temperature, the supernatants were collected and acidified using 1 N HCl. After another centrifugation at 10,000 g for 5 min at room temperature, the supernatants were collected and neutralized with 1 N NaOH to a pH of 7.0. The samples were diluted at a ratio of 1:2 with 1.3% potassium acetate in absolute ethanol and centrifuged at 12,000 g and 4°C for 30 min. The pellets were washed with cold 80% ethanol, dried at room temperature, and dissolved in 50 mM Tris-HCl buffer. The samples were further filtered using AcroPrep Advance 96-Well Filter Plates with Ultrafiltration Omega 10 K membrane filters (PALL Corp.) and digested with chondroitinase B, heparitinase, and keratanase II overnight at 37°C. The samples were analyzed by mass spectrometry using a 6460 Triple Quad instrument (Agilent Technologies) with Hypercarb columns, as described (Viana et al., 2020).

2.5.16. Glucosamine treatment

Starting from3 wk of age, homozygous *Hgsnat*^{P304L} male (n = 24) and female (n = 24) mice were randomly divided in two equal groups. The control group was administered water, and for the treatment group, water was supplemented with 10 mg/ml glucosamine (G4875-25G; Sigma-Aldrich), which would result in a dose of ∼2.0 g/kg BW/d. The dose formulation was changed twice a week. The untreated WT group included male and female siblings of *Hgsnat*^{P304L} mice (n = 14 and 13, respectively). At 16 wk, all mice were studied by YM and NOR behavioral tests and sacrificed to analyze CNS pathology as described above (Galeano et al., 2007).

2.5.17. Statistical analysis

Statistical analyses were performed using Prism v9.3.0 software (GraphPad). The normality for all data was checked using the D'Agostino and Pearson omnibus normality test. Significance of the difference was determined using t test (normal distribution) or Mann–Whitney U test, when comparing two groups. One-way ANOVA or nested ANOVA tests, followed by

Tukey's multiple comparison test (normal distribution) or Kruskal–Wallis test followed by Dunn's multiple comparisons test, were used when comparing more than two groups. Two-way ANOVA followed by Tukey's post hoc test was used for two-factor analysis. A P value of ≤0.05 was considered significant.

2.6. Online supplemental material

Fig. S1 shows the generation and skeletal phenotype of *Hgsnat*^{P304L} mice.

Fig. S2 shows a Venn diagram displaying the number of genes upregulated or downregulated in hippocampal tissues of 4-mo-old *Hgsnat*^{P304L} and *Hgsnat-Geo* mice compared with the age- and sex-matched WT mice; and the gene and protein expression data related to ER stress and UPR in the brain tissues of *Hgsnat*^{P304L} mice.

Fig. S3 shows data confirming that the missense variant Pro311Leu impairs expression, lysosomal targeting, processing, and enzymatic activity of HGSNAT.

Fig. S4 shows data providing evidence that mice treated daily with 2.0 g/kg glucosamine for 13 wk do not show alterations in growth and BW, blood glucose levels, or Astro and microgliosis in brain tissues. Table S1 lists the top 10 upregulated and downregulated genes in hippocampi of *Hgsnat-Geo* mice and *Hgsnat*^{P304L} mice compared with each other and WT mice.

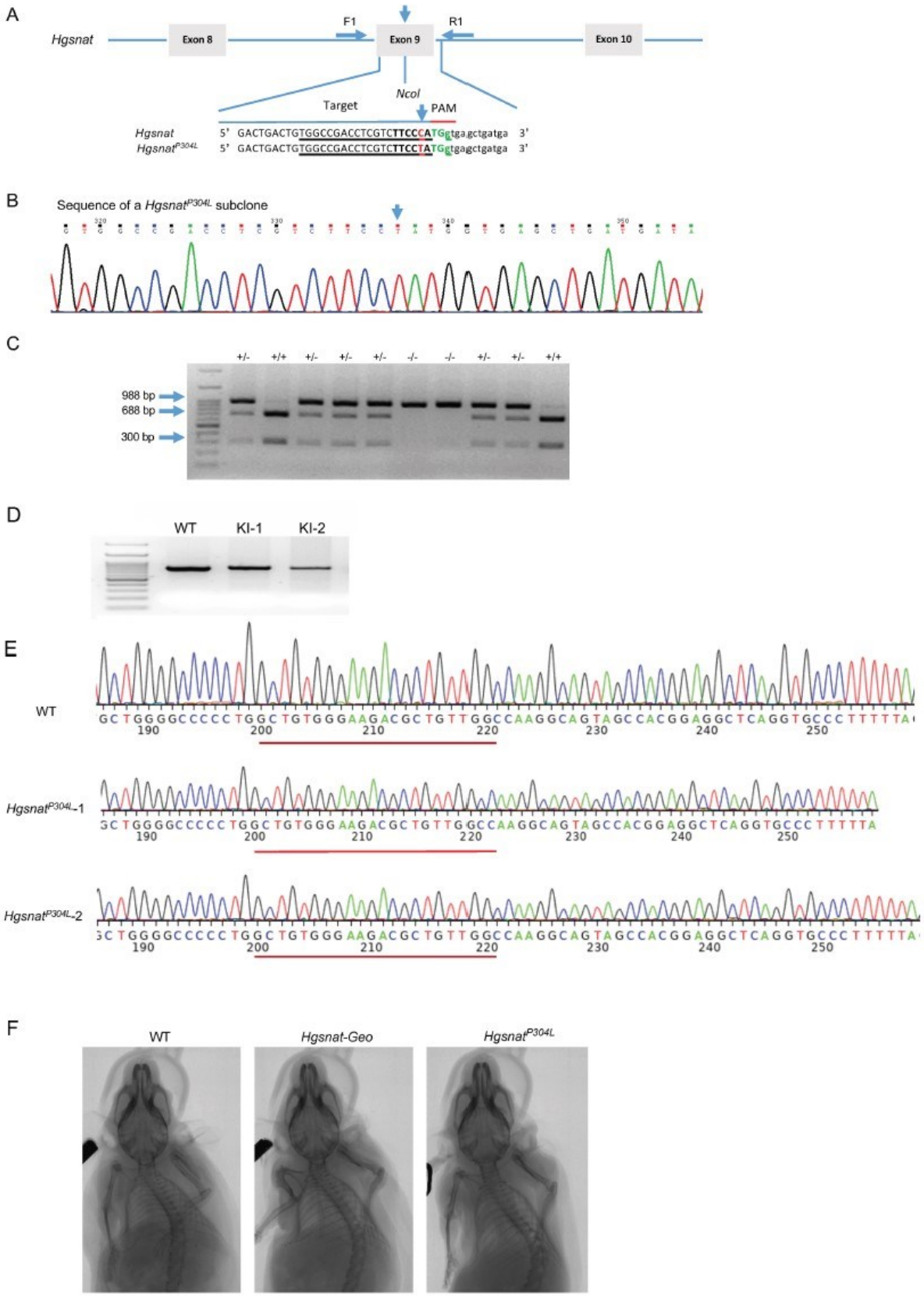
A
Hgsnat
Exon 8
F1
Exon 9
R1
Exon 10
NcoI
Target
PAM
Hgsnat 5' GACTGACTGTGGCCGACCTCGTCTTCCCATGgtga.gctgatga 3'
Hgsnat^P304L 5' GACTGACTGTGGCCGACCTCGTCTTCCTATGgtgagctgatga 3'
B
Sequence of a Hgsnat^P304L subclone
C
+/- +/+ +/- +/- +/- -/- -/- +/- +/- +/+
988 bp
688 bp
300 bp
D
WT
KI-1
KI-2
E
WT
Hgsnat^P304L-1
Hgsnat^P304L-2
F
WT
Hgsnat-Geo
Hgsnat^P304L

Figure S1. Generation and skeletal phenotype of *Hgsnat*^{P304L} mice. (A) Schema showing the Cas9/sgRNA-targeting site in Hgsnat exon 9. The sgRNA targeting sequence is underlined, and the protospacer-adjacent motif (PAM) sequence is shown in green. The c.911C>T mutation is shown in red and marked with an arrow. The C>T substitution disrupts the NcoI restriction site (shown in bold). The exon sequence is capitalized. (B) Sanger sequencing of single allele fragment obtained by PCR amplification of genomic DNA from the tail clips of the *Hgsnat*^{P304L} founder mouse showing the presence of the c.911C>T mutation. (C) Genotyping of *Hgsnat*^{P304L} mice. The DNA was extracted from clipped mouse tails and a 988-bp product amplified using a forward primer 59-ATGGAGTGCCTGATGGGAGG-39 and a reverse primer 59-GATCTAGAAACGGCCCGAAGA-39. The PCR products were further digested with NcoI and analyzed on a 2% agarose gel. The 688- and 300-bp fragments are detected for the WT allele, and an undigested 988-bp fragment, for the targeted *Hgsnat*^{P304L} allele. (D) A 763-bp fragment of the Spg7 gene, containing the potential off-target sequence 59-CTGTGGGAAGACGCTGTTGGCCA-39, was amplified by PCR from DNA extracted from tail clips of *Hgsnat*^{P304L} founder mice (KI-1 and KI-2) and a control WT mouse. (E) Sanger sequencing of a PCR product confirms the absence of mutations in the Spg7 gene fragment adjacent to the 59-CTGTGGGAAGACGCTGTTGGCCA-39 fragment homologous to the PAM sequence. (F) A high-resolution in vivo micro-CT scanner (SkyScan 1176) was used to evaluate skeletal deformities in 4-mo-old *Hgsnat-Geo* and *Hgsnat*^{P304L} mice. The mice were anesthetized by isoflurane flow and the images were taken from the dorsal side. Both *Hgsnat-Geo* and *Hgsnat*^{P304L} mice do not develop abnormalities of skull bones. Panels show typical images of three mice analyzed per genotype.

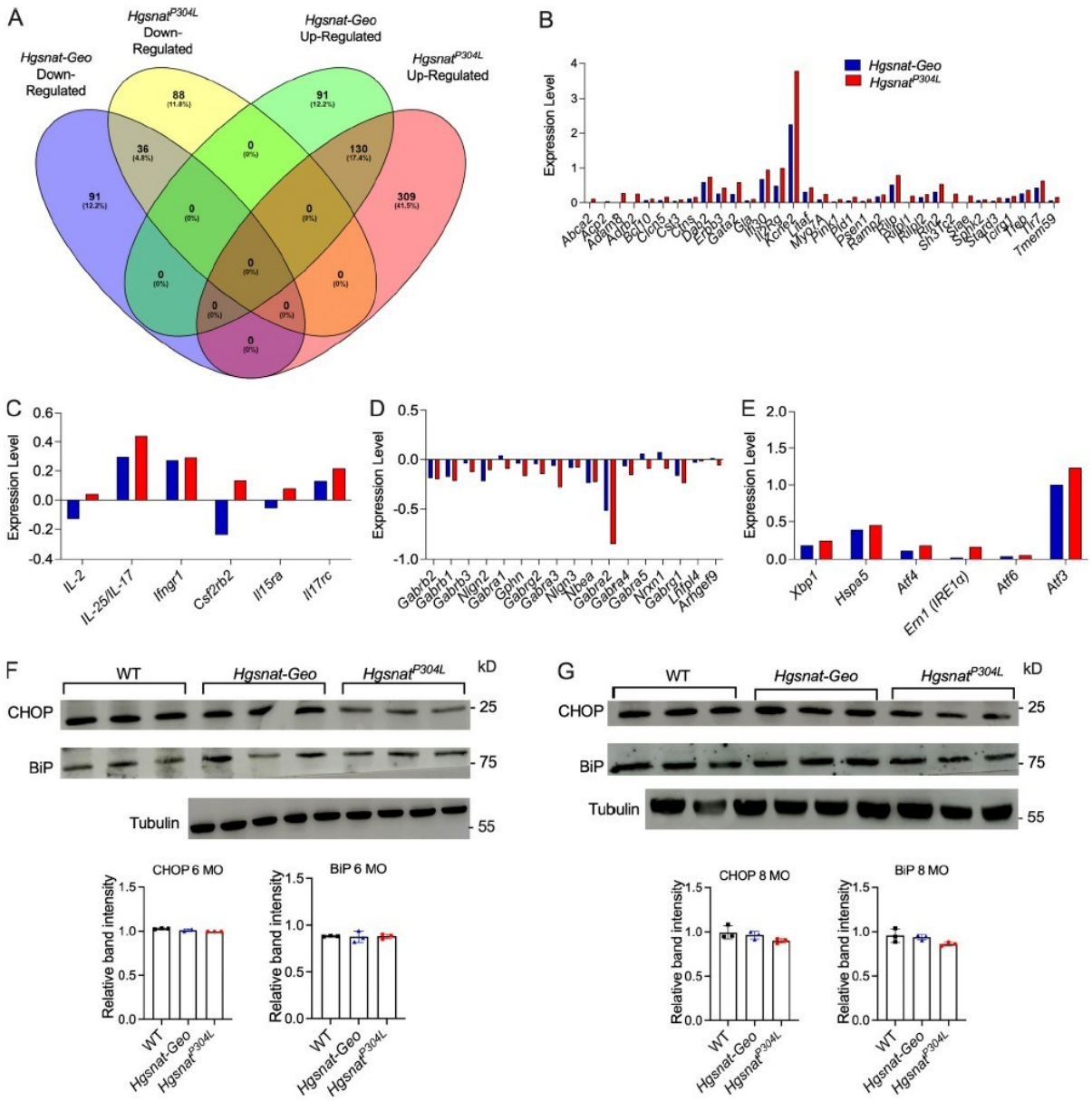

Figure S2. ER stress and UPR in the brain tissues of *Hgsnat*^{P304L} mice. (A) A higher number of hippocampal genes with altered expression levels is found in *Hgsnat*^{P304L} than in *Hgsnat-Geo* mice. Venn diagram showing the number of genes that were upregulated or downregulated in hippocampal tissues of 4-mo-old *Hgsnat*^{P304L} and *Hgsnat-Geo* mice compared with the age- and sex-matched WT mice. Three mice (two male and one female) were studied for each genotype. (B–E) The expression levels of genes involved in lysosomal biogenesis (B), inflammatory response (C), and ER stress/UPR (E) show a trend for a greater increase, while the expression of genes involved in inhibitory synaptic transmission (D) show a trend for further decrease in *Hgsnat*^{P304L} compared with *Hgsnat-Geo* mice. (F and G) Normal protein levels the ER

stress markers, CHOP and BiP, are detected in brain cortex tissues of 6-mo-old (F) and 8-mo-old (G) WT, *Hgsnat*^{P304L}, and *Hgsnat-Geo* mice by immunoblot. Graphs show band intensity values measured using ImageJ software. Individual results, means, and SD of experiments with three mice per genotype, per age are shown. P values were calculated using one-way ANOVA with Tukey post hoc test. Source data are available for this figure: Source Data FS2.

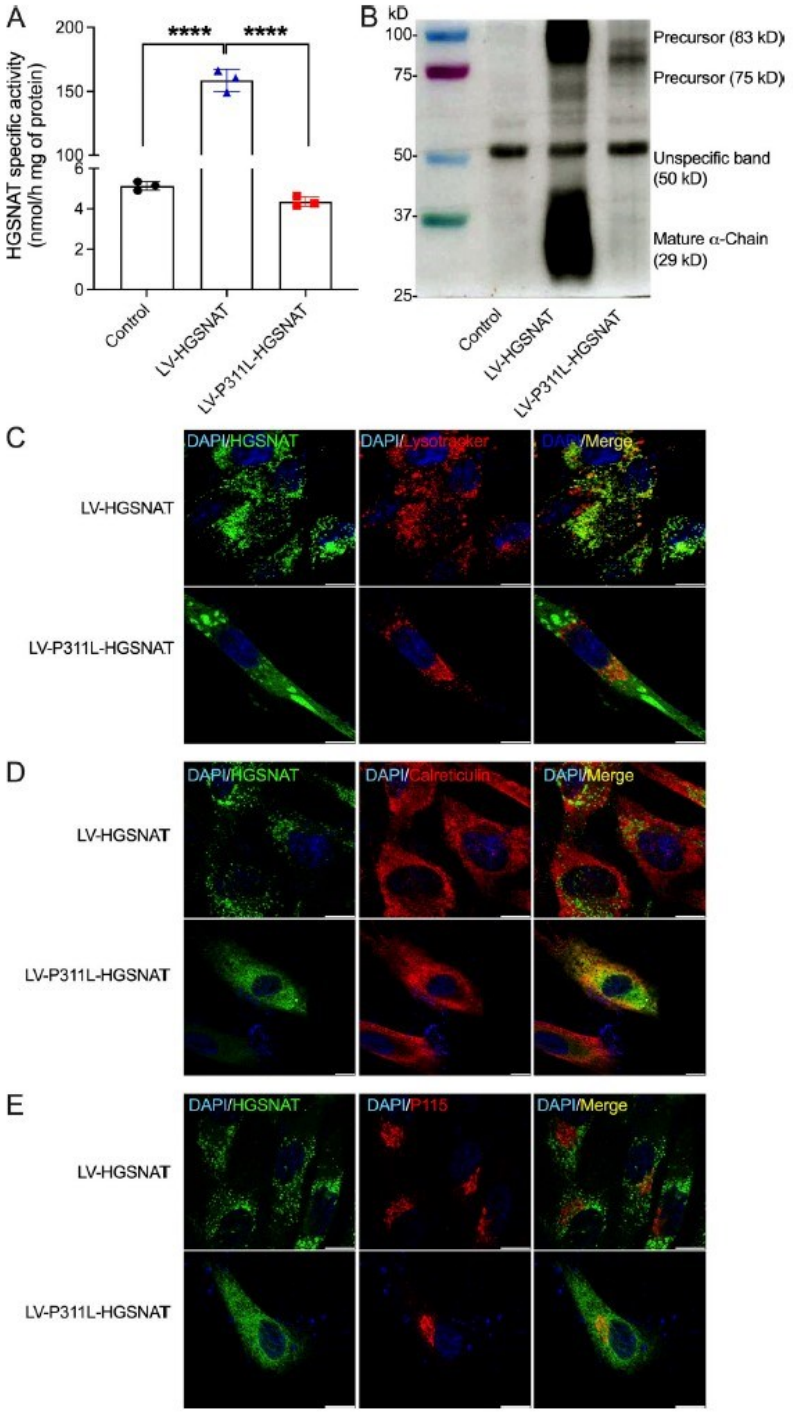

Figure S3. The missense variant Pro311Leu affects expression, lysosomal targeting, processing, and enzymatic activity of HGSNAT. (A) Pro311Leu HGSNAT mutant lacks enzymatic activity. The N-acetyltransferase activity was measured in homogenates of primary cultured skin fibroblasts of healthy control donor (Control) or fibroblasts transduced with LV vectors encoding for the GFP-tagged WT HGSNAT (LV HGSNAT) or the Pro311Leu mutant (LV-P311LHGSNAT). The graph shows individual values, means, and SD of three independent experiments. P values were calculated by one-way ANOVA followed by Tukey post hoc test; ****, $P < 0.0001$. (B) The 75-kD (with EGFP tag) non glycosylated precursor is the main HGSNAT form detected in the homogenates of cells transduced with the mutant virus, while the fully glycosylated 83-kD precursor and the cleaved 29-kD α-subunit are detected in cells expressing the WT enzyme. The 50-kD band represents a nonspecific cross-reacting protein also present in non transduced cells. The panel shows a representative blot from three independent experiments yielding similar results. (C and D) The Pro311Leu HGSNAT mutant protein is not targeted to lysosomes. Representative confocal images show fibroblast cells transduced with LV vectors encoding for the GFP-tagged WT HGSNAT (LV-HGSNAT) and or the Pro311Leu mutant (LV-P311LHGSNAT). (E) Cells grown on glass slides were labeled with Lysotracker Red for 1 h before fixation (C) or stained for the ER (anti-Calreticulin antibodies; D) or Golgi (anti-P115 antibodies; E; red). Scale bar equals 10 μm. Panels show typical images of triplicate experiments.

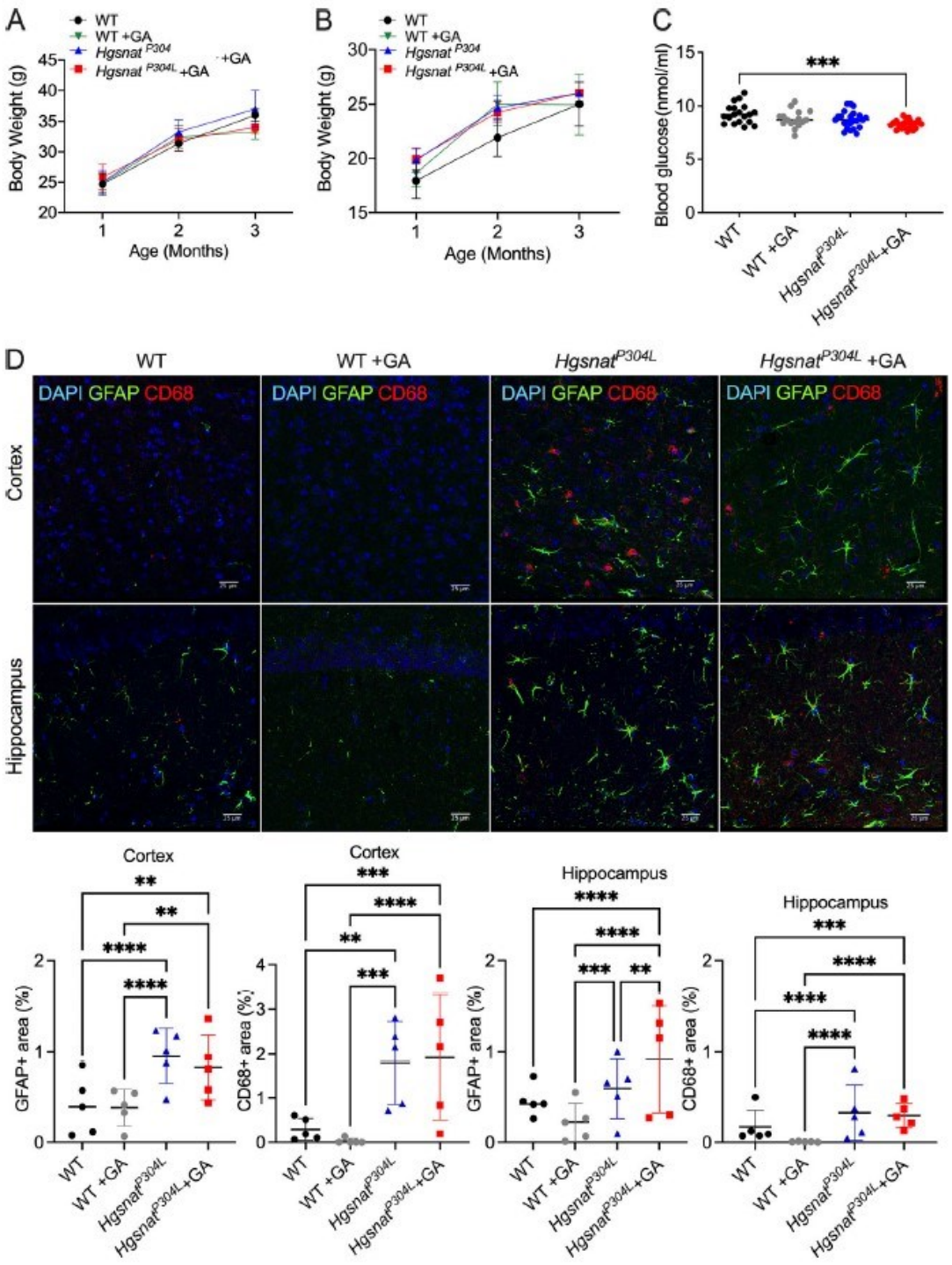

Figure S4. Mice treated daily with 2.0 g/kg BW glucosamine (GA) for 13 wk do not show alterations in growth and BW, blood glucose levels, or astro- and microgliosis in brain tissues. (A and B) BW was measured monthly, between the ages of 1 and 3 mo. Mean values and SD obtained for 12mice per genotype, per sex, per treatment are shown. (C) The blood glucose levels were tested at the age of 4 mo. Individual

data, means, and SD obtained for ≥24 mice per genotype, per treatment are shown. P values were measured using two-way ANOVA (A and B) and one-way ANOVA (C) with Tukey post hoc tests. (D) Levels of activated CD68+ microglia and GFAP+ astrocytes are not changed in the hippocampus and somatosensory cortex of 4-mo-old *Hgsnat*^{P304L} mice treated with glucosamine. Panels show representative images of somatosensory cortex (layers 4–5) and hippocampus of 4-mo-old WT, and *Hgsnat*^{P304L} mice treated or not with glucosamine and stained for GFAP (green) and CD68 (red). Scale bars equal 25 μm. Bar graph shows quantification of CD68+ and GFAP+ area with ImageJ software. Individual results, means, and SD of experiments with five mice per genotype, per treatment are shown. P values were calculated using nested one-way ANOVA test with Tukey post hoc test. **, P < 0.01; ***, P < 0.001; ****, P < 0.0001.

Table S1. The top 10 upregulated and downregulated genes in *Hgsnat-Geo* mice and *Hgsnat*^{P304L} mice as compared with WT mice and *Hgsnat*^{P304L} mice as compared with *Hgsnat-Geo* mice. Complete results are available for download and analysis at the following address:

WT/KI:

https://maayanlab.cloud/biojupies/notebook/IAykq58fQ

WT/KO:

https://maayanlab.cloud/biojupies/notebook/m2KTE2Z4W

KO/KI:

https://maayanlab.cloud/biojupies/notebook/8Hq6GUKin

1.1 The top 10 upregulated genes in *Hgsnat-Geo* mice as compared with WT mice

Gene Symbol	logFC	AveExpr	t	P-value	Adj.P.Val	B
Gm15446	3.963596	3.298196	25.95803	5.09E-09	8.00E-05	2.83828
Lyz2	3.293204	3.47975	11.79959	2.40E-06	0.018907	2.05529
Tmem254a	1.637335	3.025582	10.69658	5.06E-06	0.019894	1.423174
Tmem254b	1.637335	3.025582	10.69658	5.06E-06	0.019894	1.423174
Ly9	3.165477	-0.32953	9.831997	9.52E-06	0.029949	-1.91727
Mpeg1	1.380629	5.344022	8.07209	4.06E-05	0.106301	1.835164
Lilrb4a	2.845683	-1.42679	7.39661	7.58E-05	0.170301	-2.79881
Cst7	3.299472	-0.71795	6.989179	0.000113	0.220437	-2.45246
Clec7a	2.958558	0.58566	6.803532	0.000136	0.220437	-1.60498

Cd68	1.33784	3.060377	6.776075	0.00014	0.220437	0.173089

1.2 The top 10 downregulated genes in *Hgsnat-Geo* mice as compared with WT mice

Gene Symbol	logFC	AveExpr	t	P-value	Adj.P.Val	B
Tnfrsf18	-1.02505	1.123303	-4.41071	0.002245	0.965579	-2.15811
Tgfb1i1	-0.72034	3.124157	-4.25156	0.002783	0.965579	-1.55517
Gm16432	-0.82374	2.677928	-4.06556	0.003593	0.98568	-1.83306
Tmem91	-0.61836	2.40964	-3.97921	0.004053	0.98568	-1.98018
Col2a1	-1.12817	-0.09692	-3.94625	0.004245	0.98568	-2.93069
Cxcl15	-0.81951	1.966697	-3.76807	0.005465	0.998245	-2.28399
Phldb3	-1.32778	-1.23601	-3.65429	0.006436	0.998245	-3.43336
Sptssb	-1.05821	0.310449	-3.63897	0.006581	0.998245	-2.93564
Gdpd2	-0.66009	2.526844	-3.63574	0.006612	0.998245	-2.2641
Mcm10	-1.07276	0.078383	-3.63064	0.006661	0.998245	-3.021

1.3 The top 10 upregulated genes in *Hgsnat*^{P304L} mice as compared with WT mice

Gene Symbol	logFC	AveExpr	t	P-value	Adj.P.Val	B
Gm15446	3.863174	3.274976	31.89635	5.80E-11	9.21E-07	11.93097
Zfp781	6.678025	-2.12467	15.55362	4.61E-08	0.000367	2.134689
Gm3095	4.992654	-2.95406	10.01197	2.39E-06	0.012683	0.616014
Tmem254b	1.436813	2.935904	9.158899	5.18E-06	0.015925	4.51273
Tmem254a	1.436813	2.935904	9.158899	5.18E-06	0.015925	4.51273
Sema3b	2.028503	1.460513	9.001059	6.01E-06	0.015925	3.850118
Trpv4	2.375905	1.397375	8.776806	7.46E-06	0.01625	3.660536
Trf	0.703259	7.395393	8.682262	8.18E-06	0.01625	4.148475
Mobp	0.779389	9.230635	8.448458	1.03E-05	0.018209	3.909972
Car14	1.312602	2.812631	7.765717	2.09E-05	0.033208	3.239745

1.4 The top 10 downregulated genes in *Hgsnat*^{P304L} mice as compared with WT mice

Gene Symbol	logFC	AveExpr	t	P-value	Adj.P.Val	B
Plxnd1	-0.53093	4.796305	-5.33373	0.000397	0.100643	0.233987
Oprk1	-1.10921	0.966172	-5.006	0.000627	0.129846	-0.01527
Dcx	-0.52407	4.870583	-4.81783	0.000821	0.137388	-0.52297
Gm5884	-3.88558	-0.98275	-4.53303	0.001246	0.170947	-0.94441
Tmem181b-ps	-1.02276	6.272376	-4.48815	0.001332	0.173558	-1.11689
Tmem181a	-0.70504	8.02711	-4.31821	0.001719	0.210769	-1.39994

Gm3173	-3.71812	-2.42109	-4.27973	0.001823	0.21311	-1.60701
Cntnap3	-0.93077	2.250784	-4.18608	0.002103	0.219739	-1.12029
Pde11a	-0.76544	4.031976	-4.15494	0.002206	0.22343	-1.41855
Gm14253	-1.9134	0.027017	-3.95317	0.003017	0.255198	-1.43675

1.5 The top 10 upregulated genes in *Hgsnat*^{P304L} mice as compared with *Hgsnat-Geo* mice

Gene Symbol	logFC	AveExpr	t	P-value	Adj.P.Val	B
Gm42421	4.052645	-2.63085	5.214733	0.000774	0.999853	-4.52378
Gm3095	3.670507	-2.34643	4.229227	0.002795	0.999853	-4.52615
Xkr7	1.708508	-1.3427	3.981301	0.003947	0.999853	-4.49992
Foxb1	1.423888	-1.0626	3.518206	0.007702	0.999853	-4.50034
Gm13543	1.678381	-1.66592	3.356957	0.009787	0.999853	-4.52317
Scnn1a	0.537885	2.606791	3.285439	0.010896	0.999853	-4.20182
Gm13369	2.098103	-1.5228	3.263089	0.011269	0.999853	-4.52148
5031410I06Rik	4.496545	-1.07879	3.240814	0.011654	0.999853	-4.50863
Lrrc43	1.200727	-1.02501	3.22557	0.011925	0.999853	-4.50728
Pcsk4	0.928758	0.128132	3.209835	0.012212	0.999853	-4.45661

1.6 The top 10 downregulated genes in *Hgsnat*^{P304L} mice as compared with *Hgsnat-Geo* mice

Gene Symbol	logFC	AveExpr	t	P-value	Adj.P.Val	B
Rab11b-ps2	-2.66777	0.558057	-5.55964	0.00051	0.999853	-4.33989
Gm5884	-3.6254	-1.07655	-3.67126	0.006155	0.999853	-4.49694
Duxbl1	-4.11426	-1.6153	-3.52989	0.007571	0.999853	-4.51799
Btg3	-0.61514	3.991453	-3.32243	0.010307	0.999853	-3.97252
Ddx3y	-4.95021	3.824088	-2.93646	0.018542	0.999853	-4.0868
Lilrb4a	-1.34239	-0.7047	-2.80853	0.022597	0.999853	-4.51101
Eif2s3y	-5.06998	3.206903	-2.79523	0.023069	0.999853	-4.20187
Nmrk2	-0.89672	-0.23561	-2.79509	0.023074	0.999853	-4.49442
Gm10357	-1.60994	0.746493	-2.78907	0.02329	0.999853	-4.44375
Gm28064	-1.01025	-0.79637	-2.75859	0.02442	0.999853	-4.5159

2.7. Data availability

The RNA sequencing data generated in this study are available at Sequence Read Archive website, accession no. PRJNA832487. Any other data, analytic methods, and study materials can be provided upon request for purposes of reproducing the results or replicating the procedure.

2.8. Acknowledgments

The authors thank Dr. Jeffrey A.Medin, Dr. MontyMcKillop, Dr. Christian Beaus´ejour, and Ga¨el Moquin-Beaudry for the help in production of LV-HGSNAT-GFP and LV-P311L-HGSNAT-GFP. We also thank Jeannie Mui and the Facility for Electron Microscopy Research (McGill University) for help with the TEM, Dr. Elke Küster-Sch¨ock and the Plateforme d'Imagerie Microscopique (Centre Hospitalier Universitaire Sainte-Justine) for help with life imaging microscopy, Mitra Cowan and the McGill Integrated Core for Animal Modeling for help with mouse production, and Dr. Mila Ashmarina for critically reading the manuscript and helpful advice.

This work has been partially supported by an operating grant PJT-156345 from the Canadian Institutes of Health Research, Elisa Linton Sanfilippo Research Laboratory endowed fund, and gifts from JLK Foundation, Jonah's Just Began Foundation, and Sanfilippo Children's Research Foundation (Australia) to A.V. Pshezhetsky. F.M. Platt is a Wellcome Trust Investigator in Science and a Wolfson Royal Society Merit Award holder. D.A. Priestman was supported by the Mizutani Foundation and R. Heon-Roberts by scholarships from the Canadian MPS Society and the Canadian Glycomics Network.

Authors' contributions: M. Taherzadeh, X. Pan, P. Bose, R. Heon-Roberts, A.L.A. Nguyen, TM. Xu, C. Par´a, D. Priestman, N. Fnu, and S. Khan conducted experiments and acquired data; X. Pan, M. Taherzadeh; P. Bose, R. Heon-Roberts, A.L.A. Nguyen, TM. Xu, D.A. Priestman, N. Fnu, S. Khan, S. Tomatsu, F.M. Platt, C.R. Morales, Y. Yamanaka, and A.V. Pshezhetsky analyzed data; A.V. Pshezhetsky designed the experiments and wrote the manuscript (first draft); X. Pan,M. Taherzadeh, P. Bose, S. Khan, S. Tomatsu, N. Fnu, D.A. Priestman, C.R. Morales, and A.V.

Pshezhetsky wrote the manuscript (editing). All authors read and approved the final version of the manuscript.

Disclosures: A.V. Pshezhetsky reported personal fees from Phoenix Nest Inc. and grants from Phoenix Nest Inc. outside the submitted work. No other disclosures were reported.

Submitted: 8 September 2021

Revised: 26 February 2022

Accepted: 2 May 2022

2.9. References

Akkerman, S., A. Blokland, O. Reneerkens, N.P. van Goethem, E. Bollen, H.J. Gijselaers, C.K. Lieben, H.W. Steinbusch, and J. Prickaerts. 2012. Object recognition testing: Methodological considerations on exploration and discrimination measures. Behav. Brain Res. 232:335–347. https://doi.org/10.1016/j.bbr.2012.03.022

Amegandjin, C.A., M. Choudhury, V. Jadhav, J.N. Carrico, A. Quintal, M. Berryer, M. Snapyan, B. Chattopadhyaya, A. Saghatelyan, and G. Di Cristo. 2021. Sensitive period for rescuing parvalbumin interneurons connectivity and social behavior deficits caused by TSC1 loss. Nat. Commun. 12:3653. https://doi.org/10.1038/s41467-021-23939-7

Antunes, M., and G. Biala. 2012. The novel object recognition memory: Neurobiology, test procedure, and its modifications. Cogn. Process. 13: 93–110. https://doi.org/10.1007/s10339-011-0430-z

Arora, K., and A.P. Naren. 2016. Pharmacological correction of cystic fibrosis: Molecular mechanisms at the plasma membrane to augment mutant CFTR function. Curr. Drug Targets. 17:1275–1281. https://doi.org/10.2174/1389450117666151209114343

Asano, N., S. Ishii, H. Kizu, K. Ikeda, K. Yasuda, A. Kato, O.R. Martin, and J.Q. Fan. 2000. In vitro inhibition and intracellular enhancement of lysosomal alpha-galactosidase A activity in Fabry lymphoblasts by 1- deoxygalactonojirimycin and its derivatives. Eur. J. Biochem. 267: 4179–4186. https://doi.org/10.1046/j.1432-1327.2000.01457.x

Ausseil, J., N. Desmaris, S. Bigou, R. Attali, S. Corbineau, S. Vitry, M. Parent, D. Cheillan, M. Fuller, I. Maire, et al. 2008. Early neurodegeneration progresses independently of microglial activation by heparan sulfate in the brain of mucopolysaccharidosis IIIB mice. PLoS One. 3:e2296. https://doi.org/10.1371/journal.pone.0002296

Bartsocas, C., H. Grobe, J.J. van de Kamp, K. von Figura, H. Kresse, U. Klein, and M.A. Giesberts. 1979. Sanfilippo type C disease: Clinical findings in four patients with a new variant of mucopolysaccharidosis III. Eur. J. Pediatr. 130:251–258. https://doi.org/10.1007/BF00441361

Berger-Plantinga, E.G., J.A. Vanneste, J.E. Groener, and M.J. van Schooneveld. 2004. Adult-onset dementia and retinitis pigmentosa due to mucopolysaccharidosis III-C in two sisters. J. Neurol. 251:479–481. https://doi.org/10.1007/s00415-004-0368-5

Beriault, D.R., and G.H. Werstuck. 20122012. The role of glucosamineinduced ER stress in diabetic atherogenesis. Exp. Diabetes Res. 2012:187018. https://doi.org/10.1155/2012/187018

Bhaumik, M., V.J. Muller, T. Rozaklis, L. Johnson, K. Dobrenis, R. Bhattacharyya, S. Wurzelmann, P. Finamore, J.J. Hopwood, S.U. Walkley, and P. Stanley. 1999. A mouse model for mucopolysaccharidosis type III A (Sanfilippo syndrome). Glycobiology. 9:1389–1396. https://doi.org/10.1093/glycob/9.12.1389

Bifsha, P., K. Landry, L. Ashmarina, S. Durand, V. Seyrantepe, S. Trudel, C. Quiniou, S. Chemtob, Y. Xu, R.A. Gravel, et al. 2007. Altered gene expression in cells from patients with lysosomal storage disorders suggests impairment of the ubiquitin pathway. Cell Death Differ. 14:511–523. https://doi.org/10.1038/sj.cdd.4402013

Boyd, R.E., G. Lee, P. Rybczynski, E.R. Benjamin, R. Khanna, B.A. Wustman, and K.J. Valenzano. 2013. Pharmacological chaperones as therapeutics for lysosomal storage diseases. J. Med. Chem. 56:2705–2725. https://doi.org/10.1021/jm301557k

Campeau, E., V.E. Ruhl, F. Rodier, C.L. Smith, B.L. Rahmberg, J.O. Fuss, J. Campisi, P. Yaswen, P.K. Cooper, and P.D. Kaufman. 2009. A versatile viral system for expression and depletion of proteins in mammalian cells. PloS One. 4:e6529. https://doi.org/10.1371/journal.pone.0006529

Chao, H.T., H. Chen, R.C. Samaco, M. Xue, M. Chahrour, J. Yoo, J.L. Neul, S. Gong, H.C. Lu, N. Heintz, et al. 2010. Dysfunction in GABA signalling mediates autism-like stereotypies and Rett syndrome phenotypes. Nature. 468:263–269. https://doi.org/10.1038/nature09582

Chatham, J.C., and R.B. Marchase. 2010. Protein O-GlcNAcylation: A critical regulator of the cellular response to stress. Curr. Signal Transduct. Ther. 5:49–59. https://doi.org/10.2174/157436210790226492

Choi, Y., A.B. Tuzikov, T.V. Ovchinnikova, N.V. Bovin, and A.V. Pshezhetsky. 2015. Novel direct assay for acetyl-CoA: α-Glucosaminide N-acetyltransferase using BODIPY-glucosamine as a substrate. JIMD Rep. 28:11–18. https://doi.org/10.1007/8904_2015_501

Croce, A., J.G. Pelletier, M. Tartas, and J.C. Lacaille. 2010. Afferent-specific properties of interneuron synapses underlie selective long-term regulation of feedback inhibitory circuits in CA1 hippocampus. J. Physiol. 588:2091–2107. https://doi.org/10.1113/jphysiol.2010.189316

De Pasquale, V., G. Scerra, M. Scarcella, M. D'Agostino, and L.M. Pavone. 2021. Competitive binding of extracellular accumulated heparan sulfate reduces lysosomal storage defects and triggers neuronal differentiation in a model of Mucopolysaccharidosis IIIB. Biochim. Biophys. Acta Mol. Cell Res. 1868:119113. https://doi.org/10.1016/j.bbamcr.2021.119113

Desnick, R.J. 2004. Enzyme replacement and enhancement therapies for lysosomal diseases. J. Inherit. Metab. Dis. 27:385–410. https://doi.org/10.1023/B:BOLI.0000031101.12838.c6

Ellgaard, L., and A. Helenius. 2003. Quality control in the endoplasmic reticulum. Nat. Rev. Mol. Cell Biol. 4:181–191. https://doi.org/10.1038/nrm1052

Ellgaard, L., M. Molinari, and A. Helenius. 1999. Setting the standards: Quality control in the secretory pathway. Science. 286:1882–1888. https://doi.org/10.1126/science.286.5446.1882

Ennaceur, A., and J. Delacour. 1988. A new one-trial test for neurobiological studies of memory in rats. 1: Behavioral data. Behav. Brain Res. 31:47–59. https://doi.org/10.1016/0166-4328(88)90157-x

Fan, J.Q., S. Ishii, N. Asano, and Y. Suzuki. 1999. Accelerated transport and maturation of lysosomal alpha-galactosidase A in Fabry lymphoblasts by an enzyme inhibitor. Nat. Med. 5:112–115. https://doi.org/10.1038/4801

Fedele, A.O., and J.J. Hopwood. 2010. Functional analysis of the HGSNAT gene in patients with mucopolysaccharidosis IIIC (Sanfilippo C Syndrome). Hum. Mutat. 31:E1574–E1586. https://doi.org/10.1002/humu.21286

Feldhammer, M., S. Durand, L. Mrazova, R.M. Boucher, R. Laframboise, R. Steinfeld, J.E.Wraith, H. Michelakakis, O.P. van Diggelen, M. Hrebicek, et al. 2009a. Sanfilippo syndrome type C: Mutation spectrum in the heparan sulfate acetyl-CoA: Alpha-glucosaminide N-acetyltransferase (HGSNAT) gene. Hum. Mutat. 30:918–925. https://doi.org/10.1002/humu.20986

Feldhammer, M., S. Durand, and A.V. Pshezhetsky. 2009b. Protein misfolding as an underlyingmolecular defect in mucopolysaccharidosis III type C. PLoS One. 4:e7434. https://doi.org/10.1371/journal.pone.0007434

Fougerat, A., X. Pan, V. Smutova, N. Heveker, C.W. Cairo, T. Issad, B. Larrivee, J.A. Medin, and A.V. Pshezhetsky. 2018. Neuraminidase 1 activates insulin receptor and reverses insulin resistance in obese mice. Mol. Metabol. 12:76–88. https://doi.org/10.1016/j.molmet.2018.03.017

Frustaci, A., C. Chimenti, R. Ricci, L. Natale, M.A. Russo, M. Pieroni, C.M. Eng, and R.J. Desnick. 2001. Improvement in cardiac function in the cardiac variant of Fabry's disease with galactose-infusion therapy. N. Engl. J. Med. 345:25–32. https://doi.org/10.1056/NEJM200107053450104

Galeano, B., R. Klootwijk, I. Manoli, M. Sun, C. Ciccone, D. Darvish, M.F. Starost, P.M. Zerfas, V.J. Hoffmann, S. Hoogstraten-Miller, et al. 2007. Mutation in the key enzyme of sialic acid biosynthesis causes severe glomerular proteinuria and is rescued by N-acetylmannosamine. J. Clin. Invest. 117:1585–1594. https://doi.org/10.1172/JCI30954

Germain, D.P., D.A. Hughes, K. Nicholls, D.G. Bichet, R. Giugliani, W.R. Wilcox, C. Feliciani, S.P. Shankar, F. Ezgu, H. Amartino, et al. 2016. Treatment of Fabry's disease with the pharmacologic chaperonemigalastat. N. Engl. J. Med. 375:545–555. https://doi.org/10.1056/NEJMoa1510198

Gomez-Grau, M., E. Garrido, M. Cozar, V. Rodriguez-Sureda, C. Dominguez, C. Arenas, R.A. Gatti, B. Cormand, D. Grinberg, and L. Vilageliu. 2015. Evaluation of aminoglycoside and non-aminoglycoside compounds for stop-codon readthrough therapy in four lysosomal storage diseases. PLoS One. 10:e0135873. https://doi.org/10.1371/journal.pone.0135873

Helenius, A., T. Marquardt, and I. Braakman. 1992. The endoplasmic reticulum as a protein-folding compartment. Trends Cell Biol. 2:227–231. https://doi.org/10.1016/0962-8924(92)90309-b

Heon-Roberts, R., A.L.A. Nguyen, and A.V. Pshezhetsky. 2020. Molecular bases of neurodegeneration and cognitive decline, the major burden of Sanfilippo disease. J. Clin. Med. 9:344. https://doi.org/10.3390/jcm9020344

Huang, D.W., B.T. Sherman, and R.A. Lempicki. 2009. Bioinformatics enrichment tools: Paths toward the comprehensive functional analysis of large gene lists. Nucleic Acids Res. 37:1–13. https://doi.org/10.1093/nar/gkn923

Li, H.H., W.H. Yu, N. Rozengurt, H.Z. Zhao, K.M. Lyons, S. Anagnostaras, M.S. Fanselow, K. Suzuki, M.T. Vanier, and E.F. Neufeld. 1999. Mouse model of Sanfilippo syndrome type B produced by targeted disruption of the gene encoding alpha-N-acetylglucosaminidase. Proc. Natl. Acad. Sci. USA. 96:14505–14510. https://doi.org/10.1073/pnas.96.25.14505

Lotfi, P., D.Y. Tse, A. Di Ronza, M.L. Seymour, G. Martano, J.D. Cooper, F.A. Pereira, M. Passafaro, S.M. Wu, and M. Sardiello. 2018. Trehalose reduces retinal degeneration, neuroinflammation and storage burden caused by a lysosomal hydrolase deficiency. Autophagy. 14:1419–1434. https://doi.org/10.1080/15548627.2018.1474313

Maegawa, G.H.B., M. Tropak, J. Buttner, T. Stockley, F. Kok, J.T. Clarke, and D.J. Mahuran. 2007. Pyrimethamine as a potential pharmacological chaperone for late-onset forms of GM2 gangliosidosis. J. Biol. Chem. 282:9150–9161. https://doi.org/10.1074/jbc.M609304200

Martins, C., P.F.V. de Medeiros, S. Leistner-Segal, L. Dridi, N. Elcioglu, J. Wood, M. Behnam, B. Noyan, L. Lacerda, M.T. Geraghty, et al. 2019. Molecular characterization of a large group of Mucopolysaccharidosis type IIIC patients reveals the evolutionary history of the disease. Hum. Mutat. 40:1084–1100. https://doi.org/10.1002/humu.23752

Martins, C., H. Hulkova, L. Dridi, V. Dormoy-Raclet, L. Grigoryeva, Y. Choi, A. Langford-Smith, F.L. Wilkinson, K. Ohmi, G. DiCristo, et al. 2015. Neuroinflammation, mitochondrial defects and neurodegeneration in mucopolysaccharidosis III type C mouse model. Brain. 138:336–355. https://doi.org/10.1093/brain/awu355

Matos, L., I. Canals, L. Dridi, Y. Choi, M.J. Prata, P. Jordan, L.R. Desviat, B. Perez, A.V. Pshezhetsky, D. Grinberg, et al. 2014. Therapeutic strategies based on modified U1 snRNAs and chaperones for Sanfilippo C splicing mutations. Orphanet J. Rare Dis. 9:180. https://doi.org/10.1186/s13023-014-0180-y

Matsuda, J., O. Suzuki, A. Oshima, Y. Yamamoto, A. Noguchi, K. Takimoto, M. Itoh, Y. Matsuzaki, Y. Yasuda, S. Ogawa, et al. 2003. Chemical chaperone therapy for brain pathology in G(M1)-gangliosidosis. Proc. Natl. Acad. Sci. USA. 100:15912–15917. https://doi.org/10.1073/pnas.2536657100

Miller, K.L., and D.O. Clegg. 2011. Glucosamine and chondroitin sulfate. Rheum. Dis. Clin. North Am. 37:103–118. https://doi.org/10.1016/j.rdc.2010.11.007

Monaco, A., V. Maffia, N.C. Sorrentino, I. Sambri, Y. Ezhova, T. Giuliano, V. Cacace, E. Nusco, M. De Risi, E. De Leonibus, et al. 2020. The amyloid inhibitor CLR01 relieves autophagy and ameliorates neuropathology in a severe lysosomal storage disease. Mol. Ther. 28:1167–1176. https://doi.org/10.1016/j.ymthe.2020.02.005

Nakamura, K., M. Koike, K. Shitara, Y. Kuwana, K. Kiuragi, S. Igarashi, M. Hasegawa, and N. Hanai. 1994. Chimeric anti-ganglioside GM2 antibody with antitumor activity. Cancer Res. 54:1511–1516

Narita, A., K. Shirai, S. Itamura, A. Matsuda, A. Ishihara, K. Matsushita, C. Fukuda, N. Kubota, R. Takayama, H. Shigematsu, et al. 2016. Ambroxol chaperone therapy for neuronopathic Gaucher disease: A pilot study. Ann. Clin. Transl. Neurol. 3:200–215. https://doi.org/10.1002/acn3.292

Neville, D.C.A., V. Coquard, D.A. Priestman, D.J. te Vruchte, D.J. Sillence, R.A. Dwek, F.M. Platt, and T.D. Butters. 2004. Analysis of fluorescently labeled glycosphingolipid-derived oligosaccharides following ceramide glycanase digestion and anthranilic acid labeling. Anal. Biochem. 331: 275–282. https://doi.org/10.1016/j.ab.2004.03.051

Pan, X., C.B.P. De Aragão, J.P. Velasco-Martin, D.A. Priestman, H.Y. Wu, K. Takahashi, K. Yamaguchi, L. Sturiale, D. Garozzo, F.M. Platt, et al. 2017. Neuraminidases 3 and 4 regulate neuronal function by catabolizing brain gangliosides. FASEB J. 31:3467–3483. https://doi.org/10.1096/fj.201601299R

Par´a, C., P. Bose, L. Bruno, E. Freemantle, M. Taherzadeh, X. Pan, C. Han, P.S. McPherson, J.C. Lacaille, E. Bonneil, et al. 2021. Early defects in mucopolysaccharidosis type IIIC disrupt excitatory synaptic transmission. JCI Insight. 6:e142073. https://doi.org/10.1172/jci.insight.142073

Parenti, G. 2009. Treating lysosomal storage diseases with pharmacological chaperones: From concept to clinics. EMBO Mol. Med. 1:268–279. https://doi.org/10.1002/emmm.200900036

Parenti, G., S. Fecarotta, G. la Marca, B. Rossi, S. Ascione, M.A. Donati, L.O. Morandi, S. Ravaglia, A. Pichiecchio, D. Ombrone, et al. 2014. A chaperone enhances blood alpha-glucosidase activity in Pompe disease patients treated with enzyme replacement therapy. Mol. Ther. 22: 2004–2012. https://doi.org/10.1038/mt.2014.138

Parker, H., S.M. Ellison, R.J. Holley, C. O'Leary, A. Liao, J. Asadi, E. Glover, A. Ghosh, S. Jones, F.L. Wilkinson, et al. 2020. Haematopoietic stem cell gene therapy with IL-1Ra rescues cognitive loss in mucopolysaccharidosis IIIA. EMBO Mol. Med. 12:e11185. https://doi.org/10.15252/emmm.201911185

Popov, N. 1985. Effects of D-galactosamine and D-glucosamine on retention performance of a brightness discrimination task in rats. Biomed. Biochim. Acta. 44:611–622

Ruijter, G.J.G., M.J. Valstar, J.M. van de Kamp, R.M. van der Helm, S. Durand, O.P. van Diggelen, R.A. Wevers, B.J. Poorthuis, A.V. Pshezhetsky, and F.A. Wijburg. 2008. Clinical and genetic spectrum of Sanfilippo type C (MPS IIIC) disease in The Netherlands. Mol. Genet. Metabol. 93:104–111. https://doi.org/10.1016/j.ymgme.2007.09.011

Sawkar, A.R., W.C. Cheng, E. Beutler, C.H. Wong, W.E. Balch, and J.W. Kelly. 2002. Chemical chaperones increase the cellular activity of N370S betaglucosidase: A therapeutic strategy for Gaucher disease. Proc. Natl. Acad. Sci. USA. 99:15428–15433. https://doi.org/10.1073/pnas.192582899

Scriver, C.R., A.L. Beaudet, W.S. Sly, D. Valle, J.B. Stanbury, J.B.Wyngaarden, and D.S. Fredrickson. 2001. The Metabolic and Molecular Bases of Inherited Disease. McGraw-Hill, Health Professions Division, New York.

Stephenson, R.O., Y. Yamanaka, and J. Rossant. 2010. Disorganized epithelial polarity and excess trophectoderm cell fate in preimplantation embryos lacking E-cadherin. Development. 137:3383–3391. https://doi.org/10.1242/dev.050195

Tropak, M.B., S.P. Reid, M. Guiral, S.G. Withers, and D. Mahuran. 2004. Pharmacological enhancement of beta-hexosaminidase activity in fibroblasts from adult Tay-Sachs and Sandhoff Patients. J. Biol. Chem. 279:13478–13487. https://doi.org/10.1074/jbc.M308523200

Valstar, M.J., G.J.G. Ruijter, O.P. van Diggelen, B.J. Poorthuis, and F.A. Wijburg. 2008. Sanfilippo syndrome: A mini-review. J. Inherit. Metab. Dis. 31:240–252. https://doi.org/10.1007/s10545-008-0838-5

Viana, G.M., D.A. Priestman, F.M. Platt, S. Khan, S. Tomatsu, and A.V. Pshezhetsky. 2020. Brain pathology in mucopolysaccharidoses (MPS) patients with neurological forms. J. Clin. Med. 9:396. https://doi.org/10.3390/jcm9020396

Link between chapter 2 and chapter 3

In the previous chapter, we demonstrated that disrupted catabolism of HS in the brain of MPS IIIC mice (*Hgsnat*^{P304L} and *Hgsnat-Geo*) causes multifaceted pathological responses that include neuroinflammation, impairment of autophagy, neuronal accumulation of misfolded proteins, and synaptic defects. We described how this gray matter pathology contributes to cognitive deterioration in MPS IIIC mouse models and revealed that synaptic deficits play a key role in the pathophysiology of the disease. In addition, studies conducted by other groups have reported that functional impairment in MPS III patients and animal models is correlated with cortical and cerebellar atrophy, ventricular volume increase, and other abnormalities in brain structure that can be detected by CT or MRI scans. This suggests that appearance of clinical neurological symptoms is associated with pathological grey matter lesions, including neuronal loss [186, 187]. However, much less is known about white matter injuries and, in particular, demyelination in patients with MPS III. Although several case reports have shown the presence of diffuse high-intensity signals in the white matter of MPS IIIA and IIIB patients [178, 179], other studies have reported the absence of white-matter lesions in most MPS III cases [188].

Despite the fact that white and grey matter pathologies are typically viewed as distinct phenomena, they are often interconnected. In many cases, neuronal pathologies affect both the grey and white matter regions. Since neurons have cell bodies and dendrites in the grey matter and their axons in the white matter, damage to the grey matter often affects the white matter near the injury site. Thus, our next research aim was to study whether white matter injury also plays a role in the pathophysiology of MPS III. Our results described in the next chapter, reveal that persistent demyelination is a key component of CNS pathology in MPSIIIC and most likely of other diseases of the MPS III spectrum.

Chapter 3

Severe Central Nervous System Demyelination in Sanfilippo Disease

CHAPTER 3:Severe Central Nervous System Demyelination in Sanfilippo Disease

Mahsa Taherzadeh[1, 2], Erjun Zhang [1], Irene Londono[1], Sheng-Kwei Song[3], Sophie Wang[4], Jonathan D. Cooper[4], Timothy E. Kennedy[2,5], Carlos R. Morales[2], Zesheng Chen[1], Gregory A. Lodygensky[1] and Alexey V. Pshezhetsky[1, 2]

[1]Department of Pediatrics, Centre Hospitalier Universitaire Sainte-Justine Research Centre, University of Montreal, Montreal, QC, Canada;

[2]Department of Anatomy and Cell Biology, McGill University, Montreal, QC, Canada;

[3]Department of Radiology, Washington University School of Medicine, St. Louis, MO, USA.

[4]Pediatric Storage Disorders Laboratory (PSDL), Departments of Pediatrics, Genetics and Neurology, Washington University School of Medicine, St. Louis, MO, USA.

[5]Department of Neurology and Neurosurgery, Montreal Neurological Institute, McGill University, Montreal, QC, Canada

Corresponding author:
Alexey V. Pshezhetsky
CHU Sainte-Justine
3175 Côte Ste-Catherine, Montréal (QC) H3T 1C5 – Canada
Tel. (514) 345-4931/2736,
E-Mail: alexei.pchejetski@umontreal.ca

3.1. Abstract

Neurodegeneration and chronic progressive neuroinflammation are well-documented in neurological lysosomal storage diseases, including Sanfilippo disease or mucopolysaccharidosis III (MPS III). Since chronic neuroinflammation has been linked to white matter tract pathology and defects in axonal transmission, we analysed axonal myelination and white matter density in the mouse model of MPS IIIC and human post-mortem brain samples from MPS IIIA, C, and D patients. Analyses of corpus callosum (CC) and spinal cord tissues by immunohistochemistry revealed substantially reduced levels of myelin-associated proteins including Myelin Basic Protein, Myelin Associated Glycoprotein, and Myelin Oligodendrocyte Glycoprotein. Furthermore, ultrastructural analyses revealed disruption of myelin sheath organization and reduced myelin thickness in the brains of MPS IIIC mice and human MPS IIIC patients compared to healthy controls. Oligodendrocytes (OLs) in the CC of MPS IIIC mice were scarce, while examination of the remaining cells revealed numerous enlarged lysosomes containing heparan sulfate, GM3 ganglioside or "zebra bodies" consistent with accumulation of lipids and myelin fragments. In addition, OLs contained swollen mitochondria with largely dissolved cristae, resembling those previously identified in the dysfunctional neurons of MPS IIIC mice. When brains of 7-month-old MPS IIIC mice were analysed by ex-vivo Diffusion Basis Spectrum Imaging to assess microarchitectural changes in the corpus callosum, we found compelling signs of demyelination (26% increase in radial diffusivity) and tissue loss (76% increase in hindered diffusivity). Our findings demonstrate an import role for white matter injury in the pathophysiology of MPS III. Moreover, this study reveals specific parameters and brain regions for MRI analysis, a crucial non-invasive method to evaluate disease progression and therapeutic response in neurological lysosomal storage diseases.

3.2. Abbreviations

APC (CC-1): Adenomatous polyposis coli (APC) clone CC1

ARSA: Arylsulfatase A

BSA: Bovine serum albumin

CC: Corpus callosum

CCAC: Canadian Council on Animal Care

CNS: Central Nervous System

CT-scan: Computed tomography-scan

DBSI: Diffusion Basis Spectrum Imaging

DTI: Diffuse tension imaging

EGFP: Enhanced green fluorescent protein

EM: Electron microscopy

GAG: Glycosaminoglycan

GALC: β-galactocerebrosidase

GNS: N-acetylglucosamine-6-sulfate sulfatase

HGSNAT: Heparan sulphate acetyl-CoA: α-glucosaminide N-acetyltransferase

HS: Heparan sulphate

IHC: Immunohistochemistry

KI: Knock-in

LAMP: Lysosomal associated membrane protein

LSD: Lysosomal storage disorder

MAG: Myelin-associated glycoprotein

MBP: Myelin basic protein

MLD: Metachromatic leukodystrophy

MOG: Myelin oligodendrocyte glycoprotein

MPS: Mucopolysaccharidosis

MRI: Magnetic resonance imaging

NAGLU: N-acetyl-α-D-glucosaminidase

NF-M: Neurofilament medium chain

NPC: Niemann-Pick disease type C

OCT: Optimum cutting temperature

OL: Oligodendrocyte

Oligo2: Oligodendrocyte transcription factor2

PFA: Paraformaldehyde

SC: Spinal cord

SGSH: N-sulfoglucosamine sulfohydrolase

SSC: Somatosensory cortices

TEM: Transmission electron microscopy

WT: Wild type

3.3. Introduction

About two-thirds of patients diagnosed with Lysosomal Storage Diseases (LSDs), a group of inherited metabolic disorders affecting lysosomal catabolism, show neurological symptoms and/or have pathological changes in the central nervous system (CNS) (reviewed in [1, 2]). Two of such disorders, Krabbe disease, caused by deficiency of β-galactocerebrosidase (GALC), and Metachromatic leukodystrophy (MLD), caused by deficiency of arylsulfatase A (ARSA), belong to the class of leukodystrophies, manifesting with fundamental abnormalities in the CNS, including white matter pathology and progressive degeneration of myelin sheaths (reviewed in [3]). Progressive myelin defects in these disorders are believed to be caused by two specific sphingolipids accumulating in the brains of affected patients, galactosylceramide also known as psychosine in the case of Krabbe disease and sulfatide in the case of MLD (reviewed in [3]). Both galactosylceramide and sulfatide are important components of myelin sheaths and are generated by myelin-producing cells, oligodendrocytes (OLs) in CNS, and Schwann cells in the peripheral nervous system. However, when the levels of galactosylceramide and sulfatide are drastically increased, as a result of genetic deficiencies of GALC and ARSA, respectively, they become highly toxic for OLs and Schwann cells. Because of progressive myelin loss, both Krabbe and MLD patients, especially those having an infantile-onset form of the disease caused by complete or almost complete deficiencies of the enzymes involved, manifest with a severe neurological impairment and deterioration leading ultimately to death before the age of 5 years [4-6]. In both Krabbe disease and MLD, MRI brain imaging was especially instrumental for the identification and characterization of white matter defects. In particular, extensive white matter defects were found in centrum semiovale, corpus callosum, and middle cerebellar peduncles of Krabbe patients by diffuse tension imaging (DTI) [7]. In infantile MLD patients, hyperintensity of T2-weighted

MRI signals was observed in corpus callosum and in parieto-occipital regions suggesting defects in periventricular and central white matter [8]. Signs of demyelination (or delayed myelination) have been also detected by MRI in patients with multiple sulfatase deficiency, most likely due to the secondary deficiency of ARSA and the storage of sulfatide [9].

Since glycosphingolipids are critical components of myelin sheaths [10, 11], demyelination and white matter pathology have been also reported in patients affected with lysosomal glycosphingolipidoses, including Fabry disease, neurological forms of Gaucher disease (reviewed in [3]) and, most recently, infantile forms of Niemann-Pick disease type C (NPC) [12]. In the latter case, demyelination was proposed to results from the secondary storage of GM3 ganglioside in the lysosomes of OLs leading to their dysfunction [13]. White matter abnormalities have also been reported in patients diagnosed with other LSDs involving ganglioside accumulation, GM1 gangliosidosis [14] and GM2 gangliosidosis/Tay-Sachs disease [15].

Mucopolysaccharidosis type III (MPS III) or Sanfilippo disease, remains the most prevalent untreatable neurological lysosomal disorder (reviewed in [16]). MPS III is a spectrum of four conditions (MPS IIIA-D), caused by defects in the genes encoding the enzymes involved in lysosomal degradation of a glucosamine, heparan sulfate (HS). In MPS III, HS accumulates in brain tissue and causes neuronal dysfunction and death leading to neuropsychiatric problems, developmental delays, childhood dementia, blindness and death during the second decade of life (reviewed in [16]). MPS IIIA was found to be caused by defects in N-sulfoglucosamine sulfohydrolase (SGSH) [17], MPS IIIB, by defects in N-acetyl-α-D-glucosaminidase (NAGLU) [18], MPS IIIC, by defects in acetyl-CoA:alpha-glucosaminide N-acetyltransferase (HGSNAT) [19], and MPS IIID, by defects in N-acetylglucosamine-6-sulfate sulfatase (GNS) [20].

Previous studies involving MPS III patients and animal models revealed that disrupted catabolism of HS in the brain causes multifaceted pathological response, from neuroinflammation and oxidative stress to impairment of autophagy, neuronal accumulation of misfolded proteins, GM2 or GM3 gangliosides, and synaptic defects. Together, these processes contribute to neuronal dysfunction and neurodegeneration which lead to cognitive and motor decline in patients (reviewed in [16]). Importantly, in most Sanfilippo patients the rate of progressive functional impairment correlates with that of cortical and cerebellar atrophy, ventricular volume increase and other brain abnormalities, detected by computed tomography-scan (CT-scan) or magnetic resonance imaging (MRI), suggesting that these symptoms are associated with neuronal loss and pathological grey matter lesions (reviewed in [21, 22]). Much less is known, however, about the white matter defects and, in particular, axonal pathology and demyelination in the MPS III patients. While some case reports have indicated the presence of diffuse high-intensity signal in the white matter of MPS IIIA and IIIB patients [23, 24], other studies reported an absence of white-matter lesions in most MPS III cases [25].

Here, for the first time, we report that progressive severe demyelination is a hallmark of CNS pathology in both human MPS IIIC patients and the mouse *Hgsnat*^{P304L} model [26] of the disease. We also demonstrate that, in the brains of MPS IIIC mice, the disruption of myelination results from reduced OL numbers and substantial pathological changes in OL morphology.

3.4. Materials and Methods

3.4.1. Study approval

All animal experiments were approved by the Animal Care and Use of CHU Ste-Justine Research Ethics Committee (approval numbers 2020-2658 and 2022-3452) and performed in accordance with the Canadian Council on Animal Care guidelines. Ethical approval for the research involving human tissues was granted by Research Ethics Board of CHU Ste-Justine.

3.4.2. Animals

The knock-in mouse model of MPS IIIC, *Hgsnat*^{P304L}, expressing the HGSNAT enzyme with human missense mutation P304L, on a C57BL/6J genetic background, has been previously described [189].

Mouse studies were performed in accordance with the Canadian Council on Animal Care (CCAC) in the CCAC-accredited animal facility of the CHU Ste-Justine. All mice were housed in an enriched environment in poly-carbonate cages under 12:12 h light:dark cycles in a temperature- and humidity-controlled room. Mice had access to a normal rodent chow and water *ad libitum*. The animals were bred as homozygous couples for both WT and *Hgsnat*^{P304L} strains. Experiments were conducted using both male and female mice and the data analyzed to identify potential differences between sexes. Since no differences between sexes were observed in the experiments, the data for males and females were combined.

3.4.3. Analysis of human brain tissues

Post-mortem brain tissues from two patients with MPS IIIC, fixed in 10% buffered formalin, were collected for neuropathological examination. The first brain was provided by the Anatomic Gift Registry while the second brain was donated for research purposes by the parents

of the patient. Brain tissues of age-matched patients without CNS pathology were provided, together with clinical descriptions, by the Neuromax biobank of CHU Sainte-Justine.

The brains underwent gross examination by a neuropathologist (ZC), and representative regions were sampled and processed for paraffin embedding. Four-µm sections were cut from the formalin fixed paraffin embedded (FFPE) blocks, stained with Haematoxylin-Eosin (H&E), Saffron (HES), periodic acid-Schiff stain (PAS) and Luxol Fast Blue (LFB), and examined under the light microscope.

In addition, frozen or paraformaldehyde (PFA) fixed cerebral cortices from MPS patients (1 case of MPSIIIA, 1 case of MPSIIIC and 1 case of MPSIIID) and age-matched controls with no pathological changes in the central nervous system were provided by NIH NeuroBioBank (project 1071, MPS Synapse). Upon arrival to the laboratory, the samples were embedded in Tissue-Tek® optimum cutting temperature (OCT, Sakura, USA) compound and stored at -80ºC. 40 µm thick brain sections were cut and stored in cryopreservation buffer (0.05 M sodium phosphate buffer pH 7.4, 15% sucrose, 40% ethylene glycol) and stored at -20ºC until immunohistochemical labelling.

3.4.4. Immunohistochemistry

Mice were perfused with 4% PFA in PBS. Following perfusion, brains were isolated and post-fixed in 4% PFA in PBS overnight. Brains were further incubated in 30% sucrose for 48 h at 4ºC, embedded in OCT, cut into sequential 40 µm-thick coronal cross-sections using a Cryostat Epredia CryoStar NX50, and then kept at -20ºC in cryopreservation buffer (0.05 M sodium phosphate buffer pH 7.4, 15% sucrose, 40% ethylene glycol). For immunofluorescence analysis, brain slices were permeabilized and blocked with 5% bovine serum albumin (BSA), and 0.3% Triton X-100 in PBS for 2 h at room temperature. Sections were then incubated with primary

antibodies, diluted with 1% BSA and 0.1% Triton X-100 in PBS at 4ºC overnight. The antibodies and their dilutions are shown in the Table 1.

Table 1: Antibodies and their dilutions used for immunochemistry

Antigen	Host/Target species	Dilution	Manufacturer
APC (CC-1)	Mouse monoclonal	1:200	Abcam (ab16794)
Olig-2	Rabbit polyclonal	1:200	Sigma-Aldrich (AB9610)
GFAP	Rabbit anti-mouse	1:200	DSHB (8-1E7-s)
CD68	Rabbit polyclonal	1:200	Abcam (ab125212)
Heparan sulfate (10E4 epitope)	Mouse anti-mouse	1:200	AMSBIO (F58-10E4)
Lysosomal-associated membrane protein 1 (LAMP1)	Rat anti-mouse	1: 50	DSHB (ABL-93-s)
Myelin-associated glycoprotein (MAG)	Mouse monoclonal	1:200	Abcam (ab89780)
Myelin Basic Protein (MBP)	Rabbit monoclonal	1:300	Abcam (ab218011)
Myelin oligodendrocyte glycoprotein (MOG)	Rabbit monoclonal	1:500	Abcam (ab233549)
Neurofilament medium chain (NF-M)	mouse anti-mouse	1:200	DSHB (2H3-s)

Mouse brain sections were washed with PBS and counterstained with Alexa Fluor® 488-conjugated goat anti-mouse IgG (A21202), Alexa Fluor® 555-conjugated goat anti-rabbit IgG (A21428), and Alexa Fluor® 633-conjugated goat anti-mouse IgG (A21094) (dilution 1:400, all

from Thermo Fisher Scientific) for 2 h at room temperature. To quench autofluorescence, the mouse brain sections were dipped briefly in TrueBlack® Lipofuscin Autofluorescence Quencher (dilution 1:10, Biotium, 23007) for 1 min, and then washed with PBS. The slides were mounted with Prolong Gold Antifade mounting reagent with DAPI (Invitrogen, P36935) and captured using a Laser scanning confocal microscope (Leica TCS SP8: 20x, 40x, and 63x oil objective, N.A. 1.4). Z-stack projections were conducted with a step size of 0.3 μm to represent images.

For the analysis of spinal cord, adjacent one-in-forty-eight series of 40 μm coronal sections from each mouse were stained on slides using a modified immunofluorescence protocol [28, 29]. Sections were labeled with rat anti-CD68 (1:400, Bio-Rad MCA1957) or rat anti-MBP (1:500, Merck Millipore, MAB386) primary antibodies followed by AlexaFluor546 goat anti-rat (1:500, Invitrogen A11081) for CD68, or AlexaFluor488 goat anti-rat (1:500, Invitrogen A48262) for MBP. Slides were counterstained with TrueBlack Lipofuscin Autofluorescence Quencher (Biotium).

To quantify microgliosis (CD68-positive activated microglia) and myelination (MBP immunoreactivity), semiautomated thresholding image analysis was performed as described previously [28, 29]. This involved collecting slide-scanned images at 10x magnification (Zeiss Axio Scan Z1 Fluorescence Slide Scanner) from each animal. Contours of appropriate anatomical regions were then drawn and images were subsequently analyzed using *Image-Pro Premier* (Media Cybernetics) using an appropriate threshold that selected the foreground immunoreactivity above the background. All thresholding data (CD68 and MBP) were expressed as the percentage of area within each anatomically defined region of interest that contained immunoreactivity above the set threshold for that antigen ("% immunoreactivity").

3.4.5. Image processing and analysis

Unless indicated otherwise, images were processed and quantified using ImageJ 1.50i (National Institutes of Health, Bethesda, MD, USA). Quantification was performed in a double-blind fashion. Three-dimensional images were generated using Imaris (Oxford Instruments, version 9.6) software (Bitplane).

3.4.6. Immunoblotting

Half-brain sections from 6-month-old mice were homogenized in a non-denaturing lysis buffer (50 mM Tris-HCl, pH 7.4, 150 mM NaCl, 1% NP-40, 0.25% sodium deoxycholate, 0.1% SDS, 2 mM EDTA, 1 mM PMSF), supplemented with protease and phosphate inhibitor cocktails (Sigma-Aldrich, cat# 4693132001 and 4906837001). The homogenates were cleared by centrifugation at 13,000 x g at 4ºC for 25 min and the protein concentration in the collected supernatant was measured using a Pierce BCA Protein Assay Kit (Thermo Fisher Scientific). Protein extracts (20 µg of protein for each sample), were incubated in a boiling bath for 10 min and analyzed by SDS-PAGE on 4–20% precast polyacrylamide gradient gel (Bio-Rad, 4561096). Western blot analyses were performed according to standard protocols using antibodies against MBP (1:1000, Abcam,: cat# ab218011), MAG (1:1000, Abcam, cat# ab89780), and α-tubulin (1:2000, DSHB, cat# 12G10) as a control. The immunoblots were revealed by chemiluminescence with SuperSignalWest Pico PLUS (Thermo Fisher Scientific, Waltham, MA, USA). Detected bands were quantified using ImageJ 1.50i software (National Institutes of Health, Bethesda, MD, USA) and normalised for the intensity of the α-tubulin band.

3.4.7. Transmission Electron Microscopy Analysis

To prepare sections for Transmission Electron Microscopy (TEM) analysis, 3 mice from each genotype were anesthetized with sodium pentobarbital (50 mg/kg BW) and perfused with

phosphate-buffered saline (PBS, pH 7.4), followed by 2% paraformaldehyde / 2.5% glutaraldehyde in 0.1 M sodium cacodylate buffer, pH 7.4. The brains were incubated in the same fixative for 24 h at 4°C, washed with MilliQ H_2O, and post-fixed with 1% osmium tetroxide, 1.5% potassium ferrocyanide in H_2O for 2 h, at 4°C. The samples were further dehydrated in a graded bath of acetone and MilliQ H_2O with increasing concentrations of 30%, 50%, 70%, 80%, 90%, and 3 x 100% for 8 min. The samples were infiltrated with 100% Epon, embedded in a rubber embedding mold, and polymerized in the oven at 60°C for 48 hrs. Once the resin was polymerized, semi-thin (1.0 μm) sections of the corpus callosum were dissected and stained with 1% toluidine blue before being mounted on glass slides and examined with a Leica DMS light microscope to select regions of interest. The sections were cut into ultrathin (70–80 nm) sections, placed on 200 Mesh copper grids, stained with lead citrate, and examined at 80 kV on an FEI Tecnai G2 Spirit (FEI Company, Hillsboro, OR) electron microscope equipped with a Morada CCD digital camera (Olympus, Tokyo, Japan). Micrographs were taken with 2900 x and 4800 x magnification.

To quantify the number of myelinated axons, a minimum of 10 images were analyzed for each animal. All myelinated axons within the counting frame were counted and included in the statistical analysis. Then, for each micrograph, 5 randomly selected axons were used to analyze axonal parameters including axonal diameter, myelin thickness and g-ratio, using ImageJ software.

3.4.8. Preclinical high-field MRI

Two groups of 7-month-old mice (10 WT and 8 MPS IIIC) were imaged using a preclinical scanner at the Cerebral Imaging Centre of the Douglas Mental Health University Institute (Montreal, Canada). Animals were perfused with PBS followed by 4% PFA in PBS, under terminal anesthesia, and brains were carefully removed and immersed in 4% PFA in PBS for 5 h. Brains

were then mounted in a syringe with Fomblin oil for *ex vivo* MR imaging, using a solenoid coil custom-built to fit the syringe.

Imaging was carried out on a 7T Bruker MRI scanner. 2D spin-echo sequences with pulsed gradients were used to acquire diffusion-weighted data. Imaging included 1 b0 and 25 b-values ($0 < b \leq 3000$ s/mm^2) with different directions for each b-value, a field of view 12 mm × 12 mm, resolution, 0.15 × 0.15 × 0.4 mm^3, and TR/TE: 3300 ms/32 ms. DBSI and DIPY-DTI (non-linear algorithm) were used for reconstruction as described [30, 31]. On two consecutive slices, regions of interest (ROI) were manually selected on corpus callosum in color-coded fractional anisotropy (FA) maps extracted from DTI.

3.4.9. Statistical analysis

Statistical analyses were performed using Prism GraphPad 9.3.0. software (GraphPad Software San Diego, CA). The normality for all data was checked using the D'Agostino & Pearson omnibus normality test. Significance of the difference was determined using a Student's t-test, when comparing two groups, and one-way ANOVA test followed by Tukey's multiple comparison test, when comparing more than two groups. Two-way ANOVA followed by Bonferroni or Tukey's post hoc tests was used for two-factor analysis. The Mann-Whitney test was used on metrics extracted from DBSI when normality was not attainted. A P-value less than 0.05 was considered significant.

3.5. Results

3.5.1. Massive reduction of myelin-associated proteins in MPS IIIC mice

Chronic progressive neuroinflammation and microgliosis (increased brain levels of proinflammatory activated microglia) are well documented in lysosomal storage diseases including MPS IIIC. As chronic neuroinflammation and microglial activation can alter white

matter tracts and interrupt communication between neurons [32], we hypothesized that pathological changes in axon tracts might include a loss of myelin with decreased white matter density and contribute to CNS pathology in MPS IIIC patients. To investigate this hypothesis, we examined the integrity of myelination in our recently described *Hgsnat*^{P304L} mouse model expressing the mutant HGSNAT Pro304Leu variant [26]. These mice reveal progressive pathological alterations in the cortical and subcortical gray matter, including pronounced synaptic defects, astromicrogliosis and neurodegeneration [26].

To assess for the presence of myelination defects, we first examined the levels of myelin-associated proteins, Myelin Basic Protein (MBP), Myelin Associated Glycoprotein (MAG) and Myelin Oligodendrocyte Glycoprotein (MOG), in the somatosensory cortices (SSC) and corpus callosum (CC) by immunohistochemical analysis of brain sections of 6-month-old *Hgsnat*^{P304L} mice compared with WT mice matched for age, sex, and genetic background. The immunoreactivity detected for each protein was significantly reduced in the CC of MPS IIIC mice at 6 months of age compared with WT counterparts (Figure 1A-C). In SSC, levels of MAG were significantly reduced, while nonsignificant trends toward a decrease were observed for MBP and MOG (Figure 1D-F). The axonal marker, Neurofilament medium chain protein (NF-M), also showed a non-significant trend toward a decrease in both areas. Together, these results were consistent with white matter injury in the brain of 6-month-old *Hgsnat*^{P304L} mice.

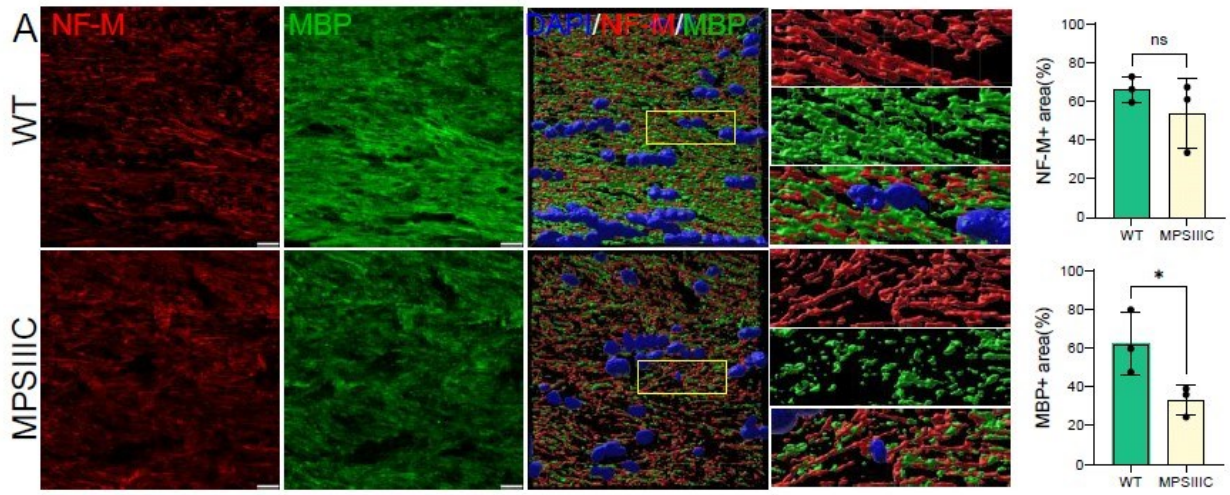
A
NF-M
MBP
DAPI/NF-M/MBP
WT
MPSIIIC
NF-M+ area(%)
MBP+ area(%)
ns
*
WT
MPSIIIC

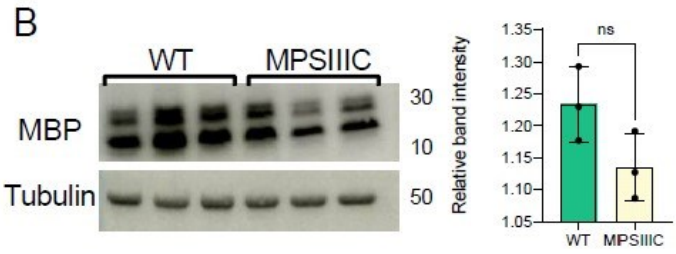
B
WT
MPSIIIC
MBP
Tubulin
30
10
50
Relative band intensity
ns
WT
MPSIIIC

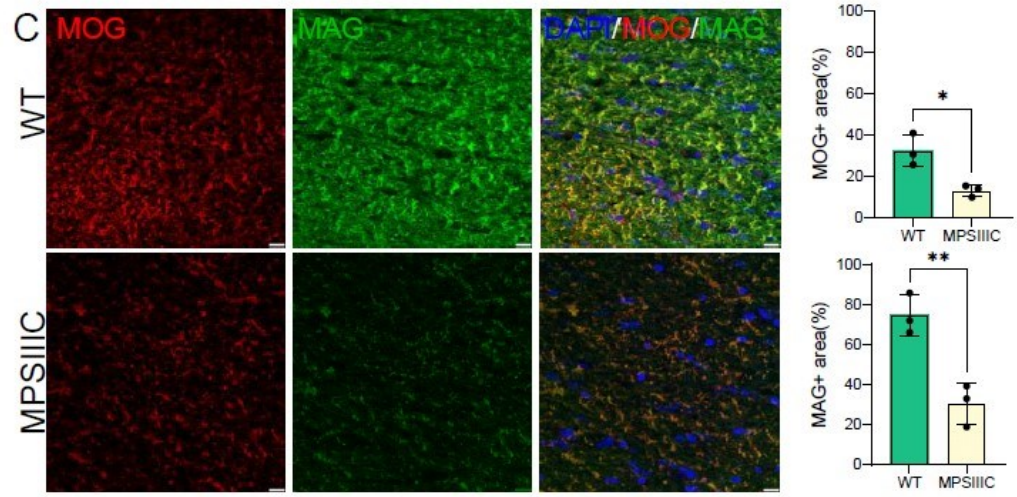
C
MOG
MAG
DAPI/MOG/MAG
WT
MPSIIIC
MOG+ area(%)
MAG+ area(%)
*
**
WT
MPSIIIC

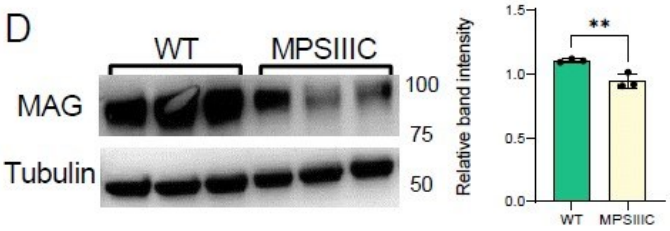
D
WT
MPSIIIC
MAG
Tubulin
100
75
50
Relative band intensity
**
WT
MPSIIIC

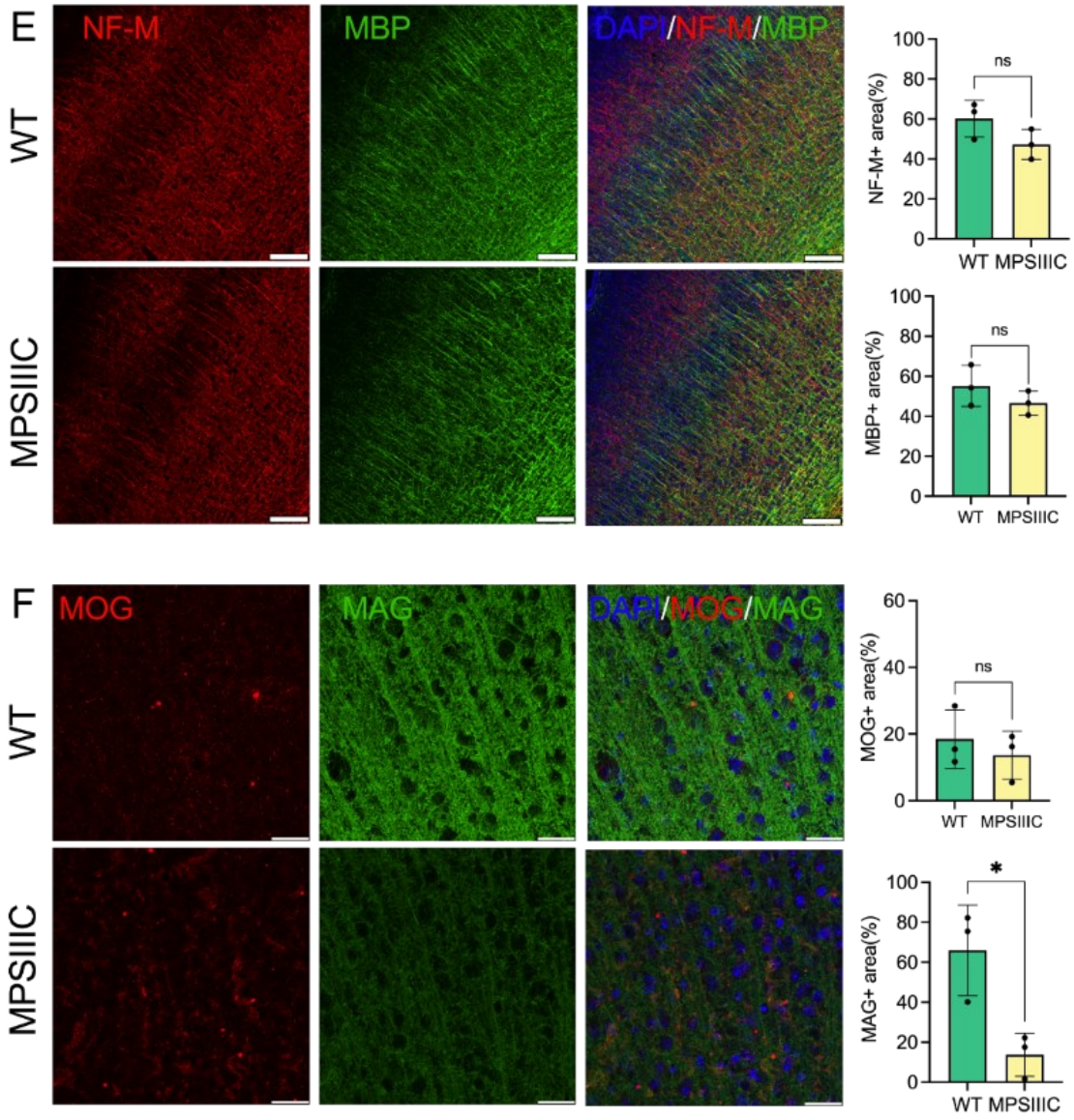

Figure 1. Myelin-associated proteins MBP, MAG, and MOG are reduced in the CC of MPSIIIC, compared with WT mice, suggesting myelin loss. (A) Panels show representative images of the CC of 6-month-old WT and MPSIIIC mice (left) and three-dimensional (3D) enlarged images of the areas marked by yellow boxes (right). MBP+ areas (green) on the surface of neurofilament medium chain (NF-M)+ axons (red) are reduced. The graphs show quantification of MBP+ and NF-M+ areas by ImageJ software. **(B)** Immunoblotting shows trend for reduction of MBP in the total brain homogenates of MPSIIIC mice. **(C)** IHC analysis reveals a reduction of MAG and MOG in CC of MPSIIIC mice compared with WT mice. Graphs show quantification of MAG+ and MOG+ stained area by ImageJ software. **(D)** Western blots of total protein extracts from brains of 6-month-old MPSIIIC mice confirm reduction of MAG. The graph shows intensities of MAG immunoreactive bands, quantified with ImageJ software and normalized by the

intensity of tubulin immunoreactive bands. **(E)** No significant differences in MBP labelling in the cortex are detected by IHC between MPSIIIC and WT mice. **(F)** Level of MAG (green) labelling is reduced in the cortex of MPSIIIC compared with WT mice, while MOG (red) labelling shows only a non-significant trend for decrease. In all panels DAPI (blue) was used as a nuclear counterstain and scale bars equal 10 μm. All graphs show individual data, means and SD obtained for 3 mice per genotype. P-values were calculated using an unpaired t-test (*, $p<0.05$; **, $p<0.01$, ns, nonsignificant).

In the spinal cord of 6-month-old MPSIIIC mice, immunostaining for the microglial marker CD68 revealed numerous intensely stained microglia with enlarged cell soma in the grey and white matter, while age matched WT mice revealed only few lightly stained microglia with a small cell soma (Figure 2). Immunostaining for MBP revealed intense immunoreactivity within the spinal white matter of mice of both genotypes. Thresholding image analysis confirmed that significantly more CD68 immunoreactivity was present in both the dorsal and ventral grey matter of MPSIIIC mice. We detected a moderate yet significant reduction in the intensity of MBP immunoreactivity in the dorsal funiculus of MPSIIIC mice, but no significant difference in MBP immunoreactivity between genotypes in the ventral funiculus (Figure 2).

3.5.2. Reduction of myelin thickness and axon degeneration in the CC of MPSIIIC mice

To determine if changes in the amounts of myelin associated proteins in the CC coincided with alterations in myelin structure, three MPSIIIC and three age/sex matched WT mice were examined at the ultrastructural level by TEM followed by quantification of axon diameters and myelin thickness. We detected a relative scarcity of myelinated axonal profiles in MPSIIIC mice, and the axons that were myelinated had an average g-ratio (axon diameter/myelinated fiber diameter) of 0.803 ± 0.134, that was significantly higher than the one for WT mice, 0.76 ± 0.15, indicating a reduced thicknesses of myelin sheaths (Figure 3). Scatter plots of g-ratios vs axonal

diameter indicated hypomyelination of axons of all sizes in MPSIIIC mice. At the same time, no difference in the mean axonal diameters was detected between WT and mutant mice.

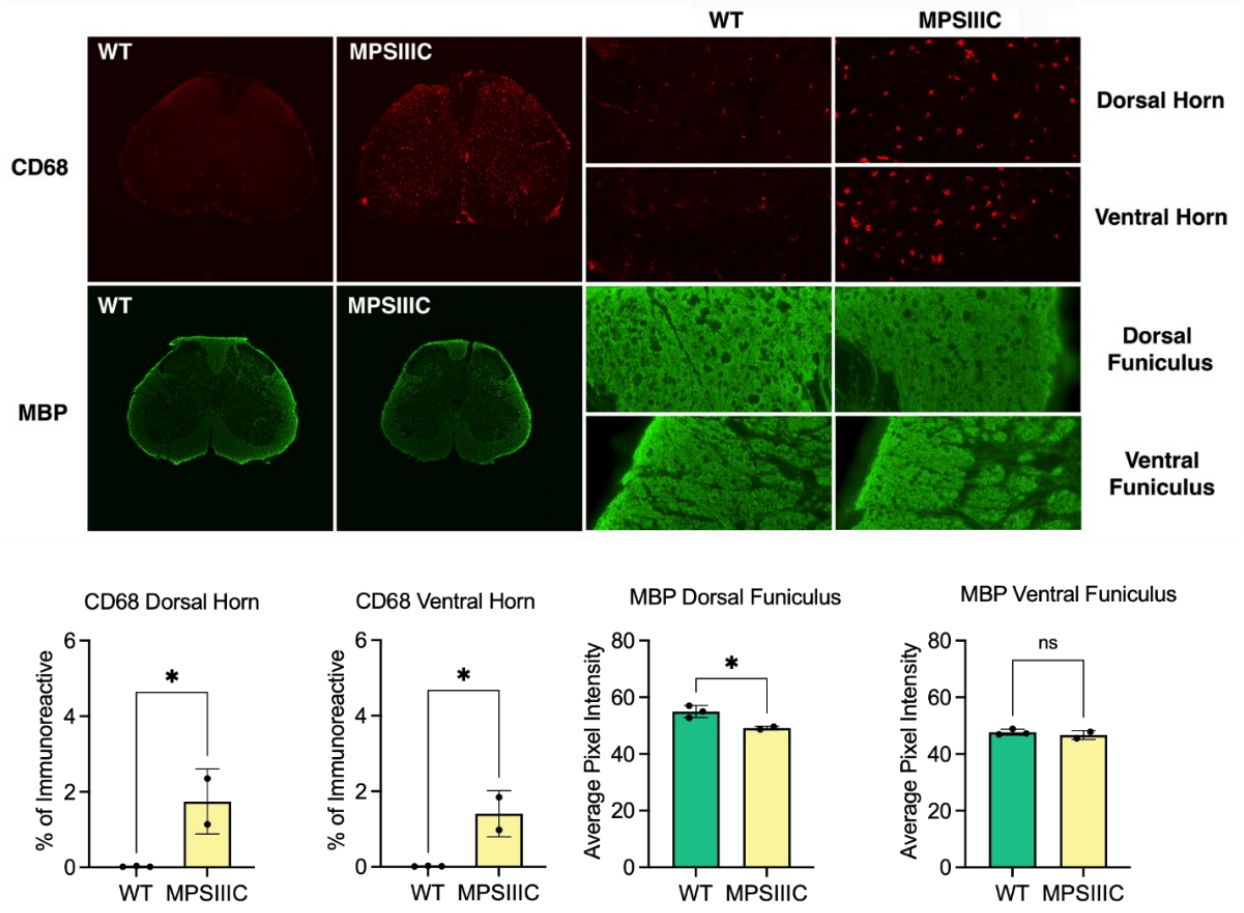

Figure 2. Microglial activation and white matter changes in the lumbar spinal cord of 6-month-old MPSIIIC mice. Representative images of immunostaining for the microglial marker CD68 (red) and myelin basic protein (MBP green) in the lumbar cord of 6-month-old *Hgsnat*^{P304L} (MPSIIIC) mice and age-matched wild type (WT) control mice. Numerous CD68 immunoreactive microglia with enlarged cell soma are present in the gray and white matter of the dorsal and ventral horn of MPSIIIC mice but are virtually absent in WT mice at this age. Compared to age-matched control WT mice, MBP immunoreactivity is moderately reduced in the dorsal funiculus of 6-month-old MPSIIIC mice, but unchanged in the ventral funiculus. Quantitative thresholding image analysis confirmed these observations revealing significantly elevated CD68 immunoreactivity in the dorsal and ventral horn of 6-month-old HSGNAT KI vs. age-matched WT mice. Similarly there was significantly less MBP immunoreactivity in the dorsal funiculus of 6-month-old HSGNAT KI vs. age-matched WT mice, but no significant change in the ventral funiculus.

All graphs show individual data, means and SD obtained for 2 mice per genotype. P-values were calculated using an unpaired t-test (*, $p<0.05$; **, $p<0.01$, ns, nonsignificant).

Notably, in control animals, myelin thickness showed the expected positive correlation with axon diameter ($R2 = 0.25$), while, in MPSIIIC mice, myelin thickness did not significantly correlate with axon diameter ($R2 = 0.08$).

TEM examination revealed defects in myelination along axons in CC (empty myelin sheath and splits in the compact myelin) with axonal swelling (spheroids) containing accumulated storage and/or transport vesicles. Similar swellings that coincided with microtubule defects were previously reported by us in hippocampal CA1 pyramidal neurons and in cultured neurons of another MPSIIIC model (*Hgsnat-Geo* mice) along with the evidence that the swellings disrupt synaptic vesicle precursor transport along axons [36].

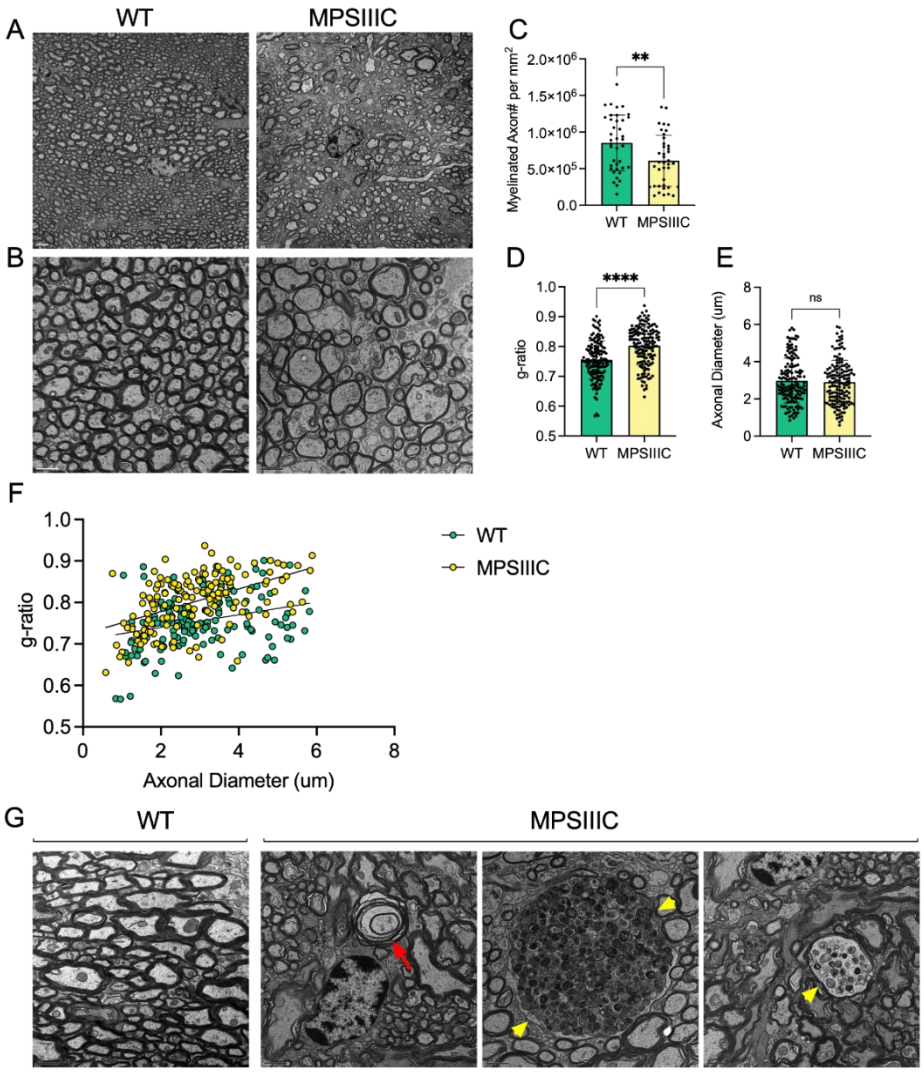

Figure 3. Transmission electron microscopy reveals reduced myelin thickness, decreased number of myelinated axons, structural defects in myelin sheaths and axonal swelling in the corpus callosum of MPSIIIC mouse. Panels **(A)** and **(B)** show representative TEM images of CC of 6-month-old MPSIIIC and WT mice taken at lower (2000X) and higher (4000X) magnifications, respectively. Scale bars equal 2 mm **(A)** and 1 mm **(B)**. **(C)** The graph shows quantification of myelinated axon density (mean number of myelinated axons per square millimeter) in CC of WT and MPSIIIC mice. **(D)** G-ratio values for myelinated axons in CC of MPSIIIC mice are significantly higher than those for axons of WT mice. **(E)** Axonal diameters are similar in WT and MPSIIIC mice. **(F)** Scatter plot depicting g-ratio versus axonal diameter values. Graphs in panels **(D-E)** show individual values, means and SD and in the panel **(F)** individual values and linear regression plots. Sections from 3 mice per genotype (50 randomly selected axons per mouse) were analyzed. **(G)** Electron micrographs show an absence of pathological changes in the axons of WT

mice. In contrast, degenerated axons with empty myelin sheath and split myelin (red arrow), as well as large axonal swellings containing accumulating vesicles (yellow arrowheads), are observed in MPSIIIC mice.

3.5.3. Activated microglia in CC of MPSIIIC mice accumulate myelin debris

Microglia phagocytose myelin sheaths to modify myelination and preserve its integrity and function [33, 34]. To verify if this process is altered in the brain tissues of MPS IIIC mice, we analysed them using IHC and detected MBP-positive puncta in ILB4-positive (Figure 4A) and CD68-positive (Supplementary figure S1) microglia in the CC. This puncta was not present in the tissues of WT mice. Moreover, MBP-positive puncta in microglia localized inside enlarged LAMP1-positive vacuoles, confirming lysosomal accumulation of MBP fragments in these cells. The IHC results were confirmed by TEM examination revealing that microglia in the CC of MPS IIIC mice were enlarged and contained vacuoles with so called “zebra bodies”, consistent with myelin accumulation (Figure 4B, boxed). We also detected electrolucent vacuoles most probably containing HS and other glycosaminoglycans (Figure 4B, arrows) [35]. In the WT mice, the microglia remained small and did not contain enlarged vacuoles (Figure 4B). Notably, CD68-positive activated microglia were detected in MPSIIIC brain as early as P25, when the levels of MBP in the CC are still intact (Supplementary figure S2), suggesting that demyelination was likely not caused by direct action of the immune cells.

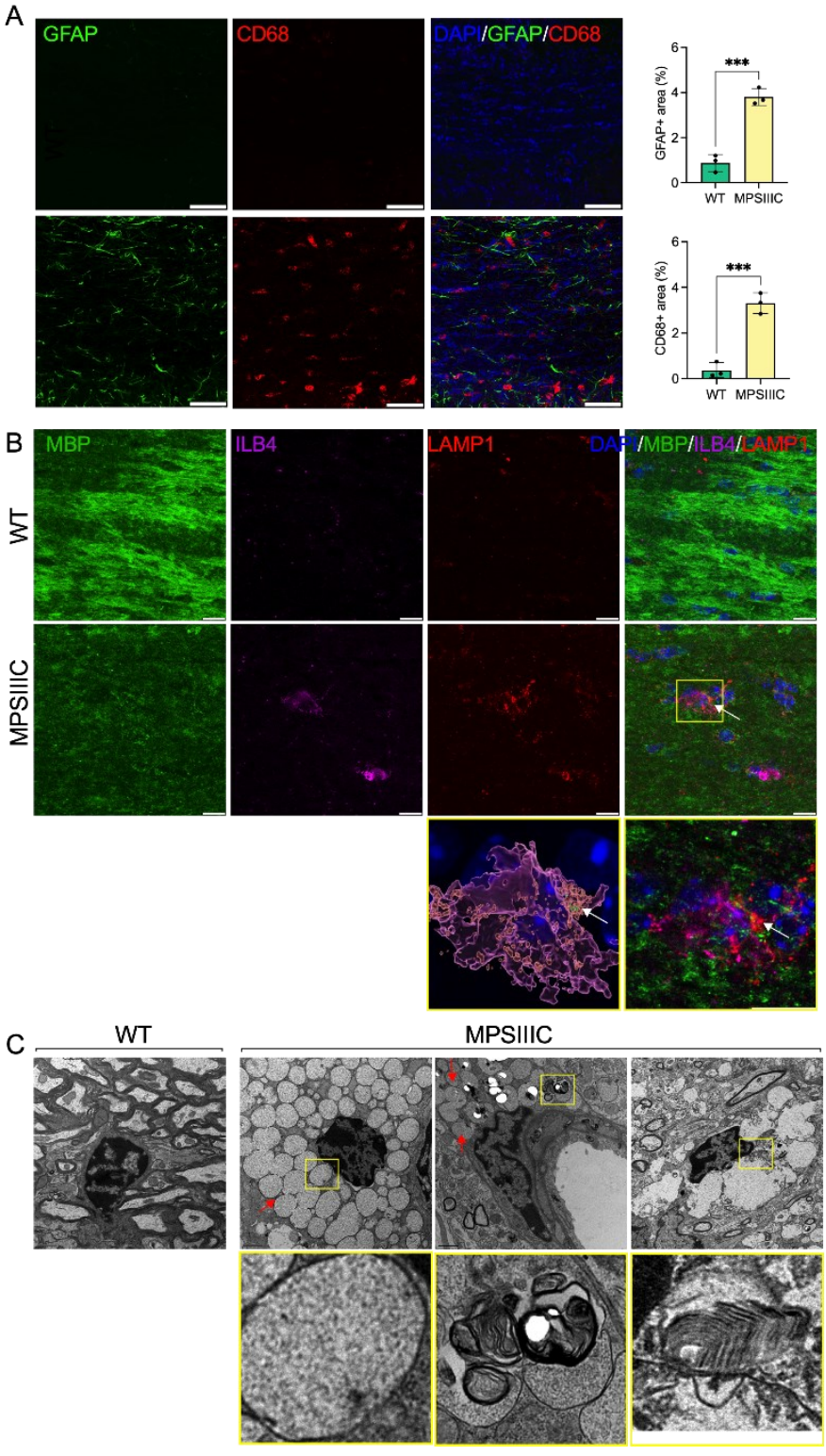

Figure 4. Microglia in CC of MPSIIIC but not of WT mice show lysosomal accumulation of myelin fragments and GAGs. (A) Panels show representative confocal microscopy images of CC tissue of 6-

month-old WT and MPSIIIC mice labelled with antibodies against GFAP (green) and CD68 (red), markers for astrocytes and activated microglia, respectively. DAPI (blue) was used as a nuclear counterstain. Scale bar equals 50 μm. **(B)** Panels show representative confocal microscopy images of the CC of 6-month-old MPSIIIC and WT mice labelled with fluorescent isolectin b4 (ILB4, purple), and antibodies against MBP (green), and LAMP1 (red). DAPI (blue) was used as a nuclear counterstain. Scale bars equal 10 μm. The enlarged confocal image of the boxed area shows the colocalization of MBP+ puncta with LAMP1+ lysosomal marker inside ILB4+ activated microglia in the CC of a MPSIIIC mouse. 3D reconstruction shows that MBP+ puncta (arrows) are located inside the LAMP1+ lysosome of a microglia cell. **(C)** Both electron-lucent vacuoles (arrow) consistent with HS storage, and those containing "zebra bodies", indicative of myelin debris (boxed), are detected in microglia in the CC of MPSIIIC mouse. Microglia in the CC of WT mouse are small and do not contain storage vacuoles. Scale bar equals 1 μm.

3.5.4. Oligodendrocyte dysfunction in MPSIIIC mice

To understand the mechanism underlying demyelination, we analyzed the abundance and morphological phenotype of OLs in the CC of MPSIIIC and WT mice. To study oligodendrocyte maturation, we performed co-immunostaining of the brain tissues with antibodies against Olig2, a marker expressed both by oligodendrocytes (OLs) and oligodendrocyte precursor cells (OPCs), and antibodies against CC1, a marker of mature OLs. Our data (Figure 5A and Supplementary figure S3) showed that the majority of CC1-positive cells in the CC of WT mice were co-labelled for Olig2. On the other hand, in the brains of MPSIIIC mice, we found a significant reduction of CC1-positive, Oligo2-positive as well as Olig2/CC1 double-positive cells suggesting either the reduced production of OLs or their increased degeneration (Figure 5A and Supplementary figure S3). The reduced number of OLs coincided with severe morphological changes observed in most of the remaining cells. Specifically, the number and size of LAMP1-positive vacuoles in OLs were increased, consistent with a lysosomal storage phenotype (Figure 5B). Our previous studies revealed that HGSNAT deficiency and impairment of HS catabolism resulted in intralysosomal accumulation of both primary (HS) and secondary (gangliosides) storage materials in neurons and microglia in the brains of MPSIIIC mice [35, 36].

To investigate if both compounds are also stored in OLs of MPSIIIC mice, brain tissues were studied by immunohistochemistry using the 10E4 monoclonal antibody, specific for a native HS epitope, and the anti-GM3 ganglioside monoclonal antibody. These experiments revealed increased storage of both HS and GM3 gangliosides in multiple Oligo2-positive cells (Figure 5C and Supplementary figure S4). TEM analysis further confirmed that OLs in the CC of MPSIIIC mice (identified by the shape and pattern of their nuclei and the presence of multiple microtubular structures in the cytoplasm [37]) contained multiple storage vacuoles. Some vacuoles exhibited an electro-lucent content compatible with storage of HS [38] (marked with red arrowheads and boxed in Figure 5D), while others contained zebra bodies suggesting storage of myelin fragments or/and sphingolipids [39] (marked with yellow arrowheads and boxed in Figure 5D). In addition, OLs in the CC of MPSIIIC mice contained swollen mitochondria with largely dissolved cristae (marked with asterisks in Figure 5D), similar to those we have previously identified in the neurons of MPSIIIC mice [35].

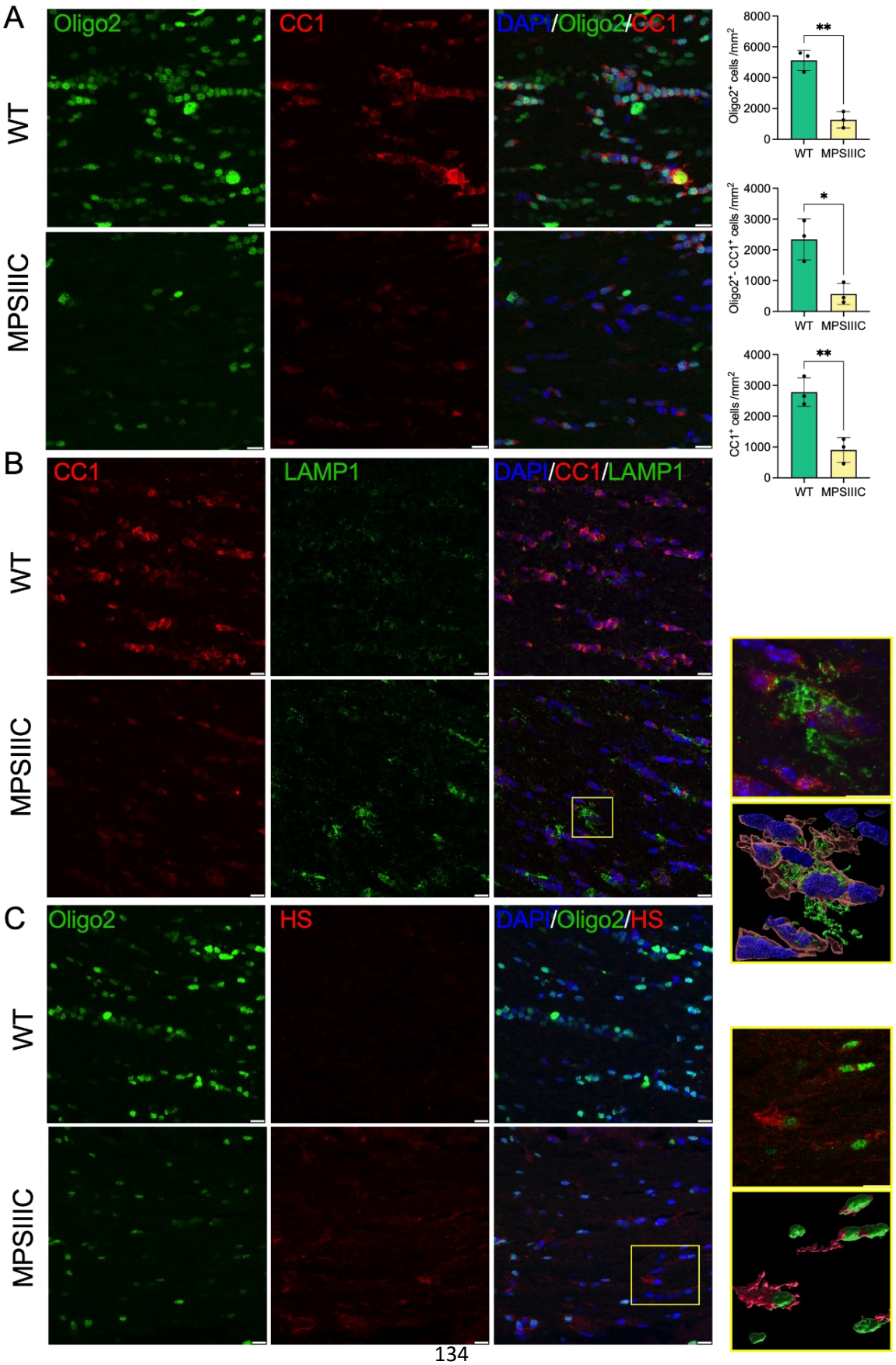
A
Oligo2
CC1
DAPI/Oligo2/CC1
WT
MPSIIIC
Oligo2+ cells /mm2
8000
6000
4000
2000
0
**
WT
MPSIIIC
Oligo2+- CC1+ cells /mm2
4000
3000
2000
1000
0
*
WT
MPSIIIC
CC1+ cells /mm2
4000
3000
2000
1000
0
**
WT
MPSIIIC
B
CC1
LAMP1
DAPI/CC1/LAMP1
WT
MPSIIIC
C
Oligo2
HS
DAPI/Oligo2/HS
WT
MPSIIIC

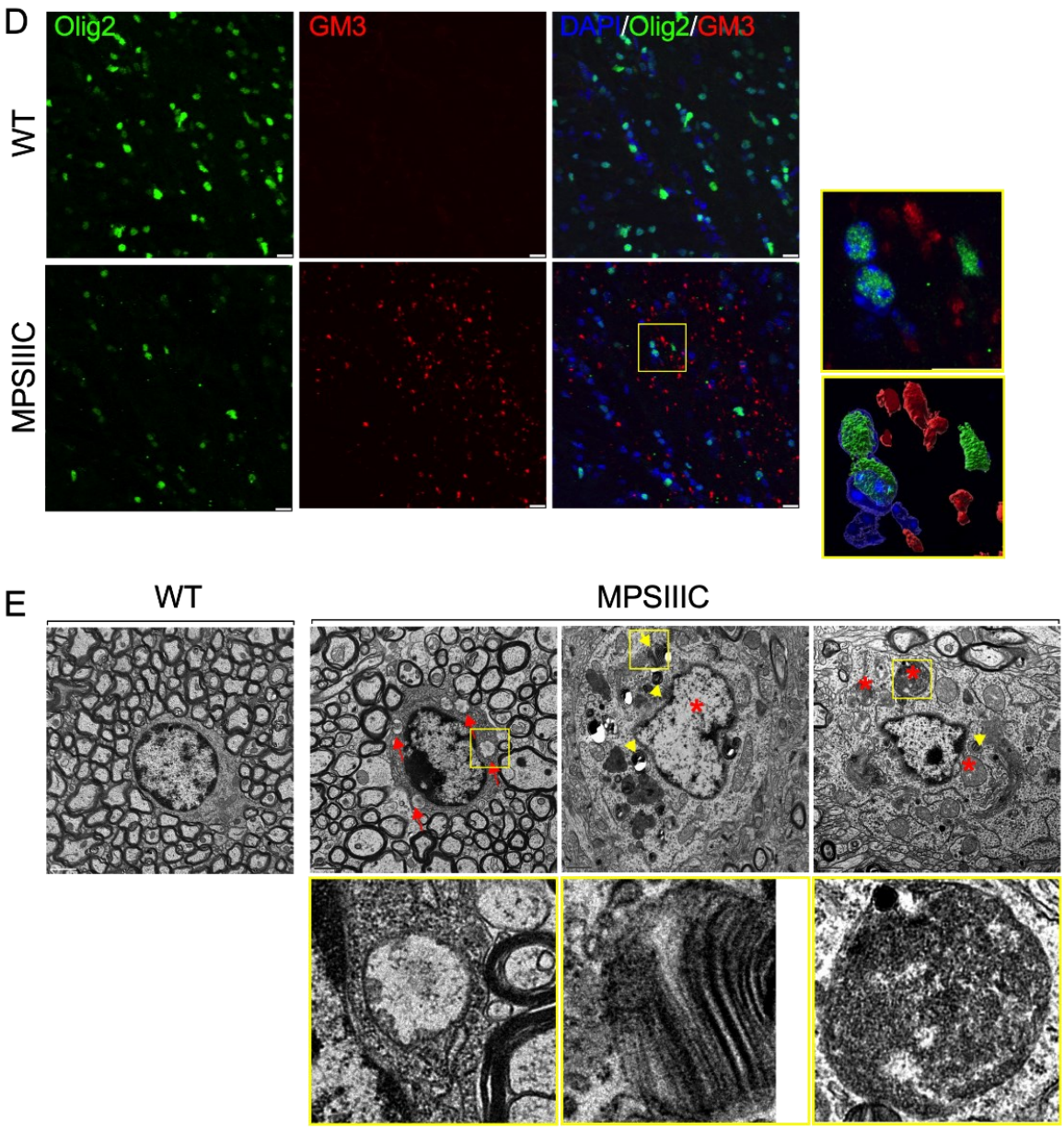

Figure 5. Oligodendrocytes in CC of MPSIIIC mice show reduced abundance, maturation and morphological abnormalities. (A) Representative confocal microscopy images of CC of 6-month-old WT and MPSIIIC mice immunolabelled for OL lineage marker Olig2 (green) and mature OL marker CC1 (red)**.** Graphs show quantification of Oligo2+, CC1+ and Oligo2+/CC1+ cells (the number of cells per mm^2) in WT and MPSIIIC mice. **(B)** Images of CC of 6-month-old WT and MPSIIIC mice immunolabelled for CC1 (red) and LAMP1 (green). Reconstructed 3D images of cells in the enlarged area boxed in the right panel show a significant increase in the size and abundance of LAMP1+ puncta consistent with presence of enlarged lysosomes in the OLs of MPSIIIC mice. **(C)** Representative images of CC of 6-month-old WT and MPSIIIC mice immunolabelled for Olig2 (green) and HS (red) show the accumulation of HS in the

Olig2+ cells. **(D)** Images of CC of 6-month-old WT and MPSIIIC mice immunolabelled for Olig2 (green) and GM3 (red) show accumulation of GM3 ganglioside in the OLs of MPSIIIC mice. For all panels DAPI (blue) was used as a nuclear counterstain. Bars equal 10 μm. **(E)** TEM micrographs of OLs reveal numerous storage vacuoles, both electrolucent (red arrows) and those containing zebra bodies (yellow arrowheads), as well as swollen mitochondria with largely dissolved cristae (asterisks). High magnification images of boxed areas show a detailed view of storage deposits. Scale bars equal 1 μm. All graphs show individual data, means and SD obtained for 3 mice per genotype. P-values were calculated using an unpaired t-test.

3.5.5. High-field magnetic resonance diffusion imaging analysis of MPSIIIC mice reveals microarchitectural changes in the corpus callosum compatible with demyelination

In the corpus callosum, DTI analysis identified clear signs of white matter injury with significant increases in Radial diffusivity (RD, 26%, $p=0.003$), an indicator of demyelination [40, 41], and Mean diffusivity (MD, 15%, $p=0.02$) a measure known to inversely correlate with white matter maturation (Figures 6). The DBSI analysis showed an increase in Hindered fraction (HF, 76%, $p<0.01$) and in Water fraction (WF, 134%, $p<0.02$), that revealed loss of tissue in the CC of MPSIIIC mouse brains compared to controls (Figure 6).

3.5.6. Myelination defects are pronounced in brain tissues of human MPSIII patients

We further analysed if axonal demyelination was also present in post-mortem tissues collected during autopsy of two MPSIIIC patients whose families provided informed consent for the use of the tissue in this research. The first patient was a 35-year-old Caucasian male with known diagnosis of MPSIIIC. He was wheelchair-dependent since the age of 17 and had the mental capacity of a 2-year-old. The second patient was an 17-year-old female with MPSIIIC diagnosed by biochemical assay of HGSNAT activity at the age of 7 years. The diagnosis was further confirmed by molecular analysis revealing that the patient was homozygous for the c.494-1G>A/p.[P164_S187delinsQSCYVTQAGVRWHHLGSLQALPPGFTPFSYLSLLSSWN, L165PfsX5] mutation affecting the conserved consensus sequence of the splice acceptor site in intron 4 [42].

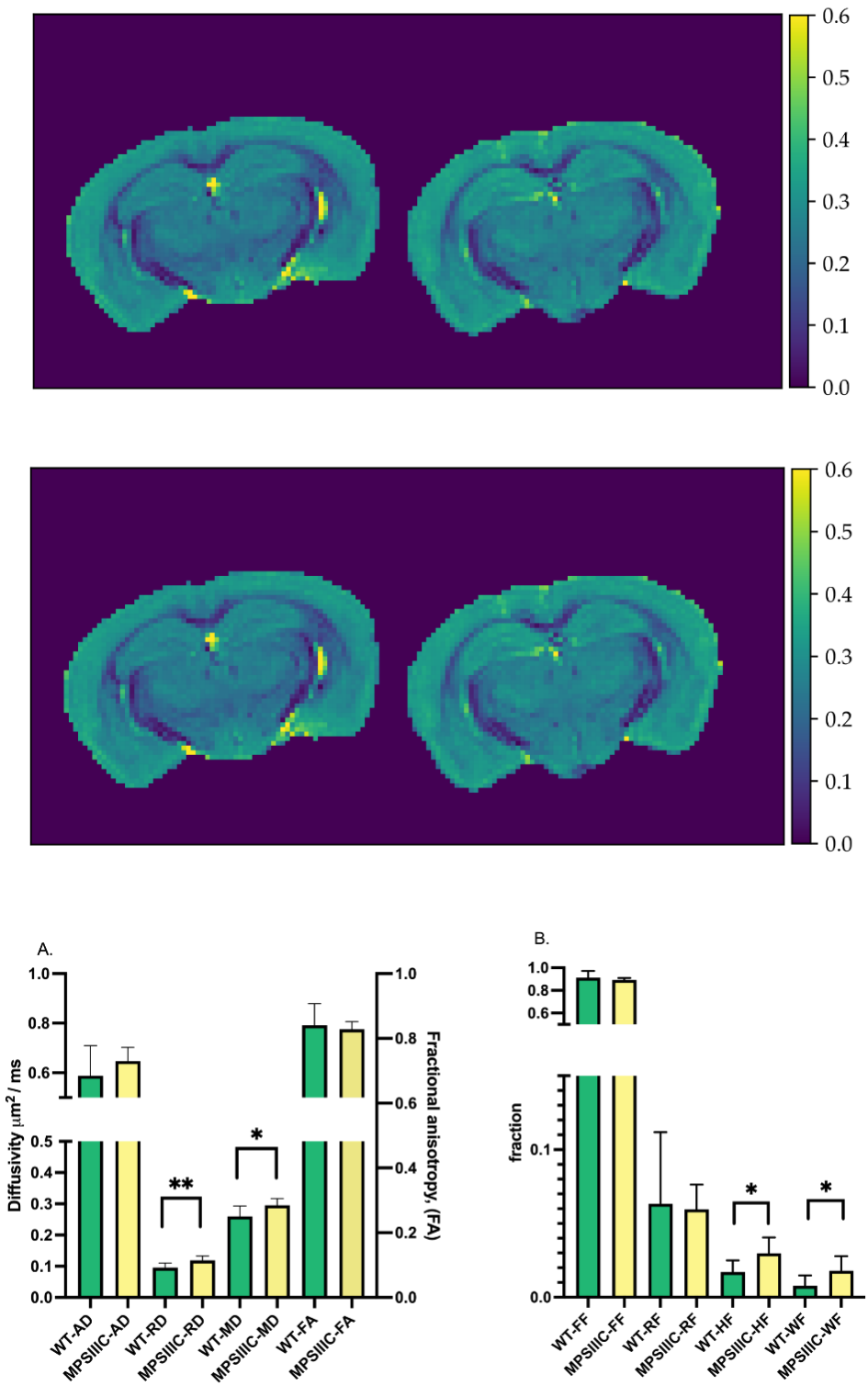

Figure 6: Diffusion maps from DTI and diffusion metrics from DTI and DBSI for WT and MPSIIIC mice. (A) Representative images of Radial diffusivity and Mean diffusivity maps for brains of WT and MPSIIIC mice demonstrating an increase for both parameters in MPSIIIC brain compared to WT mice.

Arrows show the corpus callosum. Diffusivity scale ($\mu m^2/ms$) is shown in the right sidebar. Abbreviations: RD, Radial diffusivity; MD, Mean diffusivity. **(B)** Bar plots of diffusion metrics from DTI (left) and DBSI (right) of WT and MPSIIIC mice. Abbreviations: RD, Radial diffusivity; MD, Mean diffusivity; HF, Hindered fraction, WF, Water fraction; Graphs show means ± SD for 8 WT (green bars) and 10 MPSIIIC (yellow bars) mice. **, $p<0.01$, * $p<0.05$.

On gross examination, the brain of the first patient showed severe cortical atrophy with fibrotic leptomeninges and enlarged lateral ventricles. The brain of the second patient had a marked decrease in brain weight of 974 g (normal: 1233 ± 115 g [43]) with severe cortical atrophy and enlarged lateral ventricles. However, it did not show any significant leptomeningeal fibrosis. On histological examination, both MPS brains showed neurons with abundant PAS-positive cytoplasmic inclusions (Figure 7A) at each of the three levels of the brain examined. These inclusions did not show LFB staining, except for the temporal lobe cortical neurons of the second patient (Figure 7B). HES sections of subcortical white matter in MPS brains showed slightly increased cellularity (Figure 7C, D) compared to the control brain. The first patient had a focal demyelinating lesion located at the anterior commissure with several hemosiderin-laden macrophages located in proximity (Figure 7E, F, G). LFB staining did not reveal any other regions with profound demyelination.

Further examination of the tissues of the second patient by IHC revealed that both CC and the spinal cord (SC) of the patient contained multiple CD68-positive microglia and activated GFAP-positive astrocytes consistent with pronounced neuroinflammation (Supplementary figure S5).

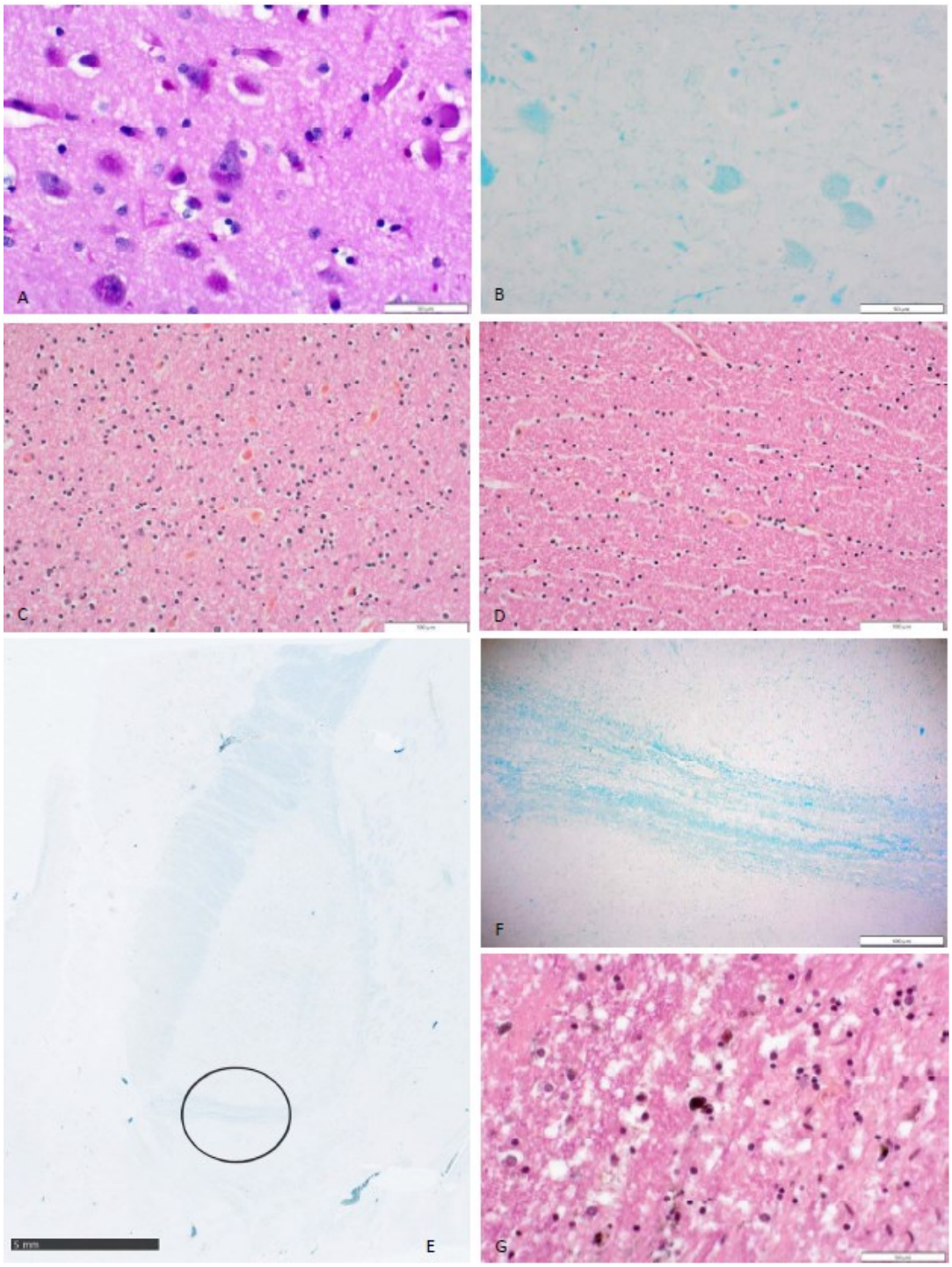

Figure 7. Histopathological examination of human brain tissue in MPSIIIC. (A) PAS-positive neuronal inclusions. (B) LFB-positive neuronal inclusions in temporal lobe neurons of patient 2. **(C)** Whiter matter hypercellularity in patient 2 compared to control **(D)**. **(E)** Focal demyelinating lesion in the anterior commissure of patient 1, seen in higher magnification in **(F)**. **(G)** Several hemosiderin-laden macrophages are adjacent to the lesion.

To assess myelination, fixed tissues of CC and SC were examined by IHC using antibodiesagainst MBP (Figure 8A and B) and MAG (Figure 9) which revealed substantially reduced levels of both markers. To determine if the levels of myelin-associated proteins are also reduced in patients affected with other subtypes of MPSIII, we analyzed PFA-fixed somatosensory cortex of post-mortem tissue, collected at autopsy and donated to the NIH NeuroBioBank. Samples of 3 MPSIII patients (MPSIIIA, MPSIIIC, and MPSIIID) and 3 non-MPS controls, matched for age and sex, were examined (project 1071, MPS Synapse). The age, cause of death, sex, race and available clinical and neuropathological information for the patients and controls are shown in Supplementary Table S1. All MPS patients had complications from their primary disease and died prematurely (before the age of 25 years). None of the patients had received enzyme replacement therapy or hematopoietic stem cell transplantation. This analysis confirmed that the amount of MBP was significantly reduced in cortices from all three MPS patients (Figure 8C), suggesting that demyelination may be a hallmark common to most subtypes of Sanfilippo disease. CC tissues from a 35-year-old MPSIIIC patient did not show any immunoreactivity for MBP or MAG, potentially due to post-mortem changes, which complicated analysis of these markers. We were also unable to achieve immunolabeling of tissues derived from a 35-year-old nor a 17-year-old patient using antibodies against CC1 and Oligo2.

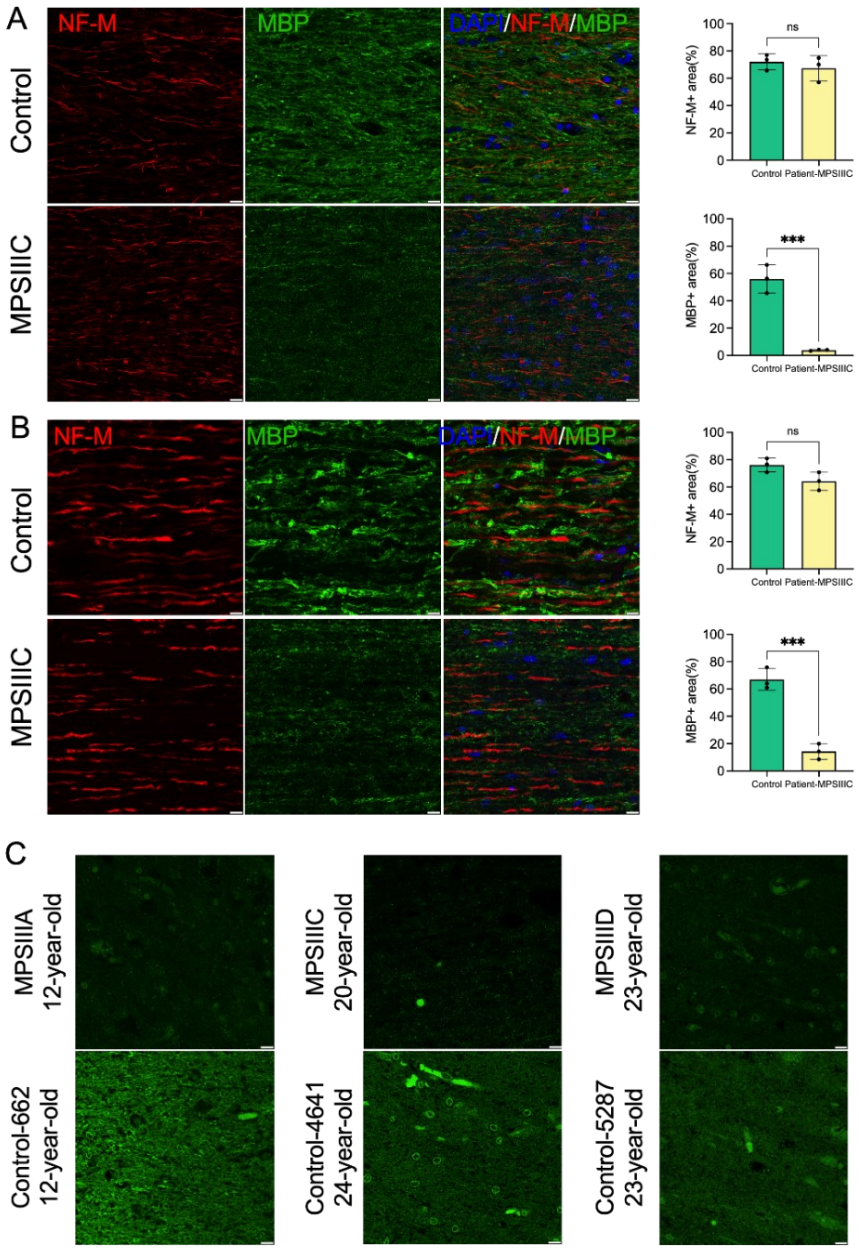

Figure 8. MBP levels are decreased in the brain and spinal cord of human MPSIII patients. IHC analysis reveals a significant reduction of MBP+ areas (green) on the surface of NF-M+ axons (red) in the CC **(A)** and SC **(B)** of 17-year-old MPS IIIC patient compared with age/sex matching control without a neurological disease. Scale bars equal 10 μm. Graphs show quantification of MBP+ and NF-M+ areas by ImageJ software. Individual results, means and SD of quantification performed in 3 adjacent areas are shown. P-values were calculated using an unpaired t-test. **(C)** MBP immunolabelling is also less pronounced in cortex of adult MPSIIIA, MPSIIIC and MPSIIID patients compared with age/sex matching non-MPS controls. Scale bars equal 10 μm.

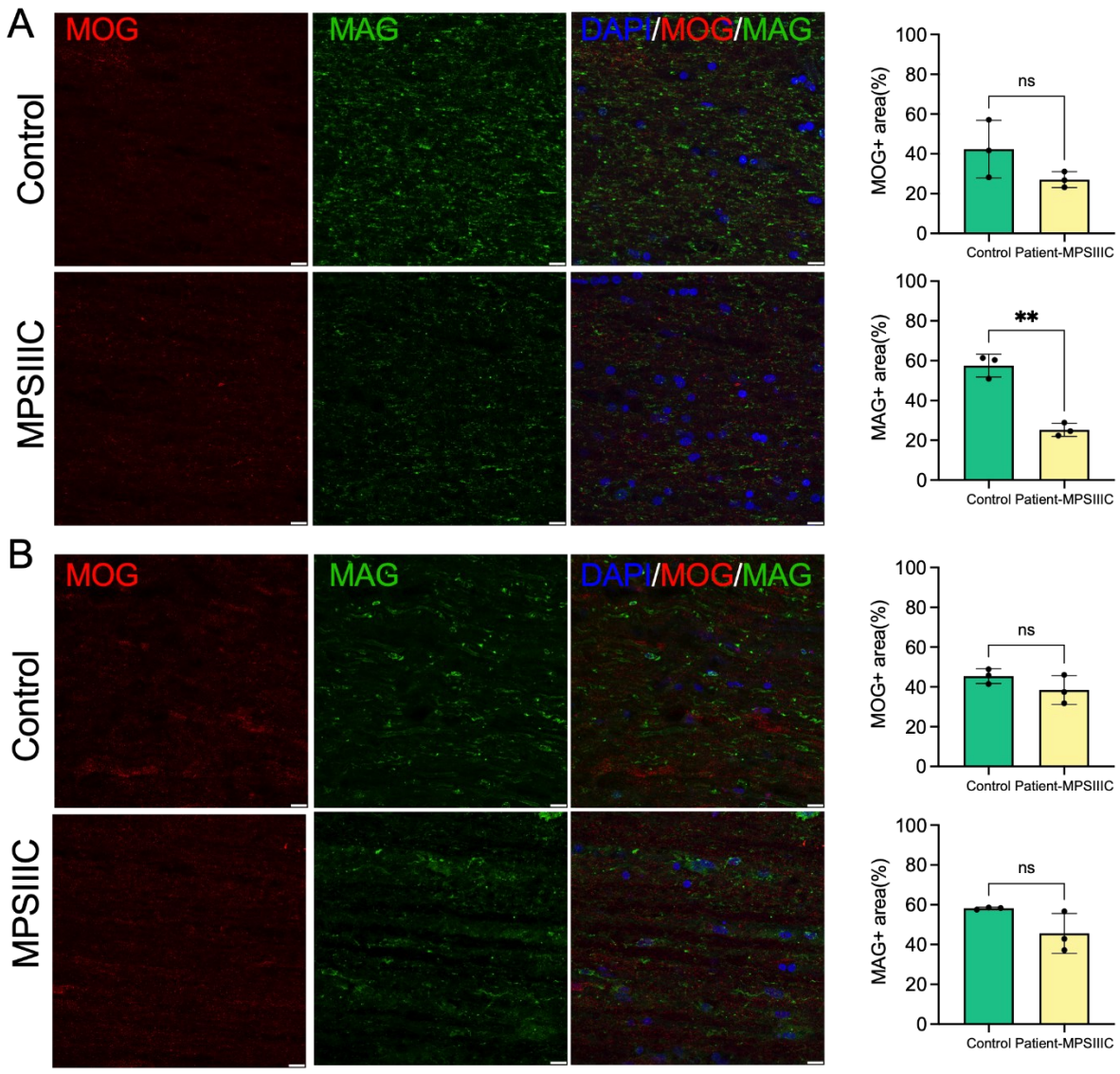

Figure 9. MAG levels are reduced in the CC but not in the SC of the 17-year-old MPSIIIC patient compared to control, while MOG levels show a non-significant trend toward a decrease. Panels show representative images ofwhat CC **(A)** and SC **(B)** of MPSIIIC patient and control stained with MAG+ (green) and MOG+ (red). Scale bars equal 10 µm. Graphs show quantification of MAG+ and MOG+ areas by ImageJ software. Individual results, means and SD of quantification performed in 3 adjacent areas are shown. P-values were calculated using an unpaired t-test.

Despite somewhat poor morphology of CC tissues of the 17 y/o and 35 y/o MPSIIIC patients, probably due to their post-mortem provenance, TEM analysis confirmed the presence of multiple microglia containing enlarged electrolucent vacuoles, similar to those present in the

microglia in the CC of the MPSIIIC mouse brain, and consistent with storage of HS and other GAGs. OLs in the CC of the 17-year-old MPSIIIC patient also contained electrolucent vacuoles as well as the vacuoles with multilamellar inclusions, consistent with myelin accumulation (Figure 10). Multiple axons in the CC of the patients showed signs of degeneration with outfolded and split myelin containing cytoplasmic materials inside the sheaths. Axonal swellings containing vesicles, similar to those present in the MPSIIIC mice, were also detected. These structural abnormalities were not observed in the CC of the age and sex-matched non-MPS patient.

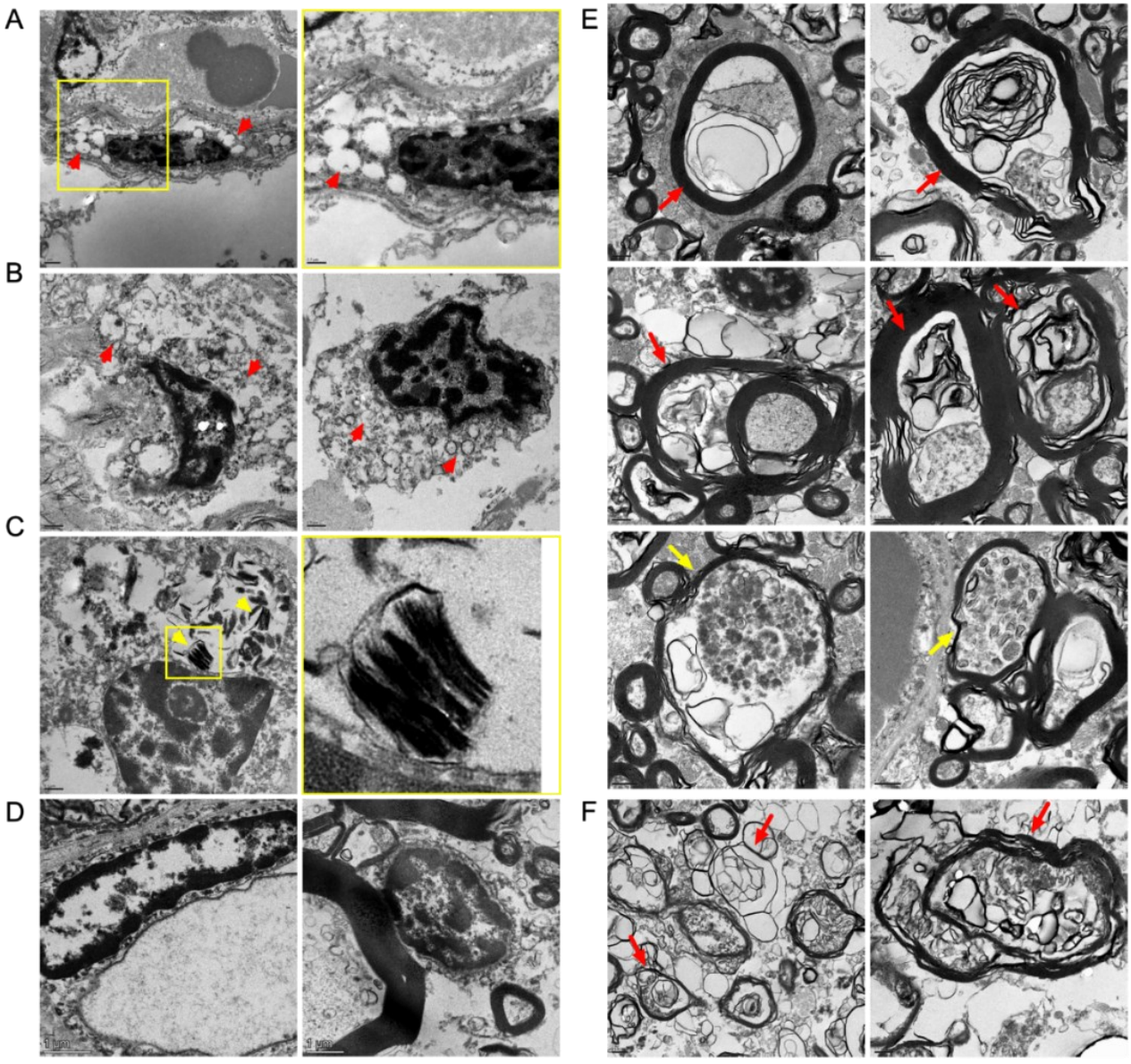

Figure 10. TEM analysis confirms microgliosis, pathological changes in oligodendrocyte morphology and axonopathy in the CC of MPSIIIC patients. Electron micrographs show electron-lucent vacuoles (red arrowheads) consistent with HS storage in microglia of the CC of the 17-year-old **(A)** and 35-year-old **(B)** MPSIIIC patients. Oligodendrocytes in the CC of the 17-year-old MPSIIIC patient contain zebra bodies consistent with myelin accumulation (**C,** yellow arrowheads). Microglia (left panel) and oligodendrocytes (right panel) in the CC of control do not contain storage vacuoles (**D**). Degenerated axons with outfolded and split myelin, sometimes containing cytoplasmic pockets between the sheaths (red arrows), as well as large axonal swellings containing accumulating vesicles (yellow arrows), are observed in the CC of the 17-year-old **(E)** and 35-year-old **(F)** MPS IIIC human patients. These structural abnormalities are not observed in the CC of the age and sex-matched non-MPS patient.

3.6. Discussion

Here we identify persistent demyelination as a key component of CNS pathology in MPSIIIC, and likely associated with all diseases of the MPSIII spectrum. First, we determined that the amount of MBP, a protein marker of myelinated axons, was drastically reduced in CC of both MPSIIIC mice and MPSIIIC patients at advanced stages of the disease, consistent with myelin disruption and demyelination. Other myelin markers, MAG and MOG were also reduced. Second, ultrastructural analysis of brain tissue confirmed that the myelin sheaths in the MPSIIIC brains were reduced in thickness and revealed structural abnormalities, including outfolded, empty or split myelin. Third, regions of white matter in MPSIIIC mouse brain were massively infiltrated by activated CD68-positive microglia with lysosomal accumulation of MBP-positive elements and multilamellar fragments ("zebra bodies"), consistent with phagocytosis of myelin fragments. Occurrence of similar processes associated with demyelination and axonal degeneration have been reported in multiple white matter pathologies including ischemic injuries, multiple sclerosis and other inflammatory demyelinating diseases, optic nerve diseases, aging, and experimental models of immune encephalomyelitis (reviewed in [44-46]). In immune encephalomyelitis, activated proinflammatory microglia were reported to directly trigger the loss of myelin, however in

MPSIIIC mice, high levels of microgliosis is observed starting from a very early age (P25 or even before), while the loss of MBP was not detected before the age of 6 months. These findings support the conclusion that axonal demyelination in MPSIIIC is due to aberrant myelin maintenance by resident OLs rather than defects of early axonal development or damage caused by activated microglia or astrocytes. This was supported by our observation that OLs in the CC of MPSIIIC mice were scarce and, in general, immature. Further analysis of OL morphology revealed that they contained multiple electro-lucent vacuoles, consistent with storage of HS, and multilamellar bodies, characteristic of lipid accumulation. This was confirmed by IHC, demonstrating that OLs in MPSIIIC but not WT mice were positive for HS and GM3 ganglioside. Based on the presence of these morphological abnormalities, we speculate that the majority OLs in MPSIIIC mice are either dysfunctional or have reduced functionality.

We and others have previously demonstrated that the levels of GM3 ganglioside, together with GM2 ganglioside, lactosylceramide and glucosylceramide, are drastically increased in the brains of mouse models of MPSIII and in the brains of MPSIII human patients [35, 36, 47]. The accumulation of these secondary materials mainly occurs in pyramidal neurons in the deep cortex layers and in the CA1-CA3 regions of the hippocampus [48, 49]. Our current data show that in contrast to other brain cells, OLs in the CC solely accumulate GM3, while rare GM2-positive cells scattered across the CC are negative for the OL marker Olig2. Although the mechanism underlying the massive accumulation of GM3 ganglioside in the OLs of MPSIIIC brain requires further investigation, we are tempted to speculate that this phenomenon may be related to the development of myelin defects. Previous studies demonstrated that in Niemann-Pick type C (NP-C) the accumulation of GM3 in OLs is a prerequisite for dysfunction and demyelination [13]. Similarly to MPSIII, NP-C manifests with predominant storage of GM2 and GM3 gangliosides [50] and

myelin defects in the brain tissues (Reviewed in [3]). In the mouse model of NP-C (Npc1−/− mice) hypomyelination is pronounced in the cerebral cortex and the CC, presumably accounting for the tremor and ataxia observed in these animals [51]. The Npc1−/− mice, heterozygous for the deletion of the Siat9 (GM3 synthase) gene, showed ameliorated neuropathology, including motor disability and demyelination [13]. At the same time, deletion of Siat9 gene resulted in the enhanced neuropathological phenotype and demyelination in Npc1−/−mice, indicating that the presence (but not an excessive storage) of GM3 ganglioside is essential for OLs development [13].

Importantly, OLs in the CC of MPSIIIC mice also exhibited mitochondrial pathology; the majority of mitochondria in these cells had a dysmorphic ballooned appearance with absent cristae. Similar pathology has been previously described by our team in the hippocampal pyramidal neurons of MPSIIIC mice, which was associated with a progressive loss of mitochondrial activity and neurodegeneration [38]. In the adult brain, once myelination is complete, the long-term integrity of axons is known to depend on the supply of energy to myelinating cells that are key for preserving the connectivity and function of a healthy nervous system (Reviewed in [52]). Thus, it is tempting to speculate that mitochondrial dysfunction in OLs, associated perhaps with reduced maturation and increased degeneration, may underlie the demyelination that occurs in the MPSIIIC brain.

Major findings in the mouse MPSIII model were confirmed with the brain tissues of human MPSIIIC patients, suggesting that demyelination and white matter injury contribute to the pathology at least at the later stages of the disease. Importantly, LFB staining did not reveal regions with profound demyelination in the brains of both patients, except for one region in the brain of a 35-year-old patient, where the loss of LFB staining was associated with the presence of hemosiderin-laden macrophages suggesting an occurrence of an old micro hemorrhage. This may

explain, why myelination defects were not previously described in the majority of pathology reports where brain tissues of MPSIII patients have been examined using only traditional histochemical techniques such as HES, PAS and LFB staining. Further studies are required to determine whether patients affected with all subtypes of Sanfilippo disease show a similar degree of demyelination. We consider this to be plausible, as drastically reduced levels of MBP staining were detected in the post-mortem cortical samples of MPSIIIA and MPSIIID patients obtained from NeuroBiobank.

Magnetic resonance diffusion tensor imaging allows generation of quantitative maps that describe tissue microstructure by decomposing diffusion signals into axial diffusivity, radial diffusivity, and fractional anisotropy. We have previously shown how a reduction in radial diffusivity can reliably quantify myelination during development [53]. Consistent with this, increased radial diffusivity has been used as a biomarker of demyelination [40, 41, 54]. A more recent method, Diffusion Basis Spectrum Imaging can provide additional information for an extra-axonal compartment, such as fiber fraction, hindered diffusivity (extracellular), restricted diffusivity (intracellular) and water fraction [30]. Restricted diffusivity has, in particular, been shown to reflect inflammation with increased cellularity in a mouse model of neuroinflammation [55]. It has been also applied to detect white matter injury with edema or tissue loss [56-58]. Interestingly, our analysis of diffusivity maps of the CC of 7-month-old MSCIIIC mice revealed a significant increase in radial diffusivity, suggesting loss of myelin, together with a strong increase of mid-higher isotropic diffusivity indicative of edema and tissue loss. In line with the absence of axonal loss, our MRI analysis found no changes in fiber fraction, fractional anisotropy or axial diffusivity. On the other hand, we did not detect significant changes in restricted diffusivity, which was expected considering the high level of microgliosis in the CC of MPSIIIC mice. It is possible,

however that, the model we used was not sufficiently sensitive to detect subtle increase in local cellularity because of the very dense structure of white matter mainly composed of tightly organized fibers.

Together, our data provide novel insights into pathophysiology of Sanfilippo disease. They also identify widespread demyelination in CNS as an important biomarker of disease progression and suggest that analysis of brain myelin by MRI may become in the future a leading non-invasive method for clinical patient assessment.

3.7. Supplementary data

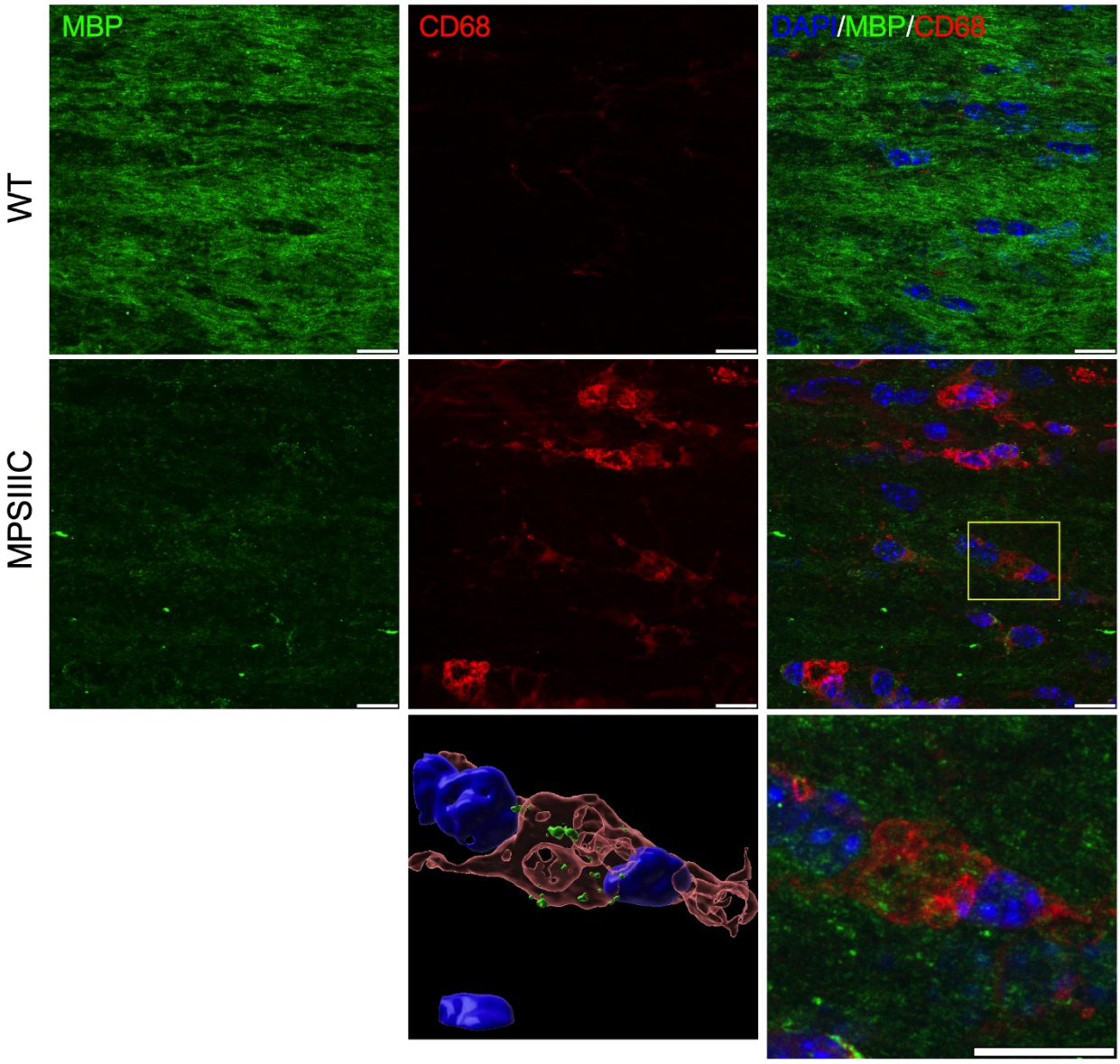

Figure S1. Intracellular aggregation of MBP in microglia in CC of MPSIIIC mice. Panels show representative confocal microscopy images of CC tissue of 6-month-old WT and MPSIIIC mice labelled with antibodies against MBP (green) and CD68 (red). DAPI (blue) was used as a nuclear counterstain. Scale bars equal 10 μm. The enlarged image of the boxed area shows a CD68+ activated microglia containing MBP+ puncta. 3D reconstruction shows that MBP+ puncta are located inside the microglia cell.

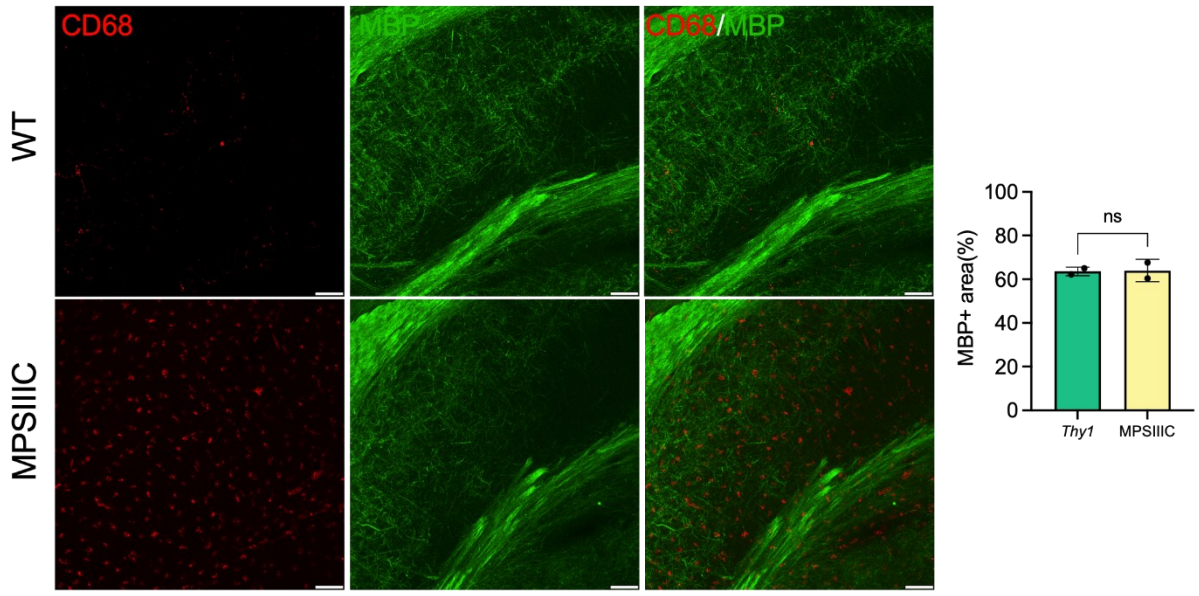

Figure S2. Microgliosis does not coincide with the loss of myelin at an early age. Panels show representative confocal microscopy images of hippocampal and CC tissues of P25 WT and MPSIIIC mice labelled with antibodies against CD68 (red) and MBP (green). Scale bars equal 50 μm.

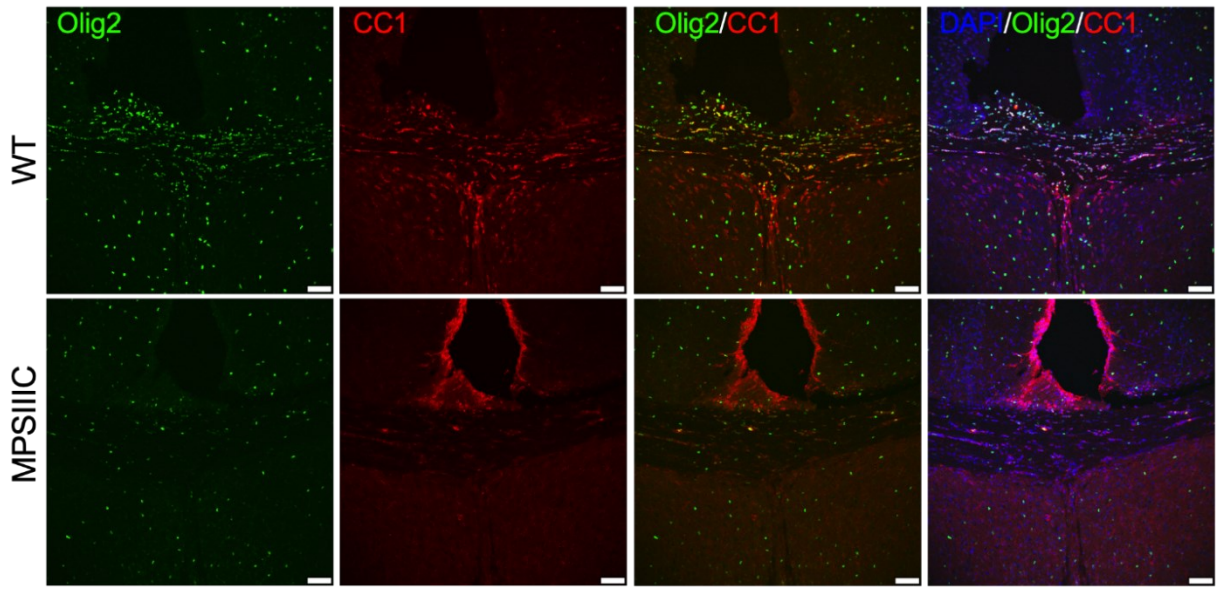

Figure S3. CC of MPSIIIC mice show reduced numbers of mature oligodendrocytes. Panels show representative images of the CC of 6-month-old WT and MPSIIIC mice immunolabelled for OL lineage marker Olig2 (green) and mature OL marker CC1 (red). DAPI (blue) was used as a nuclear counterstain. Scale bar equals 50 μm.

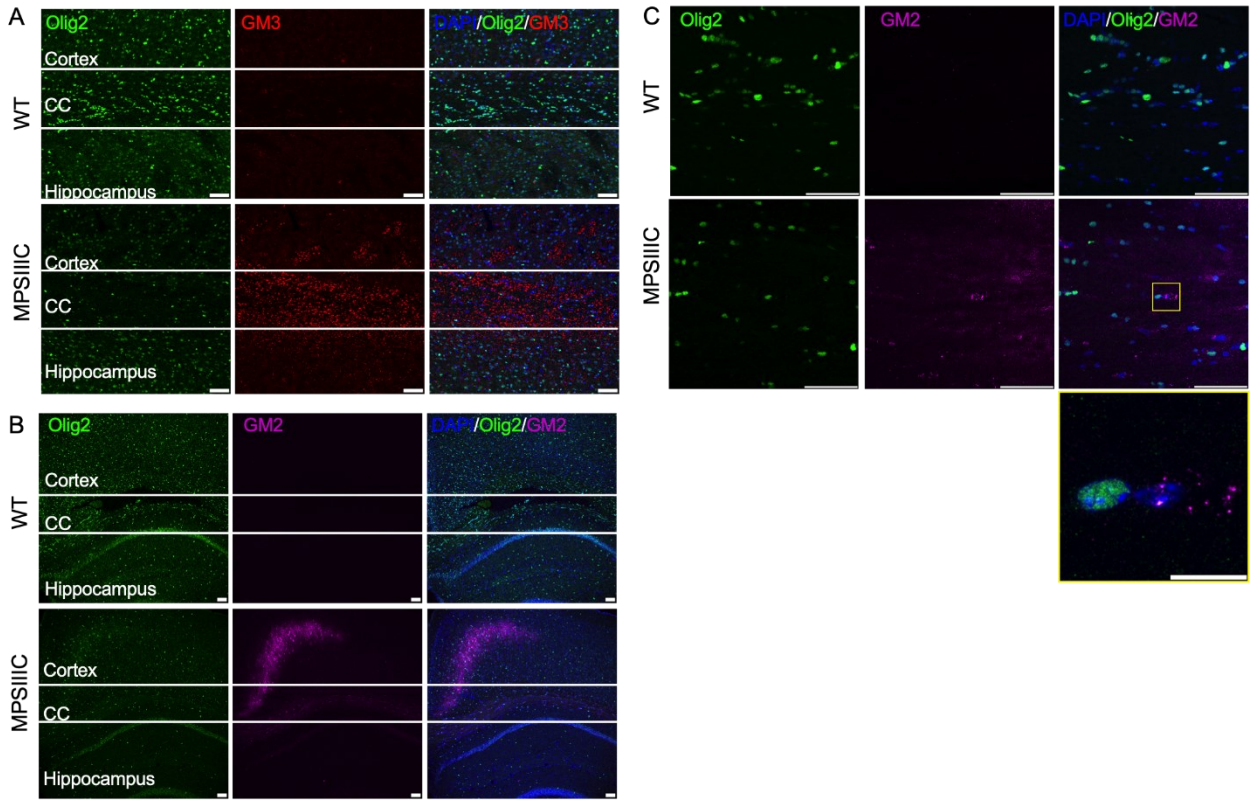

Figure S4. Secondary storage of GM3 and GM2 gangliosides in the brain of MPSIIIC mice. Panels show confocal microscopy images of the cortex, CC and hippocampus tissues of 6-month-old WT and MPSIIIC mice stained with antibodies against Olig2 (green), GM3 ganglioside (red) **(A)** and GM2 ganglioside (purple) **(B),** revealing storage of GM3 ganglioside in the CC and GM2 ganglioside in the cortex of MPSIIIC but not of WT mice. **(C)** GM2 ganglioside does not accumulate in OLs in CC tissue of 6-month-old WT and MPSIIIC mice. DAPI (blue) was used as a nuclear counterstain. Scale bar equals 50 μm for **A, B, C,** and 10 mM for the zoomed image in the panel **C**.

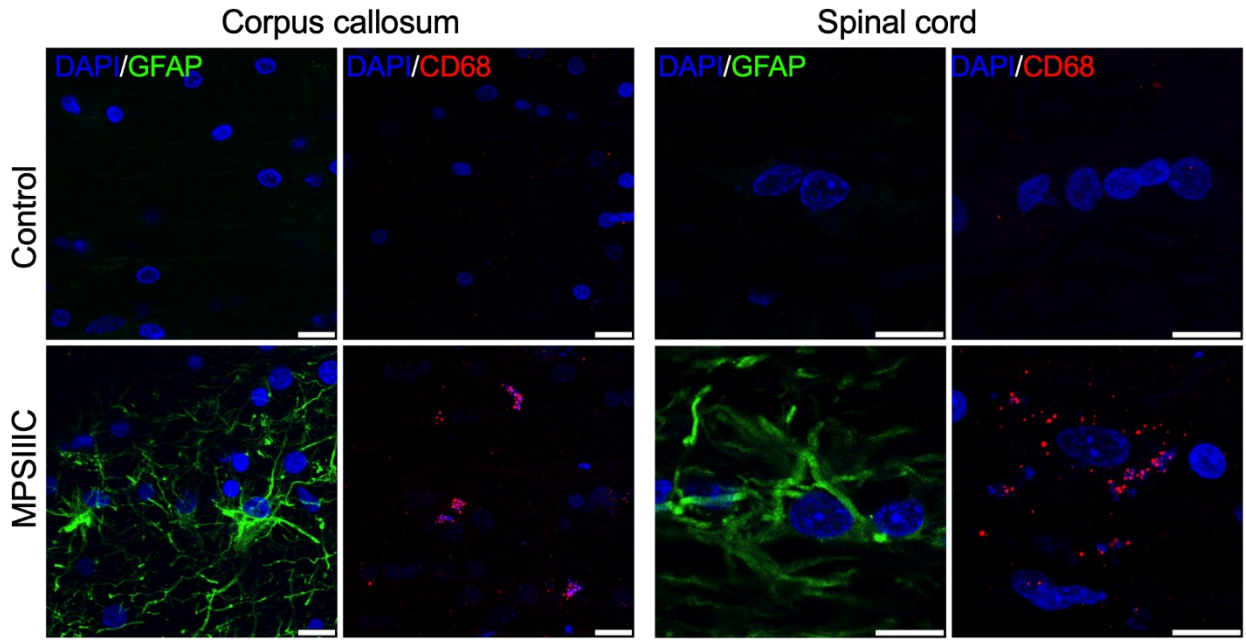

Figure S5. Pronounced astromicrogliosis in the corpus callosum and spinal cord of a 17-years-old MPSIIIC patient. Multiple GFAP-positive astrocytes (green) and C68-positive microglia (red), indicative of neuroimmune response, are detected in the CC and SC of the MPSIIIC patient but not of the age/sex matching non-MPS control.

3.8. References

1. Boustany, R.M., Lysosomal storage diseases--the horizon expands. Nat Rev Neurol, 2013. 9(10): p. 583-98.

2. Para, C., P. Bose, and A.V. Pshezhetsky, Neuropathophysiology of Lysosomal Storage Diseases: Synaptic Dysfunction as a Starting Point for Disease Progression. J Clin Med, 2020. 9(3).

3. Maegawa, G.H.B., Lysosomal Leukodystrophies Lysosomal Storage Diseases Associated With White Matter Abnormalities. J Child Neurol, 2019. 34(6): p. 339-358.

4. Wenger, D.A., M.A. Rafi, and P. Luzi, Molecular genetics of Krabbe disease (globoid cell leukodystrophy): diagnostic and clinical implications. Hum Mutat, 1997. 10(4): p. 268-79.

5. Wenger, D.A., et al., Krabbe disease: genetic aspects and progress toward therapy. Mol Genet Metab, 2000. 70(1): p. 1-9.

6. Gieselmann, V., Metachromatic leukodystrophy: genetics, pathogenesis and therapeutic options. Acta Paediatr, 2008. 97(457): p. 15-21.

7. Poretti, A., et al., Novel diffusion tensor imaging findings in Krabbe disease. Eur J Paediatr Neurol, 2014. 18(2): p. 150-6.

8. Groeschel, S., et al., Metachromatic leukodystrophy: natural course of cerebral MRI changes in relation to clinical course. J Inherit Metab Dis, 2011. 34(5): p. 1095-102.

9. Sabourdy, F., et al., Natural disease history and characterisation of SUMF1 molecular defects in ten unrelated patients with multiple sulfatase deficiency. Orphanet J Rare Dis, 2015. 10: p. 31.

10. Kishimoto, Y., Phylogenetic development of myelin glycosphingolipids. Chem Phys Lipids, 1986. 42(1-3): p. 117-28.

11. de Vries, H. and D. Hoekstra, On the biogenesis of the myelin sheath: cognate polarized trafficking pathways in oligodendrocytes. Glycoconj J, 2000. 17(3 -4): p. 181-90.

12. Lau, M.W., et al., Role of Diffusion Tensor Imaging in Prognostication and Treatment Monitoring in Niemann-Pick Disease Type C1. Diseases, 2016. 4(3).

13. Lee, H., et al., Inhibition of GM3 synthase attenuates neuropathology of Niemann-Pick disease Type C. by affecting sphingolipid metabolism. Mol Cells, 2014. 37(2): p. 161-71.

14. Tuteja, M., et al., White matter changes in GM1 gangliosidosis. Indian Pediatr, 2015. 52(2): p. 155-6.

15. Imamura, A., et al., Serial MR imaging and 1H-MR spectroscopy in monozygotic twins with Tay-Sachs disease. Neuropediatrics, 2008. 39(5): p. 259-63.

16. Heon-Roberts, R., A.L.A. Nguyen, and A.V. Pshezhetsky, Molecular Bases of Neurodegeneration and Cognitive Decline, the Major Burden of Sanfilippo Disease. J Clin Med, 2020. 9(2).

17. Kresse, H. and E.F. Neufeld, The Sanfilippo A corrective factor. Purification and mode of action. J Biol Chem, 1972. 247(7): p. 2164-70.

18. von Figura, K. and H. Kresse, The sanfilippo B corrective factor: a N-acetyl-alpha-D-glucosamindiase. Biochem Biophys Res Commun, 1972. 48(2): p. 262-9.

19. Klein, U., H. Kresse, and K. von Figura, Sanfilippo syndrome type C: deficiency of acetyl-CoA:alpha-glucosaminide N-acetyltransferase in skin fibroblasts. Proc Natl Acad Sci U S A, 1978. 75(10): p. 5185-9.

20. Kresse, H., et al., Sanfilippo disease type D: deficiency of N-acetylglucosamine-6-sulfate sulfatase required for heparan sulfate degradation. Proc Natl Acad Sci U S A, 1980. 77(11): p. 6822-6.

21. Shapiro, E.G., et al., A Prospective Natural History Study of Mucopolysaccharidosis Type IIIA. J Pediatr, 2016. 170: p. 278-87 e1-4.

22. Whitley, C.B., et al., Observational Prospective Natural History of Patients with Sanfilippo Syndrome Type B. J Pediatr, 2018. 197: p. 198-206 e2.

23. Kara, S., E.H. Sherr, and A.J. Barkovich, Dilated perivascular spaces: an informative radiologic finding in Sanfilippo syndrome type A. Pediatr Neurol, 2008. 38(5): p. 363-6.

24. Zafeiriou, D.I., et al., Serial magnetic resonance imaging findings in mucopolysaccharidosis IIIB (Sanfilippo's syndrome B). Brain Dev, 2001. 23(6): p. 385-9.

25. Reichert, R., et al., Magnetic resonance imaging findings of the posterior fossa in 47 patients with mucopolysaccharidoses: A cross-sectional analysis. JIMD Rep, 2021. 60(1): p. 32-41.

26. Pan, X., et al., Glucosamine amends CNS pathology in mucopolysaccharidosis IIIC mouse expressing misfolded HGSNAT. Journal of Experimental Medicine, 2022. 219(8): p. e20211860.

27. Feng, G., et al., Imaging neuronal subsets in transgenic mice expressing multiple spectral variants of GFP. Neuron, 2000. 28(1): p. 41-51.

28. Nelvagal, H.R., et al., Spinal manifestations of CLN1 disease start during the early postnatal period. Neuropathol Appl Neurobiol, 2021. 47(2): p. 251-267.

29. Nelvagal, H.R., et al., Cross-species efficacy of enzyme replacement therapy for CLN1 disease in mice and sheep. J Clin Invest, 2022. 132(20).

30. Wang, Y., et al., Quantification of increased cellularity during inflammatory demyelination. Brain, 2011. 134(Pt 12): p. 3590-601.

31. Garyfallidis, E., et al., Dipy, a library for the analysis of diffusion MRI data. Front Neuroinform, 2014. 8: p. 8.

32. Han, F., et al., Neuroinflammation and myelin status in Alzheimer's disease, Parkinson's disease, and normal aging brains: a small sample study. Parkinson's Disease, 2019. 2019.

33. Safaiyan, S., et al., Age-related myelin degradation burdens the clearance function of microglia during aging. Nature neuroscience, 2016. 19(8): p. 995-998.

34. Thériault, P. and S. Rivest, Microglia: senescence impairs clearance of myelin debris. Current Biology, 2016. 26(16): p. R772-R775.

35. Martins, C., et al., Neuroinflammation, mitochondrial defects and neurodegeneration in mucopolysaccharidosis III type C mouse model. Brain, 2015. 138(Pt 2): p. 336-55.

36. Pan, X., et al., Glucosamine amends CNS pathology in mucopolysaccharidosis IIIC mouse expressing misfolded HGSNAT. J Exp Med, 2022. 219(8).

37. Peters, A. and C. Folger, A website entitled "The fine structure of the aging brain". 2013, Wiley Online Library. p. 1203-1206.

38. Martins, C., et al., Neuroinflammation, mitochondrial defects and neurodegeneration in mucopolysaccharidosis III type C mouse model. Brain, 2015. 138(2): p. 336-355.

39. Pagni, F., et al., Possible pathogenetic relationship between Fabry disease and renal cell carcinoma. American Journal of Nephrology, 2012. 36(6): p. 537-541.

40. Song, S.K., et al., Dysmyelination revealed through MRI as increased radial (but unchanged axial) diffusion of water. Neuroimage, 2002. 17(3): p. 1429-36.

41. Song, S.K., et al., Diffusion tensor imaging detects and differentiates axon and myelin degeneration in mouse optic nerve after retinal ischemia. Neuroimage, 2003. 20(3): p. 1714-22.

42. Martins, C., et al., Molecular characterization of a large group of Mucopolysaccharidosis type IIIC patients reveals the evolutionary history of the disease. Hum Mutat, 2019. 40(8): p. 1084-1100.

43. Molina, D.K. and V.J. DiMaio, Normal Organ Weights in Women: Part II-The Brain, Lungs, Liver, Spleen, and Kidneys. Am J Forensic Med Pathol, 2015. 36(3): p. 182-7.

44. Alturkustani, M. and L.C. Ang, White matter cellular changes in ischemic injuries. Am J Transl Res, 2022. 14(8): p. 5859-5869.

45. Correale, J. and M.C. Ysrraelit, Multiple Sclerosis and Aging: The Dynamics of Demyelination and Remyelination. ASN Neuro, 2022. 14: p. 17590914221118502.

46. Yazdankhah, M., et al., Role of glia in optic nerve. Prog Retin Eye Res, 2021. 81: p. 100886.

47. Viana, G.M., et al., Brain Pathology in Mucopolysaccharidoses (MPS) Patients with Neurological Forms. J Clin Med, 2020. 9(2).

48. Walkley, S.U. and M.T. Vanier, Secondary lipid accumulation in lysosomal disease. Biochim Biophys Acta, 2009. 1793(4): p. 726-36.

49. McGlynn, R., K. Dobrenis, and S.U. Walkley, Differential subcellular localization of cholesterol, gangliosides, and glycosaminoglycans in murine models of mucopolysaccharide storage disorders. J Comp Neurol, 2004. 480(4): p. 415-26.

50. Zervas, M., K. Dobrenis, and S.U. Walkley, Neurons in Niemann-Pick disease type C accumulate gangliosides as well as unesterified cholesterol and undergo dendritic and axonal alterations. J Neuropathol Exp Neurol, 2001. 60(1): p. 49-64.

51. Takikita, S., et al., Perturbed myelination process of premyelinating oligodendrocyte in Niemann-Pick type C mouse. J Neuropathol Exp Neurol, 2004. 63(6): p. 660-73.

52. Nave, K.A. and H.B. Werner, Myelination of the nervous system: mechanisms and functions. Annu Rev Cell Dev Biol, 2014. 30: p. 503-33.

53. Lodygensky, G.A., et al., In vivo assessment of myelination by phase imaging at high magnetic field. Neuroimage, 2012. 59(3): p. 1979-87.

54. Song, S.K., et al., Demyelination increases radial diffusivity in corpus callosum of mouse brain. Neuroimage, 2005. 26(1): p. 132-40.

55. Wang, X., et al., Diffusion basis spectrum imaging detects and distinguishes coexisting subclinical inflammation, demyelination and axonal injury in experimental autoimmune encephalomyelitis mice. NMR Biomed, 2014. 27(7): p. 843-52.

56. Chiang, C.W., et al., Quantifying white matter tract diffusion parameters in the presence of increased extra-fiber cellularity and vasogenic edema. Neuroimage, 2014. 101: p. 310-9.

57. Isaacs, A.M., et al., Microstructural Periventricular White Matter Injury in Post-Hemorrhagic Ventricular Dilatation. Neurology, 2021. 98(4): p. e364-75.

58. Schiavi, S., et al., Non-invasive quantification of inflammation, axonal and myelin injury in multiple sclerosis. Brain, 2021. 144(1): p. 213-223.

Chapter 4

Discussion

CHAPTER 4:Discussion

4.1. Protein misfolding as a key underlying molecular defect in MPS IIIC

Over half of patients with MPS IIIC are affected by missense mutations, which prevent correct folding of the enzyme and cause its retention in the endoplasmic reticulum and degradation in proteasomes [25, 59]. However, molecules, such as pharmacological chaperones, that mimic substrate binding in the active site stabilise proper position of active site residues and shift the balance toward the properly folded state of the enzyme. As a result, the correctly folded mutant enzyme passes the quality-control system of the ER and undergoes further maturation and normal transport to the lysosome. Once a mutant enzyme-chaperone complex reaches the lysosome, the chaperone is replaced by accumulated substrate to allow the enzyme to function [59, 190, 191]. MPS IIIC is an excellent candidate for chaperone therapy because a threshold of the residual activity of approximately 15% seems to be sufficient to prevent a severe pathology. Patients with several missense HGSNAT variants (p.G133A, p.A615T, and p.R124W) and residual HGSNAT activity in tissues reduced to 15-20% of normal develop retinitis pigmentosa at the age of 50-60 years [192, 193], instead of having a deadly juvenile phenotype similar to MPS IIIC patients.

The generation of a new mouse model expressing misfolded HGSNAT protein is required for the development of molecular chaperone therapy for MPS IIIC. For this reason, we have chosen a Pro304Leu mutation, which is a mouse analog of a pathogenic human variant Pro311Leu previously found in severely affected patients with MPS IIIC [25, 59, 194]. In comparison with gene-targeted *Hgsnat-Geo* (knock-out) mice with a constitutive disruption of the gene expression [118], the knock-in $Hgsnat^{P304L}$ have a substantially more severe clinical phenotype. In particular, the lifespan of $Hgsnat^{P304L}$ mice was approximately 20 weeks shorter than that of the *Hgsnat-Geo* mice, and at sacrifice, they displayed severe enlargement of the kidney, liver, and spleen, as

opposed to the *Hgsnat-Geo* mice, which only displayed mild hepatomegaly. Previous studies of *Hgsnat-Geo* mice by Morris water maze, revealed that they have defects in spacious and working memory at about 10 months of age [118]. In addition, Novel Object Recognition test demonstrated short memory deficits in both *Hgsnat-Geo* and $Hgsnat^{P304L}$ strains at 4 months of age [189]. Elevated plus maze (anxiety and fear) and Open field (OF; anxiety and hyperactivity) tests demonstrated increased hyperactivity and reduced anxiety in $Hgsnat^{P304L}$ strains at 4 months of age. In contrast, *Hgsnat-Geo* showed hyperactivity and reduced anxiety in Open field test only between 8 (6 in the female group) and 10 months [118]. I conducted analysis of the behavior of MPS IIIC mice using a Y-maze test which not only confirmed impairment of spatial memory in both mouse models but also demonstrated that a decline in spatial memory and the behavioral abnormalities in the $Hgsnat^{P304L}$ mice start at 4 months, at least 2-3 months earlier than in the *Hgsnat-Geo* mice.

We hypothesized that a faster decline in working memory in $Hgsnat^{P304L}$ mice could be associated with an earlier onset of synaptic defects. Indeed, the reduction in the length/area of postsynaptic densities and synaptic vesicle density (number of synaptic vesicles per μm^2) in the synaptic terminals of neurons in the CA1 region of the hippocampus of $Hgsnat^{P304L}$ mice was more pronounced that in *Hgsnat-Geo* mice at both 3 and 6 months of age. Additionally, defects were observed in both glutamatergic and GABAergic synapses in CA1 and cultured hippocampal neurons of $Hgsnat^{P304L}$ mice while in the cells of *Hgsnat-Geo* mice only glutamatergic synapses were affected.

Further, using ICC, we analyzed the levels of synaptic proteins, specific for both excitatory and inhibitory synapses, in cultured hippocampal neurons from $Hgsnat^{P304L}$ mice and compared them with those in *Hgsnat-Geo* and WT mice. Our results confirmed that neurons from both

Hgsnat^{P304L} and *Hgsnat-Geo* mice showed a similar reduction in the density of PSD95+ in juxtaposition with VGLUT1+ puncta (excitatory synapses) compared with WT neurons. In contrast, the number of Gephyrin+/VGAT+ puncta in juxtaposition (inhibitory synapses) were reduced in neurons from *Hgsnat*^{P304L} mice but not in those from *Hgsnat-Geo* mice, confirming that GABAergic synapses are affected only in the knock-in mice.

Examination of brain tissues revealed that a majority of the CNS disease progression biomarkers, such as neuroimmune response, astromicrogliosis, as well as accumulation of primary and secondary storage materials, were aggravated in *Hgsnat*^{P304L} mice compared to *Hgsnat-Geo* mice of the same age. Given that in both strains, the residual brain level of HGSNAT acetyltransferase activity was reduced to below detection levels, we hypothesized that the difference in clinical severity was, most likely, caused by toxicity of the mutant misfolded HGSNAT P304L variant expressed in the cells of *Hgsnat*^{P304L} mice.

RNAseq analysis, I conducted on mouse hippocampi, revealed that the same types of pathways were changed in both knock-out and knock-in mice compared to WT mice. In particular, lysosomal biogenesis was enhanced, as were the pathways involved in inflammatory and immunological responses. In contrast, a decrease in the expression of genes related to neurogenesis and synaptic transmission has been observed. However, the number of significantly altered pathways (particularly those associated with GABAergic synapses) and the degree of gene modifications were higher in the *Hgsnat*^{P304L} mice, compared to *Hgsnat-Geo* mice, consistent with more severe CNS pathology observed in the knock-in mice. Several up-regulated pathways in the *Hgsnat*^{P304L} mice were related to the ER stress/unfolded protein response (UPR). It has been previously demonstrated that in both neurodegenerative and non-neurodegenerative LSDs, misfolded proteins carrying missense mutations can cause ER stress and activate the UPR

signaling pathway [73]. This, along with the elevated levels of ER stress indicators (O-GlcNAc-modified proteins and ubiquitinated protein aggregates) found in the hippocampal and cortical pyramidal neurons of the knock-in mice, led us to hypothesize that the expression of the misfolded HGSNAT mutant protein places extra restrictions on the ER in these cells. This can further impair proteasomal protein degradation [195], which, along with blocking autophagy, can cause aggravated neuronal dysfunction, accumulation of toxic misfolded protein aggregates, triggering an immunological response in the brain, and ultimately leading to neurodegeneration.

To test this hypothesis, we produced lentiviral vectors expressing either human WT HGSNAT or P311L HGSNAT mutant to transduce cultured hippocampal neurons generated from *Hgsnat-Geo* mouse embryos. In preliminary experiments, we transduced fibroblast cell with lentiviral vectors expressing the WT and mutant HGSNAT and confirmed that the mutant HGSNAT protein was misfolded, lacked enzymatic activity, was not subjected to proteolytic processing, was not directed to the Golgi or lysosomes, and retained in the ER. After analyzing the levels of synaptic proteins in cultured hippocampal neurons from *Hgsnat-Geo* mice that were transduced with lentiviral vectors expressing the WT human HGSNAT enzyme (LV-HGSNAT), we compared them to the levels in non-transduced cells from WT, *Hgsnat-Geo,* and *Hgsnat*^{P304L} mice. We observed a full recovery of the markers of both inhibitory and excitatory synapses, which revealed that genetic defects in HGSNAT were the primary cause of synaptic deficits. Previously, a study by Para et al. 2020 also demonstrated that striatal administration of viral vectors expressing the WT human HGSNAT enzyme (AAV-HGSNAT) rescued synaptic defects in *Hgsnat-Geo* mice and improved their behavior. In contrast, in cultured hippocampal neurons from *Hgsnat-Geo* mice transduced with lentiviral vectors expressing the mutant HGSNAT enzyme (LV-P311-LHGSNAT), the density of inhibitory synapses was reduced, and the density of excitatory

synapses was further reduced to the levels seen in *Hgsnat*^{P304L} neurons. These findings confirm the link between the mutant P311L HGSNAT protein and aggravated synaptic defects. Specifically, the expression of misfolded mutant seemed to be associated with reduced expression of proteins specific for GABAergic synapses, which defects are known to cause seizures and behavioral traits associated with autism [196]. Further advances in the natural history of Sanfilippo disease may help to determine whether patients with MPS IIIC, who have missense mutations causing protein misfolding, display a worsened phenotype.

4.2. Axonal Demyelination in Mucopolysaccharidosis III

Overall, my studies in the novel mouse model of MPS IIIC expanded our understanding of how gray matter pathology contributes to cognitive deterioration. However, the extent of white matter injury, especially demyelination, in patients with MPS III remains largely unknown. While some reports have indicated the presence of white matter abnormalities in MPS IIIA and MPS IIIB [178, 179], other studies suggested the absence of white matter lesions in the majority of MPS III cases [188]. Therefore, further research was needed to explore the potential impact of white matter damage in MPS III patients. To address this, I conducted analyses of axonal myelination in corpus callosum of *Hgsnat*^{P304L} mice using immunohistochemistry and transmission electron microscopy. I also analysed available samples from the fixed post-mortem brain tissues of patients with MPS IIIC, A and D obtained at autopsy with a consent for use in the research. Our study revealed that chronic demyelination as a critical aspect of CNS pathology in MPS IIIC and most likely in other disorders of the MPS III spectrum. First, we observed a significant reduction in the levels of MBP, a marker of myelinated axons, in the corpus callosum of both MPS IIIC mice (*Hgsnat*^{P304L} mice) and MPS IIIC patients at the advanced stages of the disease. MAG and MOG, two other proteins specific for myelin were also decreased or showed a trend towards decreasing. Second, analysis of

the brain tissues at the ultrastructural level revealed that the myelin sheaths in the corpus callosum of MPS IIIC mice had decreased thicknesses. We also observed several structural abnormalities of myelin layers, including outfolded, empty, or split myelin. Similar defects were present in the brain tissues of MPS IIIC patients. Third, the white matter regions of MPS IIIC brains were heavily infiltrated by CD68-positive activated microglia, which showed lysosomal accumulation of MBP and multilamellar fragments (zebra bodies), suggesting that myelin fragments had been phagocytosed.

Severe microgliosis leading to demyelination and axonal degeneration have been reported in various white matter pathologies, such as ischemic injuries, multiple sclerosis, other inflammatory demyelinating diseases, optic nerve diseases, aging, and experimental models of immune encephalomyelitis [197-199]. In particular, the activated proinflammatory microglia directly cause myelin loss in immune encephalomyelitis [199]. However, in the brain of *Hgsnat*^{P304L} mice, we detected a high level of microgliosis from a very young age (as early as P25), but we could not observe the loss of MBP until mice reached 6 months of age. Therefore, we speculate that axonal demyelination in MPS IIIC was not due to abnormalities in early axonal development or detrimental consequences from activated microglia or astrocytes but was instead caused by improper maintenance of myelin by resident OLs.

To verify this hypothesis, we examined the quantity and maturity of OLs in the corpus callosum of *Hgsnat*^{P304L} mice and showed that these cells were scarce and generally lacked maturation. Our previous studies revealed that HGSNAT deficiency and impairment of heparan sulfate catabolism resulted in the intralysosomal accumulation of heparan sulfate in both neurons and microglia of MPS IIIC mice.

To investigate whether heparan sulfate storage also occurs in oligodendrocytes, brain tissues were studied by immunohistochemistry using anti-heparan sulfate monoclonal antibody. These experiments revealed that heparan sulfate storage occurs in multiple oligodendrocytes. A deeper examination of the morphology of OLs using TEM revealed that they had electron-lucent vacuoles that could be associated with the heparan sulfate storage. In addition, we observed another type of storage vacuoles with an electron-dense content appearing as multilamellar bodies or "zebra bodies", typical of lipid storage. Further analysis by IHC, showed that a majority of OLs in the brain of *Hgsnat*^{P304L} mice (but not of the WT mice) were positive for GM3 ganglioside.

Notably, the majority of mitochondria in the OLs of the corpus callosum of 6-month-old *Hgsnat*^{P304L} mice exhibited a dysmorphic ballooned appearance with reduced cristae, which is an important indication of the development of mitochondrial disease. Our lab previously discovered a similar condition that was associated with a progressive decrease in mitochondrial function in the neurons of *Hgsnat-Geo* mice and neurodegeneration [118]. These morphological abnormalities were not present in the OLs in the corpus callosum of WT mice, which led us to hypothesize that the majority of OLs in MPS IIIC animals are at least partially dysfunctional.

Once myelination is completed in the adult brain, the long-term integrity of axons depends on the energy supply to the cells that produce myelin. These cells play a critical role in maintaining connections and functions of the healthy nervous system. Therefore, it is reasonable to consider that impaired mitochondria in these cells, which can lead to reduced maturation and increased degeneration, could be responsible for the demyelination observed in the brains of *Hgsnat*^{P304L} mice.

Other previous studies have shown that the levels of GM3 ganglioside and other simple glycosphingolipids, including GM2 ganglioside, lactosylceramide, and glucosylceramide, are

highly elevated in the brains of MPS III mouse models and MPS III human patients [118, 189, 200]. The most pronounced levels of GM2/GM3 gangliosides were detected in pyramidal neurons in the deep cortex layers and in CA1-CA3 areas of the hippocampus [201, 202]. Our current findings indicate that in contrast to neurons, OLs in the corpus callosum accumulate mainly GM3 but not GM2 ganglioside. Although dispersed GM2-positive cells were detected throughout the corpus callosum region, they did not express the OLs protein marker. Although additional investigations are necessary to determine the exact mechanism responsible for the drastic accumulation of GM3 ganglioside in OLs in the brains of *Hgsnat*^{P304L} mice, we hypothesize that this phenomenon may be linked to the development of myelin defects. Previous studies involving a Niemann-Pick type C (NPC) mouse model, another neurological lysosomal disease where a persistent demyelination is observed, showed that accumulation of GM3 in OLs results in their functional failure [175]. Hypomyelination, prominent in the cerebral cortex and corpus callosum of the NPC mouse model, likely explains the tremor and ataxia observed in these animals [203]. The NPC mice heterozygous for the deletion of Siat9, which encodes for GM3 synthase, demonstrated improvements in both neuropathological features, such as motor disability, and demyelination. Meanwhile, complete deletion of the Siat9 gene resulted in an aggravated neuropathological phenotype and reduced myelination in NPC1/mice, demonstrating that the presence of GM3 ganglioside is required for the development of OLs [175].

Major findings in the MPS IIIC mouse model were confirmed in brain tissues of human MPS IIIC patient, indicating that demyelination and white matter damage play a significant role in pathogenesis of MPS III, at least during the last stages of the disease.

Luxol fast blue staining, a commonly used stain to observe myelin under light microscopy, did not identify any areas with significant demyelination in brains of human patients except for

one region in the brain of a 38-year-old patient. In this particular region, the loss of Luxol fast blue staining was related to the presence of hemosiderin-laden macrophages, suggesting the presence of an old microhemorrhage. This finding may clarify why defects in myelination have not been previously observed in the majority of pathology reports, where brain tissues from patients with MPS IIIC were examined only through traditional histochemical techniques such as Haematoxylin-Eosin and periodic acid-Schiff stain and LFB staining.Importantly, we also found a reduced MBP staining in the post-mortem cortical samples of MPS IIIA and MPS IIID patients obtained from NeuroBiobank, suggesting that patients affected by all subtypes of Sanfilippo disease may exhibit a similar extent of demyelination.

The work our collaborator, Dr. Lodygensky included in our manuscript suggests that magnetic resonance imaging (MRI), generally accepted method for diagnosis of demyelinating disorders, also provides a safe and non-invasive way for clinical assessment of MPS IIIC patients. Specifically, important information on white matter integrity in MPS IIIC mice was obtained using diffusion tensor magnetic resonance imaging (DT-MRI), a recent technological tool developed for visualization and analysis of the white matter in the brain. DT-MRI produces quantitative maps that depict the tissue microstructure by decomposing diffusion signals into axial diffusivity, radial diffusivity, and fractional anisotropy [204]. In addition, Diffusion Basis Spectrum Imaging can provide additional information for an extra-axonal compartment, such as fiber fraction, hindered diffusivity (extracellular), restricted diffusivity (intracellular) and water fraction [205].

Notably, our analysis of diffusivity maps of the corpus callosum of 7-month-old MPS IIIC mice revealed a significant increase in radial diffusivity, suggesting loss of myelin, together with a strong increase of mid-higher isotropic diffusivity indicative of edema and tissue loss. Consistent with the lack of axonal degeneration, MRI examination revealed no alterations in fiber fraction,

fractional anisotropy, or axial diffusivity. On the other hand, we did not detect significant changes in restricted diffusivity, which was expected considering the high level of microgliosis in the corpus callosum of MPSIIIC mice. It is possible, however that, the model we used was not sufficiently sensitive to detect subtle increase in local cellularity because of very dense structure of white matter mainly composed of tightly organized fibers.

Together, our data provide novel insights into pathophysiology of Sanfilippo disease and introduce MRI as a safe diagnosis and imaging tool. However, further studies in human patients are necessary to confirm this finding.

Conclusion

In conclusion, the results of my doctoral research project indicate that the onset and progression of neurological abnormalities in MPS IIIC are the consequences of pathological changes in both gray and white matter.

First our studies validated the novel *Hgsnat*^{P304L} mouse strain as a model of choice for testing prognostic biomarkers of the disease and cutting-edge treatments since it closely mimics the phenotype of MPS IIIC patients with early onset and rapid progression. It also represents a valuable tool to gain deeper insights into the mechanisms underlying MPS III disease, particularly those related to the CNS pathology, as the availability of human material for research is severely limited owing to the low prevalence of MPS IIIC.

Second, my research demonstrated that misfolded mutant HGSNAT protein expression is a key contributing factor for the pathophysiology of MPS IIIC, providing another argument that the *Hgsnat*^{P304L} mouse strain a valuable model for testing the efficacy of pharmaceutical chaperones, which can restore the folding of such mutants, as a potential treatment for this disorder.

Third, our study of white matter injury in MPS IIIC mouse model and human brain samples provides novel insight into the pathophysiology of Sanfilippo disease by revealing that widespread demyelination in the central nervous system is a significant biomarker of disease progression.

Fourth, our results suggest that MRI analysis of brain myelin may potentially become an important non-invasive method for the clinical assessment of MPS III patients.

Chapter 5

References

CHAPTER 5: References

1. De Duve, C., et al., *Tissue fractionation studies. 6. Intracellular distribution patterns of enzymes in rat-liver tissue.* Biochemical Journal, 1955. **60**(4): p. 604.
2. Xu, H. and D. Ren, *Lysosomal physiology.* Annual review of physiology, 2015. **77**: p. 57.
3. Schwake, M. and P. Saftig, *Lysosomal Membrane Defects*, in *Lysosomal Storage Disorders. A Practical Guide*. 2013.
4. Sardiello, M., et al., *A gene network regulating lysosomal biogenesis and function.* Science, 2009. **325**(5939): p. 473-477.
5. Staudt, C., E. Puissant, and M. Boonen, *Subcellular trafficking of mammalian lysosomal proteins: an extended view.* International journal of molecular sciences, 2016. **18**(1): p. 47.
6. Alberts, B., et al., *Transport from the Trans Golgi Network to the cell exterior: Exocytosis*, in *Molecular Biology of the Cell. 4th edition*. 2002, Garland Science.
7. Kornfeld, S. and I. Mellman, *The biogenesis of lysosomes.* Annual review of cell biology, 1989. **5**(1): p. 483-525.
8. Lefrancois, S., et al., *The lysosomal trafficking of sphingolipid activator proteins (SAPs) is mediated by sortilin.* The EMBO journal, 2003. **22**(24): p. 6430-6437.
9. Canuel, M., Y. Libin, and C.R. Morales, *The interactomics of sortilin: an ancient lysosomal receptor evolving new functions.* Histology and histopathology, 2009.
10. Reczek, D., et al., *LIMP-2 is a receptor for lysosomal mannose-6-phosphate-independent targeting of β-glucocerebrosidase.* Cell, 2007. **131**(4): p. 770-783.
11. Janvier, K. and J.S. Bonifacino, *Role of the endocytic machinery in the sorting of lysosome-associated membrane proteins.* Molecular biology of the cell, 2005. **16**(9): p. 4231-4242.
12. Luzio, J.P., P.R. Pryor, and N.A. Bright, *Lysosomes: fusion and function.* Nature reviews Molecular cell biology, 2007. **8**(8): p. 622-632.

13. Fennelly, C. and R.K. Amaravadi, *Lysosomal biology in cancer.* Lysosomes: Methods and Protocols, 2017: p. 293-308.

14. Ballabio, A. and J.S. Bonifacino, *Lysosomes as dynamic regulators of cell and organismal homeostasis.* Nature reviews Molecular cell biology, 2020. **21**(2): p. 101-118.

15. Platt, F.M., B. Boland, and A.C. van der Spoel, *Lysosomal storage disorders: The cellular impact of lysosomal dysfunction.* Journal of Cell Biology, 2012. **199**(5): p. 723-734.

16. Yang, C. and X. Wang, *Lysosome biogenesis: Regulation and functions.* Journal of Cell Biology, 2021. **220**(6): p. e202102001.

17. Saftig, P. and J. Klumperman, *Lysosome biogenesis and lysosomal membrane proteins: trafficking meets function.* Nature reviews Molecular cell biology, 2009. **10**(9): p. 623-635.

18. Meikle, P.J., et al., *Prevalence of lysosomal storage disorders.* Jama, 1999. **281**(3): p. 249-254.

19. Platt, F.M., et al., *Lysosomal storage diseases.* Nature Reviews Disease Primers, 2018. **4**(1): p. 1-25.

20. Pará, C., P. Bose, and A.V. Pshezhetsky, *Neuropathophysiology of lysosomal storage diseases: synaptic dysfunction as a starting point for disease progression.* Journal of clinical medicine, 2020. **9**(3): p. 616.

21. Filocamo, M. and A. Morrone, *Lysosomal storage disorders: molecular basis and laboratory testing.* Human genomics, 2011. **5**(3): p. 1-14.

22. Wraith, J.E., *The clinical presentation of lysosomal storage disorders.* Acta Neurologica Taiwanica, 2004. **13**: p. 101-106.

23. Boustany, R.-M.N., *Lysosomal storage diseases—the horizon expands.* Nature Reviews Neurology, 2013. **9**(10): p. 583-598.

24. Ballabio, A. and V. Gieselmann, *Lysosomal disorders: from storage to cellular damage.* Biochimica et Biophysica Acta (BBA)-Molecular Cell Research, 2009. **1793**(4): p. 684-696.

25. Martins, C., et al., *Molecular characterization of a large group of Mucopolysaccharidosis type IIIC patients reveals the evolutionary history of the disease.* Human mutation, 2019. **40**(8): p. 1084-1100.

26. Neufeld, F., *The mucopolysaccharidoses.* The metabolic and molecular bases of inherited disease, 2001: p. 3421-3452.

27. Filocamo, M. and A. Morrone, *Lysosomal storage disorders: molecular basis and laboratory testing.* Human genomics, 2011. **5**: p. 1-14.

28. Bodamer, O.A., R. Giugliani, and T. Wood, *The laboratory diagnosis of mucopolysaccharidosis III (Sanfilippo syndrome): A changing landscape.* Molecular Genetics and Metabolism, 2014. **113**(1-2): p. 34-41.

29. Coutinho, M.F., L. Lacerda, and S. Alves, *Glycosaminoglycan storage disorders: a review.* Biochemistry research international, 2012. **2012**.

30. Khan, S.A., et al., *Epidemiology of mucopolysaccharidoses.* Molecular genetics and metabolism, 2017. **121**(3): p. 227-240.

31. Valstar, M.J., et al., *Sanfilippo syndrome: a mini-review.* Journal of inherited metabolic disease, 2008. **31**: p. 240-252.

32. Neufeld, E.F., *Lysosomal storage diseases.* Annual review of biochemistry, 1991. **60**(1): p. 257-280.

33. Seker Yilmaz, B., et al., *Novel therapies for mucopolysaccharidosis type III.* Journal of Inherited Metabolic Disease, 2021. **44**(1): p. 129-147.

34. Sugahara, K. and H. Kitagawa, *Heparin and heparan sulfate biosynthesis.* IUBMB life, 2002. **54**(4): p. 163-175.

35. Li, J.-P. and M. Kusche-Gullberg, *Heparan sulfate: biosynthesis, structure, and function.* International review of cell and molecular biology, 2016. **325**: p. 215-273.

36. Kreuger, J. and L. Kjellén, *Heparan sulfate biosynthesis: regulation and variability.* Journal of Histochemistry & Cytochemistry, 2012. **60**(12): p. 898-907.

37. Kim, B.-T., et al., *Human tumor suppressor EXT gene family members EXTL1 and EXTL3 encode α1, 4-N-acetylglucosaminyltransferases that likely are involved in heparan sulfate/heparin biosynthesis.* Proceedings of the National Academy of Sciences, 2001. **98**(13): p. 7176-7181.

38. Esko, J.D. and U. Lindahl, *Molecular diversity of heparan sulfate.* The Journal of clinical investigation, 2001. **108**(2): p. 169-173.

39. Pinhal, M.A., et al., *Enzyme interactions in heparan sulfate biosynthesis: uronosyl 5-epimerase and 2-O-sulfotransferase interact in vivo.* Proceedings of the National Academy of Sciences, 2001. **98**(23): p. 12984-12989.

40. Smeds, E., et al., *Substrate specificities of mouse heparan sulphate glucosaminyl 6-O-sulphotransferases.* Biochemical Journal, 2003. **372**(2): p. 371-380.

41. Weiss, R.J., J.D. Esko, and Y. Tor, *Targeting heparin and heparan sulfate protein interactions.* Organic & biomolecular chemistry, 2017. **15**(27): p. 5656-5668.

42. Sarrazin, S., W.C. Lamanna, and J.D. Esko, *Heparan sulfate proteoglycans.* Cold Spring Harbor perspectives in biology, 2011. **3**(7): p. a004952.

43. Christianson, H.C. and M. Belting, *Heparan sulfate proteoglycan as a cell-surface endocytosis receptor.* Matrix Biology, 2014. **35**: p. 51-55.

44. Payne, C.K., et al., *Internalization and trafficking of cell surface proteoglycans and proteoglycan-binding ligands.* Traffic, 2007. **8**(4): p. 389-401.

45. Saied-Santiago, K. and H.E. Bülow, *Diverse roles for glycosaminoglycans in neural patterning.* Developmental Dynamics, 2018. **247**(1): p. 54-74.

46. Kirn-Safran, C.B., S.S. D'Souza, and D.D. Carson. *Heparan sulfate proteoglycans and their binding proteins in embryo implantation and placentation*. in *Seminars in cell & developmental biology*. 2008. Elsevier.

47. Bink, R.J., et al., *Heparan sulfate 6-O-sulfotransferase is essential for muscle development in zebrafish.* Journal of Biological Chemistry, 2003. **278**(33): p. 31118-31127.

48. Fernández-Vega, I., et al., *Heparan sulfate proteoglycans undergo differential expression alterations in right sided colorectal cancer, depending on their metastatic character.* BMC cancer, 2015. **15**(1): p. 1-20.

49. Rops, A.L., et al., *Heparan sulfate proteoglycans in glomerular inflammation.* Kidney international, 2004. **65**(3): p. 768-785.

50. Holmes, B.B., et al., *Heparan sulfate proteoglycans mediate internalization and propagation of specific proteopathic seeds.* Proceedings of the National Academy of Sciences, 2013. **110**(33): p. E3138-E3147.

51. Ai, X., et al., *Substrate specificity and domain functions of extracellular heparan sulfate 6-O-endosulfatases, QSulf1 and QSulf2.* Journal of Biological Chemistry, 2006. **281**(8): p. 4969-4976.

52. Gong, F., et al., *Processing of macromolecular heparin by heparanase.* Journal of Biological Chemistry, 2003. **278**(37): p. 35152-35158.

53. Freeze, H.H., *Genetic disorders of glycan degradation.* Essentials of Glycobiology. 2nd edition, 2009.

54. Minami, K., et al., *Pathogenic Roles of Heparan Sulfate and Its Use as a Biomarker in Mucopolysaccharidoses.* International Journal of Molecular Sciences, 2022. **23**(19): p. 11724.

55. Andrade, F., et al., *Sanfilippo syndrome: Overall review.* Pediatrics International, 2015. **57**(3): p. 331-338.

56. Bartsocas, C., et al., *Sanfilippo type C disease: clinical findings in four patients with a new variant of mucopolysaccharidosis III.* European journal of pediatrics, 1979. **130**: p. 251-258.

57. Hřebíček, M., et al., *Mutations in TMEM76 cause mucopolysaccharidosis IIIC (Sanfilippo C syndrome).* The American Journal of Human Genetics, 2006. **79**(5): p. 807-819.

58. Fan, X., et al., *Identification of the gene encoding the enzyme deficient in mucopolysaccharidosis IIIC (Sanfilippo disease type C).* The American Journal of Human Genetics, 2006. **79**(4): p. 738-744.

59. Feldhammer, M., S. Durand, and A.V. Pshezhetsky, *Protein misfolding as an underlying molecular defect in mucopolysaccharidosis III type C.* PloS one, 2009. **4**(10): p. e7434.

60. Durand, S., et al., *Analysis of the biogenesis of heparan sulfate acetyl-CoA: α-glucosaminide N-acetyltransferase provides insights into the mechanism underlying its complete deficiency in mucopolysaccharidosis IIIC.* Journal of biological chemistry, 2010. **285**(41): p. 31233-31242.

61. Bame, K.J. and L.H. Rome, *Genetic evidence for transmembrane acetylation by lysosomes.* Science, 1986. **233**(4768): p. 1087-1089.

62. Bame, K. and L. Rome, *Acetyl-coenzyme A: alpha-glucosaminide N-acetyltransferase. Evidence for an active site histidine residue.* Journal of Biological Chemistry, 1986. **261**(22): p. 10127-10132.

63. Fedele, A.O., *Sanfilippo syndrome: causes, consequences, and treatments.* The application of clinical genetics, 2015: p. 269-281.

64. Fedele, A.O., et al., *Mutational analysis of the HGSNAT gene in Italian patients with mucopolysaccharidosis IIIC (Sanfilippo C syndrome).* Human mutation, 2007. **28**(5): p. 523-523.

65. Coutinho, M.F., et al., *Molecular characterization of Portuguese patients with mucopolysaccharidosis IIIC: two novel mutations in the HGSNAT gene.* Clinical genetics, 2008. **74**(2): p. 194-195.

66. Canals, I., et al., *Molecular analysis of Sanfilippo syndrome type C in Spain: seven novel HGSNAT mutations and characterization of the mutant alleles.* Clinical Genetics, 2011. **80**(4): p. 367-374.

67. Huh, H.J., et al., *The first Korean case of mucopolysaccharidosis IIIC (Sanfilippo syndrome type C) confirmed by biochemical and molecular investigation.* Annals of Laboratory Medicine, 2013. **33**(1): p. 75.

68. He, B., *Viruses, endoplasmic reticulum stress, and interferon responses.* Cell Death & Differentiation, 2006. **13**(3): p. 393-403.

69. Hetz, C.A. and C. Soto, *Stressing out the ER: a role of the unfolded protein response in prion-related disorders.* Current molecular medicine, 2006. **6**(1): p. 37-43.

70. Szegezdi, E., et al., *Mediators of endoplasmic reticulum stress-induced apoptosis.* EMBO reports, 2006. **7**(9): p. 880-885.

71. Wang, S. and R.J. Kaufman, *The impact of the unfolded protein response on human disease.* Journal of Cell Biology, 2012. **197**(7): p. 857-867.

72. Vitner, E.B., F.M. Platt, and A.H. Futerman, *Common and uncommon pathogenic cascades in lysosomal storage diseases.* Journal of Biological Chemistry, 2010. **285**(27): p. 20423-20427.

73. Wei, H., et al., *ER and oxidative stresses are common mediators of apoptosis in both neurodegenerative and non-neurodegenerative lysosomal storage disorders and are alleviated by chemical chaperones.* Human molecular genetics, 2008. **17**(4): p. 469-477.

74. Tessitore, A., et al., *GM1-ganglioside-mediated activation of the unfolded protein response causes neuronal death in a neurodegenerative gangliosidosis.* Molecular cell, 2004. **15**(5): p. 753-766.

75. Farfel-Becker, T., et al., *No evidence for activation of the unfolded protein response in neuronopathic models of Gaucher disease.* Human molecular genetics, 2009. **18**(8): p. 1482-1488.

76. Villani, G.R., et al., *Unfolded protein response is not activated in the mucopolysaccharidoses but protein disulfide isomerase 5 is deregulated.* Journal of inherited metabolic disease, 2012. **35**: p. 479-493.

77. Kobolák, J., et al., *Modelling the neuropathology of lysosomal storage disorders through disease-specific human induced pluripotent stem cells.* Experimental Cell Research, 2019. **380**(2): p. 216-233.

78. Bosch, M.E. and T. Kielian, *Neuroinflammatory paradigms in lysosomal storage diseases.* Frontiers in neuroscience, 2015. **9**: p. 417.

79. Edelmann, M.J. and G.H. Maegawa, *CNS-targeting therapies for lysosomal storage diseases: current advances and challenges.* Frontiers in molecular biosciences, 2020. **7**: p. 559804.

80. Verity, C., et al., *The epidemiology of progressive intellectual and neurological deterioration in childhood.* Archives of disease in childhood, 2010. **95**(5): p. 361-364.

81. Lie, P.P. and R.A. Nixon, *Lysosome trafficking and signaling in health and neurodegenerative diseases.* Neurobiology of disease, 2019. **122**: p. 94-105.

82. Bellettato, C.M. and M. Scarpa, *Pathophysiology of neuropathic lysosomal storage disorders.* Journal of inherited metabolic disease, 2010. **33**: p. 347-362.

83. Toledano-Zaragoza, A. and M.D. Ledesma, *Addressing neurodegeneration in lysosomal storage disorders: Advances in Niemann Pick diseases.* Neuropharmacology, 2020. **171**: p. 107851.

84. Rebiai, R., et al., *Synaptic function and dysfunction in lysosomal storage diseases.* Frontiers in Cellular Neuroscience, 2021: p. 55.

85. Nixon, R.A., D.-S. Yang, and J.-H. Lee, *Neurodegenerative lysosomal disorders: a continuum from development to late age.* Autophagy, 2008. **4**(5): p. 590-599.

86. Ferguson, S.M., *Axonal transport and maturation of lysosomes.* Current opinion in neurobiology, 2018. **51**: p. 45-51.

87. Ko, D.C., et al., *Cell-autonomous death of cerebellar purkinje neurons with autophagy in Niemann-Pick type C disease.* PLoS genetics, 2005. **1**(1): p. e7.

88. Pacheco, C.D., M.J. Elrick, and A.P. Lieberman, *Tau deletion exacerbates the phenotype of Niemann–Pick type C mice and implicates autophagy in pathogenesis.* Human molecular genetics, 2009. **18**(5): p. 956-965.

89. Sun, Y., et al., *Neuronopathic Gaucher disease in the mouse: viable combined selective saposin C deficiency and mutant glucocerebrosidase (V394L) mice with glucosylsphingosine and glucosylceramide accumulation and progressive neurological deficits.* Human molecular genetics, 2010. **19**(6): p. 1088-1097.

90. Chévrier, M., et al., *Autophagosome maturation is impaired in Fabry disease.* Autophagy, 2010. **6**(5): p. 589-599.

91. Takamura, A., et al., *Enhanced autophagy and mitochondrial aberrations in murine GM1-gangliosidosis.* Biochemical and biophysical research communications, 2008. **367**(3): p. 616-622.

92. Koike, M., et al., *Participation of autophagy in storage of lysosomes in neurons from mouse models of neuronal ceroid-lipofuscinoses (Batten disease).* The American journal of pathology, 2005. **167**(6): p. 1713-1728.

93. Li, X., et al., *A molecular mechanism to regulate lysosome motility for lysosome positioning and tubulation.* Nature cell biology, 2016. **18**(4): p. 404-417.

94. Kollmann, K., et al., *Lysosomal dysfunction causes neurodegeneration in mucolipidosis II 'knock-in'mice.* Brain, 2012. **135**(9): p. 2661-2675.

95. Maeda, M., et al., *Autophagy in the central nervous system and effects of chloroquine in mucopolysaccharidosis type II mice.* International journal of molecular sciences, 2019. **20**(23): p. 5829.

96. Settembre, C., et al., *A block of autophagy in lysosomal storage disorders.* Human molecular genetics, 2008. **17**(1): p. 119-129.

97. Lotfi, P., et al., *Trehalose reduces retinal degeneration, neuroinflammation and storage burden caused by a lysosomal hydrolase deficiency.* Autophagy, 2018. **14**(8): p. 1419-1434.

98. Teixeira, C.A., et al., *Early axonal loss accompanied by impaired endocytosis, abnormal axonal transport, and decreased microtubule stability occur in the model of Krabbe's disease.* Neurobiology of disease, 2014. **66**: p. 92-103.

99. Xu, S., et al., *Defects of synaptic vesicle turnover at excitatory and inhibitory synapses in Niemann–Pick C1-deficient neurons.* Neuroscience, 2010. **167**(3): p. 608-620.

100. Wilkinson, F.L., et al., *Neuropathology in mouse models of mucopolysaccharidosis type I, IIIA and IIIB.* PloS one, 2012. **7**(4): p. e35787.

101. Sambri, I., et al., *Lysosomal dysfunction disrupts presynaptic maintenance and restoration of presynaptic function prevents neurodegeneration in lysosomal storage diseases.* EMBO molecular medicine, 2017. **9**(1): p. 112-132.

102. Dwyer, C.A., et al., *Neurodevelopmental changes in excitatory synaptic structure and function in the cerebral cortex of Sanfilippo syndrome IIIA mice.* Scientific reports, 2017. **7**(1): p. 1-11.

103. Button, R.W., et al., *Accumulation of autophagosomes confers cytotoxicity.* Journal of Biological Chemistry, 2017. **292**(33): p. 13599-13614.

104. Sharma, S. and M. Lindau, *t-SNARE transmembrane domain clustering modulates lipid organization and membrane curvature.* Journal of the American Chemical Society, 2017. **139**(51): p. 18440-18443.

105. Button, R.W. and S. Luo, *The formation of autophagosomes during lysosomal defect: A new source of cytotoxicity.* Autophagy, 2017. **13**(10): p. 1797-1798.

106. White, A.B., et al., *Psychosine accumulates in membrane microdomains in the brain of krabbe patients, disrupting the raft architecture.* Journal of Neuroscience, 2009. **29**(19): p. 6068-6077.

107. Baldo, G., et al., *Shotgun proteomics reveals possible mechanisms for cognitive impairment in Mucopolysaccharidosis I mice.* Molecular Genetics and Metabolism, 2015. **114**(2): p. 138-145.

108. Vitry, S., et al., *Enhanced degradation of synaptophysin by the proteasome in mucopolysaccharidosis type IIIB.* Molecular and Cellular Neuroscience, 2009. **41**(1): p. 8-18.

109. Bayó-Puxan, N., et al., *Lysosomal and network alterations in human mucopolysaccharidosis type VII iPSC-derived neurons.* Scientific reports, 2018. **8**(1): p. 16644.

110. Llavero Hurtado, M., et al., *Proteomic mapping of differentially vulnerable pre-synaptic populations identifies regulators of neuronal stability in vivo.* Scientific reports, 2017. **7**(1): p. 12412.

111. Amorim, I.s.S., et al., *Molecular neuropathology of the synapse in sheep with CLN 5 Batten disease.* Brain and behavior, 2015. **5**(11): p. e00401.

112. Kanninen, K.M., et al., *Increased zinc and manganese in parallel with neurodegeneration, synaptic protein changes and activation of Akt/GSK3 signaling in ovine CLN6 neuronal ceroid lipofuscinosis.* PLoS One, 2013. **8**(3): p. e58644.

113. Para, C., et al., *Early defects in mucopolysaccharidosis type IIIC disrupt excitatory synaptic transmission.* JCI insight, 2021. **6**(15).

114. Tremblay, M.-È., et al., *The role of microglia in the healthy brain.* Journal of Neuroscience, 2011. **31**(45): p. 16064-16069.

115. Meldolesi, J., *Astrocytes: news about brain health and diseases.* Biomedicines, 2020. **8**(10): p. 394.

116. Vainchtein, I.D. and A.V. Molofsky, *Astrocytes and microglia: in sickness and in health.* Trends in Neurosciences, 2020. **43**(3): p. 144-154.

117. Carson, M.J., J.C. Thrash, and B. Walter, *The cellular response in neuroinflammation: The role of leukocytes, microglia and astrocytes in neuronal death and survival.* Clinical neuroscience research, 2006. **6**(5): p. 237-245.

118. Martins, C., et al., *Neuroinflammation, mitochondrial defects and neurodegeneration in mucopolysaccharidosis III type C mouse model.* Brain, 2015. **138**(2): p. 336-355.

119. Potter, G.B. and M.A. Petryniak, *Neuroimmune mechanisms in K rabbe's disease.* Journal of Neuroscience Research, 2016. **94**(11): p. 1341-1348.

120. Sakai, N., et al., *Molecular cloning and expression of cDNA for murine galactocerebrosidase and mutation analysis of the twitcher mouse, a model of Krabbe's disease.* Journal of neurochemistry, 1996. **66**(3): p. 1118-1124.

121. Luzi, P., et al., *Effects of treatments on inflammatory and apoptotic markers in the CNS of mice with globoid cell leukodystrophy.* Brain research, 2009. **1300**: p. 146-158.

122. Potter, G.B., et al., *Missense mutation in mouse GALC mimics human gene defect and offers new insights into Krabbe disease.* Human molecular genetics, 2013. **22**(17): p. 3397-3414.

123. Boddupalli, C.S., et al., *Neuroinflammation in neuronopathic Gaucher disease: Role of microglia and NK cells, biomarkers, and response to substrate reduction therapy.* Elife, 2022. **11**: p. e79830.

124. Jeyakumar, M., et al., *Storage solutions: treating lysosomal disorders of the brain.* Nature Reviews Neuroscience, 2005. **6**(9): p. 713-725.

125. Cooper, J.D., C. Russell, and H.M. Mitchison, *Progress towards understanding disease mechanisms in small vertebrate models of neuronal ceroid lipofuscinosis.* Biochimica et Biophysica Acta (BBA)-Molecular Basis of Disease, 2006. **1762**(10): p. 873-889.

126. Johansen-Berg, H. and T.E. Behrens, *Diffusion MRI: from quantitative measurement to in vivo neuroanatomy*. 2013: Academic Press.

127. Edgar, J.M. and I.R. Griffiths, *White matter structure: a microscopist's view*, in *Diffusion Mri*. 2009, Elsevier. p. 74-103.

128. Nixon, R.A., *Dynamic behavior and organization of cytoskeletal proteins in neurons: reconciling old and new findings.* Bioessays, 1998. **20**(10): p. 798-807.

129. Bearer, E. and T. Reese, *Association of actin filaments with axonal microtubule tracts.* Journal of neurocytology, 1999. **28**: p. 85-98.

130. Hoffman, P., et al., *Slowing of neurofilament transport and the radial growth of developing nerve fibers.* Journal of Neuroscience, 1985. **5**(11): p. 2920-2929.

131. CLEVELAND, D.W., et al., *Involvement of neurofilaments in the radial growth of axons.* Journal of Cell Science, 1991. **1991**(Supplement_15): p. 85-95.

132. García-Marín, V., P. García-López, and M. Freire, *Cajal's contributions to glia research.* Trends in neurosciences, 2007. **30**(9): p. 479-487.

133. Fogarty, M., W.D. Richardson, and N. Kessaris, *A subset of oligodendrocytes generated from radial glia in the dorsal spinal cord.* 2005.

134. Vallstedt, A., J.M. Klos, and J. Ericson, *Multiple dorsoventral origins of oligodendrocyte generation in the spinal cord and hindbrain.* Neuron, 2005. **45**(1): p. 55-67.

135. Bradl, M. and H. Lassmann, *Oligodendrocytes: biology and pathology.* Acta neuropathologica, 2010. **119**: p. 37-53.

136. Kessaris, N., et al., *Competing waves of oligodendrocytes in the forebrain and postnatal elimination of an embryonic lineage.* Nature neuroscience, 2006. **9**(2): p. 173-179.

137. Redwine, J.M., K.L. Blinder, and R.C. Armstrong, *In situ expression of fibroblast growth factor receptors by oligodendrocyte progenitors and oligodendrocytes in adult mouse central nervous system.* Journal of neuroscience research, 1997. **50**(2): p. 229-237.

138. Spassky, N., et al., *Sonic hedgehog-dependent emergence of oligodendrocytes in the telencephalon: evidence for a source of oligodendrocytes in the olfactory bulb that is independent of PDGFRα signaling.* 2001.

139. Yan, H. and S.A. Rivkees, *Hepatocyte growth factor stimulates the proliferation and migration of oligodendrocyte precursor cells.* Journal of neuroscience research, 2002. **69**(5): p. 597-606.

140. Jarjour, A.A., et al., *Netrin-1 is a chemorepellent for oligodendrocyte precursor cells in the embryonic spinal cord.* Journal of Neuroscience, 2003. **23**(9): p. 3735-3744.

141. Tsai, H.-H., M. Tessier-Lavigne, and R.H. Miller, *Netrin 1 mediates spinal cord oligodendrocyte precursor dispersal.* 2003.

142. Mitew, S., et al., *Mechanisms regulating the development of oligodendrocytes and central nervous system myelin.* Neuroscience, 2014. **276**: p. 29-47.

143. Raff, M.C., E.R. Abney, and R.H. Miller, *Two glial cell lineages diverge prenatally in rat optic nerve.* Developmental biology, 1984. **106**(1): p. 53-60.

144. Kuhn, S., et al., *Oligodendrocytes in development, myelin generation and beyond.* Cells, 2019. **8**(11): p. 1424.

145. Simons, M. and K. Trajkovic, *Neuron-glia communication in the control of oligodendrocyte function and myelin biogenesis.* Journal of cell science, 2006. **119**(21): p. 4381-4389.

146. Saab, A.S., I.D. Tzvetanova, and K.-A. Nave, *The role of myelin and oligodendrocytes in axonal energy metabolism.* Current opinion in neurobiology, 2013. **23**(6): p. 1065-1072.

147. Berger, T., et al., *GABA-and glutamate-activated currents in glial cells of the mouse corpus callosum slice.* Journal of neuroscience research, 1992. **31**(1): p. 21-27.

148. Yamazaki, Y., et al., *Oligodendrocytes: facilitating axonal conduction by more than myelination.* The Neuroscientist, 2010. **16**(1): p. 11-18.

149. Dougherty, K.D., C.F. Dreyfus, and I.B. Black, *Brain-derived neurotrophic factor in astrocytes, oligodendrocytes, and microglia/macrophages after spinal cord injury.* Neurobiology of disease, 2000. **7**(6): p. 574-585.

150. Boullerne, A.I., *The history of myelin.* Experimental neurology, 2016. **283**: p. 431-445.

151. Zalc, B. *The acquisition of myelin: a success story*. in *Purinergic Signalling in Neuron–Glia Interactions: Novartis Foundation Symposium 276*. 2006. Wiley Online Library.

152. Fields, R.D., *Myelination: an overlooked mechanism of synaptic plasticity?* The Neuroscientist, 2005. **11**(6): p. 528-531.

153. Fields, R.D., *A new mechanism of nervous system plasticity: activity-dependent myelination.* Nature Reviews Neuroscience, 2015. **16**(12): p. 756-767.

154. Almeida, R.G. and D.A. Lyons, *On myelinated axon plasticity and neuronal circuit formation and function.* Journal of Neuroscience, 2017. **37**(42): p. 10023-10034.

155. Berthold, C. and S. Skoglund, *Postnatal development of feline paranodal myelin-sheath segments. II. Electron microscopy.* Acta Societatis medicorum upsaliensis, 1968. **73**(3-4): p. 127-144.

156. Baumann, N. and D. Pham-Dinh, *Biology of oligodendrocyte and myelin in the mammalian central nervous system.* Physiological reviews, 2001. **81**(2): p. 871-927.

157. Morell P, Q.R.C.C.o.M.I.S.G., Agranoff BW, Albers RW, et al., editors, *Basic Neurochemistry: Molecular, Cellular and Medical Aspects. 6th edition.* 1999.

158. O'Brien, J.S., *Stability of the Myelin Membrane: Lipid molecules may impart stability to the myelin membrane through intermolecular cohesion.* Science, 1965. **147**(3662): p. 1099-1107.

159. Poitelon, Y., A.M. Kopec, and S. Belin, *Myelin fat facts: an overview of lipids and fatty acid metabolism.* Cells, 2020. **9**(4): p. 812.

160. Simons, M., et al., *Assembly of myelin by association of proteolipid protein with cholesterol-and galactosylceramide-rich membrane domains.* The Journal of cell biology, 2000. **151**(1): p. 143-154.

161. Hemmer, B., J.J. Archelos, and H.-P. Hartung, *New concepts in the immunopathogenesis of multiple sclerosis.* Nature Reviews Neuroscience, 2002. **3**(4): p. 291-301.

162. Schnaar, R.L. and P.H. Lopez, *Myelin-associated glycoprotein and its axonal receptors.* Journal of neuroscience research, 2009. **87**(15): p. 3267-3276.

163. Johns, T.G. and C.C. Bernard, *The structure and function of myelin oligodendrocyte glycoprotein.* Journal of neurochemistry, 1999. **72**(1): p. 1-9.

164. Shen, Y.-T., et al., *The roles of lysosomal exocytosis in regulated myelination.* Journal of Neurology & Neuromedicine, 2016. **1**(5).

165. Nah, J., J. Yuan, and Y.-K. Jung, *Autophagy in neurodegenerative diseases: from mechanism to therapeutic approach.* Molecules and cells, 2015. **38**(5): p. 381.

166. Wenger, D.A., M.A. Rafi, and P. Luzi, *Molecular genetics of Krabbe disease (globoid cell leukodystrophy): diagnostic and clinical implications.* Human mutation, 1997. **10**(4): p. 268-279.

167. Gieselmann, V., *Metachromatic leukodystrophy: genetics, pathogenesis and therapeutic options.* Acta Paediatrica, 2008. **97**: p. 15-21.

168. Burand Jr, A.J. and C.L. Stucky, *Fabry disease pain: patient and preclinical parallels.* Pain, 2021. **162**(5): p. 1305.

169. Maegawa, G.H., *Lysosomal leukodystrophies lysosomal storage diseases associated with white matter abnormalities.* Journal of child neurology, 2019. **34**(6): p. 339-358.

170. Giri, S., et al., *Krabbe disease: psychosine-mediated activation of phospholipase A2 in oligodendrocyte cell death.* Journal of lipid research, 2006. **47**(7): p. 1478-1492.

171. Beerepoot, S., et al., *Peripheral neuropathy in metachromatic leukodystrophy: current status and future perspective.* Orphanet Journal of Rare Diseases, 2019. **14**: p. 1-13.

172. Poretti, A., et al., *Novel diffusion tensor imaging findings in Krabbe disease.* European Journal of Paediatric Neurology, 2014. **18**(2): p. 150-156.

173. Groeschel, S., et al., *Metachromatic leukodystrophy: natural course of cerebral MRI changes in relation to clinical course.* Journal of inherited metabolic disease, 2011. **34**: p. 1095-1102.

174. Lau, M.W., et al., *Role of diffusion tensor imaging in prognostication and treatment monitoring in Niemann-pick disease type C1.* Diseases, 2016. **4**(3): p. 29.

175. Lee, H., et al., *Inhibition of GM3 synthase attenuates neuropathology of Niemann-Pick disease Type C by affecting sphingolipid metabolism.* Molecules and cells, 2014. **37**(2): p. 161.

176. Tuteja, M., et al., *White matter changes in GM1 gangliosidosis.* Indian Pediatr, 2015. **52**(2): p. 155-156.

177. Imamura, A., et al., *Serial MR imaging and 1H-MR spectroscopy in monozygotic twins with Tay-Sachs disease.* Neuropediatrics, 2008. **39**(05): p. 259-263.

178. Kara, S., E.H. Sherr, and A.J. Barkovich, *Dilated perivascular spaces: an informative radiologic finding in Sanfilippo syndrome type A.* Pediatric neurology, 2008. **38**(5): p. 363-366.

179. Zafeiriou, D.I., et al., *Serial magnetic resonance imaging findings in mucopolysaccharidosis IIIB (Sanfilippo's syndrome B).* Brain and Development, 2001. **23**(6): p. 385-389.

180. Walkley, S.U., et al., *Lysosomal compromise and brain dysfunction: examining the role of neuroaxonal dystrophy*. 2010, Portland Press Ltd.

181. Lee, S., Y. Sato, and R.A. Nixon, *Lysosomal proteolysis inhibition selectively disrupts axonal transport of degradative organelles and causes an Alzheimer's-like axonal dystrophy.* Journal of Neuroscience, 2011. **31**(21): p. 7817-7830.

182. Walkley, S.U., et al., *Neuroaxonal dystrophy in neuronal storage disorders: evidence for major GABAergic neuron involvement.* Journal of the neurological sciences, 1991. **104**(1): p. 1-8.

183. March, P.A., et al., *GABAergic neuroaxonal dystrophy and other cytopathological alterations in feline Niemann-Pick disease type C.* Acta neuropathologica, 1997. **94**: p. 164-172.

184. Pressey, S.N., et al., *Early glial activation, synaptic changes and axonal pathology in the thalamocortical system of Niemann–Pick type C1 mice.* Neurobiology of disease, 2012. **45**(3): p. 1086-1100.

185. Castelvetri, L.C., et al., *Axonopathy is a compounding factor in the pathogenesis of Krabbe disease.* Acta neuropathologica, 2011. **122**: p. 35-48.

186. Shapiro, E.G., et al., *A prospective natural history study of mucopolysaccharidosis type IIIA.* The Journal of pediatrics, 2016. **170**: p. 278-287. e4.

187. Whitley, C.B., et al., *Observational prospective natural history of patients with Sanfilippo syndrome type B.* The Journal of pediatrics, 2018. **197**: p. 198-206. e2.

188. Reichert, R., et al., *Magnetic resonance imaging findings of the posterior fossa in 47 patients with mucopolysaccharidoses: A cross-sectional analysis.* JIMD reports, 2021. **60**(1): p. 32-41.

189. Pan, X., et al., *Glucosamine amends CNS pathology in mucopolysaccharidosis IIIC mouse expressing misfolded HGSNAT.* Journal of Experimental Medicine, 2022. **219**(8): p. e20211860.

190. Maegawa, G.H., et al., *Pyrimethamine as a potential pharmacological chaperone for late-onset forms of GM2 gangliosidosis.* Journal of Biological Chemistry, 2007. **282**(12): p. 9150-9161.

191. Tropak, M.B., et al., *Pharmacological enhancement of β-hexosaminidase activity in fibroblasts from adult Tay-Sachs and Sandhoff patients.* Journal of Biological Chemistry, 2004. **279**(14): p. 13478-13487.

192. Haer-Wigman, L., et al., *Non-syndromic retinitis pigmentosa due to mutations in the mucopolysaccharidosis type IIIC gene, heparan-alpha-glucosaminide N-acetyltransferase (HGSNAT).* Human molecular genetics, 2015. **24**(13): p. 3742-3751.

193. Berger-Plantinga, E.G., et al., *Adult-onset dementia and retinitis pigmentosa due to mucopolysaccharidosis III-C in two sisters.* Journal of neurology, 2004. **251**: p. 479-481.

194. Feldhammer, M., et al., *Sanfilippo syndrome type C: mutation spectrum in the heparan sulfate acetyl-CoA: α-glucosaminide N-acetyltransferase (HGSNAT) gene.* Human mutation, 2009. **30**(6): p. 918-925.

195. Bifsha, P., et al., *Altered gene expression in cells from patients with lysosomal storage disorders suggests impairment of the ubiquitin pathway.* Cell Death & Differentiation, 2007. **14**(3): p. 511-523.

196. Chao, H.-T., et al., *Dysfunction in GABA signalling mediates autism-like stereotypies and Rett syndrome phenotypes.* Nature, 2010. **468**(7321): p. 263-269.

197. Alturkustani, M. and L.-C. Ang, *White matter cellular changes in ischemic injuries.* American Journal of Translational Research, 2022. **14**(8): p. 5859.

198. Correale, J. and M.C. Ysrraelit, *Multiple Sclerosis and Aging: The Dynamics of Demyelination and Remyelination.* ASN neuro, 2022. **14**: p. 17590914221118502.

199. Yazdankhah, M., et al., *Role of glia in optic nerve.* Progress in retinal and eye research, 2021. **81**: p. 100886.

200. Viana, G.M., et al., *Brain pathology in mucopolysaccharidoses (MPS) patients with neurological forms.* Journal of clinical medicine, 2020. **9**(2): p. 396.

201. Walkley, S.U. and M.T. Vanier, *Secondary lipid accumulation in lysosomal disease.* Biochimica et Biophysica Acta (BBA)-Molecular Cell Research, 2009. **1793**(4): p. 726-736.

202. McGlynn, R., K. Dobrenis, and S.U. Walkley, *Differential subcellular localization of cholesterol, gangliosides, and glycosaminoglycans in murine models of mucopolysaccharide storage disorders.* Journal of Comparative Neurology, 2004. **480**(4): p. 415-426.

203. Takikita, S., et al., *Perturbed myelination process of premyelinating oligodendrocyte in niemann-picktype C mouse.* Journal of Neuropathology & Experimental Neurology, 2004. **63**(6): p. 660-673.

204. O'Donnell, L.J. and C.-F. Westin, *An introduction to diffusion tensor image analysis.* Neurosurgery Clinics, 2011. **22**(2): p. 185-196.

205. Wang, Y., et al., *Quantification of increased cellularity during inflammatory demyelination.* Brain, 2011. **134**(12): p. 3590-3601.

APPENDIX

Co-first Authorship Agreement for Thesis Use

This co-first authorship agreement is between Dr. Xuefang Pan and Mahsa Taherzadeh. The authors contributed equally to the research titled 'Glucosamine amends CNS pathology in mucopolysaccharidosis IIIC mouse expressing misfolded HGSNAT' and have agreed to share co-first authorship of the publication.

Mahsa Taherzadeh, the student, will use the publication in her manuscript-based thesis, which she will submit to the Department of Anatomy and Cell Biology at McGill University as part of her Ph.D. degree. Dr. Xuefang Pan acknowledges that Mahsa Taherzadeh has the right to use the publication for this purpose and agrees not to use the publication in a thesis or any other academic work that could conflict with the student's use of the publication in her thesis.

Xuefang Pan

April, 06, 2023